LPV MODELING AND ROBUST CONTROL OF YAW AND ROLL MODES OF ROAD VEHICLES

by

Selahattin Çağlar Başlamışlı

B. Sc., in Mechanical Engineering, Middle East Technical University, 1999

M. Sc., in Mechanical Engineering, Middle East Technical University, 2001

Submitted to the Institute for Graduate Studies in
Science and Engineering in partial fulfillment of
the requirements for the degree of
Doctor of Philosophy

Graduate Program in Mechanical Engineering

Boğaziçi University

2007

LPV MODELING AND ROBUST CONTROL OF YAW AND ROLL MODES OF ROAD VEHICLES

APPROVED BY:

Assoc. Prof. İbrahim Emre Köse (Thesis Supervisor)	.....
Prof. Günay Anlaş (Thesis Co-supervisor)	.....
Emeritus Prof. Akın Tezel	.....
Assist. Prof. Hilmi Luş	.....
Prof. Levent Güvenç	.....

DATE OF APPROVAL: 26.01.2007

ACKNOWLEDGEMENTS

I would like to thank my advisors Professor Emre Köse and Professor Günay Anlaş for their guidance and support. The valuable feedback from Professor Emre Köse in Control Theory and his encouraging friendly approach inspired me to improve my work.

My special thanks go to my dear fellow graduate students of Mechanical Engineering Department at Boğaziçi University for their fruitful discussions and comments which have immense importance to the completion of this dissertation.

This thesis was supported by Tübitak Münir Birsel Scholarship. I would also like to thank Autocom for their support.

Finally, I would like to thank my parents for their encouragement and support throughout my academic career.

ABSTRACT

LPV MODELING AND ROBUST CONTROL OF YAW AND ROLL MODES OF ROAD VEHICLES

In this thesis, the usefulness of linear parameter varying (LPV) modeling of vehicle dynamics is investigated for controller synthesis to take nonlinear tire behavior into account. The H_∞ control framework is used to design combined active steering and differential controllers to improve vehicle handling during maneuvers involving large driver commanded steering angles.

Two approaches are undertaken to reduce the size of the parameter set to minimize solver time during the controller synthesis step. The first approach is built on modeling tire stiffnesses as parametric uncertainties. This leads to a linear fractional transformation (LFT) model of the combined vehicle body and tire subsystems and to the design of a static state feedback controller intended to be robust against large variations in parameters. In the second approach, a rational fit is proposed for the nonlinear tire model used, and original parametric vehicle models are derived by integrating the fitting model into the equations of motion. This leads to the design of gain-scheduled LPV controllers where scheduling is based on lateral and longitudinal tire slips.

At small driver commanded steering angles, both controllers achieve decoupling of sideslip and yaw rate modes. However, at large driver commanded steering angles, the steering response of the first controller is observed to be unstable at the physical limit of the vehicle due to the shortcomings of the parametric uncertainty model in predicting tire behavior at large lateral slip. Meanwhile, the second controller achieves

decoupling of all vehicle modes for the whole range of driver commanded steering angles up to and at the physical limit of the vehicle, revealing the importance of incorporating the tire friction circle concept into the controller synthesis.

ÖZET

YOL TAŞITLARININ DPD MODELLENMESİ VE KAYMA VE DEVRİLME KİPLERİNİN DAYANIKLI DENETİMİ

Bu tezde, doğrusal olmayan tekerlek davranışının, denetimci sentezine katılması ile ilgili olarak, doğrusal parametreleri değişken (DPD) taşıt dinamiği modellemesinin verimliliği araştırılmaktadır. Sürücü denetimindeki direksiyon açısının artan değerlerinde taşıt yol tutuşunun iyileştirilmesi için, H_∞ denetimi çerçevesinde bileşik aktif yönlendirme ve diferansiyel denetimcileri tasarlanmıştır.

Denetimci sentezi aşamasında, çözücü zamanının kısaltılması için, parametre kümesi eleman sayısının küçültülmesi doğrultusunda iki yaklaşım ele alınmıştır. Birinci yaklaşımda, tekerlek sertlikleri parametrik belirsizlikler olarak modellenmiştir. Bu yaklaşım, bileşik gövde ve tekerlek altsistemleri ile ilgili doğrusal kesirsel bir dönüşüm modelinin elde edilmesini ve büyük parametre değişimlerine dayanıklı, statik durum geri beslemeli bir denetimcinin tasarlanmasını sağlar. İkinci yaklaşımda, kullanılan doğrusal olmayan tekerlek modeline rasyonel bir fonksiyon uydurulmuş ve uydurulan fonksiyonun hareket denklemlerine katılmasıyla orijinal parametrik taşıt denklemleri türetilmiştir. Bu yaklaşım ise, parametreleri yanal ve doğrusal tekerlek kaymalarının fonksiyonu olan, DPD denetimcilerinin tasarımını sağlar.

Sürücü denetimindeki direksiyon açısının küçük değerlerinde, her iki denetimci de yanal kayma ve açısal hız kiplerinin ayrılmasını sağlar. Ancak, sürücü denetimindeki direksiyon açısının büyük değerlerinde, parametrik belirsizlik modelinin büyük yanal kayma durumundaki tekerlek davranışını göstermedeki yetersizliklerinden dolayı, ilk denetimcinin taşıtın fiziksel sınırındaki yönlendirme tepkisinin kararsız olduğu gözlenir.

İkinci denetimci ise, taşıtın gerek fiziksel sınırına kadar gerekse fiziksel sınırında olan sürücü denetimindeki bütün direksiyon açılarında, tüm taşıt kiplerinin ayrılmasını sağlayarak, tekerlek sürtünme çemberi kavramının denetimci sentezine katılmasının önemini ortaya çıkarır.

TABLE OF CONTENTS

ACKNOWLEDGEMENTS . . . iii
ABSTRACT . . . iv
ÖZET . . . vi
LIST OF FIGURES . . . xiii
LIST OF TABLES . . . xx
LIST OF SYMBOLS/ABBREVIATIONS . . . xxi
1. INTRODUCTION . . . 1
1.1. Subcomponents of Integrated Vehicle Control . . . 2
1.1.1. Anti-lock Braking Systems . . . 2
1.1.2. Active Braking and Active Differential Control . . . 4
1.1.3. Active Front Steering Control . . . 9
1.2. Research on Integrated Vehicle Control . . . 11
1.3. Motivation and Problem Statement . . . 13
1.4. Organization of the Thesis . . . 15
2. MODELING . . . 18
2.1. Basic Aspects of Tire Force Generation . . . 18
2.1.1. Nonlinear Tire Behavior . . . 18
2.2. The Magic Formula . . . 21
2.2.1. Tire Longitudinal Force . . . 22
2.2.2. Tire Cornering Force . . . 23
2.2.3. A Rational Fit to the Magic Formula . . . 24
2.3. Nonlinear Six-Degree-of-Freedom Vehicle Model . . . 30
2.3.1. Angular Kinematics . . . 31
2.3.2. Linear Kinematics . . . 33
2.3.3. Total External Forces and Moments . . . 34
2.3.4. Summary of the Governing Equations . . . 37
2.4. Linear Vehicle Models . . . 40
2.4.1. Linear Bicycle Model . . . 40
2.4.2. Linear Yaw-Roll Model . . . 41

2.5. A Parametric Bicycle Model 42
2.6. Comments 45
3. ROBUST CONTROL SYSTEM DESIGN 46
3.1. Analysis of LTI System through LMIs 46
3.1.1. H_∞ Norm 47
3.1.2. Computation of the H_∞ Norm 49
3.1.3. Linear Matrix Inequalities 50
3.1.4. Computation of the H_∞ Norm with LMIs 52
3.2. H_∞ Control of LTI Systems 52
3.2.1. Addition of Frequency Weights 54
3.3. Linear Parameter Varying Systems 55
3.3.1. Linear Fractional Transformations 56
3.3.2. Induced-$\mathcal{L}_2$ Gain of LPV System 59
3.4. H_∞ Control of LPV Systems 60
3.4.1. Disturbance Attenuation for LPV Systems 60
3.4.2. Robust Full State Feedback Controller Design 61
3.5. Comments 63
4. ROBUST WHEEL-SLIP CONTROLLER DESIGN 64
4.1. Introduction 64
4.2. Modeling of Braking Dynamics 64
4.2.1. Equations of Motion in ω and U 64
4.2.2. Equations of Motion in λ and U 66
4.3. The ABS Control Problem 69
4.4. Design Examples 72
4.4.1. Controller Design 72
4.4.2. A Qualitative Stability and Robustness Analysis for the Tuning of Design Parameters 74
4.4.3. Simulation Results for Conditions Beyond Design Specifications 77
4.5. ABS System Implementation on Full Scale Vehicle 79
4.5.1. Brake Force Proportioning 80
4.5.2. $\lambda_i^\star$ Estimation 81
4.6. Comments 84

5. ROBUST CONTROL OF VEHICLE DYNAMICS 87
5.1. Nonlinear Two-Track Yaw Plane Vehicle Model Extended with Wheel Dynamics 87
5.1.1. Exact Equations 87
5.1.2. LPV System Representation 90
5.2. The Control Objective 94
5.3. Controller Design 94
5.3.1. Reference Values 94
5.3.2. Prediction of Parameter Bounds 96
5.3.3. Selection of Frequency Weights 97
5.3.4. Explicit Controller Formulae 99
5.4. Simulation Results 100
5.4.1. Critical Maneuvers 100
5.4.2. Simulation 1: Performance of K_1 for Small δ_f 101
5.4.3. Simulation 2: Performance of K_1 on Slippery Road 102
5.4.4. Simulation 3: Performance of K_2 for Conditions Away from Nominal 102
5.5. Comments 106
6. GAIN SCHEDULED CONTROL OF VEHICLE DYNAMICS 108
6.1. Robust Gain-Scheduled LPV Controller Synthesis 108
6.2. LPV modeling of Vehicle Systems 112
6.2.1. Expression of Axle Forces with Rational Tire Model 112
6.2.2. Active Front Steering and Active Front Differential Control . . 114
6.2.3. Active Front Steering, Active Front Differential and Roll Mode Active Suspension Control 116
6.3. Controller Design 118
6.3.1. Parameter Bounds 118
6.3.2. Frequency Weights 118
6.4. Simulation Results for Integrated Active Front Steering and Active Front Differential Control 119
6.4.1. Simulation 4: Mode Decoupling at Small Driver Commanded Steering Angle 120

6.4.2. Simulation 5: Mode Decoupling at Large Driver Commanded Steering Angle . . . 120
6.4.3. Simulation 6: Controller Performance on Slippery Road . . . 120
6.5. Simulation Results for Integrated Active Front Steering, Active Front Differential and Active Suspension Control . . . 133
6.5.1. Simulation 7: Mode Decoupling at Small Driver Commanded Steering Angle . . . 133
6.5.2. Simulation 8: Controller Performance at Large Driver Commanded Steering Angle . . . 133
6.5.3. Simulation 9: Controller Performance on Slippery Road . . . 134
6.6. Comments . . . 147
7. CONTROL AUTHORITY SHARING IN ROLLOVER PREVENTION . . . 148
7.1. Motivation . . . 148
7.2. The Load Transfer Ratio (LTR) . . . 149
7.3. Steering System Model . . . 149
7.4. Automatic Vehicle Controller Model . . . 152
7.5. Controller Design . . . 153
7.6. Simulation Results . . . 154
7.6.1. Preliminary Simulation . . . 154
7.6.2. Supervisory Control . . . 155
7.6.3. First Panic Scenario . . . 156
7.6.4. Second Panic Scenario . . . 156
7.7. Comments . . . 157
8. CONCLUSIONS AND RECOMMENDATIONS FOR FURTHER WORK . . . 159
8.1. Contributions . . . 160
8.1.1. LPV Modeling of Vehicle Subsystems . . . 160
8.1.2. Rational Tire Modeling Formulation and Vehicle Parametric Descriptor Formulations . . . 160
8.1.3. Robust Anti-Lock Braking System Design . . . 160
8.1.4. Robust Integrated Vehicle Control Design . . . 161
8.1.5. Gain Scheduled Integrated Vehicle Control Design . . . 161
8.2. Recommendations for Further Work . . . 162

8.2.1. Further Verification of Controller Robustness 162
8.2.2. Enhancement of the Performance and Robustness of the LPV Controller by Scheduling on More Parameters 162
8.2.3. Consideration of Other LFT/LPV Controller Synthesis Methods 163
8.2.4. Inclusion of a Driver Model in the Control Loops 163
APPENDIX A: VEHICLE AND TIRE DATA 165
APPENDIX B: LPV MATRICES FOR ROBUST COMBINED ACTIVE STEERING AND ACTIVE DIFFERENTIAL CONTROL DESIGN 167
APPENDIX C: PARAMETRIC DESCRIPTOR REPRESENTATION OF BICYCLE AND YAW-ROLL MODELS FOR GAIN-SCHEDULED CONTROL DESIGN 173
REFERENCES 177

LIST OF FIGURES

Figure 1.1. Sketch of a typical electromechanical brake system 4

Figure 1.2. Yaw moment generation by individual wheel braking 6

Figure 2.1. Positive directions of slip angle, tire forces and moments 19

Figure 2.2. Tire behavior under pure and combined slip conditions. 20

Figure 2.3. Generic lateral tire force *vs* slip angle obtained by the Magic Formula 25

Figure 2.4. $G_{y\lambda}$ *vs* longitudinal slip obtained by the Magic Formula 26

Figure 2.5. Rational function (dashed lines with x markers) *vs* Magic Formula (solid lines) ($F_z = 1.0\,kN$; combined slip conditions) 28

Figure 2.6. Rational function (dashed lines with x markers) *vs* Magic Formula (solid lines) ($F_z = 2.5\,kN$; combined slip conditions) 28

Figure 2.7. Rational function (dashed lines with x markers) *vs* Magic Formula (solid lines) ($F_z = 4.0\,kN$; combined slip conditions) 29

Figure 2.8. Rational function (dashed lines with x markers) *vs* Magic Formula (solid lines) ($F_z = 5.5\,kN$; combined slip conditions) 29

Figure 2.9. Rational function (dashed lines with x markers) *vs* Magic Formula (solid lines) ($F_z = 7.0\,kN$; combined slip conditions) 30

Figure 2.10. Six-degree-of-freedom vehicle model. 31

Figure 2.11. Free-body diagram of unsprung mass 35

Figure 2.12. Free-body diagram of sprung mass 36

Figure 2.13. Bicycle Model 40

Figure 2.14. Vehicle response for driver's small step input ($\delta_f = 1^o$) 44

Figure 2.15. Vehicle response for driver's large step input ($\delta_f = 5^o$) 45

Figure 3.1. LTI system 47

Figure 3.2. Standard H_∞ control problem 53

Figure 3.3. H_∞ control problem augmented with frequency weights 55

Figure 3.4. LPV system with model uncertainty 56

Figure 3.5. Mass/spring/damper system 57

Figure 3.6. LPV disturbance attenuation problem 61

Figure 4.1. Quarter car braking model 65

Figure 4.2. Longitudinal braking force *vs* longitudinal slip 66

Figure 4.3. Feedback interconnection augmented with weights 70

Figure 4.4. Braking controller performance on varying μ road. 74

Figure 4.5. Variation of braking force and C_λ on varying μ road. 75

Figure 4.6. Controller performance in face of actuator delay 78

Figure 4.7. Braking controller performance (outside design range) 79

Figure 4.8. Variation of braking force (outside design range) 80

Figure 4.9. Partial braking performance during mild cornering 82

Figure 4.10. Straight-line braking performance 84

Figure 4.11. Braking performance on split μ road ($\mu_{high} = 0.7/\mu_{low} = 0.2$) . . . 85

Figure 5.1. Nonlinear two-track yaw plane vehicle model 88

Figure 5.2. Block diagram for combined active steering and active differential control problem 93

Figure 5.3. Integrated controller performance during J-turn maneuver on dry road ($\mu = 1$) (Simulation 1) 101

Figure 5.4. Integrated controller performance during sinusoidal turn maneuver on dry road ($\mu = 1$) (Simulation 1) 103

Figure 5.5. Parameter variation during J turn maneuver on dry road ($\mu = 1$) (Simulation 1) 103

Figure 5.6. Parameter variation during sinusoidal turn maneuver on dry road ($\mu = 1$) (Simulation 1) 104

Figure 5.7. Integrated controller performance during J turn maneuver on low μ road ($\mu = 0.5$) (Simulation 2) 104

Figure 5.8. Integrated controller performance during sinusoidal turn maneuver on low μ road ($\mu = 0.5$) (Simulation 2) 105

Figure 5.9. Active differential performance during J turn maneuver on low μ road ($\mu = 0.5$) (Simulation 3) 105

Figure 5.10. Active differential performance during sinusoidal steering maneuver on low μ road ($\mu = 0.5$) (Simulation 3) 106

Figure 6.1. Combined steering and differential controller performance on dry road ($\mu = 0.8$) for small driver commanded steering angle (sinusoidal steering) 121

Figure 6.2. Parameter variation on dry road ($\mu = 0.8$) for small driver commanded steering angle (sinusoidal steering) 122

Figure 6.3. Combined steering and differential controller performance on dry road ($\mu = 0.8$) for small driver commanded steering angle (J turn) 123

Figure 6.4. Parameter variation on dry road ($\mu = 0.8$) for small driver commanded steering angle (J turn) 124

Figure 6.5. Combined steering and differential controller performance on dry road ($\mu = 0.8$) for sinusoidal steering maneuver 125

Figure 6.6. Parameter variation on dry road ($\mu = 0.8$) for sinusoidal steering maneuver 126

Figure 6.7. Combined steering and differential controller performance on dry road ($\mu = 0.8$) for J turn cornering maneuver 127

Figure 6.8. Parameter variation on dry road ($\mu = 0.8$) for J turn cornering maneuver 128

Figure 6.9. Combined steering and differential controller performance on slippery road ($\mu = 0.4$) for sinusoidal steering maneuver 129

Figure 6.10. Parameter variation on slippery road ($\mu = 0.4$) for sinusoidal steering maneuver 130

Figure 6.11. Combined steering and differential controller performance on slippery road ($\mu = 0.4$) for J turn cornering maneuver 131

Figure 6.12. Parameter variation on slippery road ($\mu = 0.4$) for J turn cornering maneuver 132

Figure 6.13. Combined steering, differential and suspension controller performance on dry road ($\mu = 0.8$) for small driver commanded steering angle (sinusoidal steering) 135

Figure 6.14. Parameter variation on dry road ($\mu = 0.8$) for small driver commanded steering angle (sinusoidal steering) 136

Figure 6.15. Combined steering, differential and suspension controller performance on dry road ($\mu = 0.8$) for small driver commanded steering angle (J turn) 137

Figure 6.16. Parameter variation on dry road ($\mu = 0.8$) for small driver commanded steering angle (J turn) 138

Figure 6.17. Combined steering, differential and suspension controller performance on dry road ($\mu = 0.8$) for sinusoidal steering maneuver . . . 139

Figure 6.18. Parameter variation on dry road ($\mu = 0.8$) for sinusoidal steering maneuver 140

Figure 6.19. Combined steering, differential and suspension controller performance on dry road ($\mu = 0.8$) for J turn cornering maneuver 141

Figure 6.20. Parameter variation on dry road ($\mu = 0.8$) for J turn cornering maneuver 142

Figure 6.21. Combined steering, differential and suspension controller performance on slippery road ($\mu = 0.4$) for sinusoidal steering maneuver 143

Figure 6.22. Parameter variation on slippery road ($\mu = 0.4$) for sinusoidal steering maneuver 144

Figure 6.23. Combined steering, differential and suspension controller performance on slippery road ($\mu = 0.4$) for J turn cornering maneuver . 145

Figure 6.24. Parameter variation on slippery road ($\mu = 0.4$) for J turn cornering maneuver 146

Figure 7.1. Steering system model with rack type controller 151

Figure 7.2. Steering system model with column type controller 151

Figure 7.3. Rack-and-pinion mechanism 152

Figure 7.4. AVC activity control loop 153

Figure 7.5. Closed loop system 153

Figure 7.6. Results of preliminary simulation 154

Figure 7.7. Controlled system configuration with dead-zone 155

Figure 7.8. Results obtained with supervisory control 156

Figure 7.9. Results of first panic scenario 157

Figure 7.10. Results of second panic scenario 158

LIST OF TABLES

Table 2.1. Optimized Shape Factors at different loads 27

Table 4.1. Controller gains according to low frequency gain φ 73

Table 4.2. $\lambda^{\star}$ estimation based on μ_{eq_i} and $F_{zi}[kN]$ 83

LIST OF SYMBOLS/ABBREVIATIONS

a	Distance from the vehicle center of gravity to the front axle
$\boldsymbol{A}$	System matrix
$\boldsymbol{A_c}$	System matrix of output feedback controller
$\boldsymbol{A_d}$	System matrix of disturbance weight
$\boldsymbol{A_e}$	System matrix of output error weight
$\boldsymbol{A_{ref}}$	System matrix of reference weight
a_x/a_y	Vehicle longitudinal/lateral acceleration
b	Distance from the vehicle center of gravity to the rear axle
B_c	Damping coefficient of viscous damping acting on steering column
$\boldsymbol{B_c}$	Input matrix of output feedback controller
$\boldsymbol{B_d}$	Input matrix of disturbance weight
$\boldsymbol{B_e}$	Input matrix of output error weight
$\boldsymbol{B}$, $\boldsymbol{B_p}$, $\boldsymbol{B_w}$, $\boldsymbol{B_u}$	Input matrices of open loop system
B_r	Damping coefficient of viscous damping acting on steering rack
$\boldsymbol{B_{ref}}$	Input matrix of reference weight
B_x, $B_{x\alpha}$, B_y, $B_{y\lambda}$	Magic Formula coefficients
c	Horizontal distance from the center of gravity of sprung mass to CG
$\boldsymbol{C_c}$	Output matrix of output feedback controller
$\boldsymbol{C_d}$	Output matrix of disturbance weight
$\boldsymbol{C_e}$	Output matrix of output error weight
c_i	i^{th} suspension damping
$\boldsymbol{C}$, $\boldsymbol{C_q}$, $\boldsymbol{C_y}$, $\boldsymbol{C_z}$	Output matrices of open loop system
$\boldsymbol{C_{ref}}$	Output matrix of reference weight
C_x, $C_{x\alpha}$, C_y, $C_{y\lambda}$	Magic Formula coefficients
$C_\alpha/\ C_\lambda$	Tire lateral/longitudinal stiffness
$C_{\alpha f}/\ C_{\alpha r}$	Front/rear axle cornering stiffness
$C_{\gamma f}$	Camber thrust coefficient at the front axle

c_R	Roll damping
d	Vehicle track
$\boldsymbol{D}$	Direct feedthrough matrix
$\boldsymbol{D_c}$	Direct feedthrough matrix of output feedback controller
$\boldsymbol{D_d}$	Direct feedthrough matrix of disturbance weight
$\boldsymbol{D_e}$	Direct feedthrough matrix of output error weight
$\boldsymbol{D_{ref}}$	Direct feedthrough matrix of reference weight
$\boldsymbol{D_{qp}}$, $\boldsymbol{D_{zp}}$, $\boldsymbol{D_{yp}}$, $\boldsymbol{D_{qu}}$, $\boldsymbol{D_{zw}}$, $\boldsymbol{D_{zu}}$, $\boldsymbol{D_{qw}}$, $\boldsymbol{D_{yw}}$	Direct feedthrough matrices of open loop system
D_x, D_y	Magic Formula coefficients
e	Horizontal distance from the center of gravity of unsprung mass to CG
E_x, $E_{x\alpha}$, E_y, $E_{y\lambda}$	Magic Formula coefficients
F_x/F_{xo}	Tire longitudinal force (combined slip/pure slip)
F_y/F_{yo}	Tire lateral force (combined cornering/pure slip)
F_z/F_{zo}	Tire actual/nominal normal load
$\mathcal{F}$	Total external force
h_s	Vertical distance from the center of gravity of sprung mass to CG
h_θ	Vertical distance from the center of gravity of sprung mass to pitch axis
h_ϕ	Vertical distance from the center of gravity of sprung mass to roll axis
I_{xxs}	Moment of inertia about the x-axis of the rolling sprung mass
I_{xzs}	Product of inertia about the x-z axes of the rolling sprung mass
I_{zzs}	Moment of inertia about the z-axis of the rolling sprung mass
I_{zzu}	Moment of inertia about the z-axis of unsprung mass
J_c	Steering column mass moment of inertia
J_w	Tire mass moment of inertia
J_z	Vehicle mass moment of inertia
$\boldsymbol{\mathcal{J}_i}$	Inertia tensor of i^{th} body

K_c	Stiffness coefficient of torsional spring used for modeling steering column
$\boldsymbol{K}$	Controller
k_i	i^{th} suspension stiffness
k_R	Roll stiffness
K_r	Stiffness coefficient of linear spring assumed to be acting on steering rack
L_p, L_ϕ	Stability derivatives of yaw-roll model related to roll motion
$M/M_s/M_u$	Total/sprung/unsprung mass
M_r	Mass of steering rack
$\mathcal{M}$	Total external moment
N_r, N_β, N_δ, N_ϕ	Stability derivatives of yaw-roll model related to yaw motion
p	Roll rate
p_K, p_V, p_H, p_C, p_D, p_E	Magic Formula coefficients
r	Yaw rate
r_C, r_B, r_E, r_V	Magic Formula coefficients
r_p	Pinion radius
$\boldsymbol{R_s}/\boldsymbol{R_u}$	Position vector of sprung/unsprung mass
R_w	Tire rolling radius
R_z	Sprung mass bounce
S_{vx}, S_{vy}, $S_{Vy\lambda}$	Magic Formula coefficients
T_b	Tractive/braking torque
T_d	Driver torque on steering handwheel
$\boldsymbol{u}$	Control input
U	Vehicle speed
U_x/U_y	Vehicle longitudinal/lateral speed
v_x/v_y	Tire longitudinal/lateral speed
$\boldsymbol{w}$	Disturbance input
W_d	Disturbance weight
W_e	Output weight
W_{ref}	Reference weight

$\boldsymbol{x}$	State vector
$\boldsymbol{x_d}$	State vector of disturbance weight
$\boldsymbol{x_e}$	State vector of output error weight
x_r	Rack displacement
$\boldsymbol{x_{ref}}$	State vector of reference weight
$\boldsymbol{y}$	Measured output
Y_r, Y_β, Y_δ, Y_ϕ	Stability derivatives of yaw-roll model related to lateral motion
$\boldsymbol{z}$	Controlled output
α	Tire lateral slip angle
$\alpha^\star$	Tire lateral slip angle at which cornering force is maximum
β	Sideslip angle
γ	Disturbance attenuation level
δ_f/δ_r	Front/rear steering angle
δ_i	Uncertainty parameter
Δ	Uncertainty matrix
η_α, η_λ, η_z	Shape factors of rational model
θ	Pitch angle
θ_c	Angular position of steering handwheel
θ_R	Inclination of the roll axis
κ_K, κ_V, κ_H,	
κ_μ, κ_C	Magic Formula coefficients
λ	Tire longitudinal slip
λ_{max}	Largest eigenvalue
$\lambda^\star$	Tire longitudinal slip at which longitudinal force is maximum
λ^*	Tire longitudinal slip at which inflection of $G_{y\lambda}$ occurs
μ	Road adhesion coefficient
μ_x/μ_y	Road adhesion coefficient in longitudinal/lateral direction
μ_o	Nominal road adhesion coefficient
ρ_i	Scheduling parameter
σ_{max}	Largest singular value

ϕ	Roll angle
χ_α, χ_λ, χ_z	Rational model shape factors
ψ	Yaw angle
$\omega/\omega_s/\omega_u$	Tire/sprung mass/unsprung mass rotational speed

ABS	Anti-lock Braking System
CG	Center of Gravity (whole vehicle)
EMB	Electromechanical brake
ESP	Electronic Stability Program
GPS	Global Positioning System
ICM	Integrated Chassis Management
LFT	Linear fractional transformation
LTR	Load Transfer Ratio
LMI	Linear matrix inequality
LPV	Linear parameter varying
LTI	Linear time invariant
MIMO	Multi input multi output
PID	Proportional integral derivative
VDC	Vehicle Dynamics Control
VDM	Vehicle Dynamics Management

1. INTRODUCTION

In 2005, 65 million road vehicles were estimated to be produced and more than 800 million were registered worldwide [1]. The numbers indicate why there is a need to consider the impact of all these vehicles on the environment, safety, personal security and personal comfort. The perpetual satisfaction of the desire for personal transportation requires developing vehicles that minimize the consequences on the environment and maximize highway and fuel resources, while providing security and comfort.

Active safety is one of many vehicle control challenges automotive engineers are faced with and encompasses research fields such as:

- Collision warning and control;
- Lateral control issues for steering assist and lane keeping;
- Adaptive cruise control;
- Vehicle dynamics control (VDC).

VDC consists in the development of active chassis systems such as:

- Anti-lock braking systems (ABS) which minimize braking distance while maintaining vehicle steerability;
- Active braking systems (such as BOSCH's ESP -Electronic Stability Program) which create a stabilizing yaw moment on the vehicle through individual wheel braking;
- Active suspension systems such as the air spring system, the continuous damper control, the active roll control, and the active body control which improve handling and reduce rollover propensity by redistribution of wheel loads;
- Active steering systems such as electronic power steering, active front and rear steering which improve steering feel and vehicle handling respectively.

The integration of several of these active chassis systems for improved vehicle

handling is known under the name *Integrated Chassis Management* (ICM) (or equivalent integrated vehicle control) and constitutes the main area of investigation of this thesis.

1.1. Subcomponents of Integrated Vehicle Control

Before introducing the design philosophies of current integrated vehicle control systems, working principles of some of the active chassis systems cited above are explained in what follows.

1.1.1. Anti-lock Braking Systems

In the literature, one can distinguish between two completely different kinds of anti-lock brake system (ABS) designs: those based on logic switching from wheel deceleration information and those based on wheel slip regulation [2]. In this thesis, the wheel slip regulation approach is considered. Main design ABS design criteria appearing in the literature is given in the following paragraphs.

In [3], the design philosophy of the BOSCH ABS system is described. It is explained that the equation of motion for braking dynamics becomes nonlinear after transformation from wheel rotation to tire slip as state variable. Moreover, the nonlinear dependence of brake force on tire slip and the impossibility to control brake torque in the conventional hydraulic ABS system are claimed to be the major difficulties of the ABS design. Indeed, in such systems, a complex chain of events is triggered starting with an output command by the program to actuate the hydraulics and ending with a pressure change in the wheel brake cylinder. The exact mathematical description of these events is claimed to be far too complex to be used in the brake slip controller. For these reasons the brake slip controller is chosen to be a simple robust proportional integral derivative (PID) controller. If no correction is requested by the ESP controller, the reference longitudinal slip is set to a value which corresponds to the maximum of the μ-slip curve. Using the value of the difference between the reference longitudinal slip and an estimate of the actual slip, together with an estimate of the stationary

value of the brake force on the tire, the PID controller determines the nominal brake pressure value at each wheel.

Academic research in this field can be classified according to the control methodology used, the states and parameters to be estimated, the inclusion of actuator dynamics, methods involving linearization of nonlinear dynamics etc. Sliding mode control strategy is used in [4], emphasis being put on the ability of the control algorithm to track some preset wheel slip reference. No scheduling rule is presented for compensation against changes in road adhesion coefficient but stability is even guaranteed in the unstable region of the friction curve. In [5], a sliding mode pulse width modulator controller is designed. A genetic algorithm based estimation module for road adhesion coefficient is proposed. In [6], in order to compensate for the uncertainty associated with the state of road surface, an inverse map between vehicle deceleration and optimal slip-ratio is proposed. In [7], the authors propose a gain scheduling control structure based on longitudinal tire slip value, vehicle speed and maximum adhesion coefficient. The authors claim that tire slip and maximum friction coefficients are not directly measurable but can be estimated. Several local PID controllers that locally stabilize the system for different slopes of the friction curve and which tolerate time variations due to speed changes are designed, and convenient switchings between them are ensured. In [8] and [9], a novel dynamic tire model is proposed. Vehicle states and tire parameters are estimated online, which is used to compensate for changing road adhesion coefficient. A Lyapunov-based adaptive braking controller is designed to achieve near to maximum braking capability. The works of Petersen et al. [10, 11] have pioneered studies on the application of LMI/LPV (Linear Matrix Inequalities/ Linear Parameter Varying) control methods for the present problem. The controller design relies on local linearization and gain scheduling, the effects of this simplification being analyzed with an idealized Lyapunov-based nonlinear stability and robustness analysis, taking into account uncertain tire friction nonlinearities. Robust stability is demonstrated for a wide range of slip, tire friction and expected speed values.

Today's production ABS is a rule based control system that has exhaustive look-up tables for different braking scenarios. Controllers are tuned in a trial and error

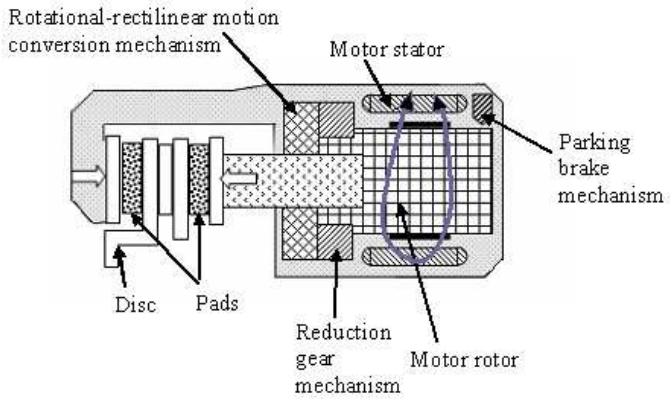


Figure 1.1. Sketch of a typical electromechanical brake system [12]

manner using simulations and exhaustive field testing [13]. The level of complexity of these systems is a serious limitation for the analysis and for the development of the current production ABS. To overcome this problem, the industrial trend is towards the development of electromechanical brakes (EMB) which will most probably replace hydraulic brakes in the near future along with the development of X-by-wire technology (Figure 1.1). These actuators allow the application of a smoother and continuous braking action on brake pad. Driver's braking command results in an electrical signal that is communicated via micro-controllers to the actuators, typically an electrical motor-driver unit. Wheel slip regulation, split μ braking and brake balancing tasks are all rendered much easier when compared to their counterparts in conventional hydraulic ABS systems. This is mainly due to the actuator dynamics which can effectively be approximated by a first order transfer function, which makes the whole system easier to control with available tools from feedback control theory.

1.1.2. Active Braking and Active Differential Control

The working principle of currently available active braking systems on the market is based on individual wheel slip control. These systems share a more or less similar control architecture. The operation of ESP, first introduced in 1995 by BOSCH, is presented in what follows [3].

From the steering angle, the accelerator pedal position and the brake pressure,

the desired vehicle response is derived while the actual vehicle response is derived from yaw rate and lateral acceleration. The system regulates the engine torque and the wheel brake pressures using traction control components to minimize the difference between the actual and the desired response. It seems reasonable to design a control system which makes the yaw rate equal to the yaw rate of the nominal motion. If this control is used on slippery road, then the lateral acceleration and the yaw rate do not correspond to each other and the sideslip angle increases rapidly. Therefore both yaw rate and sideslip angle must be limited to values that correspond to the road adhesion coefficient: both yaw rate and sideslip angle must be taken as controlled variables. Thus, one of the main tasks of ESP is to limit the vehicle sideslip angle in order to prevent vehicle spin. Another task is to keep the same angle below some characteristic value to preserve some yaw moment gain. The working principle of ESP is explained in the following paragraphs.

It is well known that both longitudinal and lateral forces developed by a tire depend on tire longitudinal and lateral slip and normal force. The lateral force a tire generates for a given lateral slip angle decreases with increasing magnitude of the longitudinal tire slip. This property is used for the control of the lateral force and the yaw moment: longitudinal tire slip is used as the basic control variable of the control algorithm. The influence of longitudinal slip on a tire is to rotate the resultant force on the controlled tire and then to change the yaw moment, the lateral force and the longitudinal force on the vehicle. This rotation can be done freely at each tire. As a result, the yaw moment on the vehicle can be changed. The control concept of ESP is explained in the following paragraph.

ESP determines by what amount the longitudinal slip at each tire shall be changed to generate the required change in yaw moment. As the bandwidth of the wheels is larger than the bandwidth of the vehicle, a cascade control structure is chosen in which the inner feedback loop controls the wheel slips and the outer feedback loop controls vehicle response. In the outer feedback loop corrections in reference longitudinal slip values of tires to be supplied to the inner feedback loop, which consists of the ABS controller, are derived from the difference between the reference and actual vehicle

responses. A model following control strategy is implemented in the outer loop: a first value of the reference yaw rate is obtained as the steady state gain between driver commanded steering angle and yaw rate obtained from the classical bicycle model. Reference yaw rate is limited by maximum road adhesion coefficient. Since the latter is generally unknown, the measured lateral acceleration is taken instead to derive an estimate of the lateral adhesion coefficient. Moreover, the vehicle sideslip angle is constrained by a decreasing function of the speed and must be kept at low levels at all times.

Once reference yaw rate and sideslip values are computed, error signals are sent to the ESP controller, typically a state-space controller. Output of the controller is a reference yaw moment. From this reference yaw moment, the required change in reference longitudinal slip values of each tire is computed. Finally, reference longitudinal slips are realized at each tire by local ABS controllers. The exact algorithms of all these processes are vaguely said to be based on state space and PID controls in [14].

Academic research in the field can be classified according to the control methodology used, the selection of the specific wheels to be braked and parameters to be estimated.

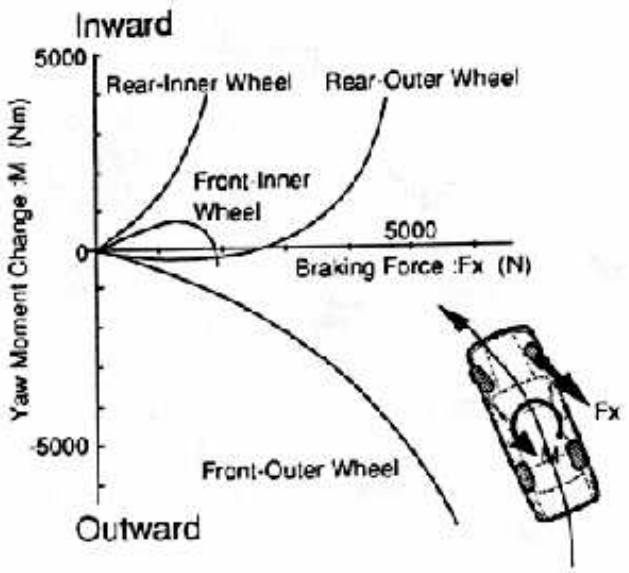


Figure 1.2. Yaw moment generation by individual wheel braking [15]

Yasui et al [15] illustrate interesting results on the selection of the wheel to be chosen for active braking (Figure 1.2). Yaw moment changes associated with the increase at each tire are computed. Braking the front outer wheel is seen to be very effective in stabilizing the vehicle motion. This is explained by the fact that both yaw moment changes due to the brake and cornering forces are seen to work in the same stabilizing direction up to large values of wheel slip, (nearly 40%). Surprisingly, stabilizing yaw moment change due to the braking of the rear-outer wheel is shown to be only up to 10% of longitudinal slip. On the other hand, the brake force yaw moment change is inward and the cornering force yaw moment change is outward for the front-inner wheel. Thus the front-inner wheel brake should be controlled over 50% of wheel slip ratio to generate an outward yaw moment. The rear-inner wheel brake does not generate an outward yaw moment. As an improvement to the previous study, Koibushi et al. [16] stress on the potential need to make use of rear wheel braking in case of understeer. During a sinusoidal steering maneuver, it is observed that the sideslip angle and wheel lateral slip angles increase suddenly, a typical oversteering situation, and can only be stabilized by decreasing the amplitude of front steering angle and braking the appropriate front wheel. Meanwhile, the results for a J turn maneuver indicate that if the front wheel slip angle exceeds a certain value by increasing the steer angle, the front wheel cornering force is saturated, and the cornering radius cannot be reduced, a typical understeering situation. Furthermore, the rear wheel slip angle is observed to be smaller than the angle at which rear tires generate maximum cornering force. It turns out that during a J turn the cornering radius may only be reduced by increasing steering angle as long as the front slip angle is kept below the tire lateral limit and the appropriate rear wheel is braked.

In [17], active braking systems involving both yaw rate feedback and full state feedback are compared. The estimation of the vehicle sideslip velocity based on integration of lateral acceleration, the use of algebraic equations using vehicle kinematics and the use of a Luenberger observer are presented. Steering angle command is observed to reach quite large values (up to 300^o of steering handwheel angle) during simulations and best results are obtained using the full state feedback strategy. In [18], yaw moment control is based on fuzzy logic. Simulations involving large driver commanded

steering angles (up to 6^o) seem to show the effectiveness of the proposed control method for the vehicle subjected to different cornering maneuvers such as lane change and J-turn under different driving conditions (dry and slippery road). In [19], a model based regulator control system is proposed for individual wheel braking. Simulation results are used to demonstrate the achievement of good yaw disturbance moment rejection. Unfortunately, maneuvers involving large driver commanded steering angles are not considered. Research presented in [20] is interesting as far as the implementation of an online optimization method for brake force distribution aiming rollover prevention is concerned. The control problem considered is divided into two subproblems: a controller design and a control allocator design. A gain scheduled discrete time linear quadratic controller following a linear reference model is used. The controller outputs the desired total requirements in lateral force and yaw moment and these are then allocated as brake forces to the four wheels by a control allocator which takes the friction circle concept into account by formulating it as a constraint of the online optimization. In [21], authors claim that a control threshold (decision to switch ESP on and off) can be determined by two basic approaches: **a)** yaw rate error and its variation, and **b)** phase plane analysis. Then they explain why the $(\beta - \dot{\beta})$ phase plane can offer more practical information about vehicle stability compared to a yaw rate-based method. Indeed, by performing a phase plane analysis with a two-degree-of-freedom vehicle model with a Magic Formula tire model, authors claim that the physical stability limit can be determined, the stable region being inside a diamond shaped area determined by saddle points. This information is then claimed to be recorded for each value of the steering angle and vehicle speed so as to trigger ESP during maneuvers. As far as controller design is concerned, sliding controllers are designed where the sliding variable is defined as a combination of the sideslip angle and the difference between the reference yaw rate and the actual yaw rate.

An alternative actuation mechanism for yaw control is active differential control as exposed in the work of Hancock et al [22]. Authors indicate that the advent of the overdriven differential makes it possible to control the magnitude and direction of torque transfer, which leads to the development of active differential control systems. Simulation results indicate that comparable results can be obtained by using the active

differential controller for a range of driving maneuvers. Authors attribute this to the use of two wheels instead of one making the vehicle controlled by active differential less prone to tire saturation. Authors conclude that an integration of the two systems can be conceived and should focus on the use of active braking only in situations where stability would be seriously compromised or when it would be deemed advantageous to reduce vehicle speed.

1.1.3. Active Front Steering Control

The active front steering system first developed by BMW consists of the addition of an electrical motor and a planetary gear set to the steering system to supply a corrective steering angle in order to improve vehicle handling. In [23], authors explain that, under normal road conditions at low and medium speeds, steering becomes more direct, requiring less steering effort of the driver, which increases the agility of the vehicle in city traffic. At high speeds, steering becomes less direct to improve directional stability. When cornering at high speeds, steering stiffens up by monitoring yaw rate: when the yaw rate sensor detects an oversteering situation, the active steering system turns wheels a few degrees towards opposite lock.

As far as academic research is concerned, several studies have been published to establish the advantages of using active front steering instead of active braking to improve drivability at low driver commanded steering angle. In [24], Ackermann et al. explain the superiority of active steering system over active braking to control yaw instabilities by comparing the yaw moment generation capacity of both systems at small driver commanded steering angle (during split μ braking for example). In [25], the loss of stability is shown to be caused by rear tire side force saturation. For the first time in the literature, the saturation characteristics of rear tires is modeled by a linear function with uncertain rear cornering stiffness. H_∞ control theory is used to design a front wheel steering controller to compensate for the instability against uncertainty. The designed controller is shown to work well on a nonlinear vehicle model, achieving robust stability and protecting the vehicle from spin. In [26], Mammar et al. obtain a linear fractional transformation (LFT) model of a bicycle model with nonlinear tire force

generation formulation. The computed diagonal uncertainty matrix contains variations in vehicle speed, front and rear tire cornering stiffnesses. The designed H_∞ controller combines a feedforward part which acts as a filter ensuring disturbance attenuation (the disturbance being the driver commanded steering angle and the objective to be minimized being yaw rate error) and a feedback part which is responsible for closed loop system stability and improved yaw damping. Simulations reveal the efficiency of the designed algorithm at various values of vehicle speed and road adhesion under lane change maneuvers. In [27], the uncertainties considered are vehicle mass, mass moment of inertia, road adhesion coefficient, and an active steering control scheduled with speed variations is implemented so as to achieve robustness against uncertainties and good rejection of yaw moment disturbances. In [28], a two degree of freedom yaw dynamics control architecture known as the disturbance observer is adapted to the vehicle yaw dynamics control problem, which is shown to robustly improve performance. Design specifications are formulated in terms of eigenvalues and in frequency domain as bounds on weighted sensitivity and complementary sensitivity functions. Feedback of yaw rate signal alone is considered. In all the above cited research, driver commanded steering angle is kept at low values and only disturbance rejection (side wind, split μ braking) properties of controllers are tested.

The main weakness of leaving the vehicle handling task to the driver's steering ability is the limited efficiency of steering at high turning angles. Shihabata [29] developed the β-method to analyze the influence of the sideslip angle of the vehicle on its maneuverability. One important result is that the sensitivity of yaw moment on the vehicle with respect to changes in the steering angle decreases rapidly as the sideslip angle increases. At large vehicle sideslip angles, variations in the steering angle hardly change the yaw moment while the absolute value of the yaw moment is then almost zero.

On dry asphalt roads the physical limit of a typical vehicle is reached at a sideslip angle of approximately $\pm 12^o$, while on ice this value is approximately $\pm 2^o$. During normal driving average drivers do not exceed $\pm 2^o$ [3]. Beyond this value the drivers are considered to have no experience. To be considered as effective at high levels

of vehicle sideslip, an active steering controller should quickly steer steering wheels towards opposite lock. The degree of correction or the rate of response may sometimes be beyond the capacities of currently produced active front steering systems. In such situations, active braking must be engaged.

1.2. Research on Integrated Vehicle Control

In the Vehicle Dynamics Management (VDM) system of BOSCH, total yaw torques are computed for the steering, suspension and brake subsystems and are then distributed as angle or torque commands in each subsystem [30]. In normal operation, the steering system controller assumes its usual function of improving drivability (i.e, speed dependent adaptation of the overall steering ratio) but, when considered as a part of VDM, is also responsible for vehicle stabilization in limit cornering maneuvers. Similarly, while the ordinary function of the active suspension system is to dampen vertical motion of the chassis and the wheels, in a critical turning maneuver, the objective of compensating for roll dynamics is of primary importance so as to improve handling by re-allocation of normal wheel loads. Results of preliminary experiments show that vehicles equipped with VDM are more easily driven when compared to vehicles equipped with ESP: the load on the driver is further reduced during critical lane change maneuvers and the braking distance is decreased during emergency braking on split μ road.

In [31], the integration of active front steering and active roll moment control systems in order to enhance vehicle controllability is proposed. A sliding mode controller is designed for the active front steering controller in order to influence the steering input of the driver by adding a correction steering angle for maintaining the vehicle yaw rate under control at all times. The active roll mode controller is designed to differentiate between the front and rear axle suspension forces in order to alter the vehicle yaw rate and to eliminate vehicle roll motion as well. The integrated control strategy is observed to provide less correction of the steering angle with better yaw rate tracking when compared to the system under the influence of active steering alone.

In [32], an integrated control structure with individual active control mechanisms, i.e. active anti-roll bars, active suspensions and an active brake mechanism, is proposed. The role of the active suspension is designated to improve passenger comfort and road holding, and to guarantee suspension working space. The role of the active anti-roll bars is designated to generate a stabilizing moment in order to balance the overturning moments generated by maneuvers. By using the active braking system, rollover prevention is claimed to be guaranteed, since active braking has the potential to reduce the lateral tire forces and to decelerate the vehicle. Authors argue that if all the control mechanisms are to be designed simultaneously, then a high-complexity model to be controlled should be constructed, including pitch, roll and vertical motions and that, in the control design, a large number of performance demands should be satisfied at the same time. Consequently, the authors have chosen to divide the control design into two tasks: a task for suspension design and another task for rollover prevention. The design of the control system is based on an H_∞ linear parameter varying method, where the varying parameters are selected as vehicle speed, lateral load transfer and a normalized fault parameter, related to malfunction of anti-roll bars. Simulations involve a step steering maneuver which brings the vehicle to impending rollover.

In [33], authors propose an ICM algorithm that achieves target vehicle responses expressed in terms of reference deceleration, yaw rate and sideslip angle commands under the assumption that all four wheels can be independently steered, driven and braked. Sliding mode control theory is used to determine total requirements in yaw moment, cornering force and brake force. The cost function in the ensuing optimization procedure is set to equalize the amount of usage at each tire while realizing the total requirements. A linear system of equations is solved at each time step to compute optimal tire force distribution in terms of longitudinal and lateral forces. Then active steering angles and traction/braking torque requirements at each wheel are found by using a simple inverse tire model. As a critique to the previous work, Ono et al [34] argue that the constraint concerning friction circle of each tire is not considered and the algorithm cannot ensure in general that tire forces of all wheels would be inside friction circles. Hence Ono et al. propose another ICM algorithm that is claimed to minimize work load of each tire while satisfying the friction circle which is set as a

constraint of the optimization problem.

In [35], authors investigate analysis and design issues concerned with the selection of possible sets of control channels that may be used to improve the maneuverability and handling of road vehicles. Based on notions of reachable sets and output function controllability, authors reach conclusions about the authority of input control channels on sets of controlled variables at steady-state. Accordingly, individual wheel torque control and rear steering are claimed to be most effective in tracking step signals in longitudinal speed, lateral speed and and yaw rate, while suspension forces are claimed to be most effective in regulating roll, pitch and bounce modes. Hence, the analysis, although based on idealistic steady-state assumptions, seems to indicate that overall control of vehicle modes should at least incorporate the conjugate action of individual wheel torque control and active suspension control.

In [36], the selection among active chassis systems in stabilizing vehicle response is based on the concept of maximum control authority, a measure of the remaining tire force generation potential of a given actuator. If based on the calculated control authority, the desired correction can be achieved by anyone of the available controllable chassis systems, then the one with the least degree of obtrusiveness and quick response is proposed to be activated. As the desired correction increases, the systems with more control authority is proposed to be activated. Unfortunately, the proposed coordination approach of active chassis systems is rather qualitative.

1.3. Motivation and Problem Statement

Part of the literature, which is especially related to the design of active steering control, is devoted to improve drivability under maneuvers executed at small driver commanded steering angle. While it is true that most of the driving process occurs in the so-called linear operation regime of tires where vehicle behavior is predictable and drivers are experienced, fatal accidents involving single vehicle crashes are mostly due to nonlinear vehicle behavior which is unfamiliar to most drivers [3]. Other part of the literature related to preserving vehicle stability at large driver commanded steering

angle is mainly based on active braking design and most of the research in this field relies on the robustness of controllers based on linear tire models in the presence of nonlinear tire characteristics, the exceptions being [25], [34] and [20] among the work cited above. Moreover, the use of active braking alone is insufficient when it comes to control more than one vehicle mode, i.e. when decoupling of sideslip and yaw rate modes is sought. In fact, the current industrial trend is towards the integration of more than one active chassis system towards achieving superior response for a range of driver commanded angles [30]. While it has been proved that active steering is efficient at small steering angles and that active braking is efficient at large steering angles [29]- [37], coordination of these controllers, i.e. during transition periods and for mode decoupling purposes, is an important issue.

Most of the research on the integration of active chassis systems to date has considered the control of each aspect of vehicle performance as a separate problem with different models being used to evaluate the performance of each of these aspects. However, when it comes to integrate several of active chassis controllers, the simple merging of individual vehicle control loops may lead to poor vehicle handling and even instability [37]. At present, the coordination of several active chassis systems constitutes a debate subject among researchers. Gordon et al [37] claim that "given the time and economic constraints of the modern automotive industry, it is not feasible to synthesize and validate the full set of vehicle controls in the form of a unified and centralized controller". An alternative proposed in [37] consists of considering hierarchical control architectures where upper level controls (i.e. ICM) coordinate the actions of lower level controls (i.e. ABS etc) through intelligent control tools (fuzzy logic, neural networks, etc). We believe that if a detailed model is available for controller synthesis, a multivariable control approach is preferable as it provides sound stability and robustness guarantees.

In the VDC industry, rule-based and proportional-integral-derivative (PID) controllers dominate due to their simplicity and their acceptable robustness in face of nonlinear vehicle behavior. On the other hand, it is obvious that the dependence of vehicle dynamics on parameters such as vehicle speed, cornering and longitudinal stiffnesses

determine the nonlinear behavior during combined cornering and driving/braking. Although they provide a sound basis for incorporating nonlinear tire behavior into controller design, optimization based control allocation methods (i.e. [20], [34], [33]) may be hard to implement in a real application. In that respect, we believe that robust control theory which allows investigating controller performance against vehicle parameter variations and especially recently developed gain scheduling control tools of nonlinear systems expressed in the linear parameter varying form may constitute an effective alternative in the coordination of active chassis systems towards integration.

To sum up, we investigate in this study the efficiency of:

1. linear parameter varying modeling of vehicle dynamics for controller synthesis to take nonlinear tire behavior into account and;
2. the H_∞ control framework in designing MIMO active steering and differential controllers to improve vehicle handling during maneuvers involving large driver commanded steering angles.

1.4. Organization of the Thesis

Chapter 2 summarizes important governing equations of vehicle dynamics. Nonlinear tire behavior is explained and the widely held integrated tire/road friction modeling formulation, the Magic Formula, is presented. A rational tire model approximating the Magic Formula for a range of tire slip is then proposed. Next, equations of motion for a six degree-of-freedom vehicle model incorporating all major vehicle modes are derived. Based on these equations, the equations of linear models such as the bicycle model and the yaw-roll model are derived. The chapter concludes with the presentation of a parametric bicycle model that approximates nonlinear vehicle behavior under large driver commanded steering angle input.

Chapter 3 presents results from H_∞ robust control theory in the linear matrix inequality framework. H_∞ robust control techniques for linear time invariant systems are introduced and extensions to linear systems with rational parameter dependence

are explained.

Chapter 4 proposes a robust control algorithm for anti-lock brake system. H_∞ control theory is applied for the design of static state feedback controllers. Stability and robustness analysis of the proposed solution are included. Necessary controller gain matrix tunings to be considered in the presence of noise and brake actuator delay are explained. Finally, the implementation of the system on a full scale vehicle is considered and implementation issues related to brake force proportioning and braking on split μ road are treated.

Chapter 5 suggests a robust control algorithm for combined active front steering and active front/rear differential controller design. Design objectives are selected as reference yaw rate and reference sideslip angle tracking during extreme cornering. In other words, decoupling of vehicle modes is sought. The design of a MIMO static state feedback controller involves obtaining an LPV representation of the nonlinear vehicle model where varying parameters arise from nonlinear tire behavior. A method for reducing the number of LPV parameters to render the problem tractable for the LMI solver at hand is proposed. Controller performance is tested for a range of driver commanded steering angles.

Chapter 6 revisits the handling problem of the previous chapter. First, a gain scheduled controller synthesis method developed for linear parameter varying systems expressed in the parametric descriptor form is presented. Then, a gain scheduled combined active steering and active differential control solution is proposed. To render the problem more challenging, rear active differential action is suppressed and vehicle stability is made totally dependent on steering and braking/traction control of front wheels. Controller synthesis is based on a parametric bicycle model which approximates nonlinear vehicle behavior at large lateral tire slip and under combined slip conditions. Secondly, an integrated vehicle control design method merging active front steering, active front differential and active suspension controllers is proposed. This time, the simulation model involves a vehicle with elevated CG. Controller synthesis is based on a parametric yaw roll mode in order to take the coupling of sideslip and yaw rate

modes with the roll mode into account. Both designs are tested for a range of driver commanded steering angles.

In Chapter 7, a prospective research direction concerning the integration of the proposed system on a commercial vehicle for rollover prevention is presented to work together with a reactive steering system warning drivers against rollover threats. The necessity of integration reveals itself again in this final configuration where steering feel is of paramount importance.

In Chapter 8, conclusions are made, a summary of the main contributions is given and recommendations for further work are included.

2. MODELING

This chapter summarizes governing equations of vehicle dynamics. First, basic aspects of tire force generation are explained. Simulations in this thesis are based on the widely held integrated tire/road friction modeling formulation, the Magic Formula, which is explained next. A simple rational tire model approximating the Magic Formula for a range of tire slip is then proposed. The accuracy of the fit is exhibited for varying normal load, tire lateral slip angle and longitudinal slip. Equations of motion for a six degree-of-freedom vehicle model incorporating all major vehicle modes are then derived. This model is particularly suitable for vehicle dynamics controller design as it provides all necessary control channels: active front and rear steering, traction/braking control of all wheels and active suspensions. Equations of linear models such as the bicycle model and the yaw-roll model are derived naturally from the nonlinear model. The chapter concludes with the presentation of a parametric bicycle model. This vehicle model is shown to approximate nonlinear vehicle behavior under large driver commanded steering angle input and is particularly suitable for gain scheduled control of vehicle dynamics as will be illustrated in Chapter 6.

2.1. Basic Aspects of Tire Force Generation

Tire characteristics determine the dynamic behavior of the road vehicle. In this section, an introduction is given to the basic aspects of the force generating properties of the pneumatic tire. Both pure and combined slip characteristics of the tire are discussed and typical features are presented.

2.1.1. Nonlinear Tire Behavior

An upright wheel rolling freely, that is without an applied driving torque, on a flat road surface, along a straight line, at zero sideslip, may be taken as the starting point with all components of slip equal to zero for the present analysis [38]. When wheel motion deviates from this, wheel slip occurs, additional tire deformation builds

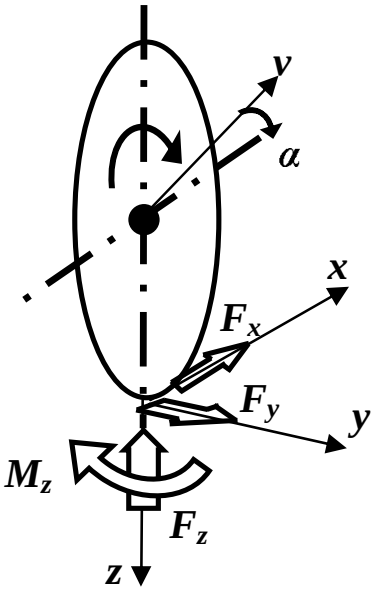


Figure 2.1. Positive directions of slip angle, tire forces and moments

up and a partial sliding in the contact patch occurs. As a result, additional horizontal forces and aligning torque are generated (Figure 2.1).

For a freely rolling wheel, forward velocity v_x and angular speed of revolution ω can be obtained from measurements. By dividing v_x by ω, the so-called effective rolling radius R_w is calculated as

$$R_w := \frac{v_x}{\omega}. \tag{2.1}$$

When a braking/tractive torque is applied about wheel spin axis, longitudinal slip arises. The definition of longitudinal slip, λ, is

$$\lambda := \frac{v_x - R_w\omega}{v_x}. \tag{2.2}$$

Its sign is taken such that, for a positive λ, a positive longitudinal force F_x arises.

Wheel slip in lateral direction (or tire sideslip angle) α is defined as

$$\tan \alpha = \frac{v_y}{v_x}. \tag{2.3}$$

The sign of α is taken such that the side force F_y is positive at positive sideslip angle.

The third and last slip quantity is the so-called spin which is due to rotation of the wheel about an axis normal to the road. Both the yaw rate resulting in path curvature when α remains zero, and the wheel camber contribute to spin. Camber angle dynamics depend on steering and suspension geometries. For simplicity, camber and spin effects are neglected throughout this study. Tire forces F_x and F_y are functions of slip components and wheel load F_z. For steady-state rectilinear motion, one has

$$F_x = F_x(\lambda, \alpha, F_z), \tag{2.4a}$$

$$F_y = F_y(\lambda, \alpha, F_z). \tag{2.4b}$$

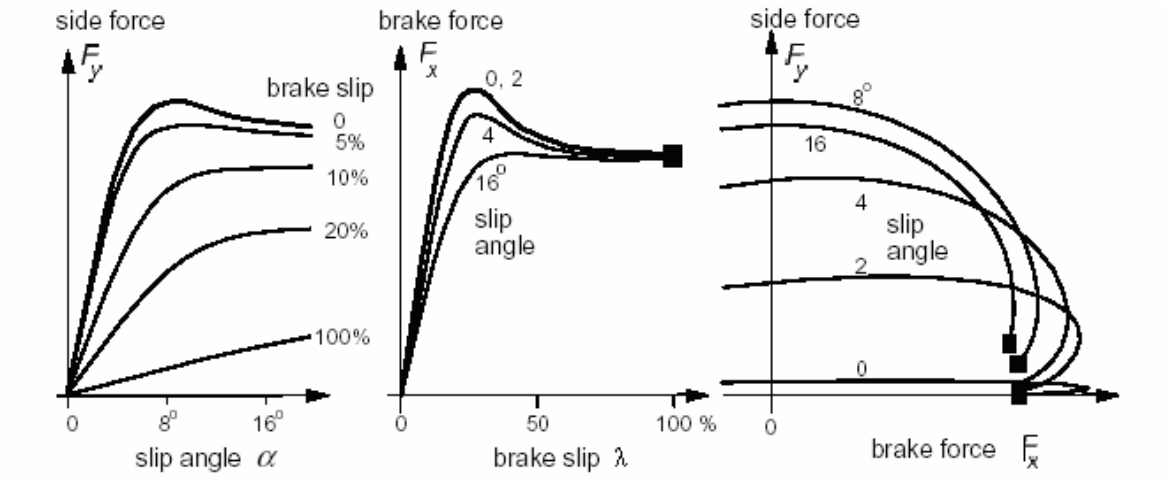


Figure 2.2. Tire behavior under pure and combined slip conditions [38]

In Figure 2.2, typical pure lateral ($\lambda = 0$) and longitudinal ($\alpha = 0$) slip characteristics are shown with a number of combined slip curves. Here, *pure slip* is defined to be the situation when either longitudinal or lateral slip occurs in isolation. The figure indicates that a drop in force arises when the other slip component is added.

The resulting situation is designated as *combined slip*. The decrease in force can be simply explained by realizing that the total horizontal friction force cannot exceed a maximum value, the radius of the so-called *friction circle*, which is dictated by the current friction coefficient and normal load.

Curves which exhibit a shape like the side force characteristics of Figure 2.2 can be represented by a mathematical formulation that has become known by the name *Magic Formula*, which is presented in more detail in the next section.

The slopes of the pure slip curves at vanishing slip are defined as the longitudinal C_λ and lateral C_α stiffnesses respectively. C_α is one of the most important parameters of the tire and is crucial for vehicle's handling and stability. Linearized force characteristics (valid at small levels of slip) can be represented by

$$F_x = C_\lambda \lambda, \tag{2.5a}$$

$$F_y = C_\alpha \alpha. \tag{2.5b}$$

2.2. The Magic Formula

The Magic Formula [38] is an empirical tire modeling formulation widely used in vehicle dynamics studies. The Magic Formula empirically computes all tire force and moment components given tire sideslip angle, longitudinal slip, camber angle, normal load, and includes the effect of vehicle speed. Modifications to be incurred in combined slip and transient situations are also included.

2.2.1. Tire Longitudinal Force

In case of pure longitudinal slip, tire longitudinal force can be obtained according to [38]:

$$F_{xo} = D_x \sin\left(C_x \arctan\left\{B_x(1-E_x)(\lambda_x) + E_x \arctan\left[B_x(\lambda_x)\right]\right\}\right) + S_{vx}. \quad (2.6)$$

where B_x, C_x, D_x, E_x, S_{vx} are coefficients which depend mainly on tire load F_z and tire camber angle which is neglected in this study. Their values are expressed as functions of a number of coefficients κ and p which are characteristic of any specific tire. They are obtained from tire tests and do not have any direct meaning. Tire data used in this study can be found in Appendix A.

$$\lambda_x = \lambda + S_{Hx} \qquad C_x = p_{Cx1}\kappa_{Cx}$$

$$D_x = \mu_x F_z \qquad \mu_x = \frac{p_{Dx1} + p_{Dx2}df_z}{1 + \kappa_{\mu V}\lambda v/v_o}\kappa_{\mu x}$$

$$E_x = (p_{Ex1} + p_{Ex2}df_z + p_{Ex3}df_z^2)(1 - p_{Ex4}sign(\lambda_x))\kappa_{Ex} \qquad B_x = \frac{K_{x\lambda}}{C_x D_x + \varepsilon_x}$$

$$K_{x\lambda} = F_z(p_{Kx1} + p_{Kx2}df_z)\exp(p_{Kx3}df_z)\kappa_{Kx\lambda} \qquad S_{Hx} = (p_{Hx1} + p_{Hx1}df_z)\kappa_{Hx}$$

$$S_{vx} = F_z(p_{Vx1} + p_{Vx2}df_z)\kappa_{Vx}\kappa'_{\mu x} \qquad df_z = \frac{F_z - F_{zo}}{F_{zo}}$$

In case of combined slip, to represent combined slip conditions, Pacejka [38] proposes a weighing factor $G_{x\alpha}$ to multiply the longitudinal force obtained for pure longitudinal slip as follows:

$$F_x = G_{x\alpha}F_{xo} \quad (2.7)$$

where

$$G_{x\alpha} = \cos\left(C_{x\alpha}\arctan\left\{B_{x\alpha}\alpha_S - E_{x\alpha}\left[B_{x\alpha}\alpha_S - \arctan(B_{x\alpha}\alpha_S)\right]\right\}\right)/G_{x\alpha o}$$

$$G_{x\alpha o} = \cos\left(C_{x\alpha}\arctan\left\{B_{x\alpha}S_{Hx\alpha} - E_{x\alpha}\left[B_{x\alpha}S_{Hx\alpha} - \arctan(B_{x\alpha}S_{Hx\alpha})\right]\right\}\right)$$

and

$$\begin{aligned}
\alpha_S &= \alpha^* + S_{Hx\alpha} \\
\alpha^* &= \tan(\alpha) \\
B_{x\alpha} &= r_{Bx1}\cos(\arctan(r_{Bx2}\lambda)) \\
C_{x\alpha} &= r_{Cx1} \\
E_{x\alpha} &= r_{Ex1} + r_{Ex2}df_z \\
S_{Hx\alpha} &= r_{Hx1}
\end{aligned}$$

where r_B, r_C, r_E and r_H are coefficients specific to the tire in consideration.

2.2.2. Tire Cornering Force

In case of pure sideslip, F_{yo} can be obtained according to

$$F_{yo} = D_y \sin\left(C_y \arctan\left\{B_y(1-E_y)(\alpha_y) + E_y \arctan\left[B_y(\alpha_y)\right]\right\}\right) + S_{vy} \tag{2.8}$$

where

$$\begin{aligned}
\alpha_y &= \alpha^* + S_{Hy} & C_y &= p_{Cy1}\kappa_{Cy} \\
D_y &= \mu_y F_z & \mu_y &= \frac{p_{Dy1} + p_{Dy2}df_z}{1 + \kappa_{\mu V} v_s/v_o}\kappa_{\mu y} \\
E_y &= (p_{Ey1} + p_{Ey2}df_z)(1 - p_{Ey3}sign(\alpha_y))\kappa_{Ey} & B_y &= \frac{K_{y\alpha}}{C_y D_y + \varepsilon_y} \\
K_{y\alpha} &= p_{Ky1}F'_{zo}\sin\left[2\arctan\left(\frac{F_z}{p_{Ky2}F'_{zo}}\right)\right] & S_{Hy} &= (p_{Hy1} + p_{Hy1}df_z)\kappa_{Hy} \\
S_{vy} &= F_z(p_{Vy1} + p_{Vy2}df_z)\kappa_{Vy}\kappa'_{\mu y}.
\end{aligned}$$

Finally, in case of combined slip, the cornering force is given by

$$F_y = G_{y\lambda}F_{xo} + S_{Vy\lambda} \tag{2.9}$$

where

$$G_{y\lambda} = \cos\left(C_{y\lambda}\arctan\left\{B_{y\lambda}\lambda_S - E_{y\lambda}\big[B_{y\lambda}\lambda_S - \arctan(B_{y\lambda}\lambda_S)\big]\right\}\right)/G_{y\lambda o}$$
$$G_{y\lambda o} = \cos\left(C_{y\lambda}\arctan\left\{B_{y\lambda}S_{Hy\lambda} - E_{y\lambda}\big[B_{y\lambda}S_{Hy\lambda} - \arctan(B_{y\lambda}S_{Hy\lambda})\big]\right\}\right)$$

and

$$\begin{aligned}
\lambda_S &= \lambda + S_{Hy\lambda}\\
B_{y\lambda} &= r_{By1}\cos(\arctan(r_{By2}(\alpha^\star - r_{By3})))\\
C_{y\lambda} &= r_{Cy1}\\
E_{y\lambda} &= r_{Ey1} + r_{Ey2}df_z\\
S_{Hy\lambda} &= r_{Hy1} + r_{Hy1}df_z\\
S_{Vy\lambda} &= D_{Vy\lambda}\sin(r_{Vy5}\arctan(r_{Vy6}\lambda))\\
D_{Vy\lambda} &= \mu_y Fz(r_{Vy1} + r_{Vy2}d_{fz})\cos(\arctan(r_{Vy4}\alpha^\star))
\end{aligned}$$

where again r_B, r_C, r_E, r_H and r_V are coefficients specific to the tires in consideration.

2.2.3. A Rational Fit to the Magic Formula

In this section, we start by considering a rational function expressed as

$$F_y(\alpha) = \frac{m_1\alpha + m_2}{\alpha^2 + n_1\alpha + n_2} \tag{2.10}$$

to approximate Magic Formula prediction of cornering force under pure lateral slip. It is possible to propose polynomials of higher degrees at the numerator and denominator of (2.10) for more accurate modeling but this would render the ensuing controller design more complex. Several relationships between coefficients are readily available:

- $\frac{m_2}{n_2} \approx 0$ if the tire is to produce low cornering force at negligible tire slip (neglecting camber and caster effects);
- $\frac{m_1}{n_2} \approx C_\alpha$;
- as the tire cornering force is an odd function of tire slip, one possibility is to have $m_2 \approx 0$ and $n_1 \approx 0$;

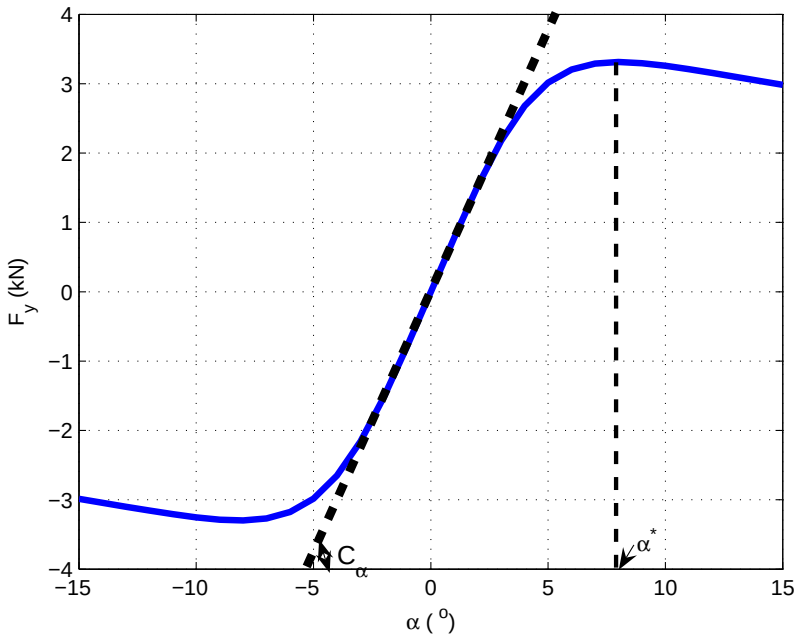


Figure 2.3. Generic lateral tire force *vs* slip angle obtained by the Magic Formula

- as the maximum cornering force occurs at $\alpha^\star$, one must have $\frac{dF_y}{d\alpha} = 0$ at $\alpha^\star$.

Given the observations above, (2.10) becomes

$$F_y = \frac{C_\alpha \alpha}{(\frac{\alpha}{\alpha^\star})^2 + 1}. \tag{2.11}$$

Denoting $\eta_\alpha = (\frac{1}{\alpha^\star})^2$, it is possible to conceive η_α as a shape factor for the model and better fits may be obtained by varying η_α and C_α around their nominal values.

Next, we assume that cornering force variation is proportional to the product of the combined variation of road adhesion coefficient and normal load. We take $\eta_z \frac{\mu F_z}{\mu_o F_{zo}}$, where μ_o stands for the nominal road adhesion coefficient, and F_{zo} stands for the nominal tire load as a factor multiplying (2.11), to account for simultaneous variations in road adhesion and normal load.

For combined slip conditions, one must also obtain a rational fit for $G_{y\lambda}$. It is possible to approximate this function by

$$G_{y\lambda} \approx \frac{1}{(\frac{\lambda}{\lambda^*})^2 + 1}$$

where λ^* corresponds roughly to the point of inflection of $G_{y\lambda}$. Again, we can define

$$\eta_\lambda := \left(\frac{1}{\lambda^*}\right)^2$$

as a shape factor to obtain better fits.

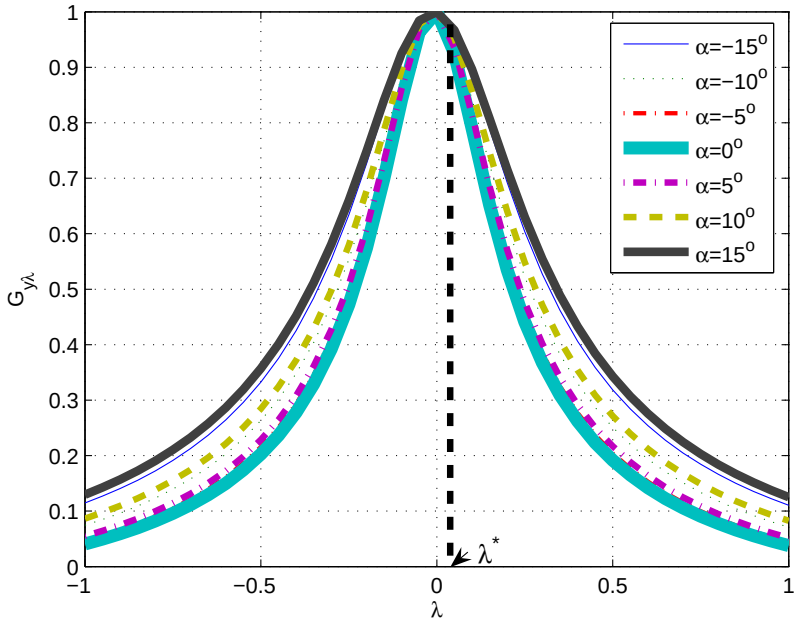


Figure 2.4. $G_{y\lambda}$ *vs* longitudinal slip obtained by the Magic Formula

To sum up, the following rational function is proposed for the approximation of lateral force under combined slip conditions:

$$F_y(\alpha, \lambda, \mu, F_z) \approx \frac{\mu F_z}{\mu_o F_{zo}} \frac{\eta_z}{\eta_\lambda \lambda^2 + 1} \frac{C_\alpha}{\eta_\alpha \alpha^2 + 1} \alpha. \tag{2.12}$$

Similarly, the following expression can be proposed for the approximation of longitudinal force under combined slip conditions:

$$F_x(\alpha, \lambda, \mu, F_z) \approx \frac{\mu F_z}{\mu_o F_{zo}} \frac{\chi_z}{\chi_\lambda \lambda^2 + 1} \frac{C_\lambda}{\chi_\alpha \alpha^2 + 1} \lambda. \tag{2.13}$$

Equation (2.12) has been used to fit the Magic Formula lateral tire force predictions for different values of normal load under combined slip conditions. Shape factors η have been optimized for each value of the normal load as can be observed in Table 2.1. It can be seen that $\eta_\alpha \in [34.5, 50.0]$, $\eta_\lambda \in [16.7, 22.2]$ and $\eta_z \in [1.0, 1.1]$. For $F_z = 1.0\,kN$ to $F_z = 7.0\,kN$, the accuracy of the fit can be assessed from Figure 2.5 to Figure 2.9.

Table 2.1. Optimized Shape Factors at different loads

Normal Load (kN)	η_α	η_λ	η_z
$F_z = 1.0$	50.0	16.7	1.1
$F_z = 2.5$	43.5	18.2	1.1
$F_z = 4.0$	40.0	20.0	1.1
$F_z = 5.5$	40.0	20.0	1.1
$F_z = 7.0$	34.5	22.2	1.0

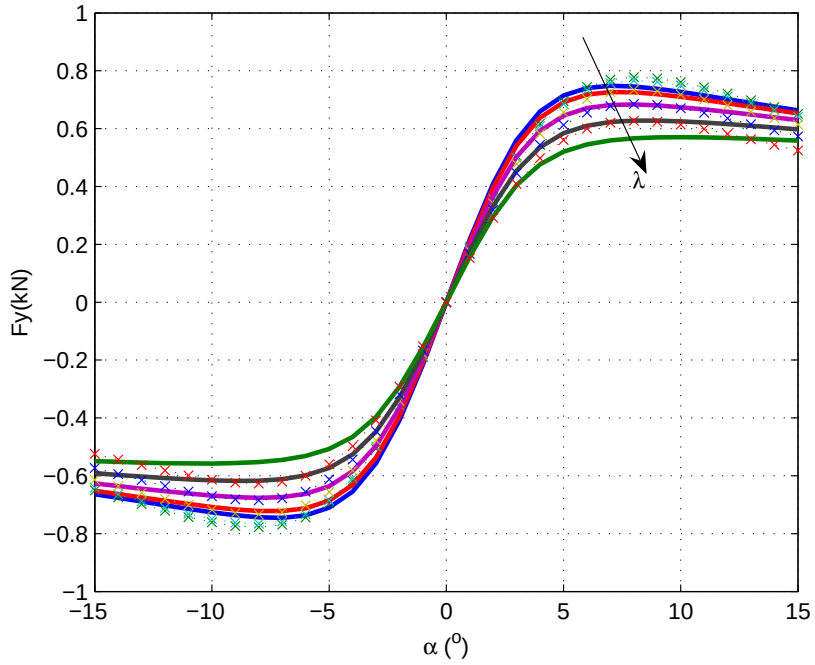


Figure 2.5. Rational function (dashed lines with x markers) *vs* Magic Formula (solid lines) ($F_z = 1.0\,kN$; combined slip conditions)

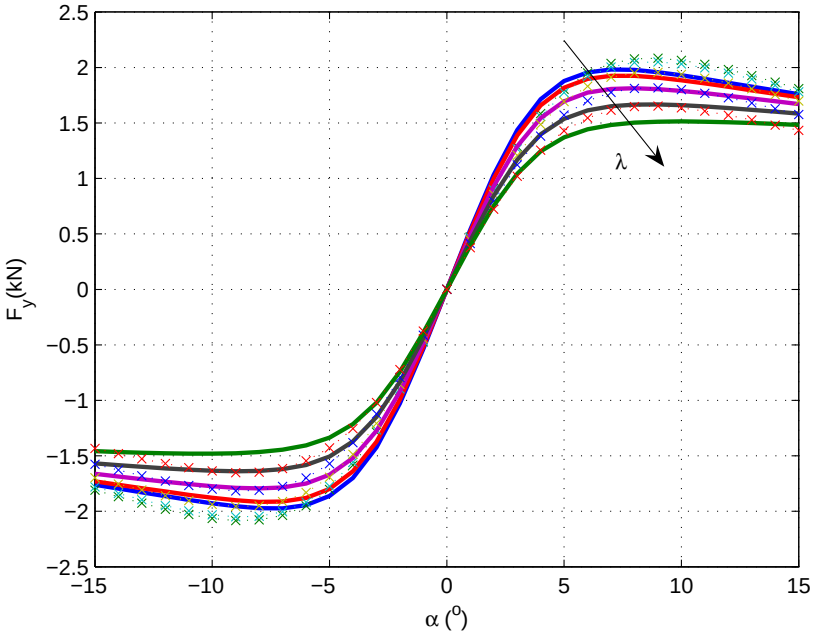


Figure 2.6. Rational function (dashed lines with x markers) *vs* Magic Formula (solid lines) ($F_z = 2.5\,kN$; combined slip conditions)

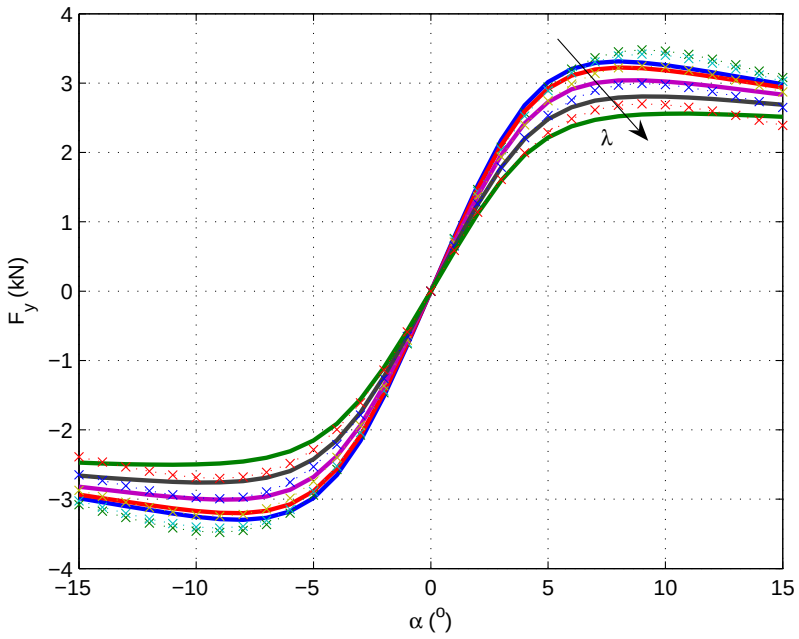


Figure 2.7. Rational function (dashed lines with x markers) *vs* Magic Formula (solid lines) ($F_z = 4.0\,kN$; combined slip conditions)

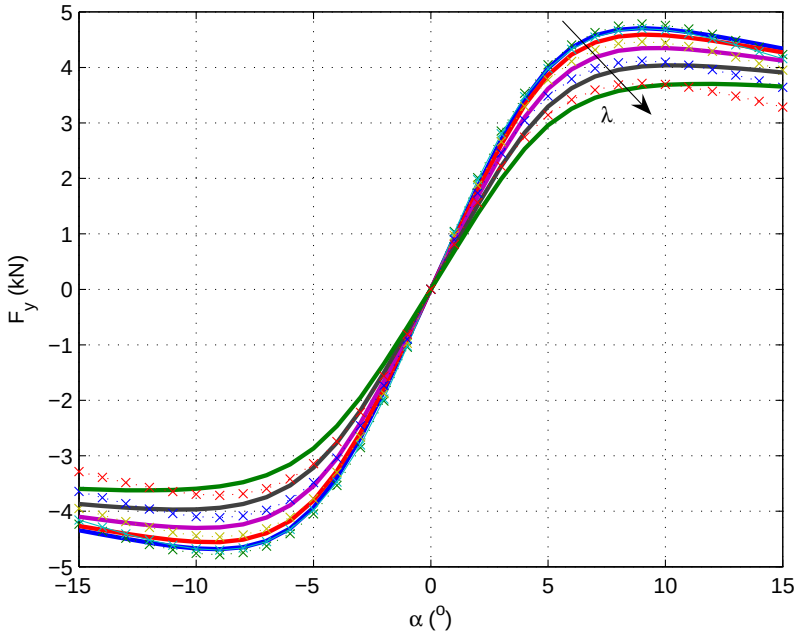


Figure 2.8. Rational function (dashed lines with x markers) *vs* Magic Formula (solid lines) ($F_z = 5.5\,kN$; combined slip conditions)

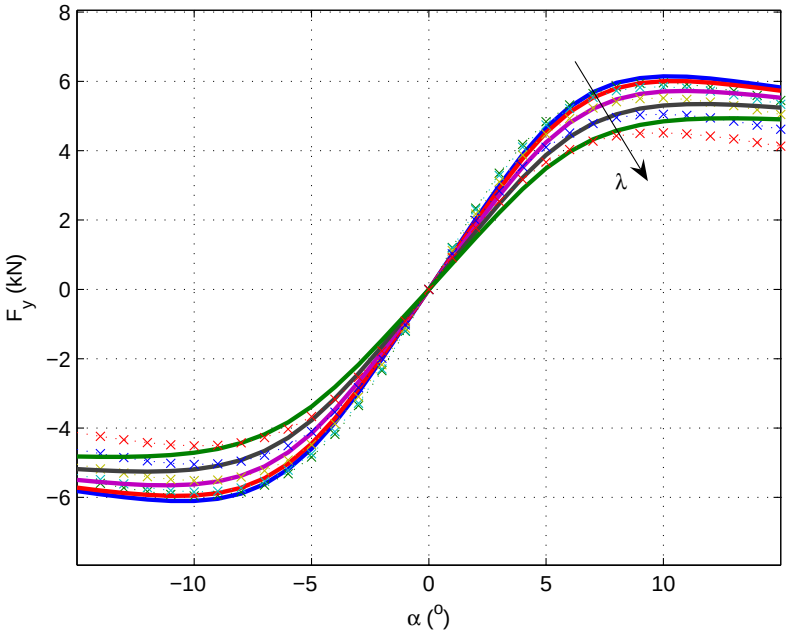


Figure 2.9. Rational function (dashed lines with x markers) *vs* Magic Formula (solid lines) ($F_z = 7.0\,kN$; combined slip conditions)

2.3. Nonlinear Six-Degree-of-Freedom Vehicle Model

Governing equations of a six-degree-of-freedom vehicle model are derived in this section. Model geometry is shown in Figure 2.10. Front (δ_f) and rear (δ_r) steering angles, braking/tractive forces F_{xi} at all wheels, and active suspension forces F_{zic} constitute control inputs. The model is divided into sprung and unsprung bodies, as shown in Figure 2.10. The unsprung mass has only three degrees of freedom and roll, pitch and bounce are not allowed. The sprung mass has the complete six degrees of freedom. Equations of motion are derived using a right handed reference frame with unit vectors **i**, **j** and **k** originally collinear with roll, pitch and yaw axes respectively with origin located at the center of gravity of the vehicle (CG). According to SAE standards, the x-axis of the undisturbed vehicle runs parallel to the ground and the z-axis points towards the ground [39]. The following modeling assumptions prevail:

- The vehicle is symmetric about the xz-plane;
- The sprung mass rotates about the roll axis and the pitch axis of the vehicle

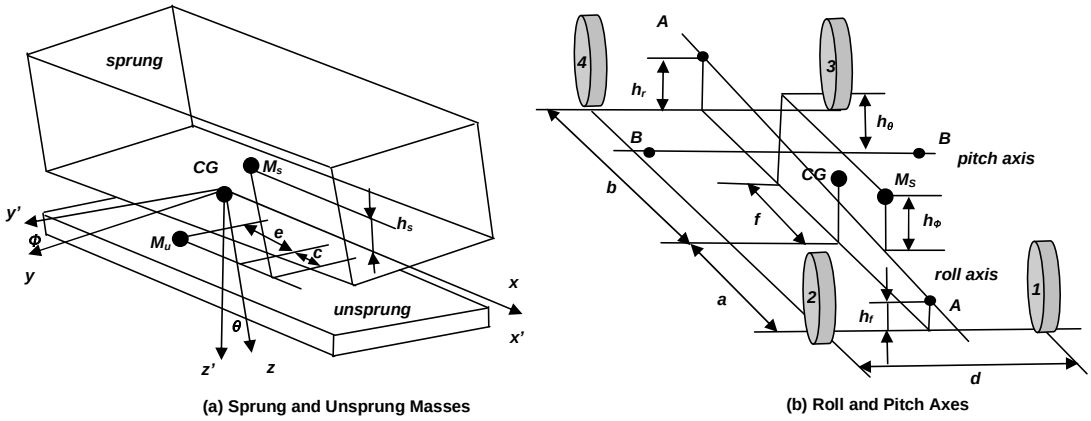


Figure 2.10. Six-degree-of-freedom vehicle model adapted from [40]

which are assumed to be fixed to the unsprung mass, i.e. front and rear roll center heights on the one hand, and left and right pitch centers on the other are assumed to be constant under rotation of the sprung mass;

- Roll axis inclination is neglected;
- The longitudinal, lateral and yaw motions of the unsprung and the sprung masses are set to be identical;
- Aerodynamics drag forces are neglected;
- Engine dynamics are neglected and simulations run in this study are assumed to occur with the clutch disengaged.

2.3.1. Angular Kinematics

An inertial reference frame with unit vectors **I**, **J** and **K** is assumed to be fixed on the road plane. For the vehicle running uniformly on a straight road (without sideslip, yaw, pitch, roll and bounce), this frame corresponds to the moving frame attached to the vehicle CG. In a combined cornering and braking maneuver, the sprung mass undergoes a complex rotation in three dimensional space where all vehicle modes are activated.

In this section, we derive expressions for the components of the absolute angular velocity of the sprung mass in the inertial frame and then simplify the equations by a

small angle assumption. If the final angular configuration of the sprung mass relative to the unsprung is assumed to be obtained by successive rotations about **j** and **i** axes, then the angular velocity vector can be expressed in terms of Euler angles ψ (yaw), θ (pitch) and ϕ (roll):

$$\boldsymbol{\omega} = \dot{\psi}\mathbf{K} + \dot{\theta}\mathbf{j} + \dot{\phi}\mathbf{i}^* \tag{2.14}$$

where $\mathbf{i}^*$ is in direction of the final roll axis after pitch rotation. Absolute yaw, pitch and roll angular velocity components ω_z, ω_y and ω_x expressed in terms of Euler angles can be obtained as:

$$\omega_x = \dot{\phi} - \dot{\psi}\sin\theta \tag{2.15a}$$

$$\omega_y = \dot{\theta}\cos\phi + \dot{\psi}\sin\phi\cos\theta \tag{2.15b}$$

$$\omega_z = \dot{\psi}\cos\phi\cos\theta - \dot{\theta}\sin\phi. \tag{2.15c}$$

Finally, components of the angular acceleration vector can be computed right away by simple time differentiation:

$$\dot{\omega}_x = \ddot{\phi} - \ddot{\psi}\sin\theta - \dot{\psi}\dot{\theta}\cos\theta \tag{2.16a}$$

$$\dot{\omega}_y = \ddot{\theta}\cos\phi - \dot{\theta}\dot{\phi}\sin\phi + \ddot{\psi}\cos\theta\sin\phi - \dot{\psi}\dot{\theta}\sin\theta\sin\phi + \dot{\psi}\dot{\phi}\cos\theta\cos\phi \tag{2.16b}$$

$$\dot{\omega}_z = \ddot{\psi}\cos\theta\cos\phi - \dot{\psi}\dot{\theta}\sin\theta\cos\phi - \dot{\psi}\dot{\phi}\cos\theta\sin\phi - \ddot{\theta}\sin\phi - \dot{\theta}\dot{\phi}\cos\phi. \tag{2.16c}$$

In vehicle dynamics, ϕ and θ can generally be assumed small, except in unstable vehicle behavior such as rollover. This assumption is further strengthened in the presence of VDC controllers that act towards reducing these angles. Hence, in this study, numerical values for absolute angular components can be taken equal to values that would be measured by observers located on corresponding Euler axes. In other words, absolute

roll, pitch and yaw angular velocity components for the sprung mass are given by

$$\omega_{sx} = \dot{\phi} = p \quad \text{(SAE notation of roll rate)} \tag{2.17a}$$

$$\omega_{sy} = \dot{\theta} \tag{2.17b}$$

$$\omega_{sz} = \dot{\psi} = r \quad \text{(SAE notation of yaw rate).} \tag{2.17c}$$

Similarly, components of the angular acceleration vector for the sprung mass are simply given by

$$\dot{\omega}_{sx} = \ddot{\phi} = \dot{p} \tag{2.18a}$$

$$\dot{\omega}_{sy} = \ddot{\theta} \tag{2.18b}$$

$$\dot{\omega}_{sz} = \ddot{\psi} = \dot{r}. \tag{2.18c}$$

The angular velocity of the unsprung mass has only a yaw component

$$\omega_{uz} = \dot{\psi} = r. \tag{2.19}$$

Similarly, the angular acceleration of the unsprung mass is given by

$$\dot{\omega}_{uz} = \ddot{\psi} = \dot{r}. \tag{2.20}$$

2.3.2. Linear Kinematics

In the following, we assume that the CG moves with the velocity vector

$$\boldsymbol{U} = U_x\mathbf{i} + U_y\mathbf{j} + U_z\mathbf{k}. \tag{2.21}$$

The position of the sprung mass expressed in the moving reference frame is given by

$$\boldsymbol{R_s} = c\mathbf{i} - h_s\mathbf{k}. \tag{2.22}$$

Successive time differentiations yield velocity and acceleration vectors as

$$\dot{\boldsymbol{R}}_{\boldsymbol{s}} = \boldsymbol{U}_{\boldsymbol{s}} = (U_x - h_s\dot{\theta})\mathbf{i} + (U_y + h_s\phi + cr)\mathbf{j} + (U_z - c\dot{\theta})\mathbf{k} \tag{2.23}$$

and

$$\begin{aligned}\ddot{\boldsymbol{R}}_{\boldsymbol{s}} = \boldsymbol{a}_{\boldsymbol{s}} = [(\dot{U}_x - r\dot{U}_y) - h_s(\ddot{\theta} + \dot{\phi}r) - \dot{\theta}(\dot{R}_z - c\dot{\theta}) - cr^2]\mathbf{i} \\ + [(\dot{U}_y + U_x r) + h_s(\ddot{\phi} - \dot{\theta}r) - \dot{\phi}(\dot{R}_z - c\dot{\theta}) + c\dot{r}]\mathbf{j} \\ + [(\ddot{R}_z - c\ddot{\theta}) - \dot{\theta}(U_x - h_s\theta) + \dot{\phi}(U_x + h_s\dot{\phi} + cr)]\mathbf{k}.\end{aligned} \tag{2.24}$$

where $\dot{R}_z = U_z$, assuming that the bounce motion of the sprung mass is equal to the vertical motion of CG. The position of the unsprung mass expressed in the moving reference frame is given by

$$\boldsymbol{R}_{\boldsymbol{u}} = -e\mathbf{i} + h_u\mathbf{k}, \tag{2.25}$$

where $h_u = \frac{M_s}{M_u}h_s$. Successive time differentiations yield velocity and acceleration vectors as follows:

$$\dot{\boldsymbol{R}}_{\boldsymbol{u}} = \boldsymbol{U}_{\boldsymbol{u}} = U_x\mathbf{i} + (U_y - er)\mathbf{j} \tag{2.26}$$

and

$$\ddot{\boldsymbol{R}}_{\boldsymbol{u}} = \boldsymbol{a}_{\boldsymbol{u}} = [(\dot{U}_x - r\dot{U}_y) + er^2]\mathbf{i} + [(\dot{U}_y + U_x r) - e\dot{r}]\mathbf{j}. \tag{2.27}$$

2.3.3. Total External Forces and Moments

The final step before the derivation of the governing equations is the determination of total external forces and moments. This can be achieved by inspection of Figure 2.11 and Figure 2.12.

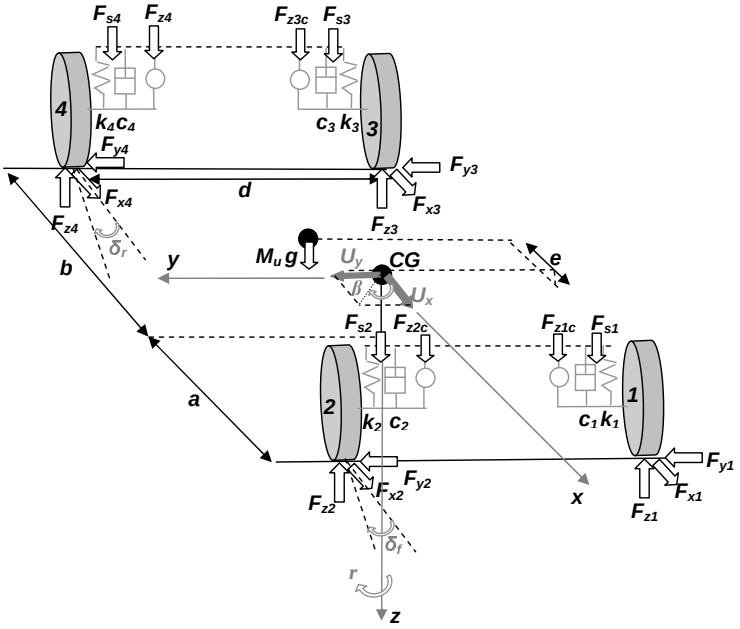


Figure 2.11. Free-body diagram of unsprung mass

The total external force in the longitudinal direction, which includes the contribution of longitudinal and lateral tire forces, is given by

$$\mathcal{F}_x = (F_{x1}+F_{x2})cos\delta_f + (F_{x3}+F_{x4})\cos\delta_r - (F_{y1}+F_{y2})\sin\delta_f - (F_{y3}+F_{y4})\sin\delta_r. \quad (2.28)$$

The total external force in the lateral direction, which again includes the contribution of longitudinal and lateral tire forces, is given by

$$\mathcal{F}_y = (F_{y1}+F_{y2})cos\delta_f + (F_{y3}+F_{y4})\cos\delta_r + (F_{x1}+F_{x2})\sin\delta_f + (F_{x3}+F_{x4})\sin\delta_r. \quad (2.29)$$

The total external force in the bounce direction, which includes the contribution of suspension forces, is given by

$$\mathcal{F}_z = -c_{z\theta}\dot{\theta} - c_{zz}\dot{R}_z - k_{zz}R_z - k_{z\theta}\theta + F_{z1c} + F_{z2c} + F_{z3c} + F_{z4c}. \quad (2.30)$$

The total external moment about the yaw axis, which includes the moment contribution

of longitudinal and lateral tire forces, is given by

$$\begin{aligned}\mathcal{M}_z = F_{x1}\left(a\sin\delta_f - \frac{d}{2}\cos\delta_f\right) + F_{x2}\left(a\sin\delta_f + \frac{d}{2}\cos\delta_f\right)\\ + F_{x3}\left(-b\sin\delta_r - \frac{d}{2}\cos\delta_r\right) + F_{x4}\left(-b\sin\delta_r + \frac{d}{2}\cos\delta_r\right)\\ + F_{y1}\left(\frac{d}{2}\sin\delta_f + a\cos\delta_f\right) + F_{y2}\left(-\frac{d}{2}\sin\delta_f + a\cos\delta_f\right)\\ + F_{y3}\left(\frac{d}{2}\sin\delta_r - b\cos\delta_r\right) + F_{y4}\left(-\frac{d}{2}\sin\delta_r - b\cos\delta_r\right). \quad (2.31)\end{aligned}$$

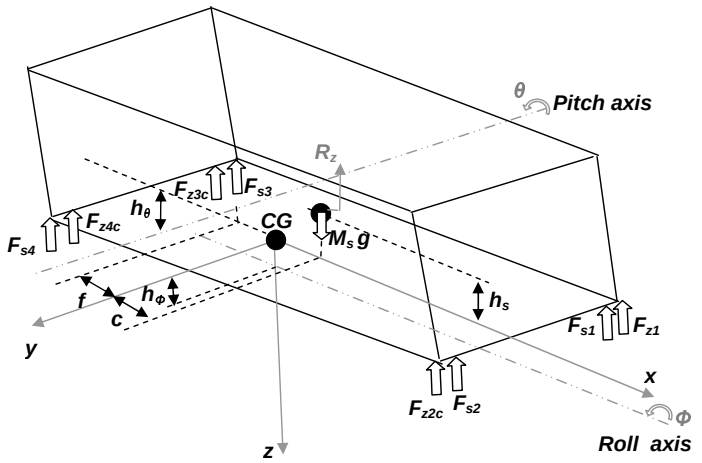


Figure 2.12. Free-body diagram of sprung mass

The total external moment about the pitch axis, which includes the moment contribution of longitudinal tire forces and suspension forces, is given by

$$\begin{aligned}\mathcal{M}_y = -c_{\theta z}\dot{R}_z - k_{\theta\theta}\theta + k_{\theta z}R_z + h_\theta\left(F_{x1} + F_{x2} + F_{x3} + F_{x4}\right)\\ - (a+f)(F_{z1c} + F_{z2c}) + (b-f)(F_{z3c} + F_{z4c}). \quad (2.32)\end{aligned}$$

The total external moment about the roll axis, which includes the moment contribution of suspension forces, is given by

$$\mathcal{M}_x = -\frac{d^2}{4}c_{zz}\dot{\phi} - \frac{d^2}{4}k_{zz}R_z + M_s g h_\phi \sin\phi + \frac{d}{2}(-F_{z1c} + F_{z2c} - F_{z3c} + F_{z4c}). \quad (2.33)$$

where

$$
\begin{aligned}
c_{\theta\theta} &:= (c_1 + c_2)(a + f)^2 + (c_3 + c_4)(b - f)^2 \\
k_{\theta\theta} &:= (k_1 + k_2)(a + f)^2 + (k_3 + k_4)(b - f)^2 \\
c_{zz} &:= c_1 + c_2 + c_3 + c_4 \\
k_{zz} &:= k_1 + k_2 + k_3 + k_4 \\
c_{z\theta} &:= -(c_1 + c_2)(a + f) + (c_3 + c_4)(b - f) \\
k_{z\theta} &:= -(k_1 + k_2)(a + f) + (k_3 + k_4)(b - f).
\end{aligned}
$$

2.3.4. Summary of the Governing Equations

For a system of n rigid bodies, the translational equation of motion is given by [41]

$$\sum_{i=1}^{n} M_i \boldsymbol{a_i} = \boldsymbol{\mathcal{F}} \tag{2.34}$$

where $\boldsymbol{\mathcal{F}}$ is the resultant force vector with components $\mathcal{F}_x$, $\mathcal{F}_y$ and $\mathcal{F}_z$. In the present case, this equation can be written as

$$M_s \boldsymbol{a_s} + M_u \boldsymbol{a_u} = \boldsymbol{\mathcal{F}}. \tag{2.35}$$

Meanwhile the rotational equation of motion about CG is given by

$$\sum_{i=1}^{n} \boldsymbol{R_i} \times M_i \ddot{\boldsymbol{R}}_{\boldsymbol{i}} + \sum_{i=1}^{n} [\boldsymbol{\mathcal{J}_i} \cdot \dot{\boldsymbol{\omega}}_{\boldsymbol{i}} + \boldsymbol{\omega_i} \times \boldsymbol{\mathcal{J}_i} \cdot \boldsymbol{\omega_i}] = \boldsymbol{\mathcal{M}} \tag{2.36}$$

where $\boldsymbol{\mathcal{M}}$ is the resultant moment vector with components $\mathcal{M}_x$, $\mathcal{M}_y$, $\mathcal{M}_z$ and where $\boldsymbol{\mathcal{J}_i}$ stands for the mass moment of inertia tensor of i^{th} body. In the present case, this equation reduces to

$$\boldsymbol{R_s} \times M_s \ddot{\boldsymbol{a}}_{\boldsymbol{s}} + \boldsymbol{R_u} \times M_u \ddot{\boldsymbol{a}}_{\boldsymbol{u}} + \boldsymbol{\mathcal{J}_s} \cdot \dot{\boldsymbol{\omega}}_{\boldsymbol{s}} + \boldsymbol{\omega_s} \times \boldsymbol{\mathcal{J}_s} \cdot \boldsymbol{\omega_s} + \boldsymbol{\mathcal{J}_u} \cdot \dot{\boldsymbol{\omega}}_{\boldsymbol{u}} + \boldsymbol{\omega_u} \times \boldsymbol{\mathcal{J}_u} \cdot \boldsymbol{\omega_u} = \boldsymbol{\mathcal{M}} \tag{2.37}$$

where inertia tensors must be evaluated about yaw, pitch and roll axes. Applying the above equations to the present case, we obtain the following set of equations.

Longitudinal dynamics:

$$M(\dot{U}_x - U_y r) - M_s\big[h_s(\ddot{\theta} + \dot{\phi} r) - \dot{\theta}(\dot{R}_z - c\dot{\theta})\big] = (F_{x1} + F_{x2})\cos\delta_f + (F_{x3} + F_{x4})\cos\delta_r - (F_{y1} + F_{y2})\sin\delta_f - (F_{y3} + F_{y4})\sin\delta_r. \quad (2.38)$$

Lateral dynamics:

$$M(\dot{U}_y + U_x r) + M_s\big[h_s(\ddot{\phi} - \dot{\theta} r) - \dot{\phi}(\dot{R}_z - c\dot{\theta})\big] = (F_{y1} + F_{y2})\cos\delta_f + (F_{y3} + F_{y4})\cos\delta_r + (F_{x1} + F_{x2})\sin\delta_f + (F_{x3} + F_{x4})\sin\delta_r. \quad (2.39)$$

Yaw dynamics:

$$\begin{aligned} I_{rr}\dot{r} + I_{r\phi\theta}\dot{\phi}\dot{\theta} + I_{r\dot{p}}(\ddot{\phi} - \dot{\theta} r) - M_s c\dot{\phi}\dot{R}_z &= F_{x1}\left(a\sin\delta_f - \frac{d}{2}\cos\delta_f\right) + F_{x2}\left(a\sin\delta_f + \frac{d}{2}\cos\delta_f\right) \\ &+ F_{x3}\left(-b\sin\delta_r - \frac{d}{2}\cos\delta_r\right) + F_{x4}\left(-b\sin\delta_r + \frac{d}{2}\cos\delta_r\right) \\ &+ F_{y1}\left(\frac{d}{2}\sin\delta_f + a\cos\delta_f\right) + F_{y2}\left(-\frac{d}{2}\sin\delta_f + a\cos\delta_f\right) \\ &+ F_{y3}\left(\frac{d}{2}\sin\delta_r - b\cos\delta_r\right) + F_{y4}\left(-\frac{d}{2}\sin\delta_r - b\cos\delta_r\right). \quad (2.40) \end{aligned}$$

Roll Dynamics:

$$I_x\ddot{\phi} - I_{\phi\theta r}\dot{\theta} r + I_{\phi r}\dot{r} + I_{\phi\phi\theta}\dot{\phi}\dot{\theta} + M_s h_\phi(\dot{U}_y + U_x r) = \frac{d}{2}(-F_{z1c} + F_{z2c} - F_{z3c} + F_{z4c}). \quad (2.41)$$

Pitch dynamics:

$$I_\theta\ddot{\theta} - M_s(f+c)\ddot{R}_z + \Big[\dot{\phi}I_{\theta\phi} - M_s(f+c)U_y\Big]\dot{\phi} + (c_{\theta\theta} + I_{\theta 2}\dot{\theta} + I_{\theta 3})\dot{\theta} + (rI_{\theta r} + \dot{\phi}I_{\theta\phi r})r + c_{\theta z}\dot{R}_z + k_{\theta\theta}\theta + k_{\theta z}R_z = h_\theta(F_{x1} + F_{x2} + F_{x3} + F_{x4}) - (a+f)(F_{z1c} + F_{z2c}) + (b-f)(F_{z3c} + F_{z4c}). \quad (2.42)$$

Bounce dynamics:

$$M_s\ddot{R}_z - M_sc\ddot{\theta} + M_s(U_y + cr + h_s\dot{\phi})\dot{\phi} + c_{z\theta}\dot{\theta} + c_{zz}\dot{R}_z + k_{zz}R_z + k_{z\theta}\theta = F_{z1c} + F_{z2c} + F_{z3c} + F_{z4c}. \quad (2.43)$$

where

$$\begin{aligned}
I_{rr} &:= I_{zzu} + I_{zzs} + M_ue^2 + M_sc^2 \\
I_{r\phi\theta} &:= I_{yys} - I_{xxs} + M_sc^2 \\
I_x &:= I_{xxs} + M_sh_\phi h_s \\
I_{\phi\theta r} &:= I_{zzs} - I_{yys} - M_sh_\phi h_s \\
I_{\phi\phi\theta} &:= -I_{xzs} + M_sh_\phi c \\
I_\theta &:= I_{yys} + M_sh_\theta h_s + M_s(f+c)c \\
I_{\theta\phi r} &:= I_{xxs} - I_{zzs} + M_sh_\theta h_s - M_s(f+c)c \\
I_{\theta r} &:= -I_{xzs} + M_sh_\theta c \\
I_{\theta\phi} &:= I_{zzs} - M_s(f+c)h_s \\
I_{\theta 2} &:= M_sh_\theta c - M_s(f+c)h_s \\
I_{r\dot{p}} &:= M_sh_sc - I_{xzs} \\
I_{\phi r} &:= -I_{xzs} + M_sh_\phi c \\
I_{\theta 3} &:= M_sh_\theta\dot{R}_z - M_s(f+c)U_y
\end{aligned}$$

2.4. Linear Vehicle Models

2.4.1. Linear Bicycle Model

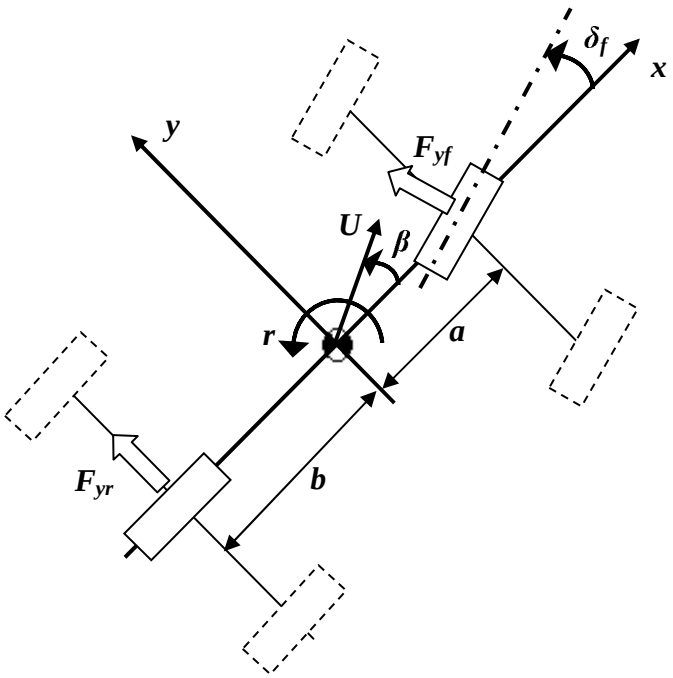


Figure 2.13. Bicycle Model

An appropriate vehicle model for low g cornering maneuver analysis is the linear bicycle model (Figure 2.13). Equations of motion for the bicycle model can be obtained by omitting tractive/braking forces and active suspension forces on the one hand and neglecting roll, pitch and bounce modes on the other

$$M(\dot{U}_y + U_x r) = F_{yf} + F_{yr}, \tag{2.44a}$$

$$J_z \dot{r} = aF_{yf} - bF_{yr} \tag{2.44b}$$

where $M = M_s + M_u$, $F_{yf} = F_{y1} + F_{y2}$, $F_{yr} = F_{y3} + F_{y4}$, and where J_z stands for the combined inertia of the entire vehicle about the z-axis. Then introducing

- a linear tire model such that $F_{yf} = C_{\alpha f}\alpha_f$ and $F_{yr} = C_{\alpha r}\alpha_r$,
- sideslip angle $\beta = \tan\frac{U_y}{U_x} \approx \frac{U_y}{U_x}$,

we obtain the classical linear bicycle model as shown below:

$$\dot{\beta} = -\frac{1}{MU}(C_{\alpha f} + C_{\alpha r})\beta + \left[-1 + \frac{1}{MU^2}(-aC_{\alpha f} + bC_{\alpha r})\right]r + \frac{1}{MU}C_{\alpha f}\delta_f \quad (2.45a)$$

$$\dot{r} = \frac{1}{J_z}(-aC_{\alpha f} + bC_{\alpha r})\beta - \frac{1}{J_z U}(a^2 C_{\alpha f} + b^2 C_{\alpha r}) + \frac{a}{J_z}C_{\alpha f}\delta_f \quad (2.45b)$$

2.4.2. Linear Yaw-Roll Model

An appropriate vehicle model for low g cornering maneuver analysis accounting for roll dynamics is the three-degree-of-freedom yaw-roll model developed by Segel [42]. This linear model includes a roll degree of freedom, ϕ, as well as the two translational degrees of freedom X and Y and the yaw degree of freedom ψ in the z-plane. Thus the vehicle has a non-rolling (unsprung) mass in the horizontal plane and a rolling (sprung) mass which is constrained to roll about an axis fixed in the non-rolling mass (similar to the six-degree-of-freedom model presented above). Equations of the linear yaw-roll model can again be derived from nonlinear vehicle equations by

- omitting traction/braking forces and active suspension forces,
- neglecting pitch and bounce modes,
- making a linear cornering force assumption and
- introducing sideslip angle.

In Segel's original work, extra assumptions are listed below:

- Roll steer $\frac{\partial \delta_r}{\partial \phi}$ and roll camber $\frac{\partial \gamma_r}{\partial \phi}$ effects are present at the rear axle,
- Roll camber $\frac{\partial \gamma_f}{\partial \phi}$ effect is present at the front axle.

When expressed in terms of the *stability derivatives* Y, N and L, the equations of motion are given by

$$(M_s + M_u)U(\dot{\beta} + r) + M_s h_\phi \ddot{\phi} = Y_\beta \beta + Y_r r + Y_\delta \delta + Y_\phi \phi \tag{2.46a}$$

$$I_{xzs}\ddot{\phi} + I_{zz}\dot{r} = N_\beta \beta + N_r r + N_\delta \delta + N_p \dot{\phi} + N_\phi \phi \tag{2.46b}$$

$$I_{xxs}\ddot{\phi} + M_s h_\phi U(\dot{\beta} + r) + I_{xz_s}\dot{r} = L_p \dot{\phi} + L_\phi \phi \tag{2.46c}$$

where stability derivatives are given by

$$\begin{aligned}
Y_r &:= \frac{bC_{\alpha r} - aC_{\alpha f}}{U} \\
Y_\delta &:= C_{\alpha f} \\
Y_\beta &:= -(C_{\alpha f} + C_{\alpha r}) \\
Y_\phi &:= C_{\alpha r}\frac{\partial \delta_r}{\partial \phi} + C_{\gamma f}\frac{\partial \gamma_f}{\partial \phi} \\
N_\beta &:= bC_{\alpha r} - aC_{\alpha f} \\
N_r &:= -\frac{a^2 C_{\alpha f} + b^2 C_{\alpha r}}{U} \\
N_\delta &:= aC_{\alpha f} \\
N_\phi &:= aC_{\gamma r}\frac{\partial \gamma_r}{\partial \phi} - bC_{\alpha r}\frac{\partial \delta_r}{\partial \phi} \\
L_p &:= -c_R \\
L_\phi &:= M_s g h - k_R.
\end{aligned}$$

2.5. A Parametric Bicycle Model

For large steering angles, parametric models are introduced in this thesis to incorporate the rational tire model presented in Section 2.2.3 into the linear bicycle and yaw-roll models in order to obtain approximations for the nonlinear six-degree-of-freedom model derived in Section 2.3. Equations of motion for the nonlinear bicycle model being given by (2.44), the following assumptions are made:

- Front tires share the same tire cornering stiffness $\frac{C_{\alpha f}}{2}$ where $C_{\alpha f}$ is the front axle cornering stiffness that usually appears in the classical bicycle model. Rear tires share the same tire cornering stiffness $\frac{C_{\alpha r}}{2}$, where $C_{\alpha r}$ is the rear axle cornering stiffness,
- Front tires share the common slip angle $\alpha_f = \delta_f - \beta - \frac{ar}{U}$ and rear tires share the common slip angle $\alpha_r = -\beta + \frac{br}{U}$ [43].

At this stage, by making use of (2.12), it is possible to express front and rear axle lateral forces as:

$$F_{yf} = \frac{\mu C_{\alpha f}}{2\mu_o F_{zfo}} \left(\frac{1}{\eta_{\lambda_1}\lambda_1^2 + 1} \frac{\eta_{z1} F_{z1}}{\eta_{\alpha_1}\alpha_f^2 + 1} + \frac{1}{\eta_{\lambda_2}\lambda_2^2 + 1} \frac{\eta_{z2} F_{z2}}{\eta_{\alpha_2}\alpha_f^2 + 1} \right) \alpha_f, \tag{2.48a}$$

$$F_{yr} = \frac{\mu C_{\alpha r}}{2\mu_o F_{zro}} \left(\frac{1}{\eta_{\lambda_3}\lambda_3^2 + 1} \frac{\eta_{z3} F_{z3}}{\eta_{\alpha_3}\alpha_r^2 + 1} + \frac{1}{\eta_{\lambda_4}\lambda_4^2 + 1} \frac{\eta_{z4} F_{z4}}{\eta_{\alpha_4}\alpha_r^2 + 1} \right) \alpha_r. \tag{2.48b}$$

Then the following simplifications can be made:

- Longitudinal slip terms are taken zero, assuming pure cornering.
- The road adhesion coefficient is taken as μ_o hence assuming driving on dry road.
- When considered as uncertain parameters, shape factors η_{α_i} and η_{zi} can be merged into a single factor η_α.

Under the above assumptions, it is possible to express front and rear axle lateral forces as follows:

$$F_{yf} = C_{\alpha f} \left(\frac{1}{\eta_\alpha \alpha_f^2 + 1} \right) \alpha_f, \tag{2.49a}$$

$$F_{yr} = C_{\alpha r} \left(\frac{1}{\eta_\alpha \alpha_r^2 + 1} \right) \alpha_r. \tag{2.49b}$$

Finally, the following parametric bicycle model is obtained:

$$\dot{\beta} = -\frac{1}{MU}(C^*_{\alpha f} + C^*_{\alpha r})\beta + \left[-1 + \frac{1}{MU^2}(-aC^*_{\alpha f} + bC^*_{\alpha r}) \right] r + \frac{1}{MU} C^*_{\alpha f} \delta_f \tag{2.50a}$$

$$\dot{r} = \frac{1}{J_z}(-aC^*_{\alpha f} + bC^*_{\alpha r})\beta - \frac{1}{J_z U}(a^2 C^*_{\alpha f} + b^2 C^*_{\alpha r}) r + \frac{a}{J_z} C^*_{\alpha f} \delta_f \tag{2.50b}$$

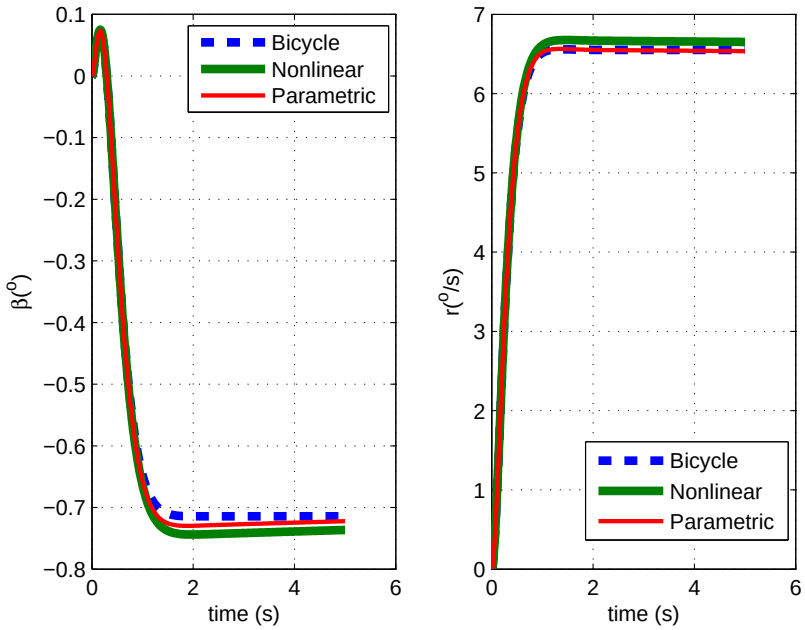


Figure 2.14. Vehicle response for driver's small step input ($\delta_f = 1^o$)

where

$$C^*_{\alpha f} := C_{\alpha f}\left(\frac{1}{\eta_\alpha \alpha_f^2 + 1}\right)$$
$$C^*_{\alpha r} := C_{\alpha r}\left(\frac{1}{\eta_\alpha \alpha_r^2 + 1}\right).$$

Following simulations displayed in Figure 2.14 and Figure 2.15 have been obtained taking $\eta_\alpha = 35$. For small values of the driver commanded steering angle, all responses match, showing that the classical bicycle model is an adequate representation of actual vehicle behavior. At larger steering angles, responses of the classical bicycle model do not predict responses of the nonlinear vehicle model anymore. However, responses of the parametric bicycle model are in good agreement with those of the nonlinear vehicle model.

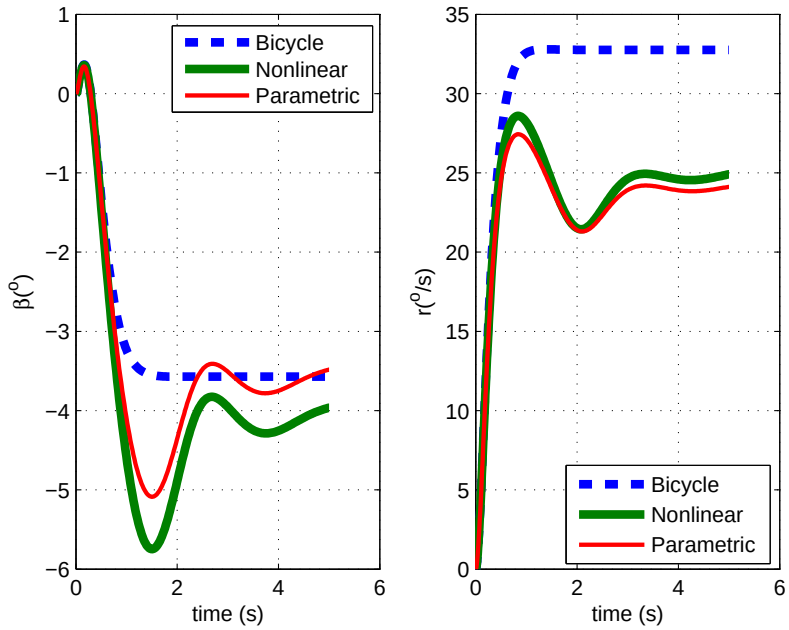


Figure 2.15. Vehicle response for driver's large step input ($\delta_f = 5^o$)

2.6. Comments

This section has introduced several vehicle models used for simulation and controller design tasks undertaken in this study. When pitch, bounce and roll modes can be neglected, i.e., a vehicle with low CG running on a smooth road at nearly constant speed, it is possible to derive a nonlinear two-track yaw plane vehicle model to reduce simulation time. As the derivation is straightforward, equations for this model will be given in Chapter 5 where the design of robust vehicle dynamics controllers is undertaken.

A major contribution of this section has been the introduction of a parametric bicycle model. Similarly, a parametric yaw-roll model could have been derived using the procedure outlined above. As these models cannot be expressed in a standard form, and depend on specific control channels included in a given vehicle dynamics controller design process, we have only provided the parametric bicycle model example to illustrate its efficiency in predicting nonlinear vehicle behavior. In Chapter 6, parametric vehicle models will constitute the modeling basis for gain scheduled controller design.

3. ROBUST CONTROL SYSTEM DESIGN

This chapter introduces concepts from robust control theory that have been used to design the VDC controllers proposed in this thesis. Preceding chapters have revealed that nonlinear vehicle behavior is mainly due to nonlinear tire behavior at large lateral tire slip.

The parametric modeling of vehicle dynamics introduced in Chapter 2 is one way to introduce tire nonlinearity for controller synthesis. Another approach consists in obtaining an uncertainty model for the tire force generation. These two approaches determine the robust control paradigm to be implemented when designing the VDC controller and will be explained in detail in this chapter.

The inherent mismatch between a system and its model is one of the main motivations for using feedback since feedback can reduce the effect of the uncertainty on the closed-loop system. In addition to uncertainties in the model, the disturbances acting on the vehicle, such as road disturbances or destabilizing ABS operation during extreme cornering, can again only be rejected by a feedback controller. Even though mere use of feedback improves the robustness of the closed-loop system, it is only in the robust control theory, that model uncertainties are explicitly taken into account during the design process, which explains the use of the H_∞ control framework in this thesis.

3.1. Analysis of LTI System through LMIs

In this section, we present the linear matrix inequality (LMI) formulation of the analysis tests for linear time invariant (LTI) systems for the H_∞ performance

characterization. We consider the system

$$\dot{\boldsymbol{x}} = \boldsymbol{A}\boldsymbol{x} + \boldsymbol{B}\boldsymbol{w} \tag{3.1a}$$

$$\boldsymbol{z} = \boldsymbol{C}\boldsymbol{x} + \boldsymbol{D}\boldsymbol{w} \tag{3.1b}$$

with $\boldsymbol{A}$ being Hurwitz (all eigenvalues of $\boldsymbol{A}$ located in the open left half complex-plane); with state variable $\boldsymbol{x} \in \mathbb{R}^n$, disturbance (performance) input $\boldsymbol{w} \in \mathbb{R}^{m_1}$ and performance output $\boldsymbol{z} \in \mathbb{R}^{p_1}$. In this work, we use the terminology performance input/output to refer to all those inputs/outputs of the system that are neither measured nor adjusted by control. In particular, a performance input can be a reference to be tracked or a disturbance to be attenuated. A performance output can be a tracking error. From our point of view, a system is a mapping from a space of input functions to a space of output functions. We recall that the transfer function associated to the system (3.1) is given by

$$G(s) := \boldsymbol{C}(sI - \boldsymbol{A})^{-1}\boldsymbol{B} + \boldsymbol{D}. \tag{3.2}$$

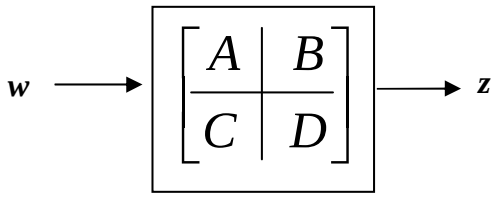


Figure 3.1. LTI system

3.1.1. H_∞ Norm

To measure the size of the input/output signals, $\mathcal{L}_p$-norms are used. The $\mathcal{L}_2$-norm, and derived from it, the H_∞ norm of an LTI system, are given special attention in this study.

Definition 3.1.1 *The space $\mathcal{L}_2[0,\infty)$ is the set of all Lebesgue-measurable functions that are square integrable, that is,*

$$\mathcal{L}_2[0,\infty) = \left\{ \boldsymbol{w} : \int_0^\infty \boldsymbol{w}(t)^T \boldsymbol{w}(t)\, dt < \infty \right\}. \tag{3.3}$$

If $\boldsymbol{w} \in \mathcal{L}_2$, its $\mathcal{L}_2$-norm is

$$\|\boldsymbol{w}\|_2 := \sqrt{\int_0^\infty \boldsymbol{w}(t)^T \boldsymbol{w}(t)\, dt}. \tag{3.4}$$

Definition 3.1.2 *The H_∞ norm of a complex transfer function that is analytic in the open right half of the complex plane is given by [44]*

$$\|G\|_\infty := \sup_{\omega \in I\!R} \sigma_{max}(G(j\omega)) \tag{3.5}$$

where σ_{max} stands for the largest singular value, i.e.,

$$\sigma_{max}(\boldsymbol{A}) = \sqrt{\lambda_{max}(\boldsymbol{A}^T \boldsymbol{A})}. \tag{3.6}$$

The H_∞ norm may be defined as the peak of the Bode magnitude plot of the associated transfer function. Moreover, it can be shown that, for zero initial conditions [44],

$$\|G\|_\infty = \sup_{\boldsymbol{w} \neq 0, \boldsymbol{w} \in \mathcal{L}_2} \frac{\|G\boldsymbol{w}\|_2}{\|\boldsymbol{w}\|_2}. \tag{3.7}$$

3.1.2. Computation of the H_∞ Norm

There are several methods available for the computation of $\|G\|_\infty$. For this purpose, we define

$$\boldsymbol{H} := \begin{bmatrix} \boldsymbol{A} + \boldsymbol{B}\boldsymbol{R}^{-1}\boldsymbol{D}^T\boldsymbol{C} & \boldsymbol{B}\boldsymbol{R}^{-1}\boldsymbol{B}^T \\ -\boldsymbol{C}^T(I + \boldsymbol{D}\boldsymbol{R}^{-1}\boldsymbol{D}^T)\boldsymbol{C} & -(\boldsymbol{A} + \boldsymbol{B}\boldsymbol{R}^{-1}\boldsymbol{D}^T\boldsymbol{C})^T \end{bmatrix}$$

where $\boldsymbol{R} := \gamma^2 I - \boldsymbol{D}^T\boldsymbol{D}$.

Theorem 3.1.3 *[45]* $\|G\|_\infty < 1$ *if and only if* $\boldsymbol{H}$ *has no eigenvalues on the imaginary axis.*

The theorem suggests the following way to compute the H_∞ norm: one selects a positive number γ; then tests if $\|G\|_\infty < \gamma$ (i.e., if $\|\gamma^{-1}G\|_\infty < 1$) by calculating the eigenvalues of the appropriate matrix; one then increases or decreases γ accordingly; the procedure is repeated. A bisection search is quite efficient: one first gets upper and lower bounds for $\|G\|_\infty$; and tries γ midway between these bounds. The procedure is continued until convergence in γ. The above routine is known as the bisection algorithm as presented in [45].

Another computation method involves the solution of an Algebraic Ricatti Equation (ARE).

Lemma 3.1.4 (Bounded Real Lemma) *[44] Given a continuous-time system realization* $G(s) = \boldsymbol{C}(sI - \boldsymbol{A})^{-1}\boldsymbol{B} + \boldsymbol{D}$*, the following are equivalent:*

(i) $\boldsymbol{A}$ *is stable and* $\|\boldsymbol{C}(sI - \boldsymbol{A})^{-1}\boldsymbol{B} + \boldsymbol{D}\|_\infty < \gamma$

(ii) The associated Hamiltonian has no pure imaginary eigenvalues

(iii) There is a symmetric stabilizing solution $\boldsymbol{P}$ *to ARE*

$$\boldsymbol{A}^T\boldsymbol{P} + \boldsymbol{P}\boldsymbol{A} + (\boldsymbol{B}^T\boldsymbol{P} + \boldsymbol{D}^T\boldsymbol{C})^T(\gamma^2 I - \boldsymbol{D}^T\boldsymbol{D})^{-1}(\boldsymbol{B}^T\boldsymbol{P} + \boldsymbol{D}^T\boldsymbol{C}) + \boldsymbol{C}^T\boldsymbol{C} = 0$$

Obviously, the H_∞ norm of the transfer function G between $\boldsymbol{w}$ and $\boldsymbol{z}$ is an important performance measure. In this thesis, its computation is given in terms of LMIs.

3.1.3. Linear Matrix Inequalities

Definition 3.1.5 *Let* $\boldsymbol{F_i} = \boldsymbol{F_i}^T, i = 0 : n$ *be given. A constraint on the variables* $x_1, x_2, ..., x_n \in I\!R$ *of the form*

$$\boldsymbol{F}(x) := \boldsymbol{F_0} + x_1\boldsymbol{F_1} + ... + x_n\boldsymbol{F_n} \succeq 0 \tag{3.8}$$

is called a linear matrix inequality (LMI).

Thus the feasible set of (3.8) is a convex set. A wide variety of problems in control theory can be written as optimization problems with LMI constraints such as multi-objective control problems. Analytic solutions to LMIs generally do not exist, but efficient numerical methods are available to find a feasible solution. In this thesis, all controller conditions have been expressed in terms of LMIs. We have used the YALMIP parser [46] and *SEDUMI* 1.1 solver [47] in our calculations.

Usually, two general cases are the subjects of the study of Linear Matrix Inequalities:

1. **Feasibility:** The test of existence for the solution $x \in \mathbb{R}^n$ of $F(x) \succeq 0$ is called a *feasibility* problem. It is called a feasible problem if there is a solution x or infeasible if such x does not exist.
2. **Optimization:** Let $\mathcal{S}$ denote the union of all possible solutions of $F(x) \succeq 0$,

and $f : \mathcal{S} \to \mathbb{R}$. In words, function f is used to quantify the optimality of that particular solution, by taking a solution and producing a scalar with an evaluation process. The problem is to determine the optimal solution among the possible solutions, i.e.,

$$V_{opt} = \inf_{x \in \mathcal{S}} f(x)$$

Example 3.1.6 *An example for the first case is the asymptotical stability of an autonomous system* $\dot{\boldsymbol{x}} = \boldsymbol{A}\boldsymbol{x}$. *From Lyapunov theory, we know that a system is asymptotically stable if and only if there exists a symmetric* $\boldsymbol{X} \in \mathbb{R}^{n \times n}$ *such that*

$$\begin{aligned} \boldsymbol{X} &\succ 0 \\ \boldsymbol{A}^T\boldsymbol{X} + \boldsymbol{X}\boldsymbol{A} &\prec 0. \end{aligned}$$

Thus, the asymptotical stability of the system is equivalent to the feasibility of the LMI

$$\begin{pmatrix} \boldsymbol{X} & 0 \\ 0 & -\boldsymbol{A}^T\boldsymbol{X} - \boldsymbol{X}\boldsymbol{A} \end{pmatrix} \succ 0$$

The problem can be put into the form of (3.8). *Due to symmetry, we parameterize* $\boldsymbol{X}$ *as*

$$\boldsymbol{F}(x) = x_1 \begin{bmatrix} 1 & 0 \\ 0 & 0 \end{bmatrix} + x_2 \begin{bmatrix} 0 & 1 \\ 1 & 0 \end{bmatrix} + x_3 \begin{bmatrix} 0 & 0 \\ 0 & 1 \end{bmatrix} = x_1\boldsymbol{X}_1 + x_2\boldsymbol{X}_2 + x_3\boldsymbol{X}_3$$

which is exactly in the form of (3.8), *with the exception of* $F_0 = 0$. *With this parametrization, we solve,*

$$\begin{aligned} \boldsymbol{F}(x) = x_1 \begin{pmatrix} \boldsymbol{X}_1 & 0 \\ 0 & -\boldsymbol{A}^T\boldsymbol{X}_1 - \boldsymbol{X}_1\boldsymbol{A} \end{pmatrix} + x_2 \begin{pmatrix} \boldsymbol{X}_2 & 0 \\ 0 & -\boldsymbol{A}^T\boldsymbol{X}_2 - \boldsymbol{X}_2\boldsymbol{A} \end{pmatrix} \\ + x_3 \begin{pmatrix} \boldsymbol{X}_3 & 0 \\ 0 & -\boldsymbol{A}^T\boldsymbol{X}_3 - \boldsymbol{X}_3\boldsymbol{A} \end{pmatrix} \succ 0 \end{aligned}$$

for x_1, x_2, x_3. After having solved the decision variables in an explicit form, we seek for the feasibility, optimality etc. of this variable vector.

3.1.4. Computation of the H_∞ Norm with LMIs

The following theorem reformulates the bounded real lemma in terms of an LMI condition.

Theorem 3.1.7 *[44] Given a continuous-time system realization $G(s) = \boldsymbol{C}(sI - \boldsymbol{A})^{-1}\boldsymbol{B} + \boldsymbol{D}$, the following are equivalent:*

(i) $\boldsymbol{A}$ *is stable and* $\|\boldsymbol{C}(sI - \boldsymbol{A})^{-1}\boldsymbol{B} + \boldsymbol{D}\|_\infty < \gamma$

(ii) There exits a matrix $P \succ 0$ *such that*

$$\begin{pmatrix} \boldsymbol{A}^T\boldsymbol{P} + \boldsymbol{P}\boldsymbol{A} & \boldsymbol{P}\boldsymbol{B} & \boldsymbol{C}^T \\ \boldsymbol{B}^T\boldsymbol{P} & -\gamma I & \boldsymbol{D}^T \\ \boldsymbol{C} & \boldsymbol{D} & -\gamma I \end{pmatrix} \prec 0$$

One can treat γ as an extra variable and, minimizing γ as the cost function, one can compute the H_∞ norm.

3.2. H_∞ Control of LTI Systems

We now consider the open-loop LTI system:

$$\dot{\boldsymbol{x}} = \boldsymbol{A}\boldsymbol{x} + \boldsymbol{B}_{\boldsymbol{w}}\boldsymbol{w} + \boldsymbol{B}_{\boldsymbol{u}}\boldsymbol{u} \tag{3.9a}$$

$$\boldsymbol{z} = \boldsymbol{C}_{\boldsymbol{z}}\boldsymbol{x} + \boldsymbol{D}_{\boldsymbol{z}\boldsymbol{w}}\boldsymbol{w} + \boldsymbol{D}_{\boldsymbol{z}\boldsymbol{u}}\boldsymbol{u} \tag{3.9b}$$

$$\boldsymbol{y} = \boldsymbol{C}_{\boldsymbol{y}}\boldsymbol{x} + \boldsymbol{D}_{\boldsymbol{y}\boldsymbol{w}}\boldsymbol{w} \tag{3.9c}$$

with state variable $\boldsymbol{x} \in \mathbb{R}^n$, and where $\boldsymbol{w} \in \mathbb{R}^{m_1}$ is the external disturbance on the system, $\boldsymbol{u} \in \mathbb{R}^{m_2}$ is the control input on the system to be designed, $\boldsymbol{z} \in \mathbb{R}^{p_1}$ is the

controlled output and $\boldsymbol{y} \in \mathbb{R}^{p_2}$ is the measured output. The overall control objective is to find a controller $\boldsymbol{K}$ which based on the information in $\boldsymbol{y}$, generates a control signal $\boldsymbol{u}$ which counteracts the influence of $\boldsymbol{w}$ on $\boldsymbol{z}$, thereby minimizing the closed-loop H_∞ norm from $\boldsymbol{w}$ to $\boldsymbol{z}$ as shown in Figure 3.2.

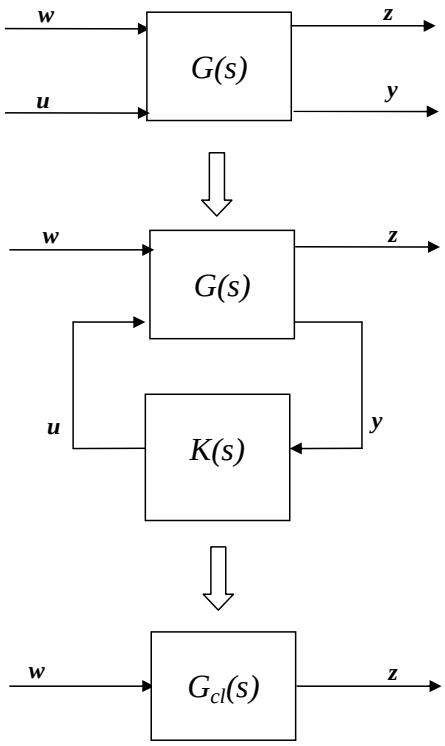


Figure 3.2. Standard H_∞ control problem

For the solution of this problem, one may design a dynamic output feedback controller of the form

$$\dot{\boldsymbol{x_c}} = \boldsymbol{A_c x_c} + \boldsymbol{B_c y} \tag{3.10a}$$

$$\boldsymbol{u} = \boldsymbol{C_c x_c} + \boldsymbol{D_c y}. \tag{3.10b}$$

The necessary and sufficient conditions for the existence of such a controller is given by the following theorem.

Theorem 3.2.1 *[48] For the system (3.9) the following two statements are equivalent:*

(i) There exists a controller of the form (3.10) that satisfies quadratic stability with disturbance attenuation γ.

(ii) There exist matrices $\boldsymbol{X}$, $\boldsymbol{Y}$, $\boldsymbol{L}$, $\boldsymbol{F}$, $\boldsymbol{G}$ and $\boldsymbol{H}$ such that:

$$\begin{pmatrix} \boldsymbol{AX} + \boldsymbol{XA}^T & & & \\ +\boldsymbol{B_u F} + \boldsymbol{F}^T \boldsymbol{B_u}^T & * & * & * \\ \boldsymbol{A}^T + \boldsymbol{C_y}^T \boldsymbol{H}^T \boldsymbol{B_u}^T & \boldsymbol{A}^T \boldsymbol{Y} + \boldsymbol{YA} & & \\ +\boldsymbol{L} & +\boldsymbol{GC_y} + \boldsymbol{C_y}^T \boldsymbol{G}^T & * & * \\ \boldsymbol{B_w}^T + \boldsymbol{D_{yw}}^T \boldsymbol{H}^T \boldsymbol{B_u}^T & \boldsymbol{B_w}^T \boldsymbol{Y} + \boldsymbol{D_{yw}}^T \boldsymbol{G}^T & -\gamma I & * \\ \boldsymbol{C_z} X + \boldsymbol{D_{zu}} \boldsymbol{F} & \boldsymbol{C_z} + \boldsymbol{D_{zu}} \boldsymbol{H} \boldsymbol{C_y} & \boldsymbol{D_{zw}} + \boldsymbol{D_{zu}} \boldsymbol{H} \boldsymbol{D_{yw}} & -\gamma I \end{pmatrix} \prec 0 \tag{3.11}$$

$$\begin{pmatrix} \boldsymbol{X} & I \\ I & \boldsymbol{Y} \end{pmatrix} \succ 0 \tag{3.12}$$

If (3.11) and (3.12) are satisfied a controller associated with $\boldsymbol{X}$ and $\boldsymbol{Y}$ is given by:

$$\boldsymbol{D_c} = \boldsymbol{H} \tag{3.13a}$$

$$\boldsymbol{C_c} = (\boldsymbol{F} - \boldsymbol{HC_y X}) \boldsymbol{S}^{-1} \tag{3.13b}$$

$$\boldsymbol{B_c} = \boldsymbol{B_u H} - \boldsymbol{Y}^{-1} \boldsymbol{G} \tag{3.13c}$$

$$\boldsymbol{A_c} = (\boldsymbol{A} + \boldsymbol{B_u HC_y} - \boldsymbol{B_u C_y}) \boldsymbol{X S}^{-1} + \boldsymbol{B_u C_c} - \boldsymbol{Y}^{-1} \boldsymbol{L S}^{-1} \tag{3.13d}$$

where $\boldsymbol{S} = \boldsymbol{X} - \boldsymbol{Y}^{-1}$.

3.2.1. Addition of Frequency Weights

The selection of frequency weights is an integral part of every H_∞ controller design. The weighting functions are chosen to reflect the design objectives and knowledge on the disturbances and sensor noise [44]. Weights are used to describe the expected or known frequency content of exogenous signals and the desired frequency content of error signals. In Figure 3.3, G and G_d represent models of the plant and disturbance dynamics respectively and $\boldsymbol{K}$ is the controller to be designed. Weights W_d, W_i and W_n may be constant or dynamic and describe the relative importance and/or frequency content of the disturbances, set points and noise signals respectively. For example, W_i may be used to shape of the steering handwheel input. Hence a low pass filter

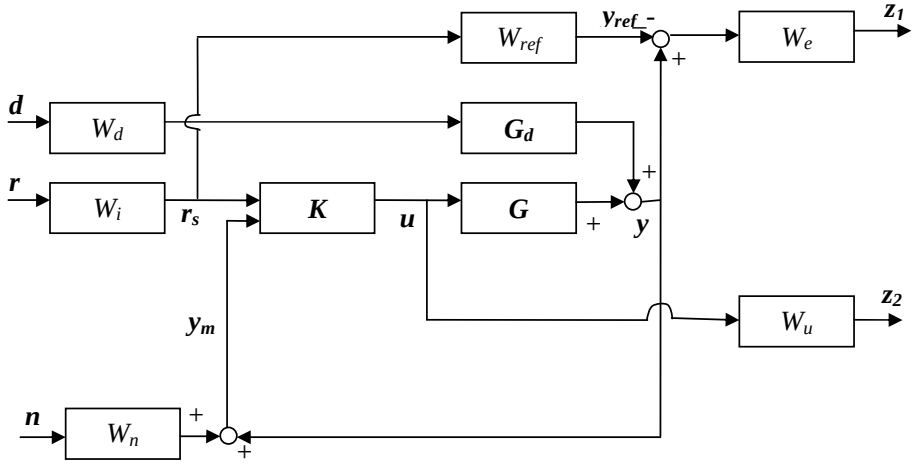


Figure 3.3. H_∞ control problem augmented with frequency weights

must be designed for W_i. The weight W_{ref} is a desired closed-loop transfer function between the weighted set point $\boldsymbol{r_s}$ and the actual output $\boldsymbol{y}$. The weights W_e and W_u reflect the desired frequency content of the error $(\boldsymbol{z} - \boldsymbol{z_{ref}})$ and the control signals $\boldsymbol{u}$, respectively. Hence, W_u may be shaped so as to prevent high frequency controller inputs. The problem can be cast into a standard H_∞ controller design problem in the general control configuration by defining

$$\boldsymbol{w} = \begin{bmatrix} \boldsymbol{d} \\ \boldsymbol{r} \\ \boldsymbol{n} \end{bmatrix}; \boldsymbol{z} = \begin{bmatrix} z_1 \\ z_2 \end{bmatrix}; \boldsymbol{y} = \begin{bmatrix} \boldsymbol{r_s} \\ \boldsymbol{y_m} \end{bmatrix} \tag{3.14}$$

3.3. Linear Parameter Varying Systems

An LPV system is a linear system whose describing matrices depend on a time-varying parameter vector $\boldsymbol{\delta}(t)$ as

$$\dot{\boldsymbol{x}} = \boldsymbol{A}(\boldsymbol{\delta}(t))\boldsymbol{x} + \boldsymbol{B_w}(\boldsymbol{\delta}(t))\boldsymbol{w} \tag{3.15a}$$

$$\boldsymbol{z} = \boldsymbol{C_z}(\boldsymbol{\delta}(t))\boldsymbol{x} + \boldsymbol{D_{zw}}(\boldsymbol{\delta}(t))\boldsymbol{w}. \tag{3.15b}$$

The vector valued time function $\boldsymbol{\delta}(t) : \mathbb{R}_+ \rightarrow \mathbb{R}^q$ denotes the parameter dependence of the matrices.

3.3.1. Linear Fractional Transformations

If $\boldsymbol{A}$, $\boldsymbol{B_w}$, $\boldsymbol{C_z}$, $\boldsymbol{D_{zw}}$ depend rationally on $\boldsymbol{\delta}(t)$, then (3.15) can be put in the form [44]:

$$\dot{\boldsymbol{x}} = \boldsymbol{A}\boldsymbol{x} + \boldsymbol{B_p}\boldsymbol{p} + \boldsymbol{B_w}\boldsymbol{w} \tag{3.16a}$$

$$\boldsymbol{q} = \boldsymbol{C_q}\boldsymbol{x} + \boldsymbol{D_{qp}}\boldsymbol{p} + \boldsymbol{D_{qw}}\boldsymbol{w}, \qquad \boldsymbol{p} = \boldsymbol{\Delta}\boldsymbol{q} \tag{3.16b}$$

$$\boldsymbol{z} = \boldsymbol{C_z}\boldsymbol{x} + \boldsymbol{D_{zp}}\boldsymbol{p} + \boldsymbol{D_{zw}}\boldsymbol{w} \tag{3.16c}$$

Here, vectors $\boldsymbol{p}$ and $\boldsymbol{q}$ are used to describe the fractional dependence of the linear system on the parameters δ_i. Furthermore, $\boldsymbol{\Delta} = \mathbf{diag}(\delta_1 I_{n_1}, ..., \delta_k I_{n_k})$, where δ_is are time-varying parameters with known bounds of variation such that

$$\delta_i(t) \in [\underline{\delta_i}, \bar{\delta}_i] \quad \forall t \geq 0, \ \forall i = 1 : k.$$

We define the set of Δs obtained at the extreme parameter values as $\boldsymbol{\Delta}_{vex}$. (Obviously, $\boldsymbol{\Delta}_{vex}$ has 2^k elements.)

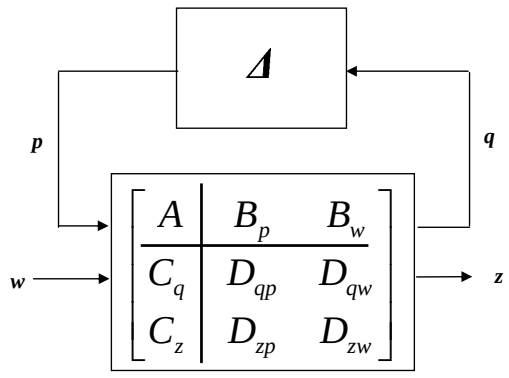


Figure 3.4. LPV system with model uncertainty

The interconnection of the linear system with such a $\boldsymbol{\Delta}$ block is known as a linear fractional transformation (LFT). System with uncertain parameters and nonlinear

systems can always be put in this form if their describing equations are manipulated so as to reflect rational dependence on operating parameters, as will be made more clear in the example that follows.

Example 3.3.1 *[44] One natural type of uncertainty is unknown coefficients in a state space model. To motivate this type of uncertainty, we will begin with a familiar mass/spring/damper system, as shown in Figure 3.5.*

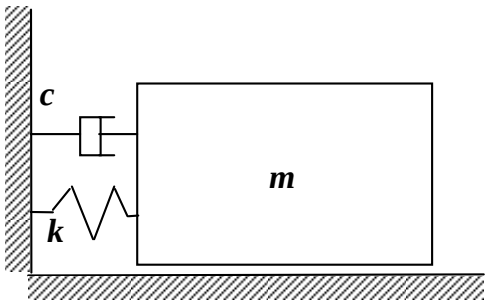


Figure 3.5. Mass/spring/damper system

The dynamical equation of the system motion can be described by

$$\ddot{x} + \frac{c}{m}\dot{x} + \frac{k}{m}x = \frac{F}{m}. \tag{3.17}$$

We suppose that the three physical parameters m, c and k are not known exactly, but are believed to be in known intervals. In particular, the actual mass m is within 10% of a nominal mass, m_o, the actual damping value c is within 20% of a nominal value, c_o and the actual spring stiffness k is within 30% of a nominal spring stiffness, k_o. Now we introduce perturbations δ_m, δ_c and δ_k, which are assumed to be unknown but lie in the interval $[-1, 1]$.

It is easy to check that $\frac{1}{m}$ can be represented as

$$\frac{1}{m} = \frac{1}{m_o(1 + 0.1\delta_m)} = \frac{1}{m_o} - \frac{0.1}{m_o}(1 + 0.1\delta_m)^{-1}. \tag{3.18}$$

Then we suppose that the states of the dynamical system are selected as $x_1 = x$, $x_2 = \dot{x}$ *and the disturbance input is selected as* $w = F$.

Equation (3.17) *may be written as*

$$\dot{x}_2 = -\frac{c}{m}x_2 - \frac{k}{m}x_1 + \frac{F}{m} \tag{3.19a}$$

$$= \left(-\frac{c}{m_o}x_2 - \frac{k}{m_o}x_1 + \frac{F}{m_o}\right)\left[1 - 0.1\delta_m(1+0.1\delta_m)^{-1}\right] \tag{3.19b}$$

$$= \left(-\frac{c_o + 0.2c_o\delta_c}{m_o}x_2 - \frac{k_o + 0.3k_o\delta_k}{m_o}x_1 + \frac{F}{m_o}\right)\left[1 - 0.1\delta_m(1+0.1\delta_m)^{-1}\right] \tag{3.19c}$$

$$= -\frac{c_o}{m_o}x_2 - \frac{k_o}{m_o}x_1 + \frac{F}{m_o} - \frac{0.2c_o\delta_c}{m_o}x_2 - \frac{0.3k_o\delta_k}{m_o}x_1$$
$$+ \frac{1}{m_o}\left[-(c_o + 0.2c_o\delta_c)x_2 - (k_o + 0.3k_o\delta_k)x_1 + F\right]\left[-0.1\delta_m(1+0.1\delta_m)^{-1}\right] \tag{3.19d}$$

Now we define

$$q_1 = 0.3k_o x_1; \quad p_1 = \delta_k q_1 \tag{3.20a}$$

$$q_2 = 0.2c_o x_2; \quad p_2 = \delta_c q_2 \tag{3.20b}$$

$$q_3 = \left[(-c_o + 0.2c_o\delta_c)x_2 - (k_o + 0.3k_o\delta_k)x_1 + F\right]\left[(1+0.1\delta_m)^{-1}\right]; \quad p_3 = \delta_m q_3 \tag{3.20c}$$

Then noting that $(1+0.1\delta_m)^{-1} = 1 - 0.1\delta_m(1+0.1\delta_m)^{-1}$, *one may express* q_3 *as*

$$q_3 = \left[(-c_o + 0.2c_o\delta_c)x_2 - (k_o + 0.3k_o\delta_k)x_1 + F\right]\left[1 - 0.1\delta_m(1+0.1\delta_m)^{-1}\right] \tag{3.21a}$$

$$= -c_o x_2 - k_o x_1 + F - p_1 - p_2 - 0.1p_3 \tag{3.21b}$$

With the above definitions, one can finally express (3.17) as

$$\dot{x}_2 = -\frac{c_o}{m_o}x_2 - \frac{k_o}{m_o}x_1 + \frac{F}{m_o} - \frac{1}{m_o}p_1 - \frac{1}{m_o}p_2 - \frac{0.1}{m_o}p_3. \tag{3.22}$$

When put into the generic LPV representation (3.16), one has:

$$\boldsymbol{A} = \begin{pmatrix} 0 & 1 \\ -\frac{k_o}{m_o} & -\frac{c_o}{m_o} \end{pmatrix} \quad \boldsymbol{B_w} = \begin{pmatrix} 0 \\ \frac{1}{m_o} \end{pmatrix} \quad \boldsymbol{B_p} = \begin{pmatrix} 0 & 0 & 0 \\ -\frac{1}{m_o} & -\frac{1}{m_o} & -\frac{0.1}{m_o} \end{pmatrix}$$

$$\boldsymbol{C_q} = \begin{pmatrix} 0.3k_o & 0 \\ 0 & 0.2c_o \\ -k_o & -c_o \end{pmatrix} \quad \boldsymbol{D_{qp}} = \begin{pmatrix} 0 & 0 & 0 \\ 0 & 0 & 0 \\ -1 & -1 & -0.1 \end{pmatrix} \quad \boldsymbol{D_{qw}} = \begin{pmatrix} 0 \\ 0 \\ -1 \end{pmatrix}$$

$$\boldsymbol{\Delta} = \boldsymbol{diag}(\delta_k, \delta_c, \delta_m)$$

3.3.2. Induced-$\mathcal{L}_2$ Gain of LPV System

One should note that no assumption has been made on the rate of change of time-varying parameters. No transfer function can be obtained for the system with time-varying parameters, so it is hard to speak of an H_∞ norm for an LPV system. Rather, an equivalent norm definition for such a system is the induced-$\mathcal{L}_2$ gain. The following theorem provides a way to calculate the induced-$\mathcal{L}_2$ gain of an LPV system from $\boldsymbol{w}$ to $\boldsymbol{z}$ of (3.16).

Theorem 3.3.2 *[49] If there exists $\boldsymbol{X} = \boldsymbol{X}^T$, $\boldsymbol{Q} = \boldsymbol{Q}^T$, $\boldsymbol{S}$, $\boldsymbol{R} = \boldsymbol{R}^T$ such that*

$$\boldsymbol{X} \succ 0 \tag{3.23}$$

$$\begin{pmatrix} \Delta \\ I \end{pmatrix}^T \begin{pmatrix} \boldsymbol{Q} & \boldsymbol{S} \\ \boldsymbol{S}^T & \boldsymbol{R} \end{pmatrix} \begin{pmatrix} \Delta \\ I \end{pmatrix} \succ 0 \qquad \forall \Delta \in \boldsymbol{\Delta}_{vex} \tag{3.24}$$

$$\begin{pmatrix} * \\ * \\ * \\ * \\ * \\ * \end{pmatrix}^T \begin{pmatrix} 0 & \boldsymbol{X} & 0 & 0 & 0 & 0 \\ \boldsymbol{X} & 0 & 0 & 0 & 0 & 0 \\ 0 & 0 & -\gamma I & 0 & 0 & 0 \\ 0 & 0 & 0 & -\frac{1}{\gamma} & 0 & 0 \\ 0 & 0 & 0 & 0 & \boldsymbol{Q} & \boldsymbol{S} \\ 0 & 0 & 0 & 0 & \boldsymbol{S}^T & \boldsymbol{R} \end{pmatrix} \begin{pmatrix} I & 0 & 0 \\ \boldsymbol{A} & \boldsymbol{B_w} & \boldsymbol{B_p} \\ 0 & I & 0 \\ \boldsymbol{C_z} & \boldsymbol{D_{qw}} & \boldsymbol{D_{zw}} \\ 0 & 0 & I \\ \boldsymbol{C_q} & \boldsymbol{D_{qw}} & \boldsymbol{D_{qp}} \end{pmatrix} \prec 0. \quad (3.25)$$

then the system (3.16) is asymptotically stable and the induced-$\mathcal{L}_2$ gain from $\boldsymbol{w}$ to $\boldsymbol{z}$ is smaller than γ. ■

3.4. H_∞ Control of LPV Systems

3.4.1. Disturbance Attenuation for LPV Systems

We now consider the open-loop LPV system:

$$\dot{\boldsymbol{x}} = \boldsymbol{A}\boldsymbol{x} + \boldsymbol{B_p}\boldsymbol{p} + \boldsymbol{B_w}\boldsymbol{w} + \boldsymbol{B_u}\boldsymbol{u} \quad (3.26a)$$

$$\boldsymbol{q} = \boldsymbol{C_q}\boldsymbol{x} + \boldsymbol{D_{qp}}\boldsymbol{p} + \boldsymbol{D_{qw}}\boldsymbol{w} + \boldsymbol{D_{qu}}\boldsymbol{u}, \qquad \boldsymbol{p} = \boldsymbol{\Delta}\boldsymbol{q} \quad (3.26b)$$

$$\boldsymbol{z} = \boldsymbol{C_z}\boldsymbol{x} + \boldsymbol{D_{zp}}\boldsymbol{p} + \boldsymbol{D_{zw}}\boldsymbol{w} + \boldsymbol{D_{zu}}\boldsymbol{u} \quad (3.26c)$$

$$\boldsymbol{y} = \boldsymbol{C_y}\boldsymbol{x} + \boldsymbol{D_{yp}}\boldsymbol{p} + \boldsymbol{D_{yw}}\boldsymbol{w}, \quad (3.26d)$$

The robust H_∞ controller design problem for an LPV plant with some rational parameter dependence can simply be stated as:

"*Find a stabilizing controller $\boldsymbol{K}$ such that the induced-$\mathcal{L}_2$ gain from $\boldsymbol{w}$ to $\boldsymbol{z}$ is less than γ for all $\boldsymbol{\Delta}$.*"

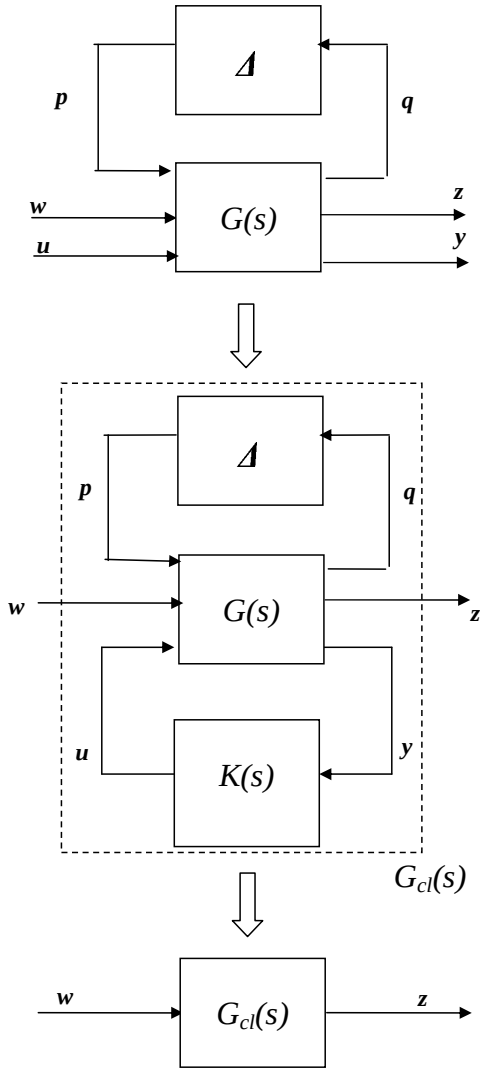


Figure 3.6. LPV disturbance attenuation problem

3.4.2. Robust Full State Feedback Controller Design

The state feedback control problem consists of designing a controller $\boldsymbol{K}$ such that the $\mathcal{L}_2$-gain from $\boldsymbol{w}$ to $\boldsymbol{z}$ is less than some specified level, γ, for all possible values of δ_is. Obviously, the entire state vector must be available for feedback. In this case, it is well-known that there is no need to search for a dynamic controller $\boldsymbol{K}(s)$ and that a *static* control law of the form $\boldsymbol{u} = \boldsymbol{K}\boldsymbol{x}$ can be found to achieve the control objective. Sufficient conditions for the existence of such a state feedback controller are given by the following theorem.

Theorem 3.4.1 *[49] For the LPV system (3.26) , there exists a state feedback control law of the form* $\boldsymbol{u} = \boldsymbol{K}\boldsymbol{x}$ *that satisfies* H_∞ *performance with disturbance attenuation* γ *if there exist matrices* $\boldsymbol{Y} = \boldsymbol{Y}^T$, $\boldsymbol{M}$, $\boldsymbol{Q} = \boldsymbol{Q}^T$, $\boldsymbol{S}$, $\boldsymbol{R} = \boldsymbol{R}^T$ *such that*

$$\boldsymbol{Q} \prec 0, \quad \boldsymbol{Y} \succ 0, \quad \boldsymbol{R} \succ 0, \tag{3.27}$$

$$\begin{pmatrix} I \\ -\Delta^T \end{pmatrix}^T \begin{pmatrix} \boldsymbol{Q} & \boldsymbol{S} \\ \boldsymbol{S}^T & \boldsymbol{R} \end{pmatrix} \begin{pmatrix} I \\ -\Delta^T \end{pmatrix} \prec 0 \qquad \forall \Delta \in \boldsymbol{\Delta}_{vex} \tag{3.28}$$

$$\begin{pmatrix} * \\ * \\ * \\ * \\ * \\ * \end{pmatrix}^T \begin{pmatrix} 0 & I & 0 & 0 & 0 & 0 \\ I & 0 & 0 & 0 & 0 & 0 \\ 0 & 0 & \boldsymbol{Q} & \boldsymbol{S} & 0 & 0 \\ 0 & 0 & \boldsymbol{S}^T & \boldsymbol{R} & 0 & 0 \\ 0 & 0 & 0 & 0 & -\frac{1}{\gamma} & 0 \\ 0 & 0 & 0 & 0 & 0 & \gamma \end{pmatrix}$$
$$\begin{pmatrix} -(\boldsymbol{A}\boldsymbol{Y} + \boldsymbol{B_u}\boldsymbol{M})^T & -(\boldsymbol{C_q}\boldsymbol{Y} + \boldsymbol{D_{qu}}\boldsymbol{M})^T & -(\boldsymbol{C_z}\boldsymbol{Y} + \boldsymbol{D_{zu}}\boldsymbol{M})^T \\ I & 0 & 0 \\ -\boldsymbol{B_p}^T & -\boldsymbol{D_{qp}}^T & -\boldsymbol{D_{zp}}^T \\ 0 & I & 0 \\ -\boldsymbol{B_w}^T & -\boldsymbol{D_{qw}}^T & -\boldsymbol{D_{zw}}^T \\ 0 & 0 & I \end{pmatrix} \succ 0. \tag{3.29}$$

When these conditions are satisfied, the controller can be taken as $\boldsymbol{K} = \boldsymbol{M}\boldsymbol{Y}^{-1}$. ■

Inequalities (3.28) and (3.29) constitute LMIs in the matrix variables $\boldsymbol{Q}$, $\boldsymbol{R}$, $\boldsymbol{S}$, $\boldsymbol{Y}$ and $\boldsymbol{M}$. As such, this formulation turns the controller design problem to a convex optimization problem. The problem can now be solved numerically using one of many suitable solvers in the literature. Furthermore, by performing a simple transformation on (3.29), one can obtain a formulation where γ appears linearly as well. Then, by treating γ as an extra variable and minimizing γ as the cost function, one can essentially obtain the smallest possible disturbance attenuation level γ^* and the controller matrix

$\boldsymbol{K}$ that yields it.

3.5. Comments

This section has basically introduced a robust state feedback controller synthesis for the solution of vehicle dynamics control problems. In Chapter 4 and Chapter 5, the wheel slip regulation and the combined sideslip and yaw modes decoupling problems will be solved using this method.

4. ROBUST WHEEL-SLIP CONTROLLER DESIGN

4.1. Introduction

In this chapter, a robust control algorithm for anti-lock brake system is proposed. The method used is based on static state feedback of longitudinal slip and does not involve controller scheduling with changing vehicle speed or road adhesion coefficient estimation as is common in the ABS literature. An improvement involving scheduling of longitudinal slip reference with longitudinal acceleration measurement is included. Electromechanical braking actuators are used in simulations and the algorithm used in this study reveals that one can obtain high performance on roads with constant and varying adhesion coefficients, displaying nice robustness properties against large vehicle speed and road adhesion coefficient variations. Guidelines are provided for tuning controller gains to cope with unknown actuator delay and measurement noise. Finally, the implementation of the system on a full scale vehicle is considered and implementation issues related to brake force proportioning and braking on split μ road are treated. The main contribution of this chapter is a wheel slip regulation algorithm that will be made part of active differential control in the following chapters for vehicle handling improvement purposes.

4.2. Modeling of Braking Dynamics

The present study is based on a quarter car model taken from [10] that consists of a single wheel attached to a mass m. The model is valid for maneuvers involving braking without cornering on *non*-split μ roads. Hence, it may be used for braking simulations on roads where the road adhesion coefficient varies along the longitudinal trajectory of the vehicle.

4.2.1. Equations of Motion in ω and U

The equations of motion of the quarter car model are given by

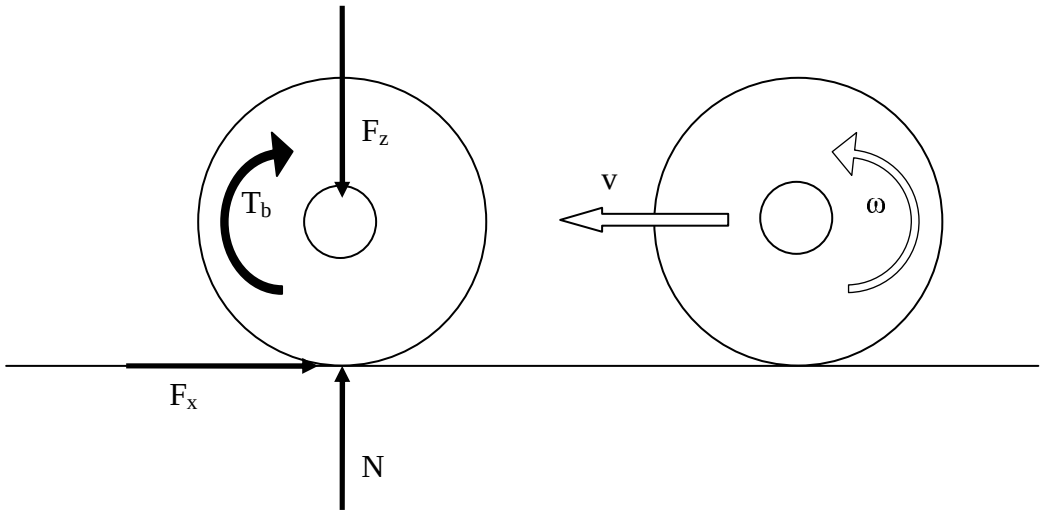


Figure 4.1. Quarter car braking model

$$m\dot{U} = F_x \tag{4.1a}$$

$$J_w\dot{\omega} = R_w F_x - T_b \tag{4.1b}$$

where T_b is the braking torque, R_w is the effective wheel radius and J_w is the tire wheel inertia. For the specific tire used in this study, typical plots of longitudinal tire force vs slip for a normal operating load F_o of $4000N$ is given in Figure 4.2. For high μ_{max}, the peak of the curves, and hence the operating point $\lambda^\star$ of the ABS controller to be selected, is close to 0.1, while for low μ_{max}, the peak is achieved at lower values.

Inspection of Figure 4.2 reveals that the loci of friction force maxima lie approximately on a straight line. Also following the line of ideas in [6], this observation makes it possible to establish an inverse map relating $\lambda^\star$ to vehicle acceleration $\dot{U} = \frac{F_x}{m}$. The following linear map equation can be shown to be valid for the tire model at hand and for a quarter car mass of $m = 400\ kg$:

$$\lambda^\star = 1.1305 \cdot 10^{-2}\dot{U} + 4.385 \cdot 10^{-3}. \tag{4.2}$$

Such a relation allows to schedule $\lambda^\star$ by online $\dot{U}$ measurements. This approach has been taken for a braking scenario on varying μ road in Section 4.4.

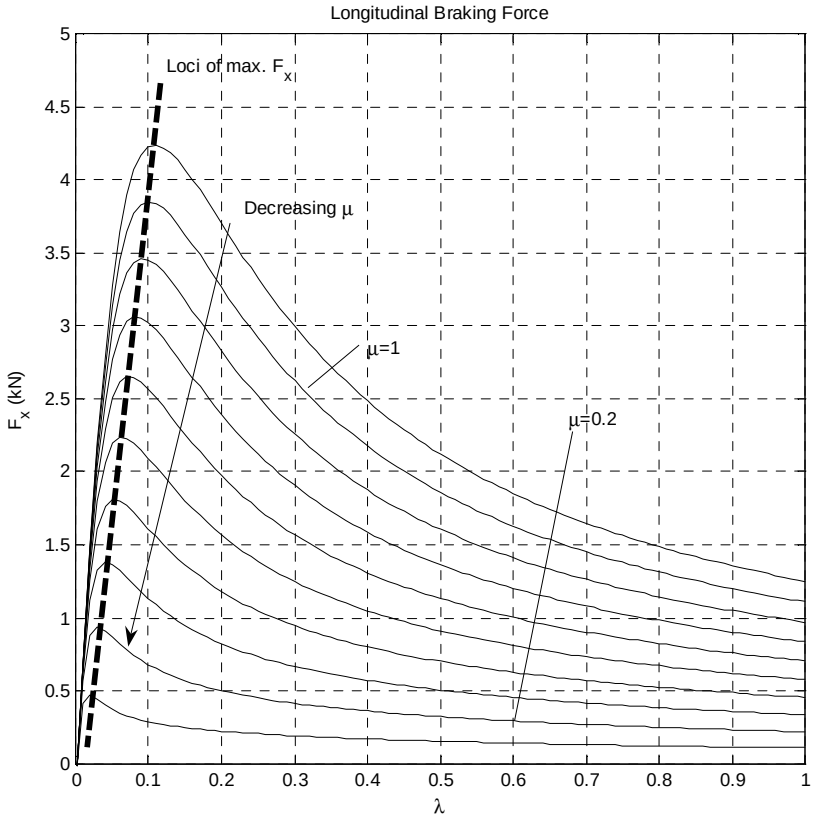


Figure 4.2. Longitudinal braking force vs longitudinal slip [38].

4.2.2. Equations of Motion in λ and U

Using the definition for λ given in (2.2), (4.1) yield

$$\dot{\lambda} = -\frac{1}{U}\left(\frac{1}{m}(1-\lambda) + \frac{R_w^2}{J_w}\right)F_x + \frac{1}{U}\frac{R_w}{J_w}T_b \tag{4.3a}$$

$$\dot{U} = \frac{1}{m}F_x. \tag{4.3b}$$

Then, we rewrite the first equation above as

$$\dot{\lambda} = \frac{1}{m}\frac{F_x}{U}\lambda - \left(\frac{1}{m} + \frac{R_w^2}{J_w}\right)\frac{C_\lambda}{U}\lambda + \frac{1}{U}\frac{R_w}{J_w}T_b, \tag{4.4}$$

where we define

$$C_\lambda := \frac{F_x}{\lambda}.$$

If one assumes that F_x, U and C_λ vary around selected nominal values of F_{xo}, U_o and $C_{\lambda o}$ as $F_x = F_{xo} + \delta_{Fx}$, $U = U_o + \delta_U$ and $C_\lambda = C_{\lambda o} + \delta_{C\lambda}$, then (4.3) can be written as

$$\dot{\lambda} = \frac{1}{m}\frac{F_{xo} + \delta_{Fx}}{U_o + \delta_U}\lambda - \left(\frac{1}{m} + \frac{R_w^2}{J_w}\right)\frac{C_{\lambda o} + \delta_{C\lambda}}{U_o + \delta_U}\lambda + \frac{1}{U_o + \delta_U}\frac{R_w}{J_w}u. \tag{4.5}$$

The first term on the right hand side can be expressed as

$$\frac{F_{xo} + \delta_{Fx}}{U_o + \delta_U}\lambda = (F_{xo} + \delta_{Fx})\left(\frac{1}{U_o} - \frac{1}{U_o^2}\delta_U(1 + \frac{\delta_U}{U_o})^{-1}\right)\lambda. \tag{4.6}$$

Defining

$$\nu_1 \ = -\frac{1}{U_o^2}\delta_U(1 + \frac{\delta_U}{U_o})^{-1}\lambda$$

or equivalently,

$$\nu_1 = \delta_U\sigma_1, \quad \sigma_1 \ = -\frac{1}{U_o^2}\lambda - \frac{1}{U_o}\nu_1$$

and

$$\nu_2 \ = \delta_{Fx}\sigma_2, \qquad \sigma_2 \ = \nu_1, \qquad \nu_3 \ = \delta_{Fx}\sigma_3, \qquad \sigma_3 \ = \frac{\lambda}{U_o}$$

then (4.6) can be written as

$$\frac{F_{xo} + \delta_{Fx}}{U_o + \delta_U}\lambda = \frac{F_{xo}}{U_o}\lambda + F_{xo}\nu_1 + \nu_2 + \nu_3. \tag{4.7}$$

In a similar manner, one can show that

$$\frac{C_{\lambda o} + \delta_{C\lambda}}{U_o + \delta_U}\lambda = \frac{C_{\lambda o}}{U_o}\lambda + C_{\lambda o}\varrho_1 + \varrho_2 + \varrho_3 \tag{4.8}$$

with

$$\begin{aligned} \varrho_1 &= \delta_U \pi_1, & \varrho_2 &= \delta_{C\lambda} \pi_2, & \varrho_3 &= \delta_{C\lambda} \sigma_3, \\ \pi_1 &= -\frac{1}{U_o^2}\lambda - \frac{1}{U_o}\varrho_1, & \pi_2 &= \varrho_1, & \pi_3 &= \frac{\lambda}{U_o}, \end{aligned}$$

and finally,

$$\frac{1}{U_o + \delta_U} T_b = \frac{1}{U_o}\lambda + C_{\lambda o} T_b + \varrho_{T_b} \tag{4.9}$$

with

$$\varrho_{T_b} = \delta_U \pi_{T_b}, \quad \pi_{T_b} = -\frac{1}{U_o^2} T_b - \frac{1}{U_o}\varrho_{T_b}.$$

By defining

$$\boldsymbol{p} := \begin{bmatrix} \nu_3 & \nu_2 & \nu_1 & \varrho_1 & \varrho_{T_b} & \varrho_3 & \varrho_2 \end{bmatrix}^T \tag{4.10a}$$

$$\boldsymbol{q} := \begin{bmatrix} \sigma_3 & \sigma_2 & \sigma_1 & \pi_1 & \pi_{T_b} & \pi_3 & \pi_2 \end{bmatrix}^T, \tag{4.10b}$$

Equation (4.3) can be put in the form

$$\dot{\lambda} = \boldsymbol{A}\lambda + \boldsymbol{B_p}\boldsymbol{p} + \boldsymbol{B_u} T_b \tag{4.11a}$$

$$\boldsymbol{q} = \boldsymbol{C_q}\lambda + \boldsymbol{D_{qp}}\boldsymbol{p} + \boldsymbol{D_{qu}} T_b, \quad \boldsymbol{p} = \boldsymbol{\Delta q} \tag{4.11b}$$

where

$$\boldsymbol{A} := \frac{F_{xo}}{mU_o} - \left(\frac{R_w^2}{J_w} + \frac{1}{m}\right)\frac{C_{\lambda o}}{U_o} \tag{4.12a}$$

$$\boldsymbol{B_p} := \begin{bmatrix} \frac{1}{m} & \frac{1}{m} & \frac{F_{xo}}{m} & -C_{\lambda o}(\frac{1}{m} + \frac{R_w^2}{J_w}) & \frac{R_w}{J_w} & -\left(\frac{1}{m} + \frac{R_w^2}{J_w}\right) & -\left(\frac{1}{m} + \frac{R_w^2}{J_w}\right) \end{bmatrix} \tag{4.12b}$$

$$\boldsymbol{B_u} := \frac{R_w}{J_w U_o}, \qquad \boldsymbol{C_q} := \begin{bmatrix} \frac{1}{U_o} & 0 & -\frac{1}{U_o^2} & -\frac{1}{U_o^2} & 0 & \frac{1}{U_o} & 0 \end{bmatrix}^T \tag{4.12c}$$

$$\boldsymbol{D_{qp}} := \begin{bmatrix} 0 & 0 & 0 & 0 & 0 & 0 & 0 \\ 0 & 0 & 1 & 0 & 0 & 0 & 0 \\ 0 & 0 & -\frac{1}{U_o} & 0 & 0 & 0 & 0 \\ 0 & 0 & 0 & -\frac{1}{U_o} & 0 & 0 & 0 \\ 0 & 0 & 0 & 0 & -\frac{1}{U_o} & 0 & 0 \\ 0 & 0 & 0 & 0 & 0 & 0 & 0 \\ 0 & 0 & 0 & 1 & 0 & 0 & 0 \end{bmatrix} \tag{4.12d}$$

$$\boldsymbol{D_{qu}} := \begin{bmatrix} 0 & 0 & 0 & 0 & -\frac{1}{U_o^2} & 0 & 0 \end{bmatrix}^T \tag{4.12e}$$

and

$$\boldsymbol{\Delta} := \begin{bmatrix} \delta_{Fx} I_2 & 0 & 0 \\ 0 & \delta_U I_3 & 0 \\ 0 & 0 & \delta_{C\lambda} I_2 \end{bmatrix}. \tag{4.13}$$

Equation (4.11) represents a linear parameter-varying system, where δ_{Fx}, δ_U and $\delta_{C\lambda}$ are treated as time-varying parameters.

4.3. The ABS Control Problem

Our control objective is to obtain a control law so as to keep λ as close as possible to some reference value $\lambda^\star$ given in (4.2). We solve the reference tracking problem formulated in a disturbance attenuation setting, where $\boldsymbol{w} = \lambda^\star$ is treated as the "disturbance input" to the system with state $\boldsymbol{x} = \lambda$ and where $\boldsymbol{z} = \lambda^\star - \lambda$ is the controlled output required to be minimized. Our goal is to design a feedback control law for the applied torque, $\boldsymbol{u} = T_b$, so that **(a)** the closed-loop system is stable and **(b)** the

$\mathcal{L}_2$-gain from the disturbance to the controlled output is minimized.

In our case, the state-space matrices $\boldsymbol{A}$, $\boldsymbol{B_p}$, $\boldsymbol{B_u}$, $\boldsymbol{C_q}$, $\boldsymbol{D_{qp}}$ and $\boldsymbol{D_{qu}}$ are given in (4.12) and

$$\boldsymbol{B_w} = 0, \quad \boldsymbol{D_{qw}} = 0, \quad \boldsymbol{C_z} = 1, \quad \boldsymbol{D_{zp}} = 0, \quad \boldsymbol{D_{zw}} = -1, \quad \boldsymbol{D_{zu}} = 0. \tag{4.14}$$

Similar to the synthesis procedure for LTI systems, the problem is now augmented with rational weights W to achieve tracking of the reference slip $\lambda^\star$. The system augmented with weights and its equivalent representation through an augmented generalized plant $\breve{G}$ is given in Figure 4.3. Finally, one has to consider adding the dynamics

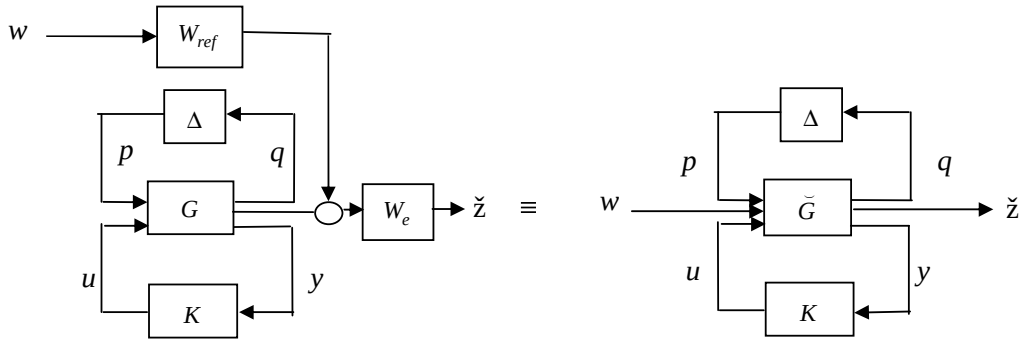


Figure 4.3. Feedback interconnection augmented with weights

of the electromechanical actuator as, in a real time application, the presence of this actuator introduces delay and may affect the performance of the control algorithm.

A filter W_{ref} with state vector $\boldsymbol{x_{ref}}$ and state-space realization

$$W_{ref} = \left[\begin{array}{c|c} \boldsymbol{A_{ref}} & \boldsymbol{B_{ref}} \\ \hline \boldsymbol{C_{ref}} & \boldsymbol{D_{ref}} \end{array}\right]$$

is added to filter out high frequency reference longitudinal slip command, which reduces the conservatism introduced by implementing controller synthesis in the $\mathcal{L}_2$-gain minimization setting.

Another filter W_e with state vector $\boldsymbol{x_e}$ and state-space realization

$$W_e = \left[\begin{array}{c|c} \boldsymbol{A_e} & \boldsymbol{B_e} \\ \hline \boldsymbol{C_e} & \boldsymbol{D_e} \end{array}\right]$$

is also added to reduce steady state tracking error.

Finally the dynamics of the electromechanical actuator with state $\boldsymbol{x_b}$ and state-space realization

$$W_b = \left[\begin{array}{c|c} \boldsymbol{A_b} & \boldsymbol{B_b} \\ \hline \boldsymbol{C_b} & \boldsymbol{D_b} \end{array}\right]$$

are added with the assumption that a simple first order filter can effectively represent the actual behavior of the actuator. In fact, the above state-space representation is nothing but $\tau_b \dot{T}_b + T_b = \tilde{T}_b$, with brake command $\tilde{T}_b$, time delay $\tau_b = 0.01s$ and actual braking torque T_b. The selection of the value of the time delay is based on [11].

The augmented LPV representation with generalized plant $\breve{G}$ and augmented state $\breve{\boldsymbol{x}} = \left[\begin{array}{cccc} \boldsymbol{x}^T & \boldsymbol{x_b}^T & \boldsymbol{x_{ref}}^T & \boldsymbol{x_e}^T \end{array}\right]^T$ is then given by

$$\breve{\boldsymbol{A}} = \begin{bmatrix} \boldsymbol{A} & \boldsymbol{BC_b} & 0 & 0 \\ 0 & \boldsymbol{A_b} & 0 & 0 \\ 0 & 0 & \boldsymbol{A_{ref}} & 0 \\ 0 & \boldsymbol{B_e C_y} & -\boldsymbol{B_e C_{ref}} & \boldsymbol{A_e} \end{bmatrix}, \breve{\boldsymbol{B}}_{\boldsymbol{p}} = \begin{bmatrix} \boldsymbol{B_p} \\ 0 \\ 0 \\ 0 \end{bmatrix}, \breve{\boldsymbol{B}}_{\boldsymbol{w}} = \begin{bmatrix} \boldsymbol{B_w} \\ \boldsymbol{B_{ref}} \\ -\boldsymbol{B_e D_{ref}} \\ 0 \end{bmatrix}, \tag{4.15a}$$

$$\breve{\boldsymbol{B}}_{\boldsymbol{u}} = \begin{bmatrix} 0 \\ \boldsymbol{B_b} \\ 0 \\ 0 \end{bmatrix}, \quad \breve{\boldsymbol{C}}_{\boldsymbol{q}} = \begin{bmatrix} \boldsymbol{C_q} & 0 & 0 & 0 \end{bmatrix}, \quad \breve{\boldsymbol{D}}_{\boldsymbol{qp}} = \boldsymbol{D_{qp}}, \quad \breve{\boldsymbol{D}}_{\boldsymbol{qu}} = \boldsymbol{D_{qu}}, \tag{4.15b}$$

$$\breve{\boldsymbol{C}}_{\boldsymbol{z}} = \begin{bmatrix} \boldsymbol{D_e C_y} & 0 & -\boldsymbol{D_e C_{ref}} & \boldsymbol{C_e} \end{bmatrix}, \quad \breve{\boldsymbol{D}}_{\boldsymbol{zw}} = -\boldsymbol{D_e D_{ref}}. \tag{4.15c}$$

Note that $\boldsymbol{D_{zp}}$, $\boldsymbol{D_{zu}}$ and $\boldsymbol{D_{qw}}$ are zero matrices of compatible dimensions and that $\boldsymbol{\Delta}$ remains unchanged.

4.4. Design Examples

In this section, a set of four robust static state feedback controllers is first designed as the solution of (3.28) and (3.29). Stability and robustness analysis of the control law follows. Finally, guidelines are derived for tuning controller gains when system parameters fall outside design bounds and for coping with actuator time delay and measurement noise.

4.4.1. Controller Design

Referring to Figure 4.2, F_x can be assumed to vary in the range $(0-6000\,N)$, from the instant braking begins until the instant reference slip $\lambda^\star$ is achieved. By inspection of the slope of the line of maximum braking force loci, C_λ can be assumed to vary in the range $(0-60000N)$. The problem is then solved with $F_{xo} = 3000N$, $\delta_{Fx} = 3000N$, $C_{\lambda o} = 30000N$ and $\delta_{C\lambda} = 30000N$. Furthermore, the initial speed is taken as 20 m/s in this section. Hence, one can take $U_o = 10$ m/s and $\delta_U = 10$ m/s.

$$W_{ref}(s) = \frac{6.28}{s + 6.28}$$

has been observed to yield quite satisfactory results. In order to have less than 0.1% steady state error,

$$W_e(s) = \frac{31.42\varphi}{s + 31.42}$$

has been designed with several low frequency gains φ as indicated in Table 4.1, resulting in the different controller gains displayed in the same table, the control law being given

by

$$\tilde{T}_b = u = kx + k_b x_b + k_r x_{ref} + k_e x_e.$$

In the next section, an in-depth analysis exploring the stability and robustness properties of the proposed control law is provided.

Table 4.1. Controller gains according to low frequency gain φ

Controller	φ	k	k_b	k_r	k_e
K_1	1000	$-1.369 \cdot 10^6$	$-1.423 \cdot 10^3$	$1.369 \cdot 10^6$	$-1.492 \cdot 10^7$
K_2	2000	$-3.064 \cdot 10^6$	$-2.111 \cdot 10^3$	$3.064 \cdot 10^3$	$-4.917 \cdot 10^7$
K_3	3000	$-1.142 \cdot 10^7$	$-6.121 \cdot 10^3$	$1.142 \cdot 10^7$	$-2.374 \cdot 10^8$
K_4	4000	$-1.644 \cdot 10^8$	$-6.810 \cdot 10^4$	$1.644 \cdot 10^8$	$-4.101 \cdot 10^9$

Braking performance on varying μ road can be observed in Figure 4.4 and Figure 4.5. The μ profile is given in the upper left plot of Figure 4.4. Following a dry road portion ($\mu_{max} = 1.0$), a sudden transition to a slippery road ($\mu_{max} = 0.2$) is observed, still followed by a road portion with a medium level of adhesion coefficient ($\mu_{max} = 0.6$). We have also assumed the possibility of constructing an optimal hypothetical controller K_{opt}, which has direct access to the instantaneous road adhesion coefficient data and which can use this information to generate maximum achievable braking.

As wheel dynamics are much faster than vehicle dynamics, it has been found advantageous to arbitrarily initiate $\lambda^\star$ at a value as high as 0.1 at the onset of braking while waiting for longitudinal acceleration to build up and then to implement the map described in (4.2). Braking forces developed by optimal and actual controllers are shown in Figure 4.5. It is seen that the performance of controllers with reference scheduling nearly equals that of K_{opt}.

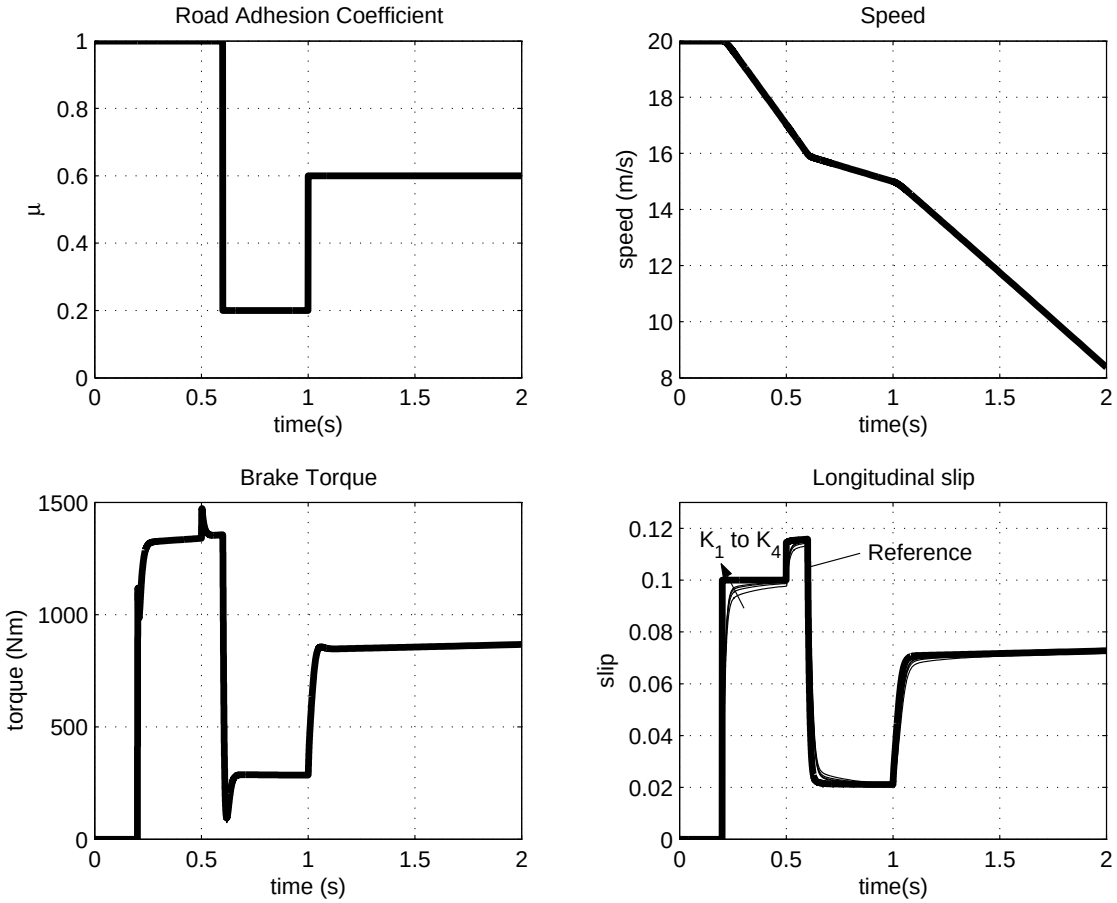


Figure 4.4. Braking controller performance on varying μ road.

4.4.2. A Qualitative Stability and Robustness Analysis for the Tuning of Design Parameters

The analysis provided in this section aims to show that the controller gains displayed in Table 4.1 fulfill certain conditions that guarantee controller robustness against unconsidered model uncertainties. More specifically, it is shown that the full state feedback nature of the control law can **(a)** achieve close to exact $\lambda^\star$ tracking independently from the instantaneous value of vehicle speed and road adhesion coefficient, **(b)** take into account actuator delay and, **(c)** ensure some degree of noise rejection by correct tuning of controller gains.

The derivation made here is *qualitative in nature* and is based on the essential assumption that U and F_x are slow-varying parameters when compared to λ and $\lambda^\star$.

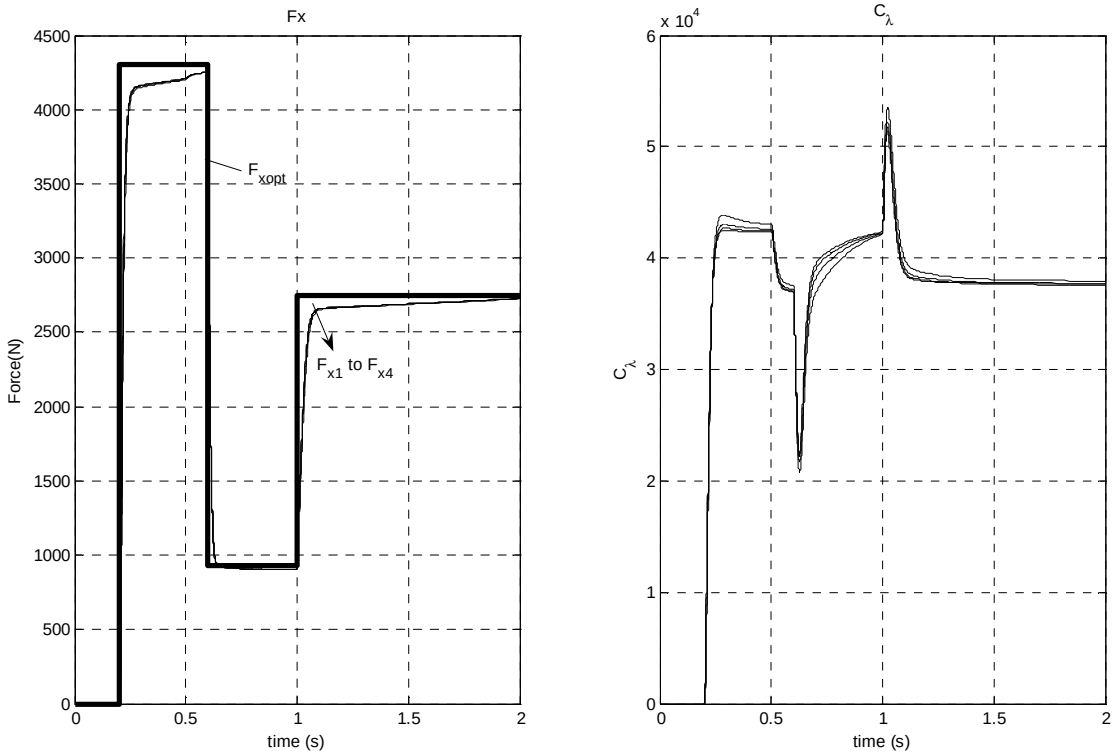


Figure 4.5. Variation of braking force and C_λ on varying μ road.

The justification lies in the fact that vehicle dynamics are slower than wheel dynamics and that tire relaxation makes F_x lag behind λ. Filters W_e and W_{ref} are assumed to be of first order with common filter pole placed at some φ_0 (for simplifying the following derivation).

After substitution of filter dynamics, the Laplace transform of brake command $u = \tilde{T}_b$ is given by

$$U(s) = k\Lambda(s) + \frac{k_e\varphi_0}{s+\varphi_0}(\Lambda(s) - \Lambda^\star(s)) + \frac{k_r\varphi_0}{s+\varphi_0}\Lambda^\star(s) + k_b X_b(s), \tag{4.16}$$

where $\Lambda(s)$, $\Lambda^\star(s)$, $X_b(s)$ stand for Laplace transforms of λ, $\lambda^\star$ and x_b respectively. The actual brake torque applied by the electromechanical actuator has been modelled in this study as the response of a first order filter with internal state x_b and input $\tilde{T}_b$ such that $\tau_b\dot{T}_b + T_b = \tilde{T}_b$. Assuming that $|k_b| \gg \tau_b$ (and obviously $k_b < 0$ for stability),

the Laplace transform of the actual brake torque is given by

$$T_b(s) = \frac{\Lambda(s)}{\tau_b(s-k_b)}\frac{ks+\varphi_0(k+k_e)}{s+\varphi_0} + \frac{\Lambda^\star(s)}{\tau_b(s-k_b)}\frac{\varphi_0(k_r-k_e)}{s+\varphi_0} \tag{4.17}$$

By further assuming that $|k_b| \gg \varphi_0$, the order of the transfer function from $\Lambda(s)$ and $\Lambda^\star(s)$ to $T_b(s)$ can be reduced, yielding

$$T_b(s) = -\frac{1}{\tau_b k_b}\Lambda(s)\frac{ks+\varphi_0(k+k_e)}{s+\varphi_0} - \frac{1}{\tau_b k_b}\Lambda^\star(s)\frac{\varphi_0(k_r-k_e)}{s+\varphi_0}. \tag{4.18}$$

Defining $\varphi_1 := \frac{1}{U}(\frac{1}{m}(1-\lambda) + \frac{R_w^2}{J_w})$ and $\varphi_2 := \frac{R_w}{J_w U}$, and assuming that **(a)** the Laplace Transform of the brake force can be approximated as $C_\lambda\Lambda(s)$ and **(b)** $\frac{\lambda}{m} \approx 0$, (4.3) can be equivalently expressed as

$$s\Lambda(s) - \underbrace{\lambda(0)}_{\approx 0} + \varphi_1 C_\lambda \Lambda(s) = \varphi_2 T_b(s). \tag{4.19}$$

Substituting for $T_b(s)$ and assuming that the initial condition $\lambda(0)$ is negligible in all short time intervals (the numerical value of λ being constrained to the interval $(0.0-0.1)$), the transfer function between the reference slip and the desired longitudinal slip can be expressed as

$$\frac{\Lambda(s)}{\Lambda^\star(s)} = \frac{\varphi_2\varphi_0\frac{k_e-k_r}{k_b\tau_b}}{s^2 + s(\varphi_0 + \varphi_1 C_\lambda + \varphi_2\frac{k}{k_b\tau_b}) + (\varphi_1 C_\lambda\varphi_0 + \varphi_2\varphi_0\frac{k+k_e}{k_b\tau_b})}. \tag{4.20}$$

Requiring $|k| \gg |k_b|$, $k < 0$, $|k_e| \gg |k_b|$ and $k_e < 0$ ensures closed-loop system stability as long as $\varphi_2\frac{k}{k_b\tau_b} \gg \varphi_0 + \varphi_1 C_\lambda > 0$ and $\alpha_2\varphi_0\frac{k+k_e}{k_b\tau_b} \gg \varphi_1 C_\lambda\alpha_0 > 0$. Furthermore, the same relationships make the DC gain of the system close to $\frac{k_e-k_r}{k_e+k}$, which indicates that taking $k_r = -k$ is necessary for tracking accuracy, *independently from parameter variations during braking.*

For the second order system (4.20), it is possible to define

- an "Effective Damping ratio" $\zeta_{eff} := \frac{k}{2}\sqrt{\frac{\varphi_2}{(k+k_e)k_b\tau_b}}$ and
- an "Effective Natural Frequency" $\omega_{n_{eff}} := \sqrt{\frac{\varphi_2\varphi_0}{\tau_b}}\sqrt{\frac{k+k_e}{k_b}}$.

Based on the above definitions, the following qualitative remarks can be made:

1. The bandwidth of the closed loop system is inversely proportional to k_b. Hence, taking k_b higher than its design value is expected to improve noise rejection.
2. In the presence of high actuator delay, taking k_b lower than its design value is expected to improve tracking by increasing $\omega_{n_{eff}}$ and hence the bandwidth of the system.
3. Inspection of design gains given in Table 4.1 indicates that designed control laws render the closed-loop system overdamped. For overdamped systems, settling time is proportional to $\frac{\zeta_{eff}}{\omega_{n_{eff}}}$ which is itself proportional in this study to $\frac{k}{k_e}$. Hence, taking $|k_e| > |k|$ is expected to improve settling time.

The above discussion explains why the relative magnitudes and signs of control gains in Table 4.1 guarantee satisfactory behavior of the closed-loop system.

4.4.3. Simulation Results for Conditions Beyond Design Specifications

Before proceeding into the design steps in the case of general variations in vehicle model and road adhesion, we give here a performance result for increased actuator delay to display the effect of tuning k_b. Inspection of ζ and ω_n formulae indicates that one can expect to conserve controller performance by keeping the product $\tau_b k_b$ constant: hence decreasing k_b in the presence of increasing actuator delay is expected to restore tracking performance, which can be seen in Figure 4.6, where the performance of K_4 with tuned gain k_b is displayed. Substantial steady state error is observed when the design value of k_b is used for a situation in which time delay τ_b is increased ten times. Decreasing the value of k_b ten times restores controller performance: both tracking and rise time are as good as the original design for low actuator time delay.

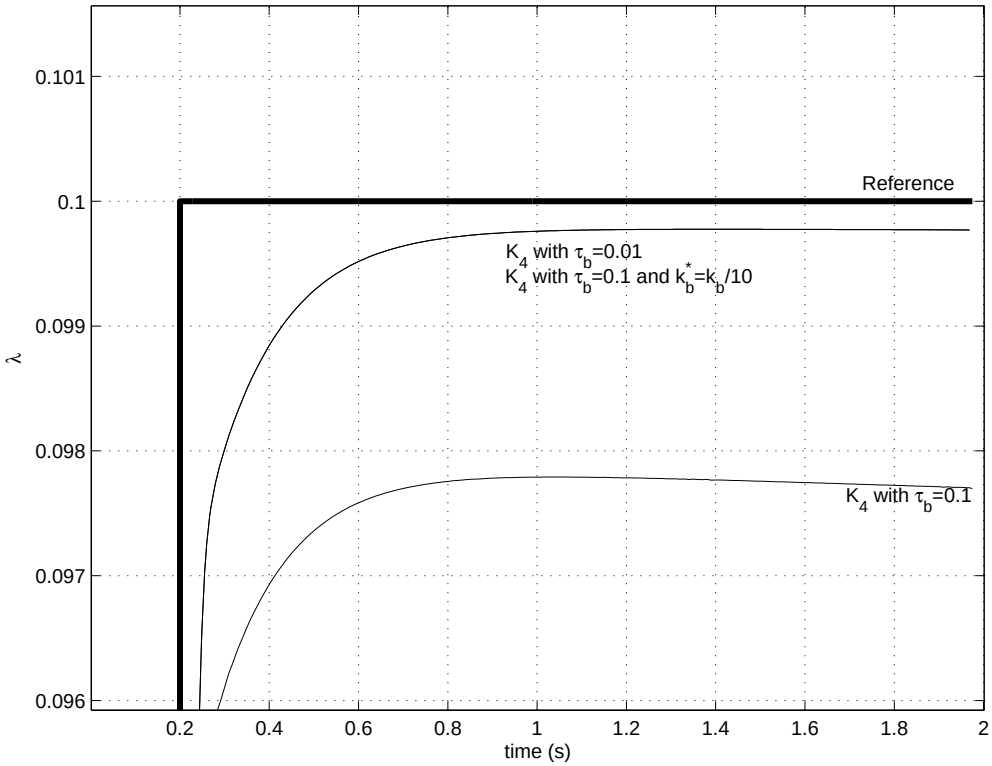


Figure 4.6. Controller performance in face of actuator delay

As a last case study, the performance of the proposed braking control law has been tested against general variations in the vehicle model and road conditions:

- Vehicle mass has been increased by 50%;
- Actuator delay has been taken as $\tau_b = 0.1\ s$ (ten times the design value);
- White noise has been added to the measured longitudinal slip λ such that signal-to-noise ratio $S/N \approx 15$;
- Initial vehicle speed has been taken as $U_o = 40\ m/s$ (outside allowable range);
- Braking on varying μ road has been considered.

The performance of K_4 is considered in what follows. The main design conflict lies in the tuning strategy of k_b due to the presence of both measurement noise and high actuator delay, while robustness of the control law against vehicle mass variation, road adhesion coefficient variation (both being interpreted as varying F_x) and large vehicle speed variation is already guaranteed. We have chosen to put more emphasis on noise rejection so as to limit actuator activity. The reason for this choice can be

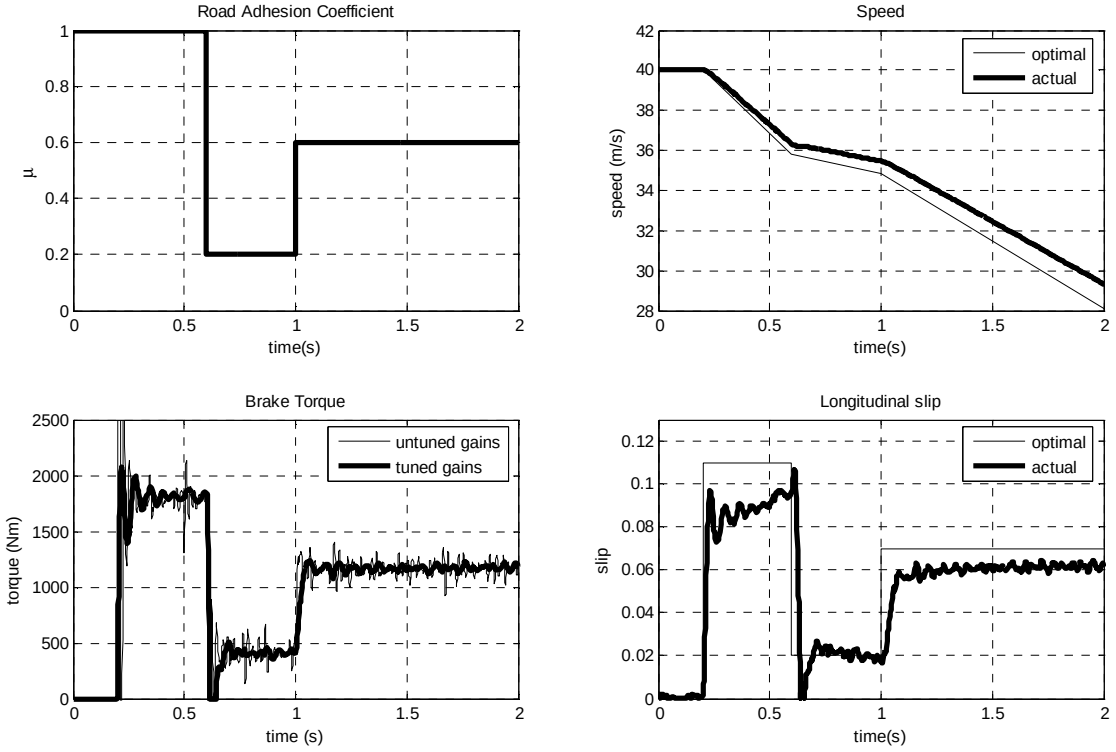


Figure 4.7. Braking controller performance (outside design range)

understood from the torque response displayed in Figure 4.7 for the actuator operating with untuned gains. Clearly, noise leads to chattering and must be rejected. Hence, the value of k_b has been increased to eight times its design value. The following decrease in bandwidth has resulted both in a decrease in the rise time of slip response and steady-state error in tracking. To compensate for steady-state error, the extra degree of freedom presented by the possibility of tuning k_r has been used, whose value has been increased by a factor of five. Inspection of Figure 4.7 and Figure 4.8 reveals that the decrease in bandwidth leads to a slight decrease in deceleration as reference $\lambda^\star$ tracking is impaired. However, tuning of the gains is observed to effectively limit actuator chattering.

4.5. ABS System Implementation on Full Scale Vehicle

The implementation of the proposed ABS system on a full scale vehicle requires using brake force proportioning. Furthermore, we also propose in this section a more

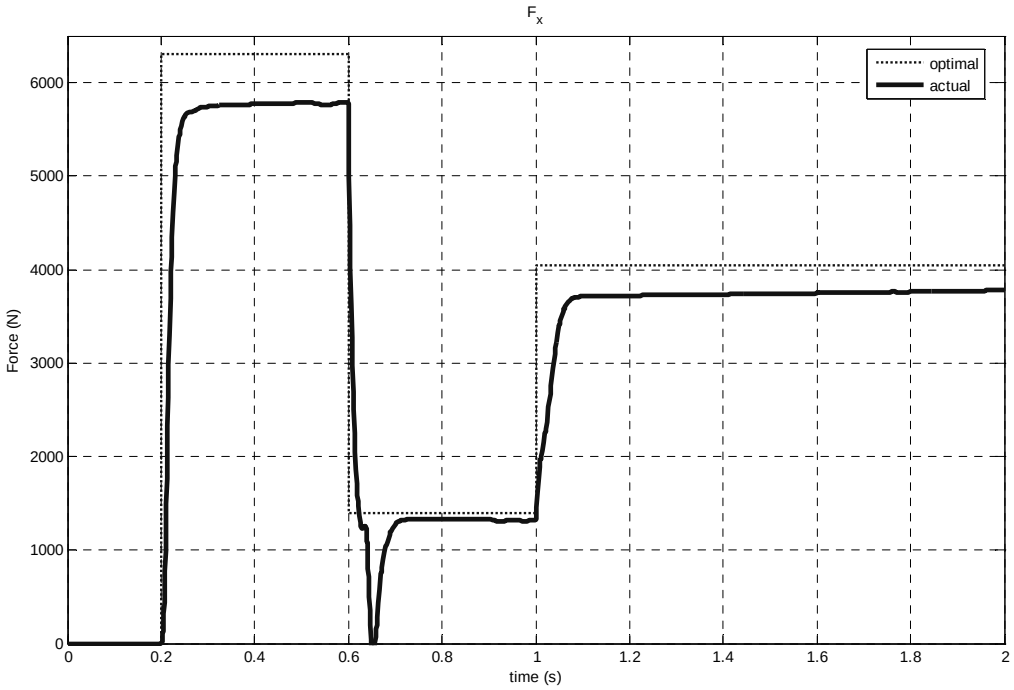


Figure 4.8. Variation of braking force (outside design range)

realistic design where conventional braking is used while operating away from the maximum point of the μ-slip. ABS is designed to cut in as soon as wheel deceleration reaches some predetermined limit.

4.5.1. Brake Force Proportioning

For straight-line braking on a level surface in the absence of any aerodynamic effects, optimum braking in terms of maximizing vehicle deceleration is defined by the following equation [50]:

$$\mu_f = \mu_r := \frac{a_x}{g} \tag{4.21}$$

where μ_f is front tire-road friction coefficient and μ_r is rear tire-road friction coefficient.

It can be shown that dynamic axle loads yield the following dynamic braking

forces:

$$F_{xf} = \frac{b + h\frac{a_x}{g}}{a+b} Mg\mu_{tf} \tag{4.22a}$$

$$F_{xr} = \frac{a - h\frac{a_x}{g}}{a+b} Mg\mu_{tr} \tag{4.22b}$$

where μ_{tf} and μ_{tr} can be considered as degree of utilization of tire. By setting these coefficients equal to the vehicle deceleration, optimum axle brake forces are obtained as

$$F_{xfopt} = \frac{b + h\frac{a_x}{g}}{a+b} Mg\frac{a_x}{g} \tag{4.23}$$

$$F_{xropt} = \frac{a - h\frac{a_x}{g}}{a+b} Mg\frac{a_x}{g}. \tag{4.24}$$

Simulation results during mild cornering (lane change maneuver with initial speed $U_o = 72\,kph$ consisting in shifting the lateral position of the vehicle by $H = 1\,m$ over a distance of $L = 5\,m$) are shown in Figure 4.9. The brake demand by the driver is half the maximal braking capacity of the vehicle. As expected, optimal braking is achieved.

During combined cornering and braking maneuvers on low μ roads, the braking capacity of tires decreases as some of the friction potential is used for generating cornering force. In such cases, if the ABS is not activated, wheel lock-up may occur, leading to poor vehicle handling. This issue is treated in the next section.

4.5.2. $\lambda_i^\star$ Estimation

In a combined cornering and braking maneuver, the vehicle longitudinal acceleration measurement is of no use for the estimation of the maximizing $\lambda^\star$: each wheel is under the action of a different lateral slip and a different normal load. Therefore, wheel deceleration measurements may be used to activate ABS.

As explained in [3], in the stable zone of braking, the wheel deceleration is limited to relatively low rates so that when the driver presses harder on the brake pedal, the

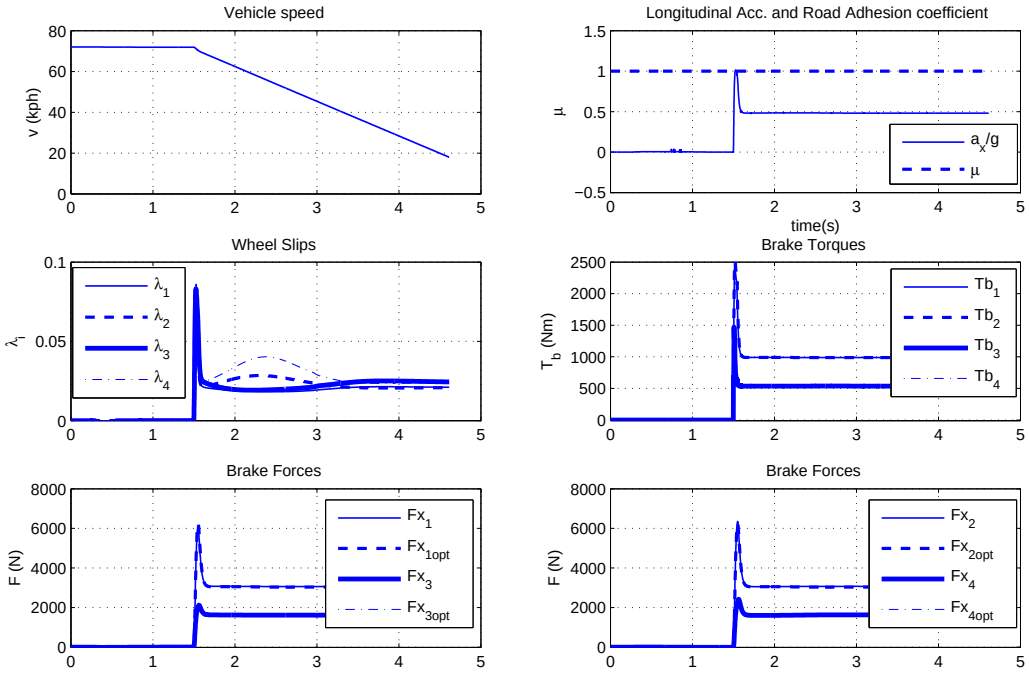


Figure 4.9. Partial braking performance during mild cornering

car brakes harder without the wheels locking up. In the unstable zone, on the other hand, the driver only needs to apply slightly more pressure to the brake pedal to induce instantaneous wheel lock-up. This characteristic means that very often the wheel deceleration and acceleration can be used to determine the degree of wheel slip for optimum braking.

Hence, as soon as wheel deceleration starts to build up at an increasing rate, the wheel can be considered on its way to lock up: ABS must be activated and must maintain wheel slip at its level measured at the onset of activation. However, this activation method is based on heuristics and must be extensively tested and tuned under varying road adhesion.

An equivalent approach for estimating $\lambda^\star$ is proposed in this section. First of all, we skip the activation step as the tuning process requires a huge amount of simulation work and simply assume that we have an ideal ABS activation mechanism. Here, we propose to calculate $\lambda^\star$ offline as a function of normal load and estimated road friction.

A wheel-based metric for road adhesion coefficient estimation is [43]

$$\mu_{eqi} = \frac{T_{bi} - J_w\dot{\omega}}{R_w F_{zi}} g. \tag{4.25}$$

As wheel normal loads may vary substantially during high-g braking, the estimation of $\lambda^\star$ based on this friction estimation alone may be inadequate: one must also consider the effect of normal load variation on the locus of $\lambda^\star$. One must even take into account variations in tire lateral angle during cornering while braking. Hence, we have built a look-up table that maps μ_{eq_i} and F_{zi} to $\lambda_i^\star$. For the tire used in simulations presented in this study, $\lambda^\star$ values are given in Table 4.2.

Table 4.2. $\lambda^\star$ estimation based on μ_{eq_i} and $F_{zi}[kN]$

μ_{eq_i}	$F_{zi}=1$	$F_{zi}=2$	$F_{zi}=3$	$F_{zi}=4$	$F_{zi}=5$	$F_{zi}=6$	$F_{zi}=7$	$F_{zi}=8$
0.1	0.025	0.018	0.017	0.015	0.014	0.013	0.012	0.011
0.2	0.038	0.033	0.030	0.027	0.026	0.025	0.024	0.023
0.3	0.051	0.046	0.042	0.040	0.037	0.035	0.033	0.031
0.4	0.064	0.058	0.054	0.051	0.047	0.045	0.043	0.041
0.5	0.075	0.068	0.065	0.061	0.058	0.055	0.052	0.049
0.6	0.087	0.079	0.075	0.071	0.067	0.064	0.060	0.057
0.7	0.097	0.091	0.085	0.081	0.077	0.073	0.069	0.065
0.8	0.108	0.100	0.095	0.090	0.086	0.081	0.077	0.074
0.9	0.118	0.11	0.104	0.099	0.094	0.089	0.084	0.080
1.0	0.127	0.119	0.113	0.107	0.102	0.097	0.092	0.088

Straight-line braking performance on varying-μ road is shown in Figure 4.10. It can be seen that the brake force distribution between front and rear is again achieved in an optimal fashion by adjusting $\lambda^\star$ values according to the entries of Table 4.2.

For emergency braking on split μ road (Figure 4.11), following strategies have been considered:

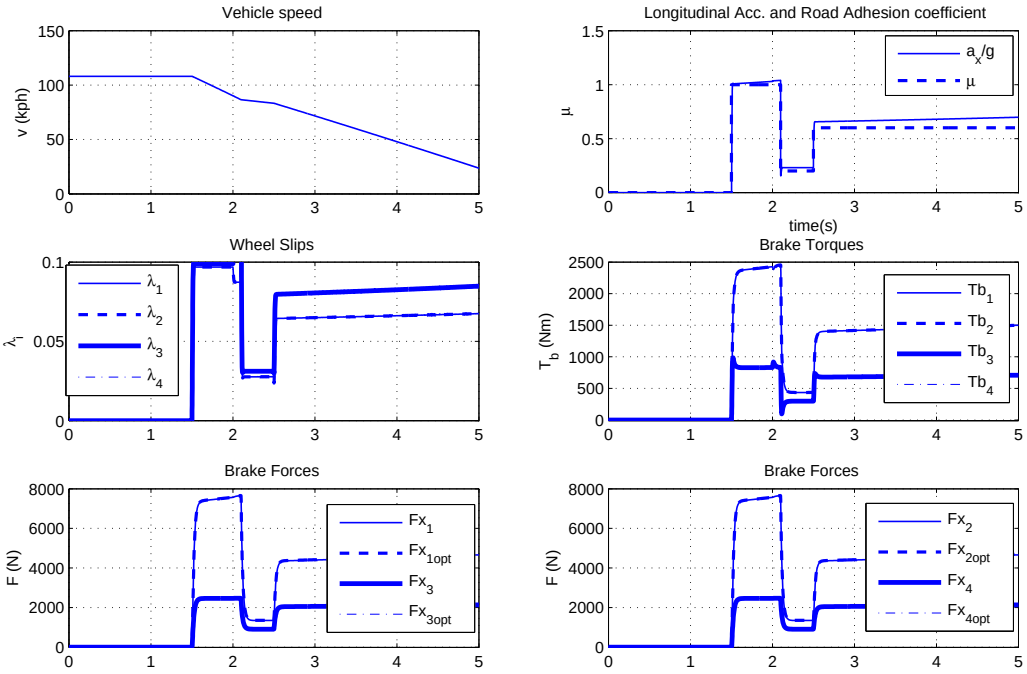


Figure 4.10. Straight-line braking performance

- "Select low" strategy (which consists in equating the brake torque applied on the wheel rolling on the high adhesion side of the road to the torque applied on the wheel rolling on the low adhesion side of the road) has been implemented on both front and rear axles;
- As soon as a large braking torque difference is detected for wheels on the same axle while the steering angle is small, the split μ braking condition is recognized and "select low" is activated;
- $\lambda^\star$ value for braked wheels on the low μ side of the road is adjusted through mapping from Table 4.2 in order to maximize friction on this side.

4.6. Comments

A static state feedback control algorithm for ABS control has been proposed. The robustness of the controller against model uncertainties such as tire longitudinal force and road adhesion coefficient has been guaranteed through the satisfaction of

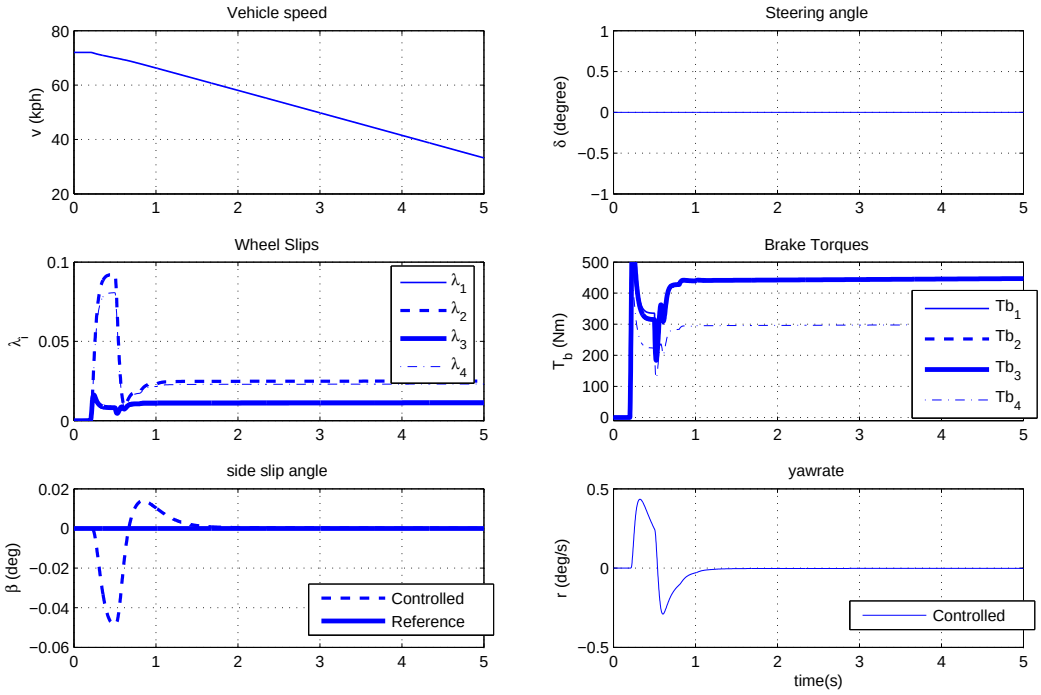


Figure 4.11. Braking performance on split μ road ($\mu_{high} = 0.7/\mu_{low} = 0.2$)

a set of linear matrix inequalities. Scheduling of the controller with vehicle speed is not necessary, which is convenient as far as the implementation of the controller is considered. The bottleneck in implementation then resides in the estimation of the vehicle speed in computing the instantaneous value of longitudinal slip.

For straight-line braking, scheduling of the reference $\lambda^\star$ according to online acceleration measurements has been shown to improve controller performance up to near optimal (when noise rejection is not an issue). Robustness of the controller against actuator time delays along with a method for tuning controller gains has been addressed. Further tuning strategies have been given through a general robustness analysis, where especially the design conflict imposed by noise rejection and actuator time delay has been addressed.

Implementation issues on a full-scale vehicle (brake force proportioning) for partial and emergency braking during cornering and on split μ road have been discussed.

The use of EMB actuators have revealed to be especially useful as long as the maximizing value of the longitudinal slip can be calculated online.

The efficiency of the present algorithm in tracking reference wheel slip values will be important especially in the design of vehicle dynamics controllers in Chapter 6.

5. ROBUST CONTROL OF VEHICLE DYNAMICS

In this chapter, robust control tools are used for the design of combined active steering and active differential controllers for handling improvement of road vehicles. Vehicle plane dynamics are first expressed in the generic linear parameter varying form where vehicle parameters such as speed, cornering and braking stiffnesses are treated as interval uncertainties. Then, static state feedback controllers ensuring robust performance against changing road conditions are designed. Performance of combined active steering and active differential controllers is evaluated for moderate values of driver commanded steering angle, for different values of road adhesion coefficient and at speeds higher than nominal.

5.1. Nonlinear Two-Track Yaw Plane Vehicle Model Extended with Wheel Dynamics

5.1.1. Exact Equations

The model taken from [43] includes states (vehicle speed U, sideslip β, yaw rate r, tire longitudinal slips λ_i) and control channels (front steering angle $\delta = \delta_f$ and traction/braking torques T_{bi}) which are essential for vehicle dynamics control and wheel slip control, as illustrated in Figure 5.1. The model can easily be derived from the equations of motion of the nonlinear six-degree-of-freedom model introduced in Chapter 2. Vehicle speed, sideslip and yaw dynamics are given, respectively, by

$$\dot{U} = \frac{1}{M}\Big((F_{x1} + F_{x2})\cos(\beta - \delta_f) + (F_{x3} + F_{x4})\cos\beta + (F_{y1} + F_{y2})\sin(\beta - \delta_f) + (F_{y3} + F_{y4})\sin\beta \Big), \quad (5.1)$$

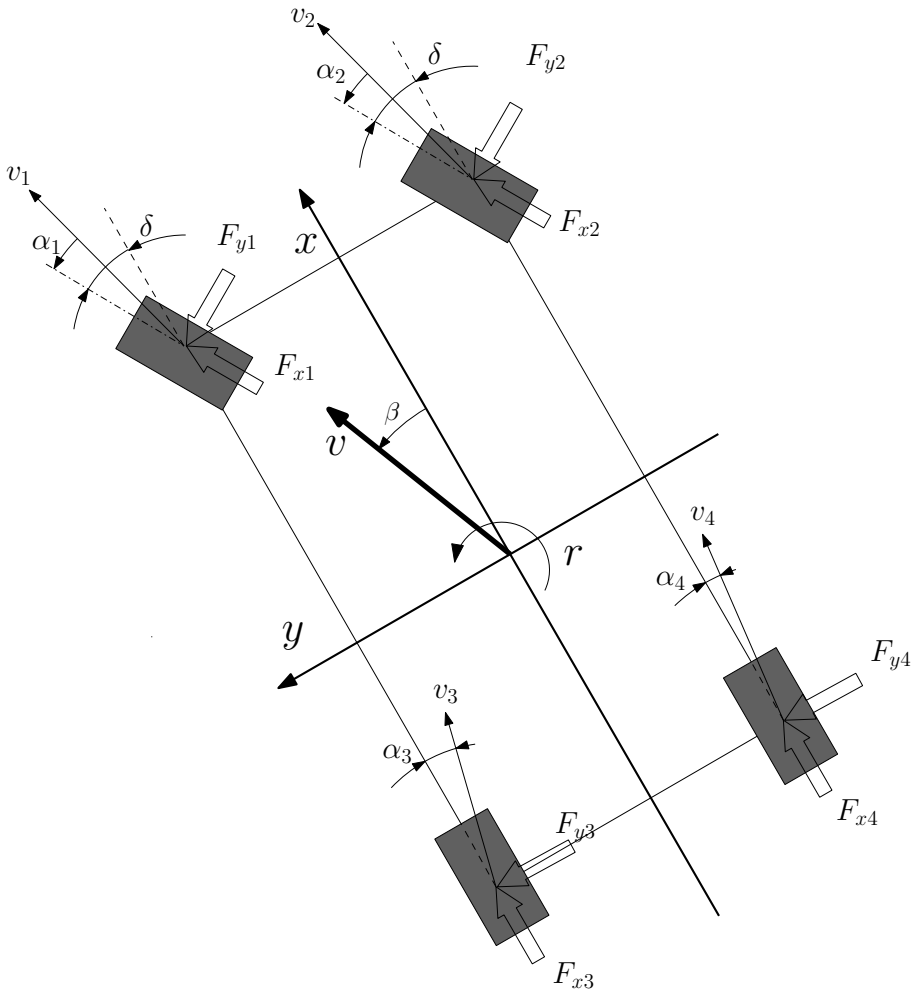


Figure 5.1. Nonlinear two-track yaw plane vehicle model

$$\dot{\beta} = \frac{1}{MU}\Big(-(F_{x1}+F_{x2})\sin(\beta-\delta_f) - (F_{x3}+F_{x4})\sin\beta + (F_{y1}+F_{y2})\cos(\delta_f-\beta) + (F_{y3}+F_{y4})\cos\beta\Big) - r, \quad (5.2)$$

$$\dot{r} = \frac{1}{J_z}\Big(F_{x1}\Big(a\sin\delta_f - \frac{d}{2}\cos\delta_f\Big) + F_{x2}\Big(a\sin\delta_f + \frac{d}{2}\cos\delta_f\Big) + \frac{d}{2}(F_{x4}-F_{x3}) + F_{y1}\Big(\frac{d}{2}\sin\delta_f + a\cos\delta_f\Big) + F_{y2}\Big(-\frac{d}{2}\sin\delta_f + a\cos\delta_f\Big) - b(F_{y3}+F_{y4})\Big). \quad (5.3)$$

Tire forces F_x and F_y depend on both tire sideslip angles and tire longitudinal slips in combined slip conditions. The main effort, while obtaining the LPV representation

of the system, consists in expressing tire forces in terms of the tire sideslip angles and longitudinal slips. For the tire sideslip angle, we consider the formulation given in [43] for small vehicle sideslip angle β, assuming that VDC controllers achieve good vehicle lateral response. In this respect, tire sideslip angles are given by

$$\alpha_1 := \delta_f - \beta - \frac{ar}{U} =: \alpha_2 \quad \text{and} \quad \alpha_3 := -\beta + \frac{br}{U} =: \alpha_4. \tag{5.4}$$

Letting ω_i denote the i^{th} wheel rotational speed and v_i the i^{th} wheel ground contact point velocity, tire longitudinal slips are given by

$$\lambda_i := \frac{v_i - R_w\omega_i}{v_i} \tag{5.5}$$

where tire ground contact point speeds are obtained from:

$$v_1 \approx U - r\left(\frac{d}{2} - a\beta\right), \qquad v_2 \approx U + r\left(\frac{d}{2} + a\beta\right) \tag{5.6a}$$

$$v_3 \approx U - r\left(\frac{d}{2} - b\beta\right), \qquad v_4 \approx U + r\left(\frac{d}{2} - b\beta\right) \tag{5.6b}$$

The dynamics of each individual wheel are given by

$$J_w\dot{\omega}_i = R_wF_{xi} - T_{bi}. \tag{5.7}$$

Given (5.5), the time derivative of i^{th} wheel longitudinal slip is given by

$$\dot{\lambda}_i = -R_w\frac{d}{dt}\frac{\omega_i}{v_i}. \tag{5.8}$$

After manipulations involving the incorporation of (5.7) in order to eliminate wheel rotational speed terms, one obtains

$$\dot{\lambda}_i = \frac{R_w}{J_wv_i}(-R_wF_{xi} + T_{bi}) + \frac{1-\lambda_i}{v_i}\dot{v}_i. \tag{5.9}$$

Equation (5.1) may be discarded if we assume the presence of an ideal tachometer providing exact vehicle speed measurement. Then, equations (5.2), (5.3) and (5.9) constitute a set of six differential equations, representing the coupled dynamics of the vehicle body and wheel subsystems. In the next section, these equations are further manipulated to obtain an LPV representation of the system.

5.1.2. LPV System Representation

In this section, equations (5.2), (5.3) and (5.9) are cast in the generic state-space form for LPV systems:

$$\dot{\boldsymbol{x}} = \boldsymbol{A}\boldsymbol{x} + \boldsymbol{B_p}\boldsymbol{p} + \boldsymbol{B_w}\boldsymbol{w} + \boldsymbol{B_u}\boldsymbol{u} \tag{5.10a}$$

$$\boldsymbol{q} = \boldsymbol{C_q}\boldsymbol{x} + \boldsymbol{D_{qp}}\boldsymbol{p} + \boldsymbol{D_{qw}}\boldsymbol{w} + \boldsymbol{D_{qu}}\boldsymbol{u}, \qquad \boldsymbol{p} = \boldsymbol{\Delta}\boldsymbol{q} \tag{5.10b}$$

$$\boldsymbol{z} = \boldsymbol{C_z}\boldsymbol{x} + \boldsymbol{D_{zp}}\boldsymbol{p} + \boldsymbol{D_{zw}}\boldsymbol{w} + \boldsymbol{D_{zu}}\boldsymbol{u} \tag{5.10c}$$

$$\boldsymbol{y} = \boldsymbol{C_y}\boldsymbol{x} + \boldsymbol{D_{yp}}\boldsymbol{p} + \boldsymbol{D_{yw}}\boldsymbol{w}, \tag{5.10d}$$

In order to introduce a simplified version of the problem, a small angle assumption is made after which all cosine terms reduce to one and all sine terms reduce to zero. The validity of the assumption has been checked later on by comparing the responses of the LPV system with that of the original nonlinear system under combined braking and steering maneuvers, implying that we assume in advance that δ_f, β and r are kept at moderate levels, i.e. stable driving. Among the δ_i parameters, one can state vehicle velocity U, tire ground contact point speeds v_i, C_{xi}, C_{yi} and ρ_i, whose respective definitions are given as

$$C_{xi} := \frac{F_{xi}}{\lambda_i}, \quad C_{yi} := \frac{F_{yi}}{\alpha_i}, \quad \text{and} \quad \rho_i := -\dot{v}_i + \frac{\dot{v}_i}{\lambda_i}. \tag{5.11}$$

In the present case, one has

$$\boldsymbol{A} = \begin{pmatrix} -\frac{C_{y1}+C_{y2}+C_{y3}+C_{y4}}{MU} & \frac{-a(C_{y1}+C_{y2})+b(C_{y3}+C_{y4})-MU^2}{MU^2} \\ \frac{-a(C_{y1}+C_{y2})+b(C_{y3}+C_{y4})}{J_z} & -\frac{a^2(C_{y1}+C_{y2})+b^2(C_{y3}+C_{y4})}{J_zU} \\ 0 & 0 \\ 0 & 0 \\ 0 & 0 \\ 0 & 0 \end{pmatrix}$$

$$\begin{pmatrix} 0 & 0 & 0 & 0 \\ -\frac{dC_{x1}}{2J_z} & \frac{dC_{x2}}{2J_z} & -\frac{dC_{x3}}{2J_z} & \frac{dC_{x4}}{2J_z} \\ -\frac{R_w^2C_{x1}+\rho_1}{J_wv_1} & 0 & 0 & 0 \\ 0 & -\frac{R^2C_{x2}+\rho_2}{J_wv_2} & 0 & 0 \\ 0 & 0 & -\frac{R_w^2C_{x3}+\rho_3}{J_wv_3} & 0 \\ 0 & 0 & 0 & -\frac{R_w^2C_{x4}+\rho_4}{J_wv_4} \end{pmatrix}$$

$$\boldsymbol{B_w} = \begin{pmatrix} \frac{C_{y1}+C_{y2}}{MU} & 0 & 0 & 0 & 0 \\ a\frac{C_{y1}+C_{y2}}{J_z} & 0 & 0 & 0 & 0 \\ 0 & \frac{R_w}{v_1J_w} & 0 & 0 & 0 \\ 0 & 0 & \frac{R_w}{v_2J_w} & 0 & 0 \\ 0 & 0 & 0 & \frac{R_w}{v_3J_w} & 0 \\ 0 & 0 & 0 & 0 & \frac{R_w}{v_4J_w} \end{pmatrix}, \qquad \boldsymbol{B_u} = -\boldsymbol{B_w}$$

where

$$\begin{aligned} \boldsymbol{x} &:= \begin{pmatrix} \beta & r & \lambda_1 & \lambda_2 & \lambda_3 & \lambda_4 \end{pmatrix}^T \\ \boldsymbol{w} &:= \begin{pmatrix} \delta_f & T_{b1} & T_{b2} & T_{b3} & T_{b4} \end{pmatrix}^T \\ \boldsymbol{u} &:= \begin{pmatrix} \delta_c & T_{b1c} & T_{b2c} & T_{b3c} & T_{b4c} \end{pmatrix}^T. \end{aligned}$$

Here, entries of the disturbance vector denote driver commanded steering wheel angle and brake torques commanded by local wheel slip controllers. The entries of the input vector denote the angle correction introduced by the active steering controller

and torque corrections applied by the active differential controller.

It is possible to regroup some of the parameters having similar bounds together in order to reduce the total number of parameters. The simplest alternative is to regroup U, v_1, v_2, v_3, v_4 and denote them all by v, to regroup C_{y1}, C_{y2}, C_{y3}, C_{y4}, C_{x1}, C_{x2}, C_{x3}, C_{x4} and denote them all by C and finally to regroup ρ_1, ρ_2, ρ_3, ρ_4 and denote them all by ρ. The main reason for this approach is the difficulty of current LMI solvers to solve the convex optimization problem described in the next section when the number of parameters increases. In fact, when the number of parameters will be reduced from 17 to 3 as explained above, the number of LMI conditions to be satisfied in (3.28) is reduced from 2^{17} to 8. The defining matrices of the system LPV representation then become

$$\boldsymbol{A} = \begin{pmatrix} -\frac{4C}{Mv} & -1+\frac{2C(-a+b)}{Mv^2} & 0 & 0 & 0 & 0 \\ \frac{2C(-a+b)}{J_z} & -\frac{2C(a^2+b^2)}{J_z v} & -\frac{dC}{2J_z} & \frac{dC}{2J_z} & -\frac{dC}{2J_z} & \frac{dC}{2J_z} \\ 0 & 0 & -\frac{R^2C}{J_w v}+\frac{\rho}{v} & 0 & 0 & 0 \\ 0 & 0 & 0 & -\frac{R_w^2 C}{J_w v}+\frac{\rho}{v} & 0 & 0 \\ 0 & 0 & 0 & 0 & -\frac{R^2C}{J_w v}+\frac{\rho}{v} & 0 \\ 0 & 0 & 0 & 0 & 0 & -\frac{R_w^2 C}{J_w v}+\frac{\rho}{v} \end{pmatrix}$$

$$\boldsymbol{B_w} = \begin{pmatrix} \frac{2C}{Mv} & 0 & 0 & 0 & 0 \\ \frac{2aC}{J_z v} & 0 & 0 & 0 & 0 \\ 0 & \frac{R_w}{J_w v} & 0 & 0 & 0 \\ 0 & 0 & \frac{R_w}{J_w v} & 0 & 0 \\ 0 & 0 & 0 & \frac{R_w}{J_w v} & 0 \\ 0 & 0 & 0 & 0 & \frac{R_w}{J_w v} \end{pmatrix}, \qquad \boldsymbol{B_u} = -\boldsymbol{B_w}.$$

Assuming that C, v and ρ vary around selected nominal values of C_o, v_o and ρ_o as $C = C_o + \delta_C$, $v = v_o + \delta_v$ and $\rho = \rho_o + \delta_\rho$ respectively, it is possible to express the generic LPV representation (5.10) for the present problem in terms of nominal values and variations. Arbitrarily fast time variations are allowed in the present setting where

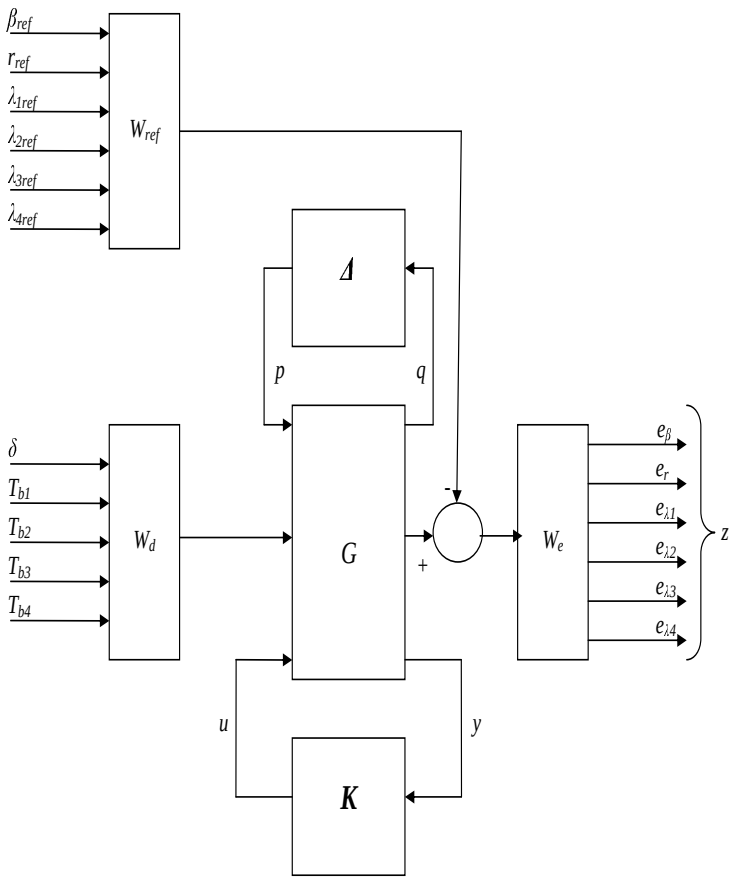


Figure 5.2. Block diagram for combined active steering and active differential control problem

the design of static state feedback controllers is sought. The defining matrices of the LPV representation can be found in Appendix B.

The problem is then augmented with rational weights to achieve desirable handling characteristics (reference yaw rate tracking and low sideslip angle during cornering). A filter $W_{ref}(s)$ is added to filter out high frequency desired body sideslip, desired yaw rate and reference longitudinal slip commands. Another filter $W_e(s)$ is added to reduce steady state tracking errors. Still another filter $W_d(s)$ is added to shape the disturbances acting on the system. Those disturbances consist of the driver commanded steering angle δ_f and the brake torques produced by local wheel slip controllers (Figure 5.2). The defining matrices of the augmented LPV system are given in Appendix B.

5.2. The Control Objective

The correct measurement of the vehicle state vector is obviously important in calculating the stabilizing control action. Yaw rate is usually measured by a gyroscope, while the estimation of sideslip angle can be based on the usage of an inverse tire model [33], the Global Positioning System (GPS) measurements [51], state observers [43]. Roll angle and roll rates can be similarly measured by rate gyroscopes or GPS [51].

In this thesis, we focus on the case where the entire augmented state vector is available for feedback. In other words,

$$\boldsymbol{y} = \breve{\boldsymbol{x}} = \left[\begin{array}{cccc} \boldsymbol{x}^T & \boldsymbol{x_{ref}}^T & \boldsymbol{x_d}^T & \boldsymbol{x_e}^T \end{array} \right]^T,$$

or equivalently, $\boldsymbol{C_y} = I$, $\boldsymbol{D_{yp}} = 0$ and $\boldsymbol{D_{yw}} = 0$. In this case, it is well-known that there is no need to search for a dynamic controller $K(s)$ and that a *static* control law of the form $\boldsymbol{u} = K\breve{\boldsymbol{x}}$ can be found to achieve the control objective which consists in keeping the $\mathcal{L}_2$-gain from disturbance $\boldsymbol{w}$ (i.e driver steering and braking inputs) to controlled output $\boldsymbol{z}$ (sideslip angle and yaw rate errors $e_\beta := \beta - \beta_{ref}$ and $e_r := r - r_{ref}$) less than some specified level, γ, for all possible values of δ_is. Sufficient conditions for the existence of such a state feedback controller are given by Theorem 3.4.1.

5.3. Controller Design

5.3.1. Reference Values

The objective of an ICM controller during cornering is two-fold: keeping the body sideslip angle as low as possible while tracking a reference yaw rate. The sideslip angle reference is constructed based on the sideslip response $\beta_{lin}(t)$ of a linear bicycle model having similar tire cornering characteristics in the linear operation range of tires and is saturated by $\beta_{max} = 2^o$, which corresponds to a desirable upper limit for good vehicle

handling [3]. Hence,

$$\beta_{ref}(t) = \min\left\{2^o sign(\beta(t)), \beta_{lin}(t)\right\} \tag{5.12}$$

where $\beta_{lin}(t)$ is obtained from

$$\beta_{lin}(s) = -\frac{C_{\alpha f}C_{\alpha r}b(a+b) - aMC_{\alpha f}U^2}{C_{\alpha f}C_{\alpha r}(a+b)^2 + MU^2(bC_{\alpha r} - aC_{\alpha f})}\frac{\delta(s)}{1+T_\beta s}. \tag{5.13}$$

The yaw rate reference is constructed based on the yaw rate response $r_{lin}(t)$ of a linear bicycle model having similar tire cornering characteristics in the linear operation range of tires and is saturated by the physical limit imposed by the current road adhesion coefficient, that is,

$$|r_{max}| \leq |\frac{\mu g}{v}|.$$

The calculation of the exact lateral road adhesion coefficient is rather complex. Rigorous estimation methods encompassing the simultaneous calculation of the adhesion coefficient and tire forces are available in the literature ([52]). The lateral road adhesion coefficient is either assumed to be known or an upper limit at the limit of adhesion is calculated according to

$$\mu_y = \frac{a_y}{g}.$$

Hence,

$$r_{ref}(t) = \min\left\{|\frac{\mu g}{v}|sign(\delta(t)), r_{lin}(t)\right\} \tag{5.14}$$

where $r_{lin}(t)$ is obtained from

$$r_{lin}(s) = -\frac{(a+b)C_{\alpha f}C_{\alpha r}U}{C_{\alpha f}C_{\alpha r}(a+b)^2 + MU^2(bC_{\alpha r} - aC_{\alpha f})}\frac{\delta(s)}{1+T_r s}. \tag{5.15}$$

In (5.13) and (5.15), T_β and T_r are design time constants [53]. Above-mentioned rules are valid for all designs achieved throughout this thesis.

5.3.2. Prediction of Parameter Bounds

Prediction of parameter bounds δ_C, δ_ρ and δ_v is important for controller design. For the tire model used in this research, F_x and F_y can both be assumed to vary in the range $(0.0 - 8.0\,kN)$. The linear regime of the tire has been analyzed to extend up to $0.14\,rad \approx 8^o$ under all operating conditions (changes in road adhesion, lateral weight transfer, combined slip). Also, a maximum longitudinal slip ratio of around 0.1 has been observed to correspond to maximum braking/tractive force under all operating conditions. Hence, C can first be assumed to vary in the range $(0 - 80\,kN)$.

It should be noted that, for small values of tire slip, $\frac{F_y}{\alpha}$ corresponds to tire cornering stiffness and, for small values of tire longitudinal slip, $\frac{F_x}{\lambda}$ corresponds to tire longitudinal stiffness. Hence, it is erroneous to choose the lower bound of C as zero as long as the tire is operating in the linear regime. Moreover, the slope of longitudinal force at small values of longitudinal slip is steep and exceeds $80\,kN$ and in fact has been observed to reach $100\,kN$ under some operating conditions. In the light of these observations, the problem has been solved with $C_o = 80\,kN$, $\delta_C = 40\,kN$. Here, the lower limit of C corresponds mainly to reduced lateral force under combined slip conditions.

A similar heuristic approach is used for selecting the bounds of ρ. The term $\frac{\dot{v}}{\lambda_i}$ dominates when longitudinal forces are present at a tire. The tire ground contact acceleration $\dot{v}$ can be shown to be close to vehicle acceleration during stable driving. When active differential control is used, the drop in vehicle speed is small and an upper bound for vehicle deceleration can safely be taken as $0.1\,m/s^2$ as will also be confirmed by following simulations. The value of λ_i varies in the range $(-0.1, 0.1)$. Again a word of caution is necessary concerning the zero crossing. For the tire to generate substantial longitudinal force, the longitudinal slip must be over 0.001 under all driving conditions. In other words, controller may be switched off in non-critical

situations where perfect tracking of yaw rate and sideslip angle regulation are not paramount. Hence, $\rho_o = 0\, m/s^2$ and $\delta_\rho = 100$ have been chosen for controller design.

Nominal vehicle speed has been taken as $v_o = 20\, m/s$ with speed variation $\delta_v = 1 m/s$ as speed variation is expected to be small when implementing active differential control.

5.3.3. Selection of Frequency Weights

The reference filter $W_{ref}(s)$ has been designed as a first order Butterworth filter with a cut-off frequency of $2\, Hz$, which generally corresponds to the upper limit of driver activity [24]. Scaling of the entries of $\boldsymbol{B_{ref}}$ is necessary to account for the upper limits of reference sideslip and yaw rate. The stability limit of the vehicle considered in this research on dry road and for $U = 72\, kph$ is attained for $\delta_f = 5^o$. The order of magnitude of the maximum expected sideslip angle can be shown to be about the same as δ_f while the maximum expected yaw rate is roughly five times higher. These observations are based on steady state system gains. Hence, the entry corresponding to sideslip angle is scaled with $\frac{5\pi}{180}$ and the entry corresponding to yaw rate is scaled with $\frac{25\pi}{180}$, finally yielding $W_{ref} = \mathbf{diag}(W_{ref1}, W_{ref2})$ where

$$W_{ref1}(s) = \frac{1.096s + 1.378}{s^2 + 2.513s + 157.9}$$
$$W_{ref2}(s) = \frac{5.483s + 68.9}{s^2 + 2.513s + 157.9},$$

which corresponds to

$$\boldsymbol{A_{ref}} = \mathbf{diag}(-2 \times 2\pi, -2 \times 2\pi)$$
$$\boldsymbol{B_{ref}} = \mathbf{diag}(2 \times 2\pi\frac{5\pi}{180}, 2 \times 2\pi\frac{25\pi}{180})$$
$$\boldsymbol{C_{ref}} = \mathbf{diag}(1, 1)$$
$$\boldsymbol{D_{ref}} = 0.$$

Decoupling of sideslip and yaw rate is imposed through zero off-diagonal elements of W_{ref}.

Similarly, the output filter $W_e(s)$ has been designed as a first order Butterworth filter with a cut-off frequency of $2\,Hz$, and in order to have a steady state error of less than 1% in achieving both side slip, $\boldsymbol{C_e}$ has been scaled with 100. Hence,

$$W_e(s) = \frac{1253s + 15790}{s^2 + 2.513s + 157.9} I_2,$$

which corresponds to

$$\begin{aligned}
\boldsymbol{A_e} &= \mathbf{diag}(-2 \times 2\pi, -2 \times 2\pi) \\
\boldsymbol{B_e} &= \mathbf{diag}(2 \times 2\pi, 2 \times 2\pi) \\
\boldsymbol{C_e} &= \mathbf{diag}(100, 100) \\
\boldsymbol{D_e} &= 0.
\end{aligned}$$

The disturbance filter $W_d(s)$ has again been modeled as a first order Butterworth filter with a cut-off frequency of $2\,Hz$ so as to reflect driver activity. Disturbances caused by local ABS controllers have been discarded in this research and the only disturbance taken into account is driver commanded steering angle. We have used

$$W_d(s) = \frac{1.096}{s + 12.57},$$

which corresponds to

$$\begin{aligned}
\boldsymbol{A_d} &= -2 \times 2\pi \\
\boldsymbol{B_d} &= 2 \times 2\pi \frac{5\pi}{180} \\
\boldsymbol{C_d} &= 1 \\
\boldsymbol{D_d} &= 0.
\end{aligned}$$

5.3.4. Explicit Controller Formulae

A very simple control strategy is used for generating longitudinal tire forces: $T_{b1} = -T_{b2} = -T_{b3} = T_{b4}$. Although clearly not optimal as far as wheel force generation capacity is concerned, this strategy has been observed to work quite well as long as longitudinal slips are at low levels where tire saturation is not an issue. Two controllers have been finally computed. An integrated controller K_1 with active steering component given by

$$\begin{aligned}\delta_c = &-6.374 \cdot 10^{-1}\beta + 1.659 \cdot 10^{-1}r + 3.762 \cdot 10^{-3}\lambda_1 + 5.038 \cdot 10^{-3}\lambda_2 \\ &+ 2.425 \cdot 10^{-3}\lambda_3 + 2.235 \cdot 10^{-3}\lambda_4 + 6.408 \cdot 10^{-3}x_{r1} \\ &+ 1.555 \cdot 10^{-1}x_{r2} - 2.714 \cdot 10^{2}x_{e1} + 6.762 \cdot 10^{2}x_{e2} \quad (5.16)\end{aligned}$$

and active differential control part

$$\begin{aligned}T_{b1} = &\ 1.916 \cdot 10^{5}\beta - 4.877 \cdot 10^{4}r - 1.758 \cdot 10^{3}\lambda_1 - 3.364 \cdot 10^{3}\lambda_2 \\ &- 1.462 \cdot 10^{3}\lambda_3 - 1.693 \cdot 10^{3}\lambda_4 - 1.935 \cdot 10^{5}x_{r1} \\ &+ 4.381 \cdot 10^{4}x_{r2} + 8.435 \cdot 10^{7}x_{e1} - 1.686 \cdot 10^{7}x_{e2} \quad (5.17)\end{aligned}$$

is designed and used in the first two series of simulations. Then, an active differential controller K_2 given by

$$\begin{aligned}T_{b1} = &\ 6.991 \cdot 10^{3}\beta - 7.110 \cdot 10^{3}r + 6.854 \cdot 10^{5}\lambda_1 - 8.779 \cdot 10^{5}\lambda_2 \\ &+ 8.843 \cdot 10^{5}\lambda_3 - 8.650 \cdot 10^{5}\lambda_4 - 4.241 \cdot 10^{3}x_{r1} + 9.811 \cdot 10^{3}x_{r2} \\ &+ 2.071 \cdot 10^{7}x_{e1} - 1.923 \cdot 10^{7}x_{e2} \quad (5.18)\end{aligned}$$

is obtained and used in a third series of simulations.

5.4. Simulation Results

5.4.1. Critical Maneuvers

NHTSA (The National Highway Traffic Safety Administration) [54] has been particularly active in the design of standard test maneuvers to measure on-road, untripped rollover propensity. Some of these tests can be used for yaw stability assessment as rollover happens as a result of severe yaw stability impairment during extreme cornering maneuvers. These include J turn, Fishhook and step steering maneuvers (sometimes including pulse braking inputs) devised according to the characteristics of the vehicle considered [54].

On the other hand, Peng et al. [55] propose to evaluate the yaw and roll stability of vehicles equipped with VDC systems differently. Their strategy is based on three fundamental steps. First, NHTSA tests are implemented and the efficiency of the VDC system is tested by comparing the maximum roll angle with the safety system turned on and then off. If the VDC passes the test, then the second test consists in computing the worst case maneuvers that may induce rollover. The worst case evaluation method developed by Ma et al [56] aims to use optimization techniques to first identify weaknesses of vehicles and then worst-case scenarios (steering input, braking input, operational parameters, environmental parameters) that impair roll stability. Their studies based on worst case maneuvers show that it is possible to destabilize the cornering vehicle with driver inputs not necessarily at maximal levels. If the vehicle (and hence the VDC) passes the second test, then a closed loop human-in-the loop simulation is performed. Including the driver model in the evaluation process enables to evaluate the performance of VDC using virtual drivers with different characteristics (mild to aggressive driving) in standard tests like the *Moose Test*. If the vehicle system passes the test again then the VDC can be tested on the field. If at any step, the test fails then the controller must be redesigned.

The determination of the worst-case disturbance inputs and human-in-the loop testing are both out of the scope of this thesis. Instead, we have chosen to consider

severe J turn and sinusoidal steering tests in this thesis.

5.4.2. Simulation 1: Performance of K_1 for Small δ_f

In a first series of simulations, performance of K_1 for small driver commanded steering angle is presented. Results for J-turn and sinusoidal maneuvers with maximum driver commanded steering angle $\delta_f = 2^o$ carried out on dry road are shown in Figure 5.3 and Figure 5.4. The response of the controlled vehicle is quite satisfactory as displayed by the sideslip angle and yaw rate curves: sideslip is completely eliminated and perfect reference tracking is achieved for both maneuvers revealing successful decoupling of vehicle modes. The action of active front steering towards increasing the commanded steering angle is to be noted. Parameter variations during these maneuvers can be observed in Figure 5.5 and Figure 5.6. Parameter bounds are relatively well satisfied for C_x and C_y. Instantaneous sharp increases that occur in ρ correspond to instants when corresponding torque direction is reversed. As explained above such an inconvenience can be avoided by switching the controller off at those instants.

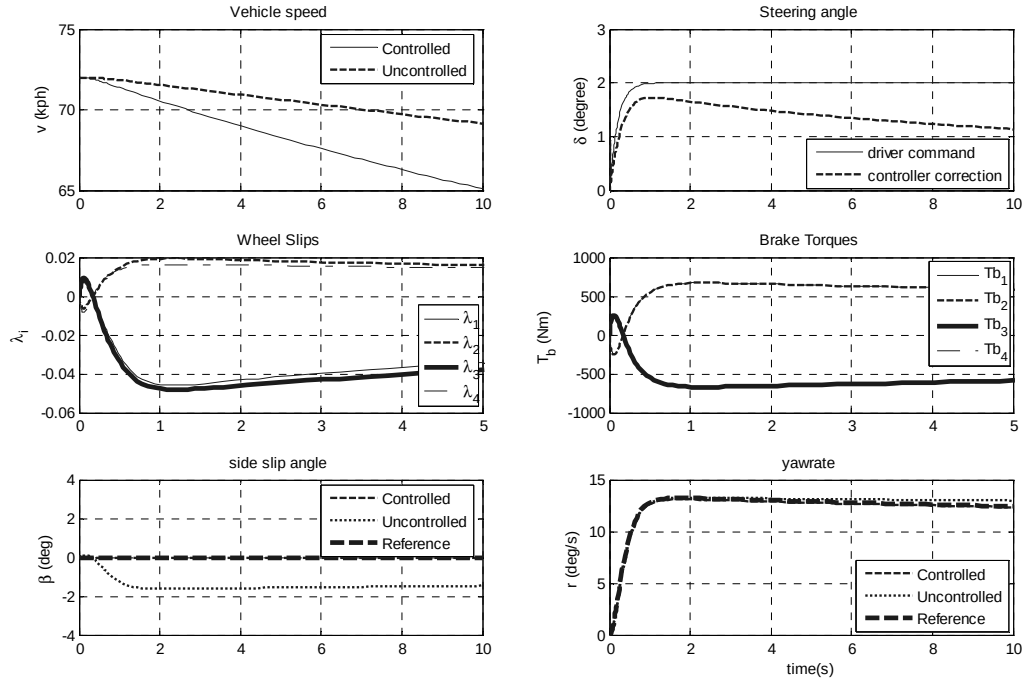


Figure 5.3. Integrated controller performance during J-turn maneuver on dry road ($\mu = 1$) (Simulation 1)

5.4.3. Simulation 2: Performance of K_1 on Slippery Road

In a second series of simulations, performance of K_1 on slippery road is investigated. Road adhesion coefficient is taken as 0.5 and initial vehicle speed is set to $90\,kph$. This time, the maximum driver commanded steering angle is $\delta_f = 1^o$. Again, the controlled vehicle achieves perfect elimination of sideslip angle and yaw rate tracking as can be witnessed from Figure 5.7 and Figure 5.8. Active steering controller correction is towards increasing driver commanded steering angle. One may note that controller correction has been limited to 2^o. It was observed that when this saturation was not externally implemented the front tires were quickly led to operate in the nonlinear regime. The reason is to be sought in modeling tire characteristics. The approach of modeling tire stiffness as an interval uncertainty can take into account variations due to combined slip and lateral load transfer, all of which can be represented as sector uncertainties in the tire force (both lateral and longitudinal) versus tire slip (both lateral and longitudinal) plane, but it does not adequately account for tire force saturation. Hence, active steering is discarded for designs involving higher values of driver commanded steering angle.

5.4.4. Simulation 3: Performance of K_2 for Conditions Away from Nominal

In a third series of simulations, performance of K_2 at high values of driver commanded steering angle (up to $\delta_f = 5^o$) is investigated for cornering maneuvers on roads with road adhesion ($\mu = 0.5$). Inspection of Figure 5.9 and Figure 5.10 shows that differential control can stabilize vehicle response for relatively large driver commanded steering angles and relatively low road adhesion coefficient achieving nicely damped vehicle response, while the uncontrolled vehicle is seen to display highly oscillatory dynamics.

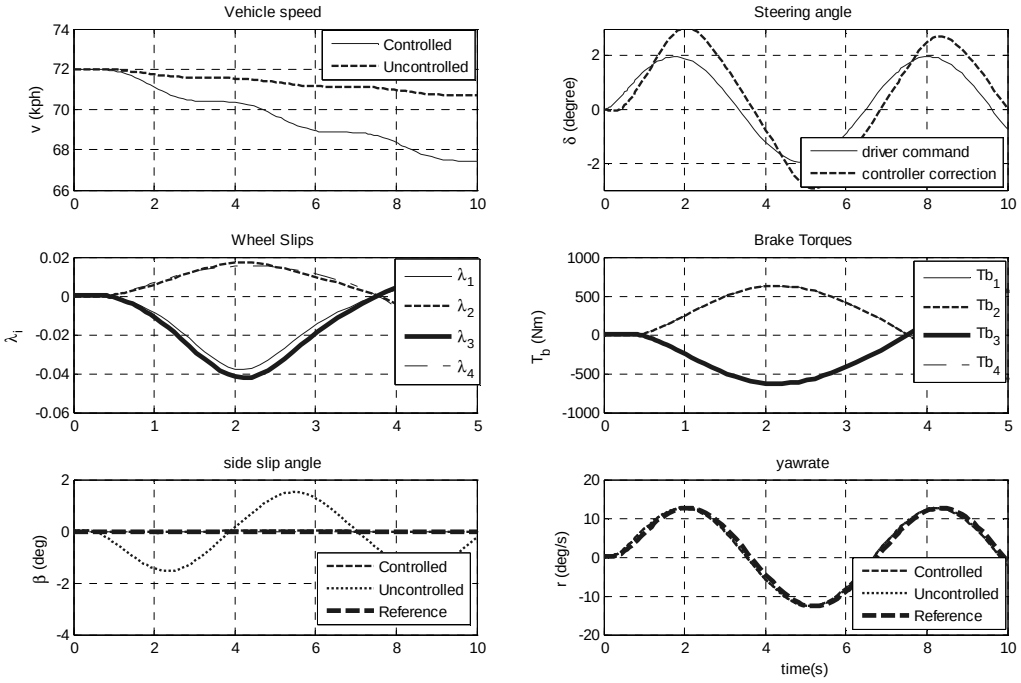


Figure 5.4. Integrated controller performance during sinusoidal turn maneuver on dry road ($\mu = 1$) (Simulation 1)

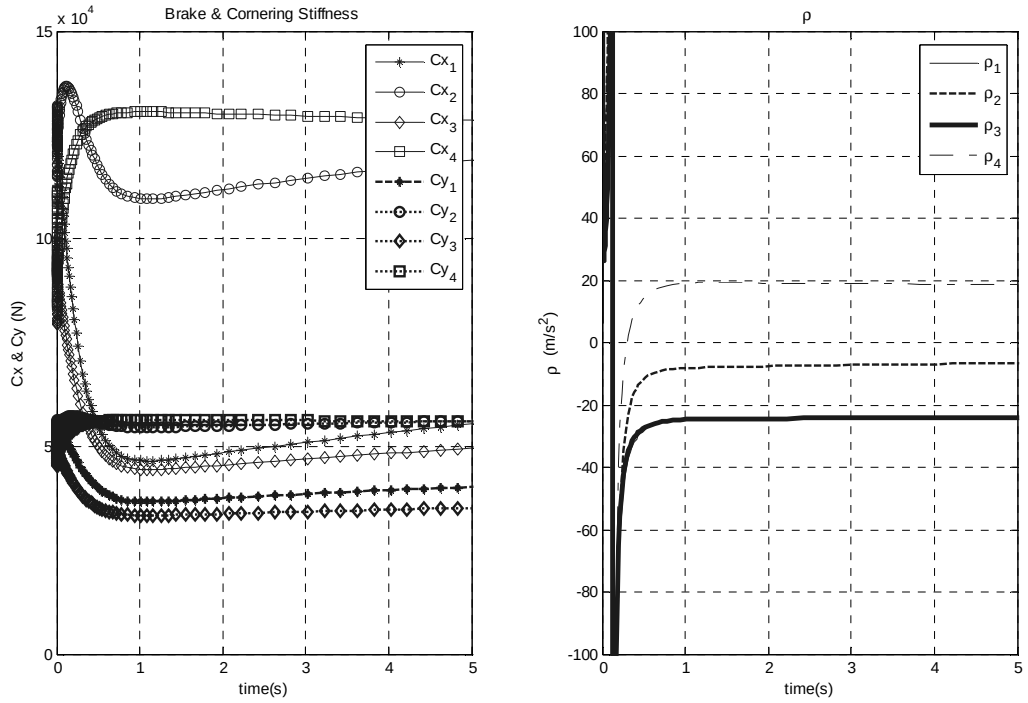


Figure 5.5. Parameter variation during J turn maneuver on dry road ($\mu = 1$) (Simulation 1)

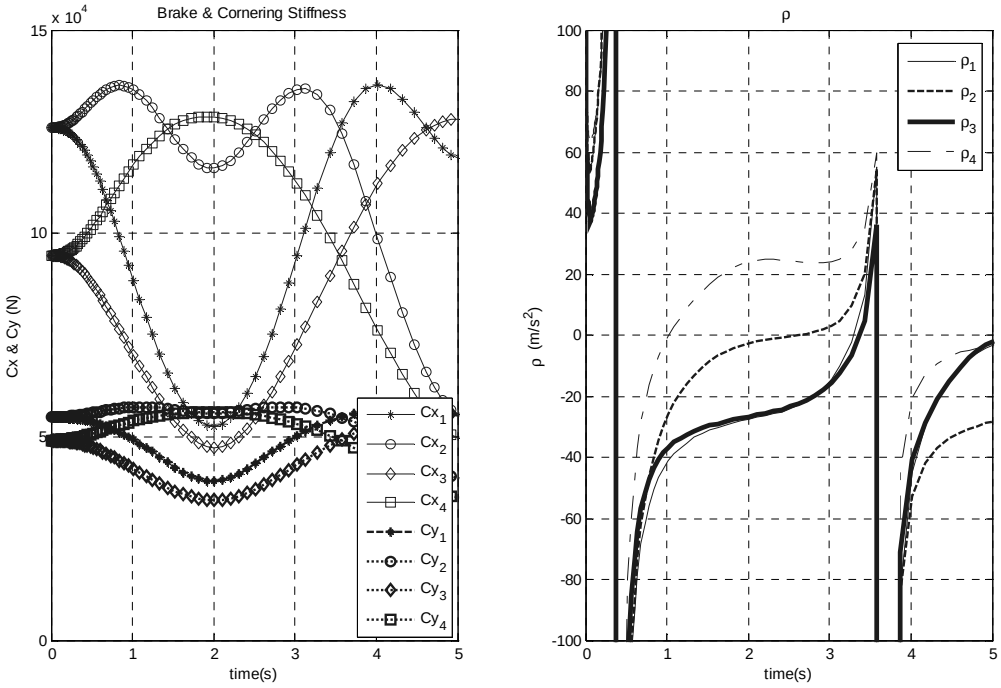


Figure 5.6. Parameter variation during sinusoidal turn maneuver on dry road ($\mu = 1$) (Simulation 1)

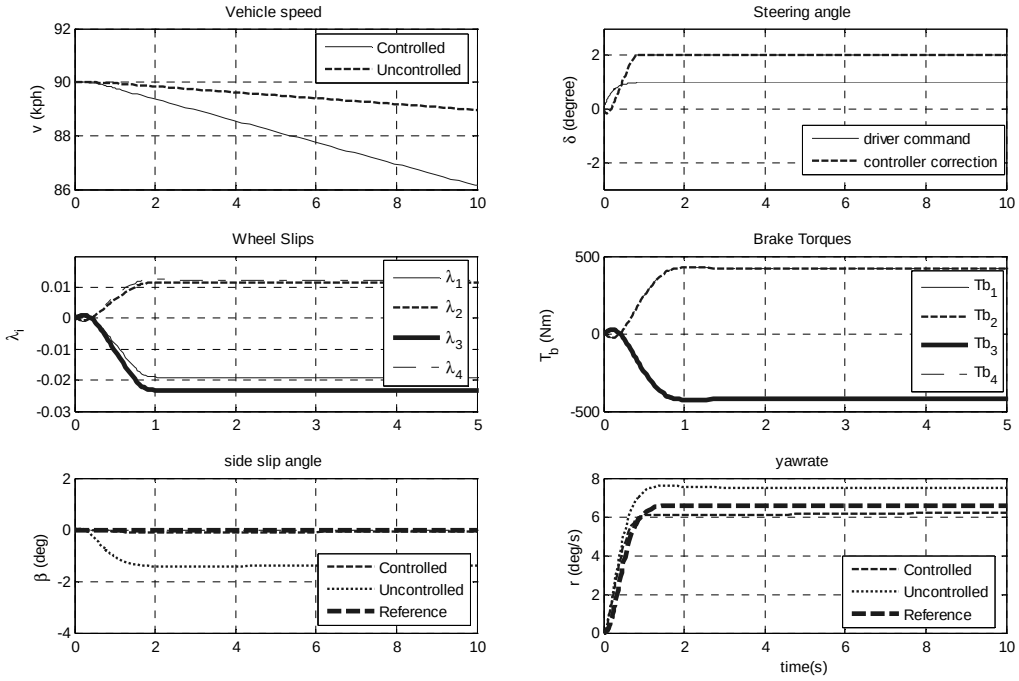


Figure 5.7. Integrated controller performance during J turn maneuver on low μ road ($\mu = 0.5$) (Simulation 2)

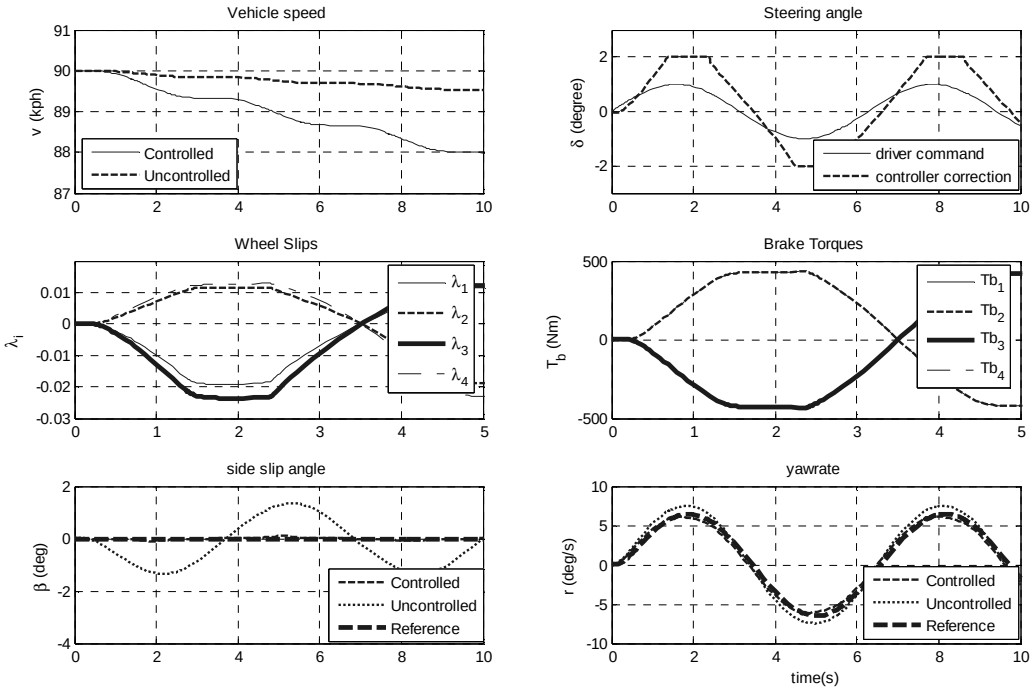


Figure 5.8. Integrated controller performance during sinusoidal turn maneuver on low μ road ($\mu = 0.5$) (Simulation 2)

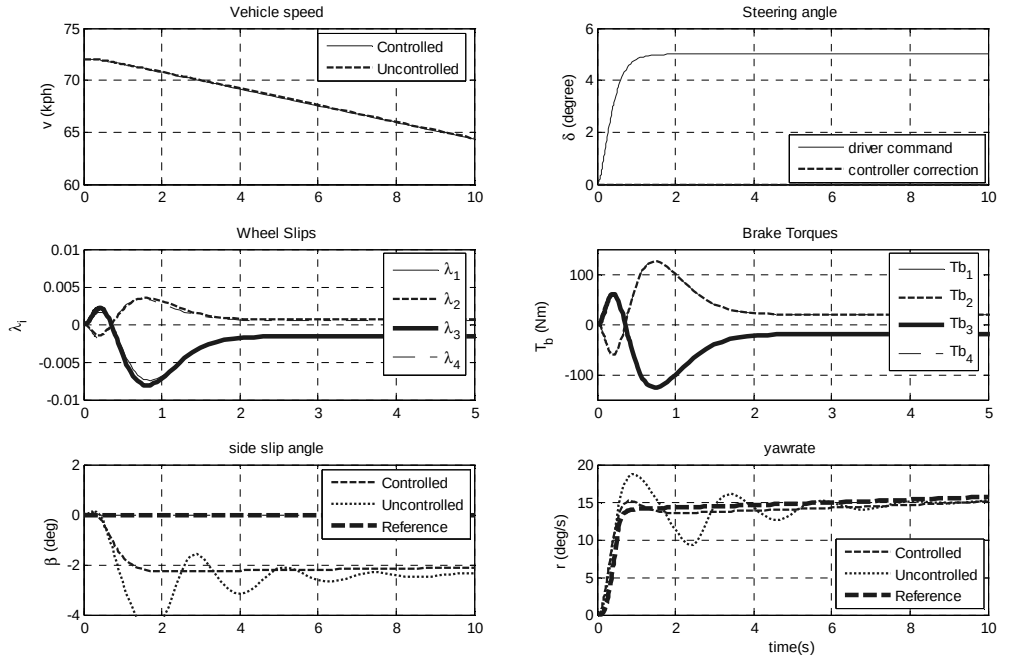


Figure 5.9. Active differential performance during J turn maneuver on low μ road ($\mu = 0.5$) (Simulation 3)

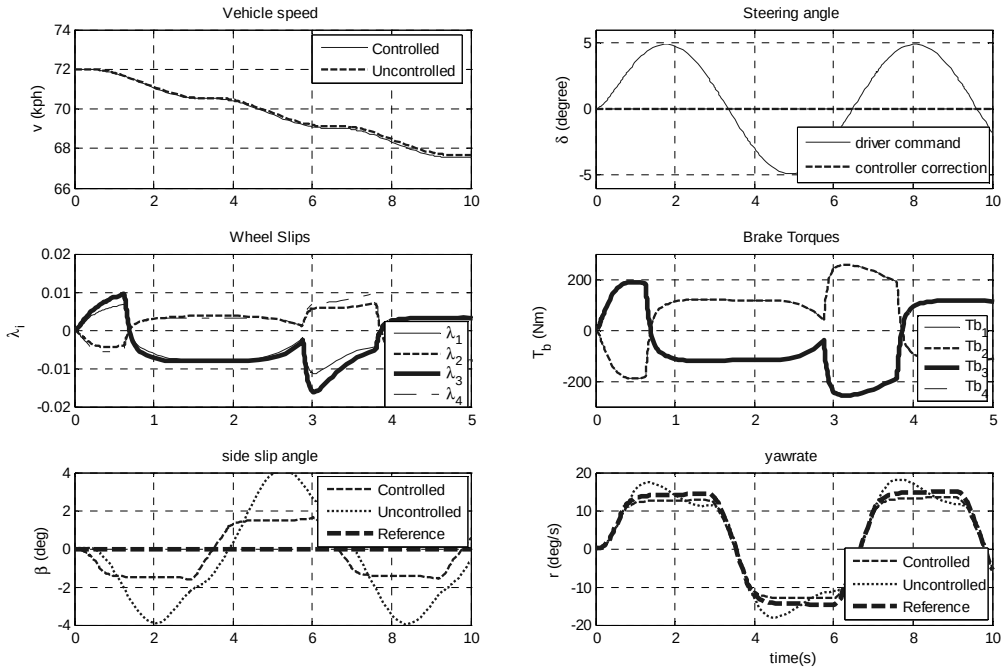


Figure 5.10. Active differential performance during sinusoidal steering maneuver on low μ road ($\mu = 0.5$) (Simulation 3)

5.5. Comments

A static state feedback control algorithm for VDC control has been proposed for the design of integrated controllers. Assuming that the entire state vector is available, it has then been possible to design a state feedback controller ensuring both robust stability and robust performance. While most previous studies in the literature have separated vehicle and tire subsystems during controller design, we have chosen in our case to unify them by coupling them through uncertain tire stiffness coefficients in order to account for nonlinear tire force generation.

Simulations have revealed the robustness of the proposed method under varying driving (changing speed) and road conditions (changing road adhesion). The decoupling property of the integrated controller under low steering angle is remarkable: sideslip angle has been completely eliminated and yaw rate has been observed to perfectly track a given reference. The action of the active steering controller has been towards increasing the driver commanded steering angle. While this has proved to

improve vehicle response at low steering angles, the effect has been clearly unwanted at high steering angles at the onset of tire saturation. One would expect the active steering to reduce total steering angle in such cases, but as the tire model does not adequately represent the saturation property of tires, this could not be achieved with the present design. Instead, active differential control has been implemented to cope with vehicle instability occurring at high driver commanded steering angle. In this case, vehicle response has been observed to be much better damped in the controlled case.

In the next chapter, a more accurate tire model accounting for tire force saturation is incorporated into the controller synthesis model to deal with side force saturation.

6. GAIN SCHEDULED CONTROL OF VEHICLE DYNAMICS

This chapter revisits the integrated control design problem of the previous chapter and presents a gain scheduled active steering control and active differential design method. First a method for robust gain scheduled LPV controller synthesis is explained. Then, parametric formulations of bicycle and yaw-roll models in which tire lateral slip angles, longitudinal slips and vehicle forward speed appear as changing vehicle parameters are introduced. These models happen to be useful in the design of vehicle dynamics controllers scheduled by vehicle parameters: after having expressed the parametric models in the parametric descriptor form, gain scheduled controllers are designed to improve vehicle handling at large steering angle. Simulations reveal the efficiency of the selected modeling and controller design methodology in enhancing vehicle handling capacity.

6.1. Robust Gain-Scheduled LPV Controller Synthesis

For the LPV controller synthesis problem treated in this thesis, we choose to overpass the complexity of the LFT stage, by describing the system in a parametric nonsingular descriptor form [57]. Main motivation for this is the inversion of parameter dependent descriptor matrix $\boldsymbol{E}$ in (6.1) which, not only creates additional rational parameter dependence but also generally necessitates extra parameter inclusion. In our case, (3.16) may be viewed as the result of such inversion and happens to be in a rather inconvenient form for parameter assignment and ensuing gain-scheduled control synthesis.

An LPV system in the descriptor form is given as

$$\begin{aligned} \boldsymbol{E}(\boldsymbol{\rho})\dot{\boldsymbol{x}} &= \boldsymbol{A}(\boldsymbol{\rho})\boldsymbol{x} + \boldsymbol{B_w}(\boldsymbol{\rho})\boldsymbol{w} + \boldsymbol{B_u}(\boldsymbol{\rho})\boldsymbol{u} \\ \boldsymbol{z} &= \boldsymbol{C_z}(\boldsymbol{\rho})\boldsymbol{x} + \boldsymbol{D_{zw}}(\boldsymbol{\rho})\boldsymbol{w} + \boldsymbol{D_{zu}}(\boldsymbol{\rho})\boldsymbol{u} \\ \boldsymbol{y} &= \boldsymbol{C_y}(\boldsymbol{\rho})\boldsymbol{x} + \boldsymbol{D_{yw}}(\boldsymbol{\rho})\boldsymbol{w} \end{aligned} \tag{6.1}$$

We assume that all system matrices are affine in the parameter vector $\boldsymbol{\rho} : \mathbb{R} \to \mathbb{R}^q$. The admissible parameter trajectories are continuously differentiable time-varying vectors such that: $\boldsymbol{\rho}(t) \in \mathcal{R}$ and $\dot{\boldsymbol{\rho}}(t) \in \mathcal{D}$ for all $t \geq 0$, where

$$\mathcal{R} := \{\boldsymbol{\rho} \in \mathbb{R}^q : \underline{\rho_\alpha} \leq \rho_\alpha \leq \overline{\rho_\alpha} \ \forall \alpha = 1 : q\} \text{ and } \mathcal{D} := \{\dot{\boldsymbol{\rho}} \in \mathbb{R}^q : \underline{\dot{\boldsymbol{\rho}}_\alpha} \leq d_\alpha \leq \overline{\dot{\rho}_\alpha} \ \forall \alpha = 1 : q\}.$$

The vertices of $\mathcal{R}$ and $\mathcal{D}$ are denoted by:

$$\mathcal{R}_{vex} := \{\rho : \rho_\alpha = \underline{\rho_\alpha} \text{ or } \overline{\rho_\alpha} \ \ \forall \alpha = 1 : q\} \text{ and } \mathcal{D}_{vex} := \{\dot{\rho} : \dot{\rho}_\alpha = \underline{\dot{\rho}_\alpha} \text{ or } \overline{\dot{\rho}_\alpha} \ \ \forall \alpha = 1 : q\}.$$

The set of admissible parameter trajectories are defined as

$$\mathcal{P} := \{\boldsymbol{\rho} : \mathbb{R} \to \mathbb{R}^q : \boldsymbol{\rho}(t) \in \mathcal{R} \text{ and } \dot{\boldsymbol{\rho}}(t) \in \mathcal{D} \ \ \forall t \geq 0\}.$$

For the LPV system in the general descriptor form (6.1), it is aimed in this section to design a controller of the form

$$\begin{aligned} \dot{\boldsymbol{x_c}} &= \boldsymbol{A_c}(\boldsymbol{\rho})\boldsymbol{x_c} + \boldsymbol{B_c}(\boldsymbol{\rho})\boldsymbol{y} \\ \boldsymbol{u} &= \boldsymbol{C_c}(\boldsymbol{\rho})\boldsymbol{x_c} \end{aligned} \tag{6.2}$$

such that the closed-loop system is asymptotically stable with $\mathcal{L}_2$-gain γ.

Theorem 6.1.1 *Assume that:*

$$\begin{bmatrix} -\gamma I & \boldsymbol{D_{zw}}^T \\ \boldsymbol{D_{zw}} & -\gamma I \end{bmatrix} \prec 0 \quad \forall \boldsymbol{\rho} \in \mathcal{R}. \tag{6.3}$$

Then, there exists a controller of the form (6.2) that asymptotically stabilizes the system (6.1) if there exist $\boldsymbol{X}(\boldsymbol{\rho}) = \boldsymbol{X}(\boldsymbol{\rho})^T \in I\!R^{n\times n}$, $\boldsymbol{Y}(\boldsymbol{\rho}) = \boldsymbol{Y}(\boldsymbol{\rho})^T \in I\!R^{n\times n}$, $\boldsymbol{F}(\boldsymbol{\rho}) \in I\!R^{m_2\times n}$

and $\boldsymbol{G}(\boldsymbol{\rho}) \in I\!R^{n \times p_2}$ *such that*

$$\begin{bmatrix} \boldsymbol{A}\boldsymbol{X}\boldsymbol{E}^T + \boldsymbol{E}\boldsymbol{X}\boldsymbol{A}^T + \boldsymbol{B_u}\boldsymbol{F}\boldsymbol{E}^T + \boldsymbol{E}\boldsymbol{F}^T\boldsymbol{B_u}^T - \boldsymbol{E}\dot{\boldsymbol{X}}\boldsymbol{E}^T & \star & \star \\ \boldsymbol{B_w}^T & -\gamma I & \star \\ \boldsymbol{C_z}\boldsymbol{X}\boldsymbol{E}^T + \boldsymbol{D_{zu}}\boldsymbol{F}\boldsymbol{E}^T & \boldsymbol{D_{zw}} & -\gamma I \end{bmatrix} \prec 0$$

$$\forall(\boldsymbol{\rho}, \dot{\boldsymbol{\rho}}) \in \mathcal{R} \times \mathcal{D} \quad (6.4)$$

$$\begin{bmatrix} \boldsymbol{A}^T\boldsymbol{Y}\boldsymbol{E} + \boldsymbol{E}^T\boldsymbol{Y}\boldsymbol{A} + \boldsymbol{G}\boldsymbol{C_y} + \boldsymbol{C_y}^T\boldsymbol{G}^T + \dot{\boldsymbol{E}}^T\boldsymbol{Y}\boldsymbol{E} + \boldsymbol{E}^T\dot{\boldsymbol{Y}}\boldsymbol{E} + \boldsymbol{E}^T\boldsymbol{Y}\dot{\boldsymbol{E}} & \star & \star \\ \boldsymbol{B_w}^T\boldsymbol{Y}\boldsymbol{E} + \boldsymbol{D_{yw}}^T\boldsymbol{G}^T & -\gamma I & \star \\ \boldsymbol{C_z} & \boldsymbol{D_{zw}} & -\gamma I \end{bmatrix} \prec 0$$

$$\forall(\boldsymbol{\rho}, \dot{\boldsymbol{\rho}}) \in \mathcal{R} \times \mathcal{D} \quad (6.5)$$

$$\begin{bmatrix} \boldsymbol{X}(\boldsymbol{\rho}) & I \\ I & \boldsymbol{E}(\boldsymbol{\rho})^T\boldsymbol{Y}(\boldsymbol{\rho})\boldsymbol{E}(\boldsymbol{\rho}) \end{bmatrix} \succ 0 \quad \forall \boldsymbol{\rho} \in \mathcal{R}. \quad (6.6)$$

In this case, the controller in (6.2) can be given by the definitions

$$\boldsymbol{C_c}(\boldsymbol{\rho}) = \boldsymbol{F}\boldsymbol{X}^{-1} \quad (6.7)$$

$$\boldsymbol{B_c}(\boldsymbol{\rho}) = -\boldsymbol{Z}^{-1}\boldsymbol{G} \quad (6.8)$$

$$\begin{aligned} \boldsymbol{A}(\boldsymbol{\rho}, \dot{\boldsymbol{\rho}}) = {} & \boldsymbol{Z}^{-1}\boldsymbol{A}^T\boldsymbol{E}^{-T}\boldsymbol{X}^{-1} + \boldsymbol{Z}^{-1}\boldsymbol{E}^T\boldsymbol{Y}[\boldsymbol{A} + \boldsymbol{B_u}\boldsymbol{C_c}] - \boldsymbol{B_c}\boldsymbol{C_y} \\ & + \boldsymbol{Z}^{-1}\boldsymbol{L}\boldsymbol{X}^{-1} + \boldsymbol{Z}^{-1}\boldsymbol{X}^{-1}\dot{\boldsymbol{X}}\boldsymbol{X}^{-1} \end{aligned} \quad (6.9)$$

where $Z(\boldsymbol{\rho}) = \boldsymbol{E}(\boldsymbol{\rho})^T\boldsymbol{Y}(\boldsymbol{\rho})\boldsymbol{E}(\boldsymbol{\rho}) - \boldsymbol{X}(\boldsymbol{\rho})^{-1} \succ 0$ *and*

$$\boldsymbol{L} = \begin{bmatrix} \boldsymbol{E}^T\boldsymbol{Y}\boldsymbol{B_w} + \boldsymbol{G}\boldsymbol{D_{yw}} & \boldsymbol{C_z}^T \end{bmatrix} \begin{bmatrix} -\gamma I & \boldsymbol{D_{zw}}^T \\ \boldsymbol{D_{zw}} & -\gamma I \end{bmatrix}^{-1} \begin{bmatrix} \boldsymbol{B_w}^T\boldsymbol{E}^{-T} \\ \boldsymbol{C_z}\boldsymbol{X} \end{bmatrix}$$

From (6.4) - (6.6), the sign definiteness of the given LMIs must be validated at each point of $\mathcal{R} \times \mathcal{D}$, hence infinite dimensional solvability conditions are obtained. To tackle this problem, assuming affine parameter dependence and multiconvexity, they can be written as finite dimensional LMIs (FDLMI) [58]. The satisfaction of (6.4), (6.5)

and (6.6) over $\mathcal{R}\times\mathcal{D}$ can be guaranteed by checking the vertices $\mathcal{R}_{vex}\times\mathcal{D}_{vex}$, provided that the second derivatives with respect to each parameter are positive semidefinite. For example, for (6.5) we require

$$\begin{bmatrix} \frac{\partial^2}{\partial\rho_i^2}(\boldsymbol{A}^T\boldsymbol{Y}\boldsymbol{E}+\boldsymbol{E}^T\boldsymbol{Y}\boldsymbol{A}+\dot{\boldsymbol{E}}^T\boldsymbol{Y}\boldsymbol{E}+ & \\ \boldsymbol{E}^T\dot{\boldsymbol{Y}}\boldsymbol{E}+\boldsymbol{E}^T\boldsymbol{Y}\dot{\boldsymbol{E}}+\boldsymbol{G}\boldsymbol{C}_{\boldsymbol{y}}+\boldsymbol{C}_{\boldsymbol{y}}{}^T\boldsymbol{G}^T) & \frac{\partial^2}{\partial\rho_\alpha^2}(\boldsymbol{E}^T\boldsymbol{Y}\boldsymbol{B}_{\boldsymbol{w}}) \\ \frac{\partial^2}{\partial\rho_\alpha^2}(\boldsymbol{B}_{\boldsymbol{w}}{}^T\boldsymbol{Y}\boldsymbol{E}) & 0 \end{bmatrix} \succeq 0$$

$$\forall(\boldsymbol{\rho},\dot{\boldsymbol{\rho}})\in\mathcal{R}_{vex}\times\mathcal{D}_{vex}. \quad (6.10)$$

Letting $(\star)$ denote the transposed version of the preceding terms, the condition above necessitates

$$\boldsymbol{A}_i^T\boldsymbol{Y}_i\boldsymbol{E}+\boldsymbol{A}_i^T\boldsymbol{Y}\boldsymbol{E}_i+\boldsymbol{A}^T\boldsymbol{Y}_i\boldsymbol{E}_i+(\star)+\boldsymbol{G}_i\boldsymbol{C}_{\boldsymbol{y}_i}+\boldsymbol{C}_{\boldsymbol{y}_i}\boldsymbol{G}_i^T+\dot{\boldsymbol{E}}^T\boldsymbol{Y}_i\boldsymbol{E}_i+\boldsymbol{E}_i^T\dot{\boldsymbol{Y}}\boldsymbol{E}_i+\boldsymbol{E}_i\boldsymbol{Y}_i\dot{\boldsymbol{E}}\succeq 0$$
$$\forall(\boldsymbol{\rho},\dot{\boldsymbol{\rho}})\in\mathcal{R}_{vex}\times\mathcal{D}_{vex}\quad\forall i=1:q \quad (6.11)$$

As for sufficiency, the following lemma is considered:

Lemma 6.1.2 : *Given a symmetric matrix* $\boldsymbol{M}=\begin{bmatrix} m_{11} & & \star \\ \vdots & \ddots & \\ m_{1n} & \dots & m_{nn}\end{bmatrix}\in\mathbb{R}^{n\times n}$,

$$\boldsymbol{M}\succeq 0 \text{ and } m_{ii}=0 \quad\Longleftrightarrow\quad \boldsymbol{M}_{\{i,i\}}\geq 0 \text{ and } m_{ij}=m_{ji}=0 \ \ \forall j=1:n,$$

where $\boldsymbol{M}_{\{i,i\}}$ *is the matrix obtained by deleting the* i^{th} *row and* i^{th} *column of* $\boldsymbol{M}$.

Therefore, if one of the diagonal elements of a positive semidefinite matrix is zero, so are all the entries on that row and column. Hence, condition (6.10) is satisfied if and only if (6.11) holds and

$$\boldsymbol{E}_i^T\boldsymbol{Y}_i\boldsymbol{B}_{\boldsymbol{w}}+\boldsymbol{E}_i^T\boldsymbol{Y}\boldsymbol{B}_{\boldsymbol{w}i}+\boldsymbol{E}^T\boldsymbol{Y}_i\boldsymbol{B}_{\boldsymbol{w}i}+\boldsymbol{G}_i\boldsymbol{D}_{\boldsymbol{y}\boldsymbol{w}_i}=0\quad\forall\rho\in\mathcal{R}_{vex}\quad\forall i=1:q. \quad (6.12)$$

Since the expressions in (6.11) and (6.12) are both affine in ρ, we need only to check

their feasibility for all $(\boldsymbol{\rho}, \dot{\boldsymbol{\rho}}) \in \mathcal{R}_{vex} \times \mathcal{D}_{vex}$. Thus we finally obtain finite dimensional LMIs.

Similarly, (6.4) and (6.6) are reduced to FDLMIs by essentially identical arguments. Regarding (6.12), we have an equality condition on the LMI variables. This can be relaxed into an inequality through the use of slack matrix variables [57], [58].

6.2. LPV modeling of Vehicle Systems

After having introduced the necessary control background for the design of gain scheduled controller, we propose in this section LPV models of the vehicle systems to be controlled.

6.2.1. Expression of Axle Forces with Rational Tire Model

In order to construct parametric models, we first need to obtain axle forces in terms of the rational tire model force predictions. Following the procedure of Section 2.5, it is possible to express front and rear axle lateral forces as

$$F_{y1} + F_{y2} = \frac{\mu C_{\alpha f}}{2\mu_o F_{zfo}} \left(\frac{1}{\eta_{\lambda_1} \lambda_1^2 + 1} \frac{\eta_{z1} F_{z1}}{\eta_{\alpha_1} \alpha_f^2 + 1} + \frac{1}{\eta_{\lambda_2} \lambda_2^2 + 1} \frac{\eta_{z2} F_{z2}}{\eta_{\alpha_2} \alpha_f^2 + 1} \right) \alpha_f \tag{6.13a}$$

$$F_{y3} + F_{y4} = \frac{\mu C_{\alpha r}}{2\mu_o F_{zro}} \left(\frac{1}{\eta_{\lambda_3} \lambda_3^2 + 1} \frac{\eta_{z3} F_{z3}}{\eta_{\alpha_3} \alpha_r^2 + 1} + \frac{1}{\eta_{\lambda_4} \lambda_4^2 + 1} \frac{\eta_{z4} F_{z4}}{\eta_{\alpha_4} \alpha_r^2 + 1} \right) \alpha_r. \tag{6.13b}$$

Similarly, it is possible to express front and rear axle longitudinal force differences as

$$F_{x1} - F_{x2} = \frac{\mu C_{\lambda f}}{2\mu_o F_{zfo}} \left(\frac{1}{\chi_{\lambda_1} \lambda_1^2 + 1} \frac{\chi_{z1} F_{z1}}{\chi_{\alpha_1} \alpha_f^2 + 1} \lambda_1 - \frac{1}{\chi_{\lambda_2} \lambda_2^2 + 1} \frac{\chi_{z2} F_{z2}}{\chi_{\alpha_2} \alpha_f^2 + 1} \lambda_2 \right) \tag{6.14a}$$

$$F_{x3} - F_{x4} = \frac{\mu C_{\alpha r}}{2\mu_o F_{zro}} \left(\frac{1}{\chi_{\lambda_3} \lambda_3^2 + 1} \frac{\chi_{z3} F_{z3}}{\chi_{\alpha_3} \alpha_r^2 + 1} \lambda_3 - \frac{1}{\chi_{\lambda_4} \lambda_4^2 + 1} \frac{\chi_{z4} F_{z4}}{\chi_{\alpha_4} \alpha_r^2 + 1} \lambda_4 \right). \tag{6.14b}$$

Then, the following simplifications are proposed:

- Road adhesion coefficient is taken as μ_o hence assuming driving on dry road;
- When considered as uncertain parameters, shape factors η_{α_i}, η_{λ_i}, η_{zi}, χ_{λ_i}, χ_{α_i} and χ_{zi} can be merged into overall factors η_α, η_λ, χ_λ and χ_α;
- As squares of slip terms, i.e. α_i^2 and λ_i^2, are small, products of squares, $\alpha_i^2\alpha_j^2$, $\alpha_i^2\lambda_j^2$ and $\lambda_i^2\lambda_j^2$ are negligible;
- Effects of lateral load transfer (i.e. decrease in axle cornering force) are included through optimization of η_α, η_λ, χ_λ and χ_α;
- In an active differential control application, tires on opposite sides of the vehicle are under the action of torques of opposite directions. This roughly translates into longitudinal slips of opposite signs for tires on the same axle: $\lambda_1 = -\lambda_2 = \lambda_f$ and $\lambda_3 = -\lambda_4 = \lambda_r$.

Under the above assumptions, it is possible to simplify front and rear axle cornering forces as

$$F_{y1} + F_{y2} = \frac{C_{\alpha f}}{\eta_\lambda \lambda_f^2 + \eta_\alpha \alpha_f^2 + 1}\alpha_f \tag{6.15a}$$

$$F_{y3} + F_{y4} = \frac{C_{\alpha r}}{\eta_\lambda \lambda_r^2 + \eta_\alpha \alpha_r^2 + 1}\alpha_r. \tag{6.15b}$$

Similarly the following relationships hold for the front and rear axle tractive/braking force differences:

$$F_{x1} - F_{x2} = \frac{C_{\lambda f}}{\chi_\lambda \lambda_f^2 + \chi_\alpha \alpha_f^2 + 1}\lambda_f \tag{6.16a}$$

$$F_{x3} - F_{x4} = \frac{C_{\lambda r}}{\chi_\lambda \lambda_r^2 + \chi_\alpha \alpha_r^2 + 1}\lambda_r. \tag{6.16b}$$

Moreover, to render the problem more challenging, we assume that active differential control is only applied to front wheels, i.e. $\lambda_r = 0$, after which, final expressions for parametric bicycle and yaw-roll models can be obtained.

6.2.2. Active Front Steering and Active Front Differential Control

The equations for a parametric bicycle model with active front steering and active front differential control can be given as

$$\dot{\beta} = -\frac{C^*_{\alpha f} + C^*_{\alpha r}}{mv}\beta + \left[-1 + \frac{-aC^*_{\alpha f} + bC^*_{\alpha r}}{MU^2} \right] r + \frac{C^*_{\alpha f}}{MU}(\delta_f + \delta_c) \tag{6.17a}$$

$$\dot{r} = \frac{-aC^*_{\alpha f} + bC^*_{\alpha r}}{J_z}\beta - \frac{a^2C^*_{\alpha f} + b^2C^*_{\alpha r}}{J_z U} r + \frac{aC^*_{\alpha f}}{J_z}\delta + \frac{dC^*_{\lambda_f}}{2J_z}(\lambda_c + \lambda_f) \tag{6.17b}$$

where

$$C^*_{\alpha f} = \frac{C_{\alpha f}}{\eta_\alpha \alpha_f^2 + \eta_\lambda \lambda_f^2 + 1}$$

$$C^*_{\alpha r} = \frac{C_{\alpha r}}{\eta_\alpha \alpha_r^2 + 1}$$

$$C^*_{\lambda_f} = \frac{C_{\lambda f}}{\chi_\alpha \alpha_f^2 + \chi_\lambda \lambda_f^2 + 1}.$$

One should note that instead of including wheel dynamics which involves considering tractive/brake torque inputs, we have here provided an alternative approach where torque inputs are realized through a fictitious slip command λ_c (λ_f above stands for a fictitious driver input taken as zero for the rest of the analysis). This is achieved by requiring the wheel slip regulator to ensure $\lambda_1 = -\lambda_2 = \lambda_c$ through application of tractive/braking torque T_{b1c} and T_{b2c}. These torques are then assumed to be distributed to the left and right wheels (traction at one side, braking at the other) by the active differential controller. The incorporation of the rational tire model contributes to implicitly taking the tire friction circle concept into account, which allows disregarding the stability of wheel dynamics.

The parametric descriptor representation of the above model with

$$\boldsymbol{x} = \begin{pmatrix} \beta & r \end{pmatrix}^T$$
$$\boldsymbol{w} = \begin{pmatrix} \delta_f & \lambda_f \end{pmatrix}^T$$
$$\boldsymbol{u} = \begin{pmatrix} \delta_c & \lambda_c \end{pmatrix}^T$$

can be found in Appendix C.

Similar to the previous chapter, the aim of the combined active steering and differential controller during cornering is two-fold: keeping the body sideslip angle as low as possible and tracking a reference yaw rate, i.e.,

$$\boldsymbol{y} = \boldsymbol{z} = \begin{pmatrix} \beta - \beta_{ref} & r - r_{ref} \end{pmatrix}^T.$$

This necessitates increasing the size of the disturbance vector to account for sideslip angle and yaw rate references which is followed by corresponding zero padding in $\boldsymbol{B_w}$ matrices and by introducing

$$\boldsymbol{C_y} = I_2 = \boldsymbol{C_z}$$
$$\boldsymbol{D_{yw}} = \begin{pmatrix} 0 & 0 & -1 & 0 \\ 0 & 0 & 0 & -1 \end{pmatrix} = \boldsymbol{D_{zw}}$$
$$\boldsymbol{D_{zu}} = 0.$$

The addition of frequency weights is explained in Section 6.3.

6.2.3. Active Front Steering, Active Front Differential and Roll Mode Active Suspension Control

The equations for a parametric yaw roll model with active front steering, active front differential and roll mode active suspension control can be given as

$$(M_s + M_u)U(\dot{\beta} + r) + M_s h\dot{p} = Y_\beta \beta + Y_r r + Y_\delta(\delta_f + \delta_c) \tag{6.18a}$$

$$I_{xz_s}\dot{p} + I_{zz}\dot{r} = N_\beta \beta + N_r r + N_\delta \delta + N_p p + N_\lambda(\lambda_f + \lambda_c) \tag{6.18b}$$

$$I_{xx_s}\dot{p} + M_s hU(\dot{\beta} + r) + I_{xz_s}\dot{r} = L_p p + L_\phi \phi + L_\zeta(\zeta_f + \zeta_c) \tag{6.18c}$$

$$p = \dot{\phi} \tag{6.18d}$$

with

$$\begin{aligned}
Y_r &:= \frac{bC^*_{\alpha f} - aC^*_{\alpha r}}{u} \\
Y_\delta &:= C^*_{\alpha f} \\
Y_\beta &:= -(C^*_{\alpha f} + C^*_{\alpha r}) \\
N_\beta &:= bC^*_{\alpha r} - aC^*_{\alpha f} \\
N_r &:= -\frac{a^2 C^*_{\alpha f} + b^2 C^*_{\alpha r}}{u} \\
N_\delta &:= aC^*_f \\
L_p &:= -c_R \\
N_\lambda &:= \frac{dC^*_{\lambda_f}}{2J_z} \\
L_\phi &:= M_s gh - k_R \\
L_\zeta &:= \frac{d}{2} M_s g.
\end{aligned}$$

Again, we have here proposed the alternative approach of realizing front tractive/braking control inputs through the fictitious slip command λ_c. Furthermore, the roll mode control input is realized through the virtual roll torque $L_\zeta \zeta_c$, where the virtual control input ζ_c ($-1 \leq \zeta_c \leq 1$) is the output of the integrated controller that acts

towards stabilizing the roll mode (ζ_f above stands for a fictitious driver input taken as zero for the rest of the analysis). In practice, this torque is realized by selecting

$$F_{z1c} = -F_{z2c} = F_{z3c} = -F_{z4c} = M_s g \frac{\zeta_c}{4}.$$

The parametric descriptor representation of the above model with

$$\begin{aligned} \boldsymbol{x} &= \begin{pmatrix} \beta & r & p & \phi \end{pmatrix}^T \\ \boldsymbol{w} &= \begin{pmatrix} \delta_f & \lambda_f & \zeta_f \end{pmatrix}^T \\ \boldsymbol{u} &= \begin{pmatrix} \delta_c & \lambda_c & \zeta_c \end{pmatrix}^T \end{aligned}$$

can be found in Appendix C.

The aim of the combined active steering, differential and suspension controller during cornering is three-fold: keeping the body sideslip angle and roll rate as low as possible on the one hand and tracking a reference yaw rate on the other:

$$\boldsymbol{y} = \boldsymbol{z} = \begin{pmatrix} \beta - \beta_{ref} & r - r_{ref} & p - p_{ref} \end{pmatrix}^T.$$

This necessitates increasing the size of the disturbance vector to account for sideslip angle, yaw rate and roll rate references which is again followed by corresponding zero padding in $\boldsymbol{B_w}$ matrices and by introducing

$$\begin{aligned} \boldsymbol{C_y} &= I_3 = \boldsymbol{C_z} \\ \boldsymbol{D_{yw}} &= \begin{pmatrix} 0 & 0 & -1 & 0 & 0 \\ 0 & 0 & 0 & -1 & 0 \\ 0 & 0 & 0 & 0 & -1 \end{pmatrix} = \boldsymbol{D_{zw}} \\ \boldsymbol{D_{zu}} &= 0. \end{aligned}$$

6.3. Controller Design

6.3.1. Parameter Bounds

Prediction of parameter bounds is important for controller design. For the tire model used in this research, F_y can be assumed to vary in the range $(0 - 8000\,N)$. The linear regime of tires has been analyzed to extend up to $\alpha = 0.14\,rad \approx 8^o$ under all operating conditions (changes in road adhesion, lateral weight transfer, combined slip). Assuming a slight excursion into the nonlinear region, we assume an upper limit of 10^o for both front and rear tire side slip angle. Under the light of these observations, the problem has been solved with

$$0 \leq \rho_1 \leq \left(10 \times \frac{\pi}{180}\right)^2$$
$$0 \leq \rho_2 \leq \left(10 \times \frac{\pi}{180}\right)^2.$$

Furthermore, under all operating conditions, maximum generated brake force is obtained below a longitudinal slip value of 0.1, i.e.

$$0 \leq \rho_3 \leq 0.1^2.$$

Initial vehicle speed has been taken as $U_o = 20\,m/s$. Speed variation is expected to be small when implementing combined active steering and differential control.

6.3.2. Frequency Weights

Expected driver commanded steering angle has been selected as 5^o, which corresponds to the steering angle leading to instability on all road conditions. Then, the filter $W_d(s)$ has been modeled as a simple scalar quantity to normalize driver input:

$$W_d(s) = \frac{5\pi}{180}.$$

Scaling of the entries of $W_{ref}(s)$ is necessary to account for expected upper limits in reference sideslip, yaw rate and roll rate. The order of magnitude of the maximum expected sideslip angle and roll rate can be shown to be about the same as δ_f while the maximum expected yaw rate is roughly five times higher. These observations are based on steady state system gains. Hence, the entry corresponding to sideslip angle and roll rate is scaled with $\frac{5\pi}{180}$ and the entry corresponding to yaw rate is scaled with $\frac{25\pi}{180}$. Simple scalar weighting has been observed to yield satisfactory results, finally yielding

$$W_{ref}(s) = \mathbf{diag}(2 \times 2\pi\frac{5\pi}{180}, 2 \times 2\pi\frac{5\pi}{180}, 2 \times 2\pi\frac{25\pi}{180}).$$

Scaling of the entries of $W_e(s)$ is necessary to reduce steady-state errors in controlled output β, r and p. It has been observed that good results were obtained by weighing more on the yaw rate and roll control channels. The following was used in the simulations:

$$\begin{aligned} A_e &= \mathbf{diag}(-2 \times 2\pi, -2 \times 2\pi, -2 \times 2\pi) \\ B_e &= \mathbf{diag}(2 \times 2\pi, 2 \times 2\pi, 2 \times 2\pi) \\ C_e &= \mathbf{diag}(8, 15, 15) \\ D_e &= 0. \end{aligned}$$

6.4. Simulation Results for Integrated Active Front Steering and Active Front Differential Control

In this first series of simulations, the nonlinear two-track yaw plane model is used. The vehicle is assumed to have a low CG. Hence decoupling of only sideslip and yaw modes is sought.

6.4.1. Simulation 4: Mode Decoupling at Small Driver Commanded Steering Angle

Firstly, controller performance is investigated for cornering maneuvers at small driver commanded steering angles (Figure 6.1 and Figure 6.3). The response of the controlled vehicle is quite satisfactory as displayed by the sideslip angle and yaw rate curves: sideslip is almost completely eliminated and nice reference tracking is achieved for both maneuvers revealing successful decoupling of vehicle modes.

6.4.2. Simulation 5: Mode Decoupling at Large Driver Commanded Steering Angle

Secondly, controller performance in nominal conditions are investigated. Results for sinusoidal steering and J turn maneuvers with maximum driver commanded steering angle $\delta_f = 5^o$ carried out on dry road are shown in Figure 6.5 and Figure 6.7. Responses of the controlled vehicle are satisfactory as displayed by the sideslip angle and yaw rate curves. Parameter variations during these maneuvers can be observed in Figure 6.6 and Figure 6.8. Parameter bounds are relatively well satisfied. It is noted that vehicle speed changes slightly during the maneuver which justifies the constant speed assumption made during controller synthesis.

6.4.3. Simulation 6: Controller Performance on Slippery Road

In a third series of simulations, controller performance is investigated on slippery road. Results for sinusoidal steering and J turn maneuvers carried out with driver commanded steering angle as large as $\delta_f = 5^o$ are shown in Figure 6.9 and Figure 6.11. Good yaw rate tracking and acceptable side slip angle response are again obtained.

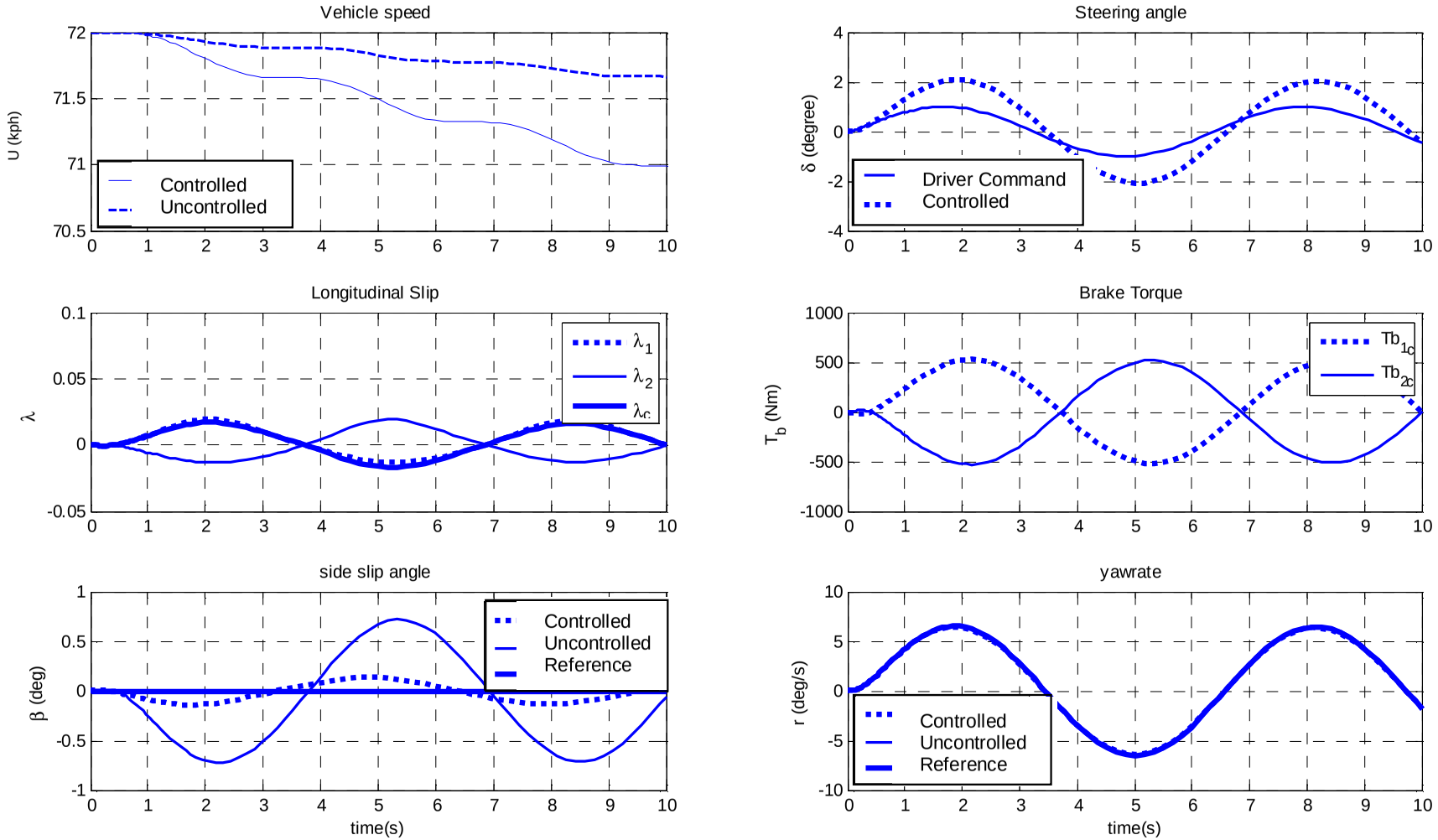


Figure 6.1. Combined steering and differential controller performance on dry road ($\mu = 0.8$) for small driver commanded steering angle (sinusoidal steering)

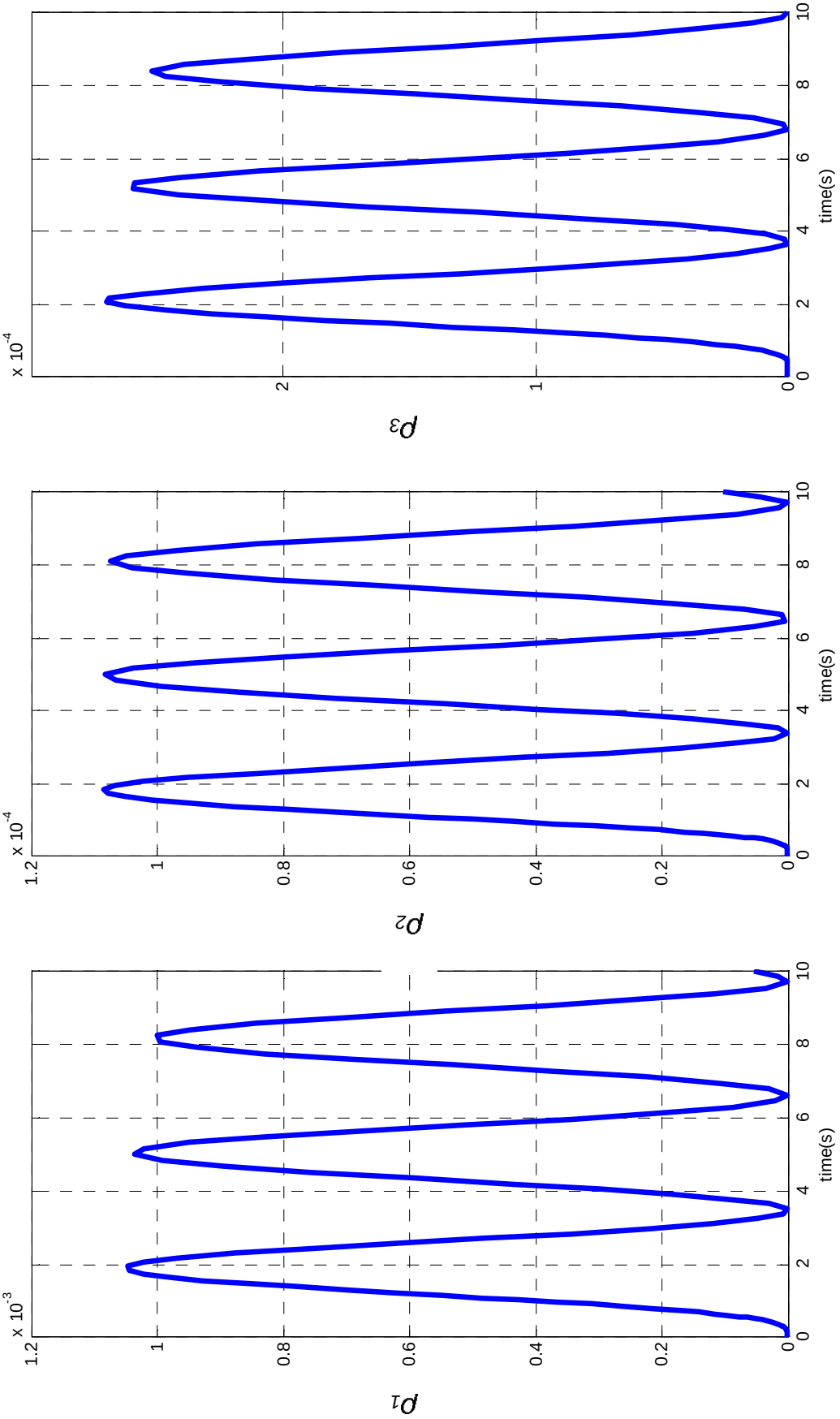


Figure 6.2. Parameter variation on dry road ($\mu = 0.8$) for small driver commanded steering angle (sinusoidal steering)

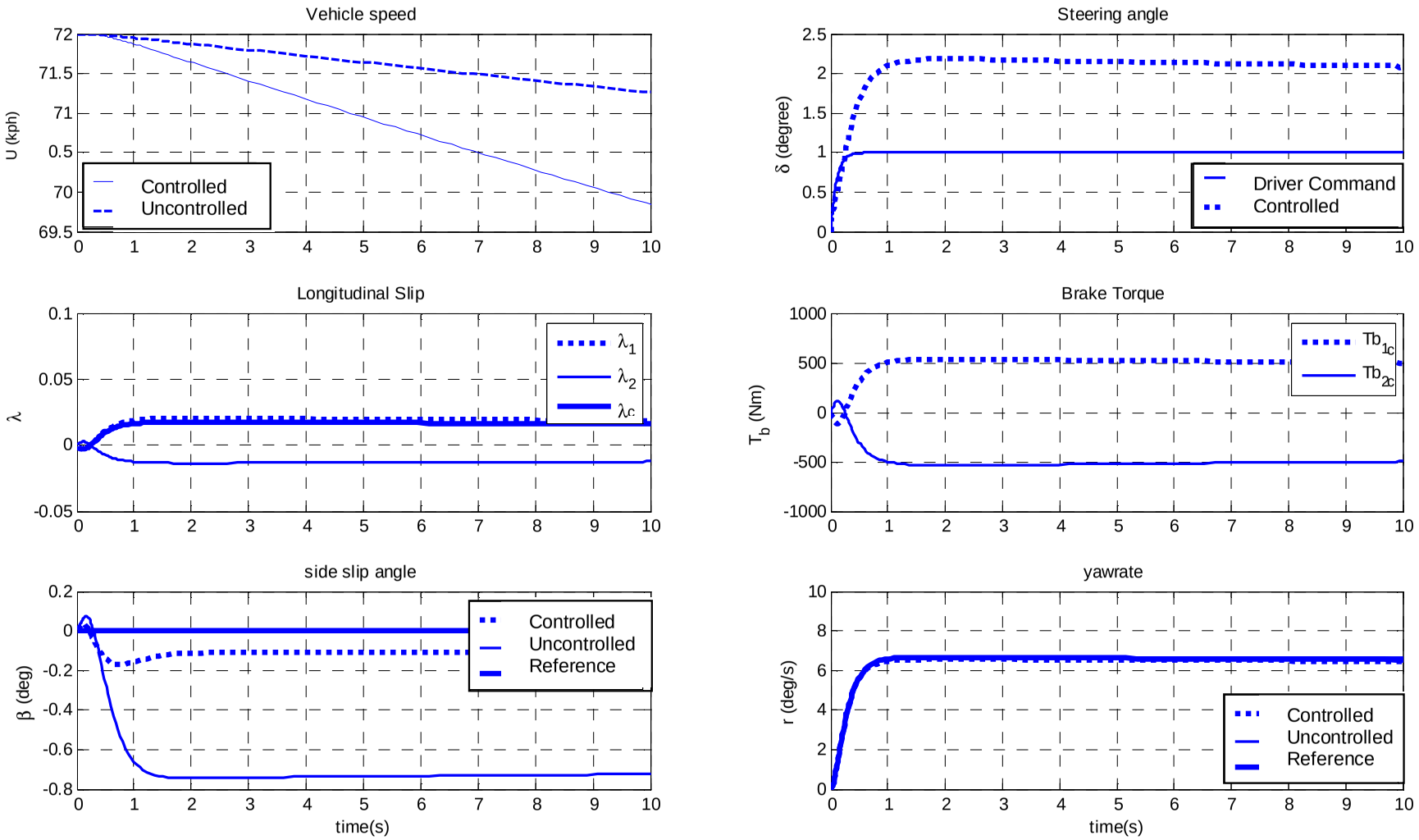


Figure 6.3. Combined steering and differential controller performance on dry road ($\mu = 0.8$) for small driver commanded steering angle (J turn)

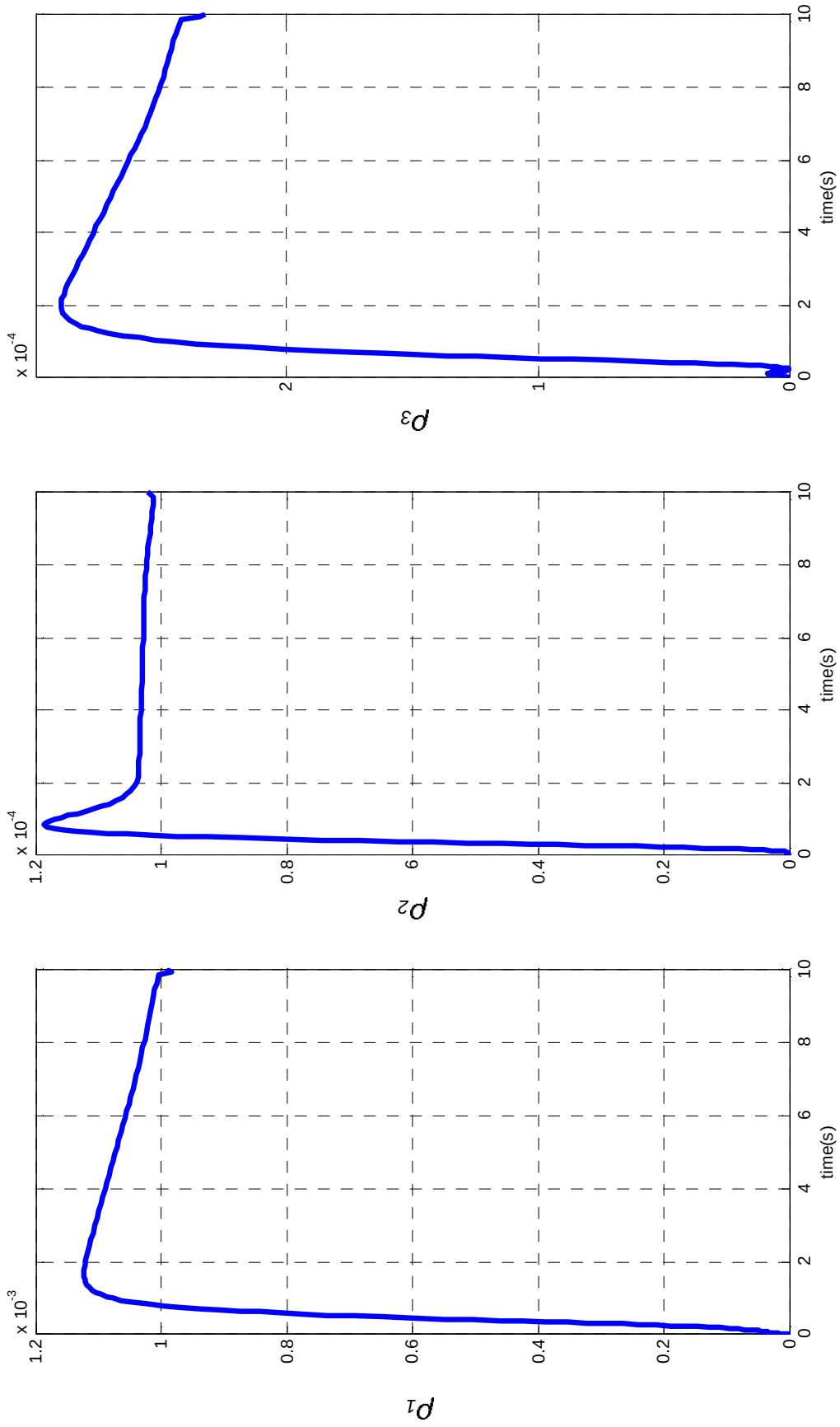


Figure 6.4. Parameter variation on dry road ($\mu = 0.8$) for small driver commanded steering angle (J turn)

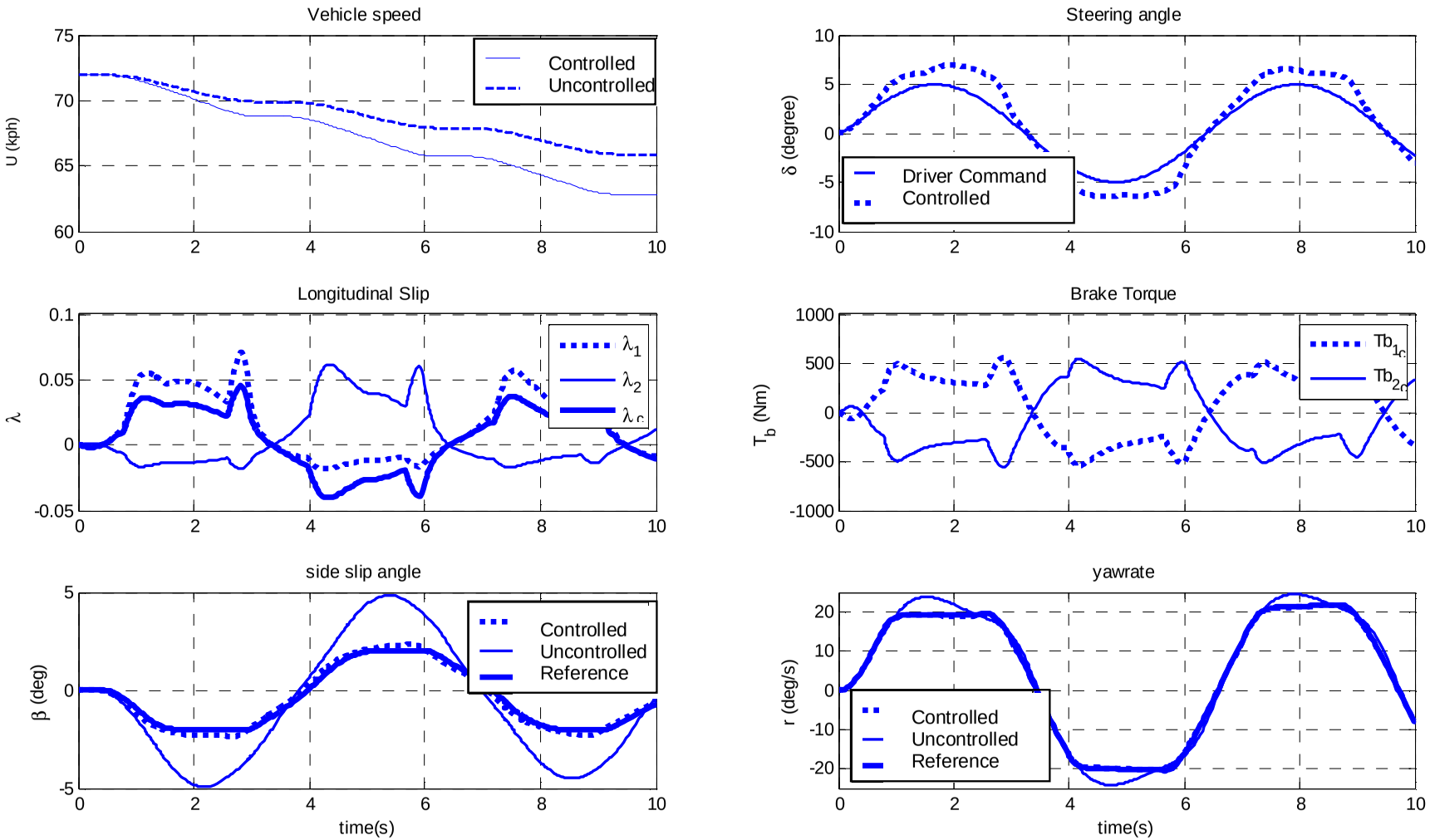


Figure 6.5. Combined steering and differential controller performance on dry road ($\mu = 0.8$) for sinusoidal steering maneuver

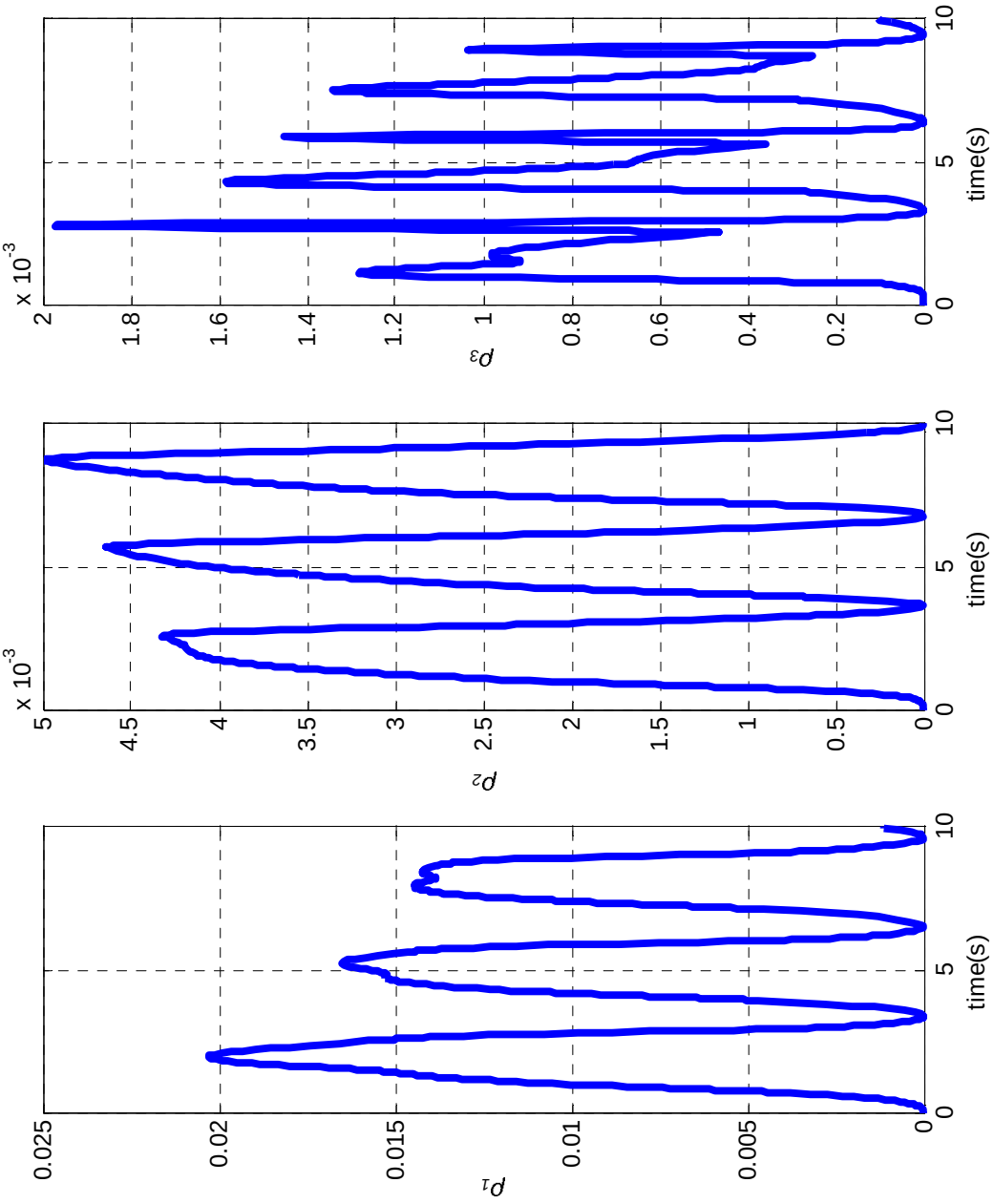


Figure 6.6. Parameter variation on dry road ($\mu = 0.8$) for sinusoidal steering maneuver

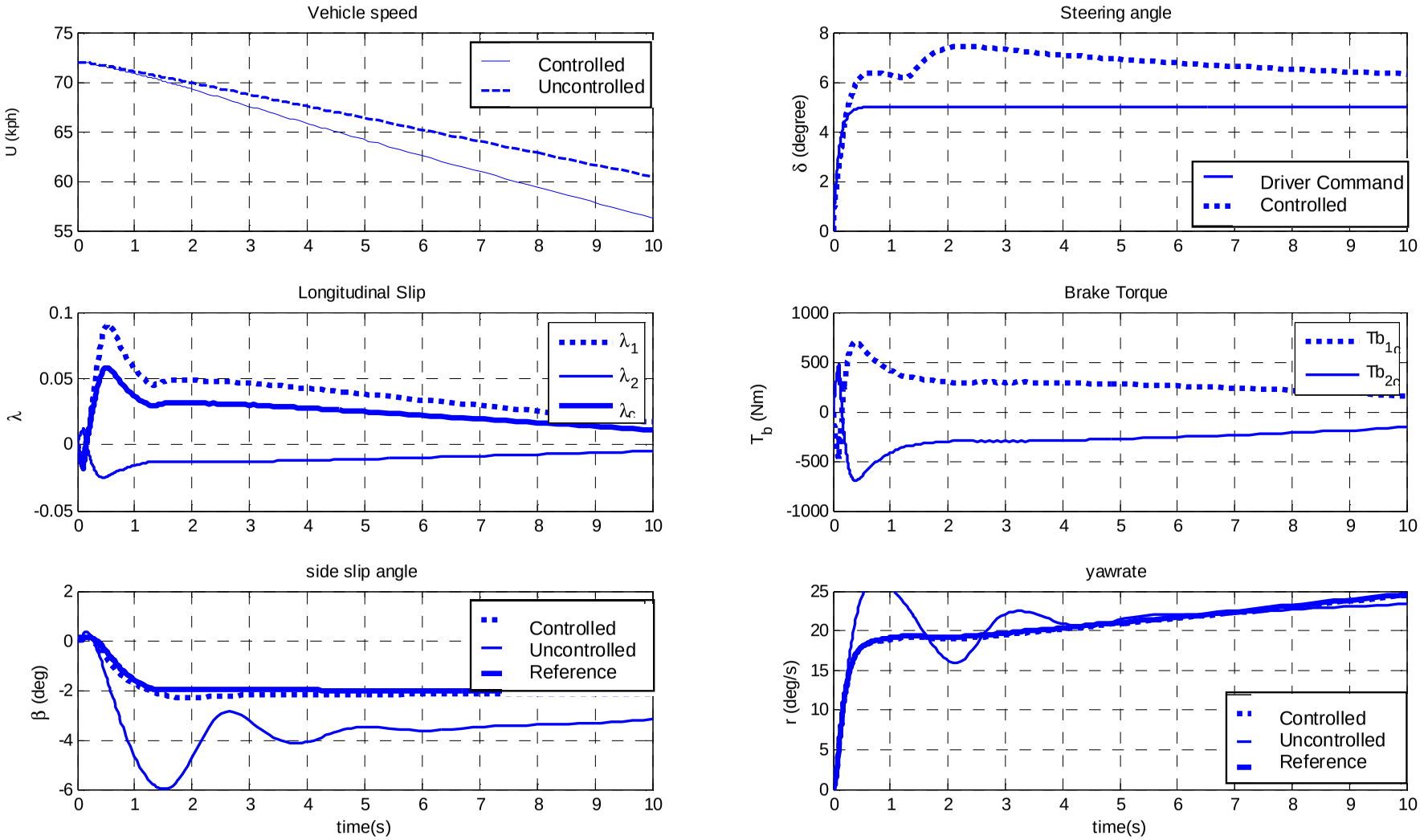


Figure 6.7. Combined steering and differential controller performance on dry road ($\mu = 0.8$) for J turn cornering maneuver

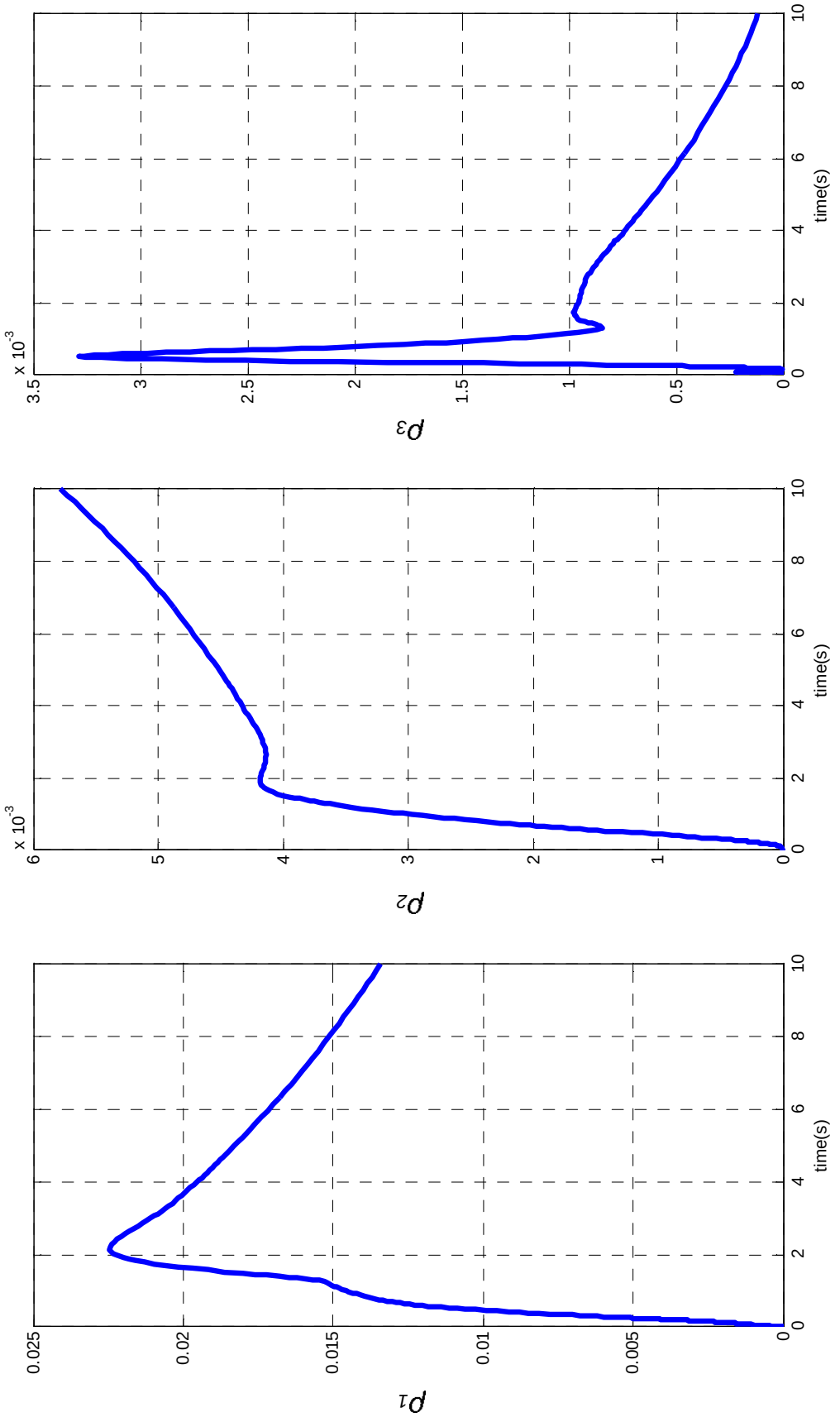


Figure 6.8. Parameter variation on dry road ($\mu = 0.8$) for J turn cornering maneuver

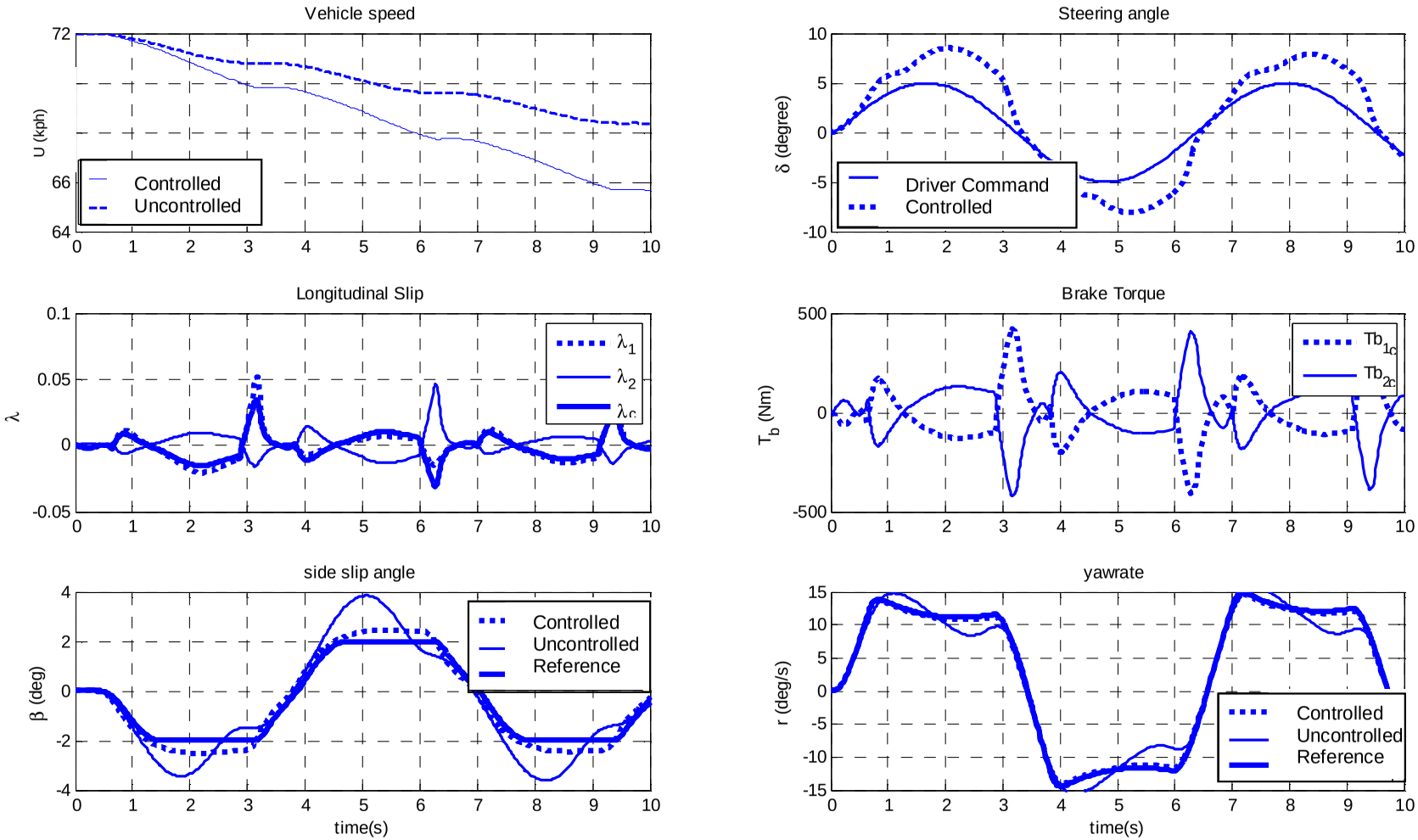


Figure 6.9. Combined steering and differential controller performance on slippery road ($\mu = 0.4$) for sinusoidal steering maneuver

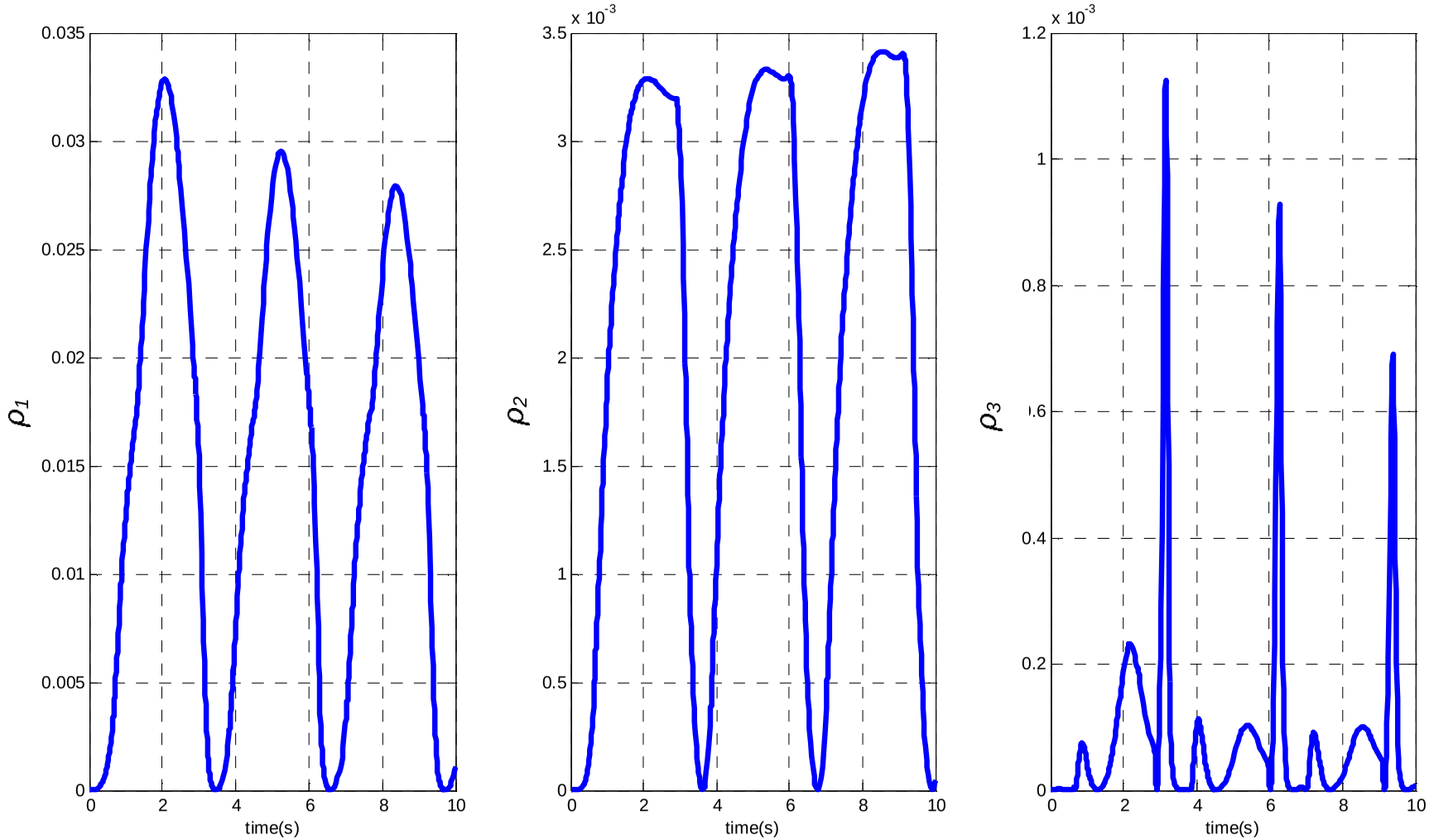


Figure 6.10. Parameter variation on slippery road ($\mu = 0.4$) for sinusoidal steering maneuver

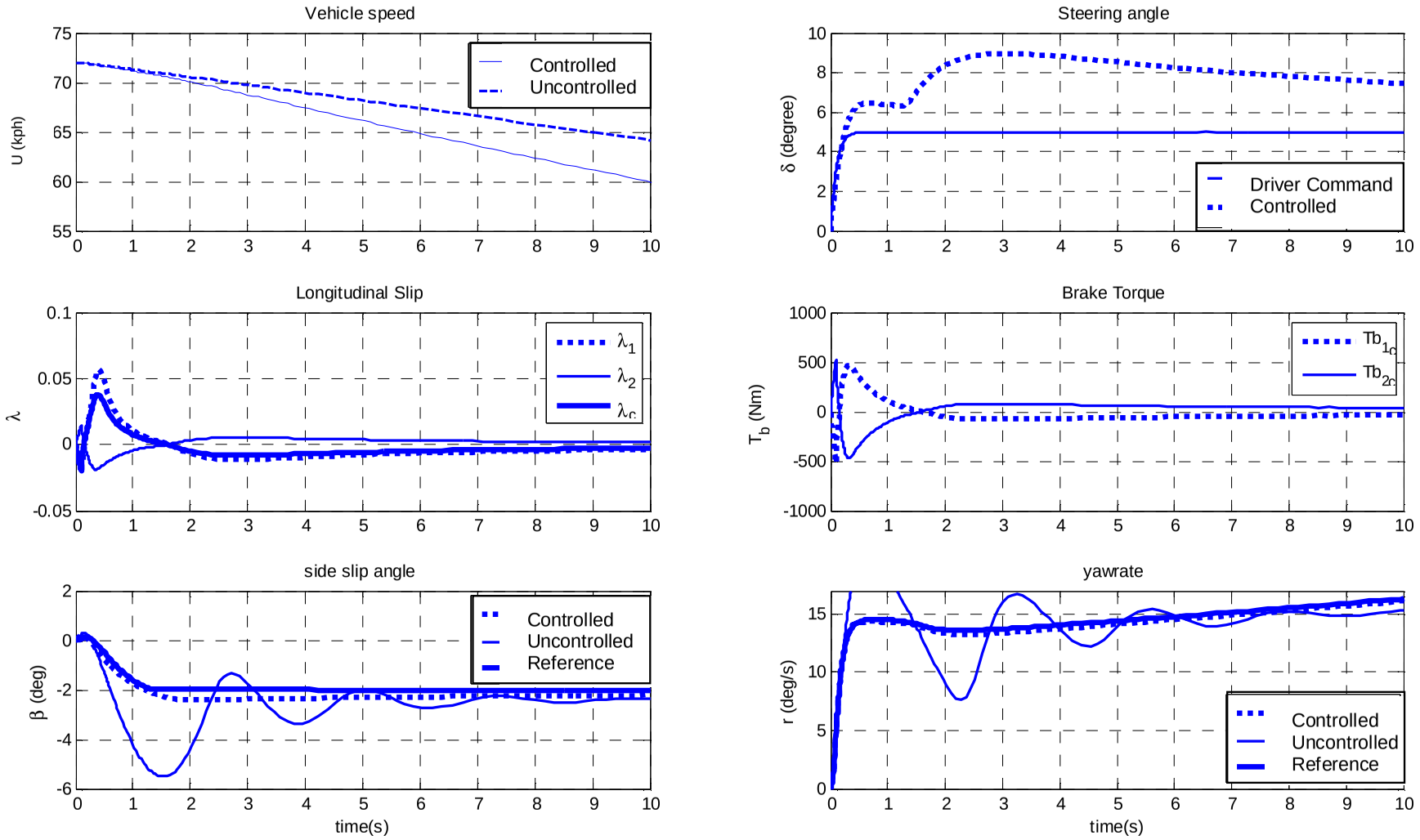


Figure 6.11. Combined steering and differential controller performance on slippery road ($\mu = 0.4$) for J turn cornering maneuver

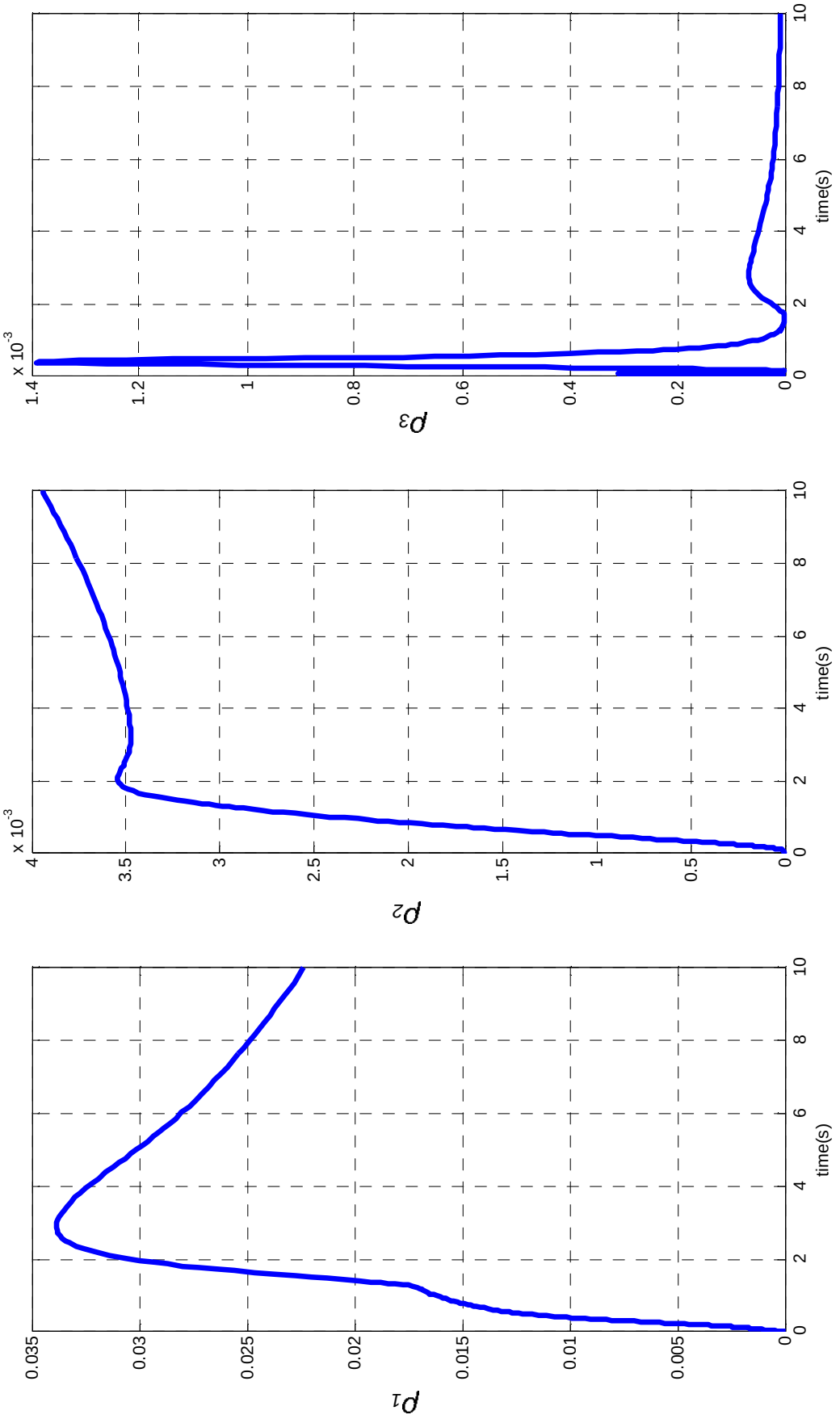


Figure 6.12. Parameter variation on slippery road ($\mu = 0.4$) for J turn cornering maneuver

6.5. Simulation Results for Integrated Active Front Steering, Active Front Differential and Active Suspension Control

In this second series of simulations, the nonlinear six-degree-of-freedom vehicle is used. The vehicle has an elevated CG, which necessitates the inclusion of the roll mode in equations of motion. Decoupling of all vehicle modes is sought.

6.5.1. Simulation 7: Mode Decoupling at Small Driver Commanded Steering Angle

For cornering maneuvers at lower driver commanded steering angles (Figure 6.13 and Figure 6.15), the response of the controlled vehicle is quite satisfactory as displayed by the sideslip angle and yaw rate curves: again sideslip is almost completely eliminated and nice reference tracking is achieved for both maneuvers revealing successful decoupling of vehicle modes. When compared with the results of the same simulation executed without suspension controllers, present steering correction and active differential control inputs are observed to be smaller.

6.5.2. Simulation 8: Controller Performance at Large Driver Commanded Steering Angle

Secondly, controller performance at large driver commanded steering angle are investigated. Results for sinusoidal steering and J turn maneuvers with maximum driver commanded steering angle $\delta_f = 5^o$ carried out on dry road are shown in Figure 6.17 and Figure 6.19. Responses of the controlled vehicle are satisfactory as displayed by the sideslip angle and yaw rate curves. Parameter variations during these maneuvers can be observed in Figure 6.18 and Figure 6.20 . Parameter bounds are relatively well satisfied. It is noted that vehicle speed changes slightly during the maneuver which justifies the constant speed assumption made during controller synthesis. When compared with the results of the same simulation executed without suspension controllers, present steering correction and active differential control inputs are observed to be smaller. Especially, the expected decrease in steering angle is achieved.

6.5.3. Simulation 9: Controller Performance on Slippery Road

In a final series of simulations, controller performance is investigated on slippery road. Results for sinusoidal steering and J turn maneuvers with driver commanded steering angle as large as $\delta_f = 5^o$ are shown in Figure 6.21 and Figure 6.23. Good yaw rate tracking and acceptable sideslip angle response are again obtained. When compared with the results of the same simulation executed without suspension controllers, present steering correction and active differential control inputs are observed to be smaller. Again, the expected decrease in steering angle is achieved.

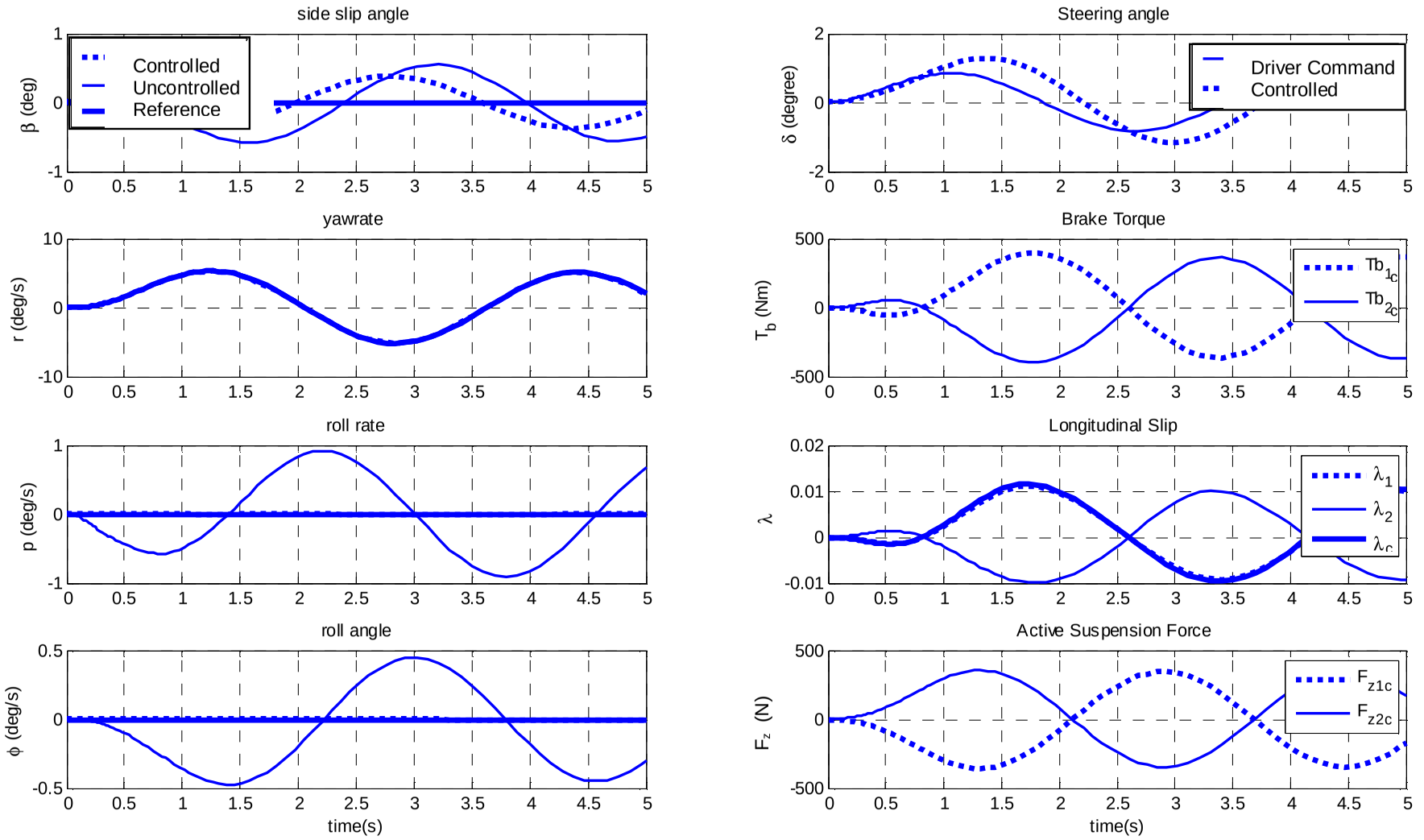


Figure 6.13. Combined steering, differential and suspension controller performance on dry road ($\mu = 0.8$) for small driver commanded steering angle (sinusoidal steering)

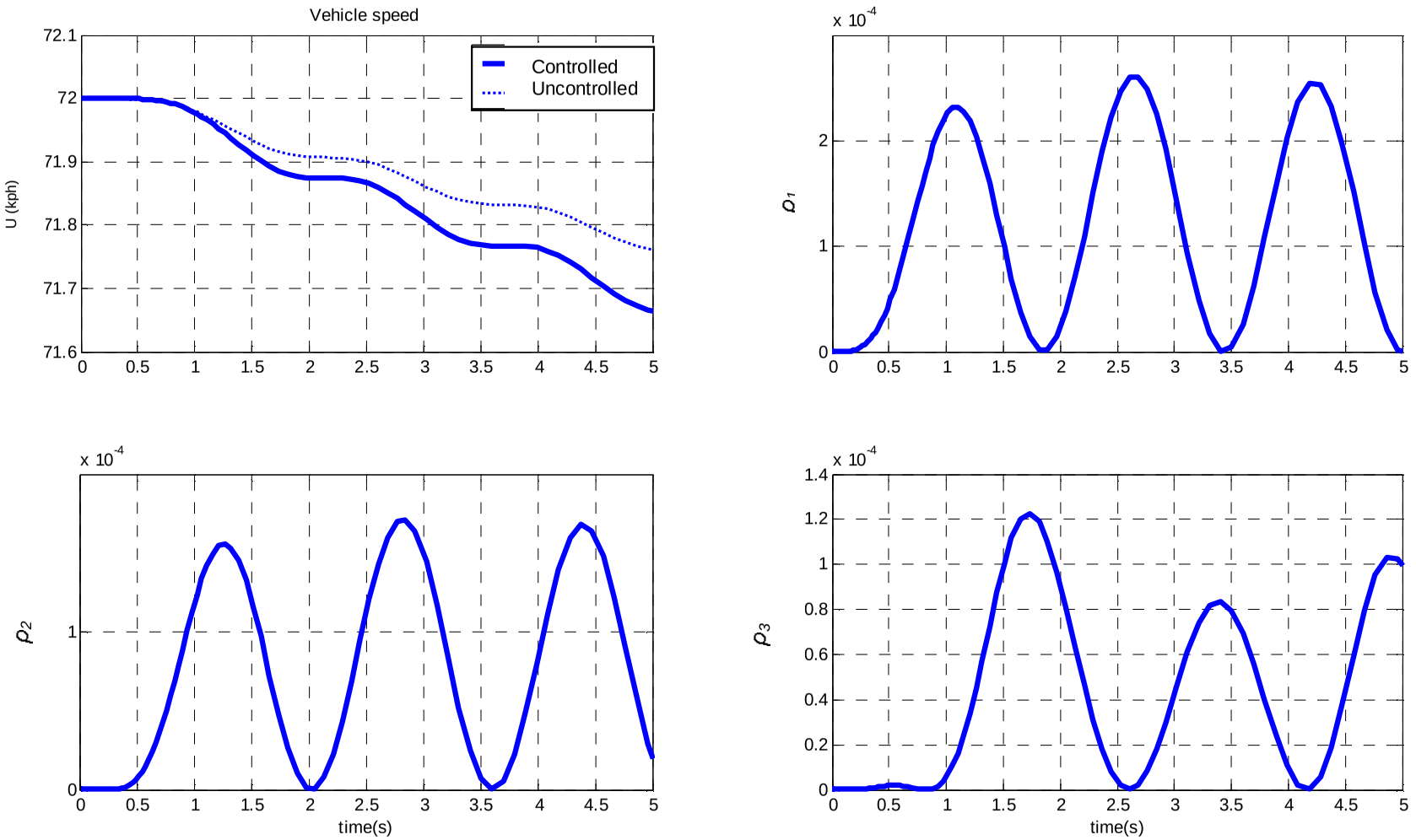


Figure 6.14. Parameter variation on dry road ($\mu = 0.8$) for small driver commanded steering angle (sinusoidal steering)

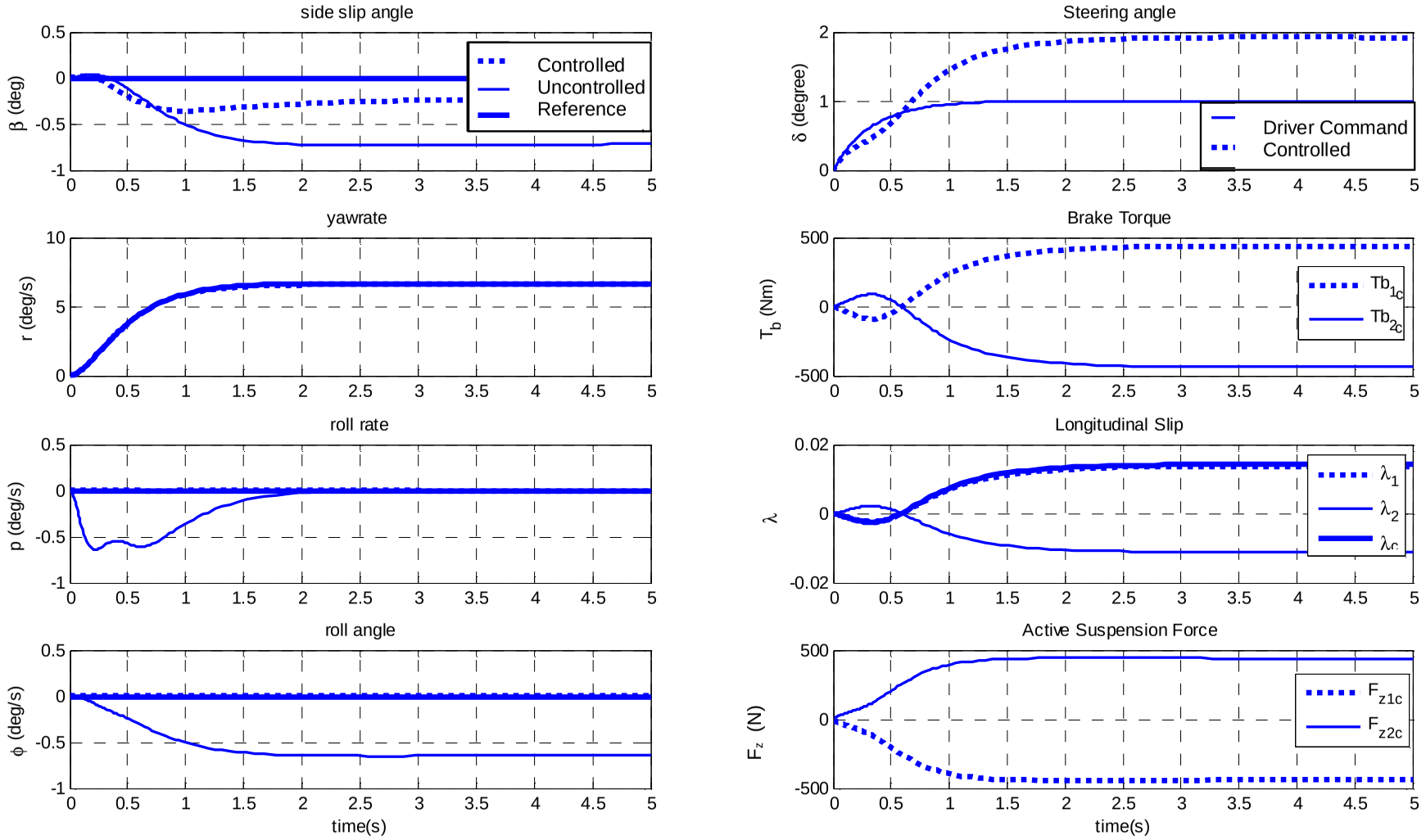


Figure 6.15. Combined steering, differential and suspension controller performance on dry road ($\mu = 0.8$) for small driver commanded steering angle (J turn)

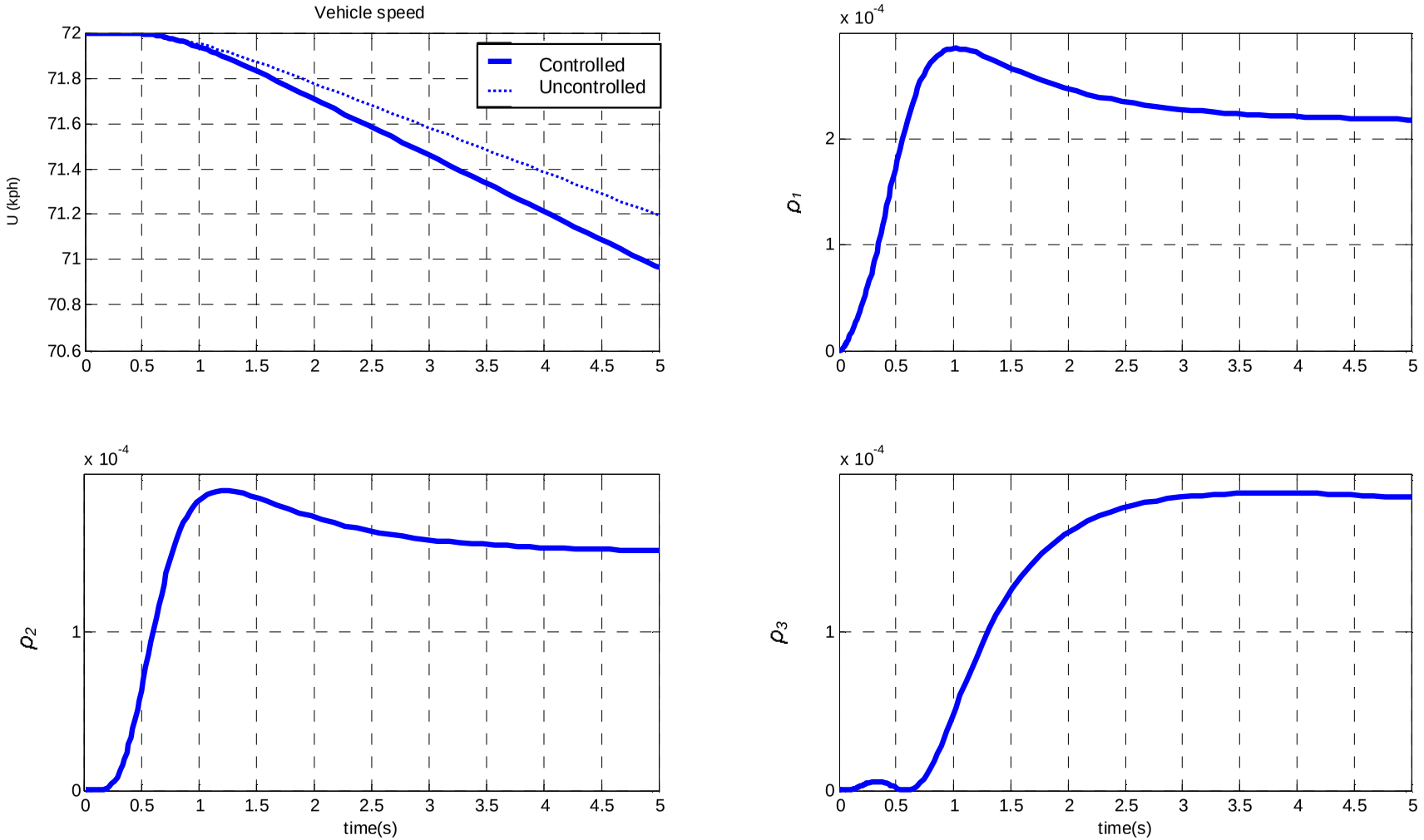


Figure 6.16. Parameter variation on dry road ($\mu = 0.8$) for small driver commanded steering angle (J turn)

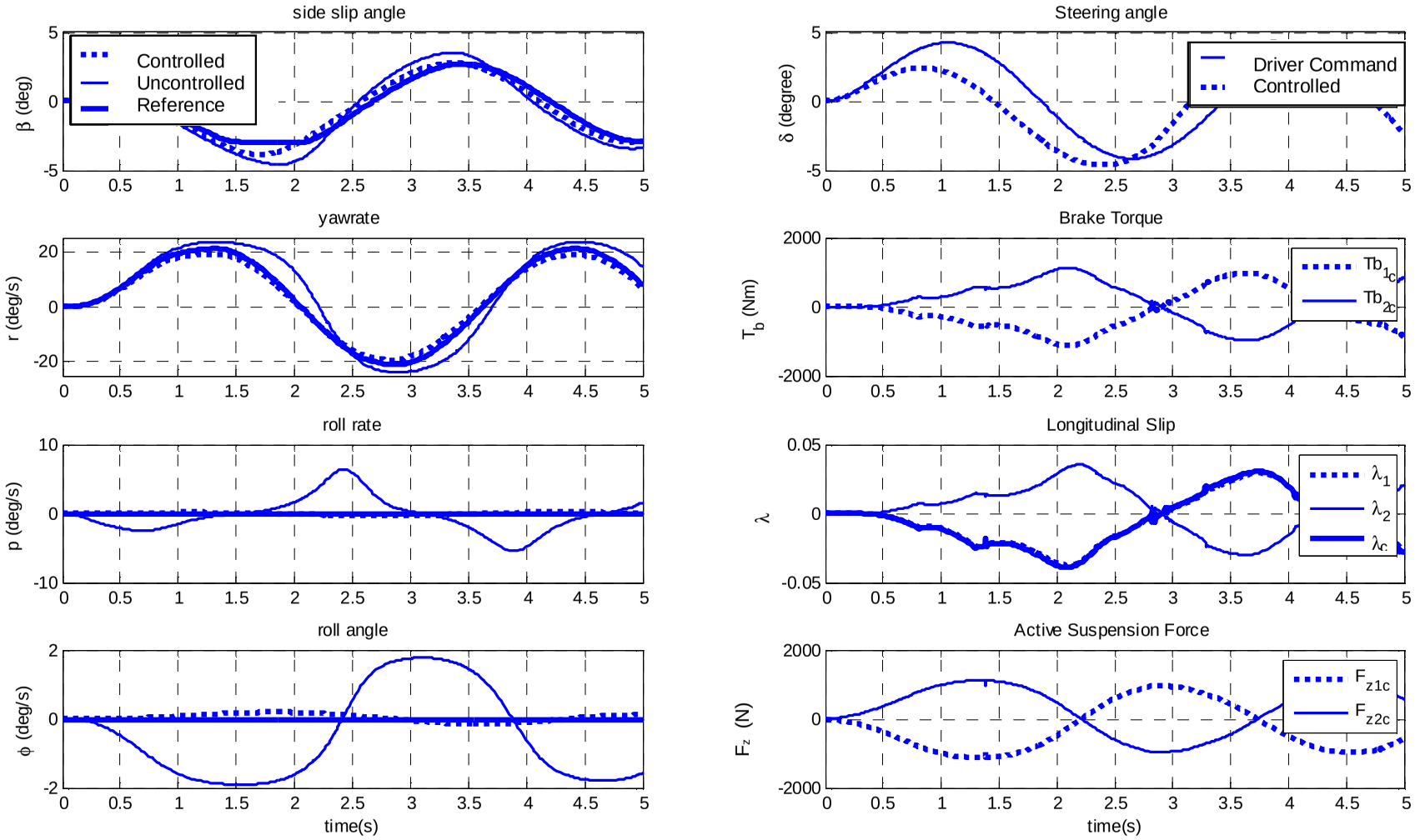


Figure 6.17. Combined steering, differential and suspension controller performance on dry road ($\mu = 0.8$) for sinusoidal steering maneuver

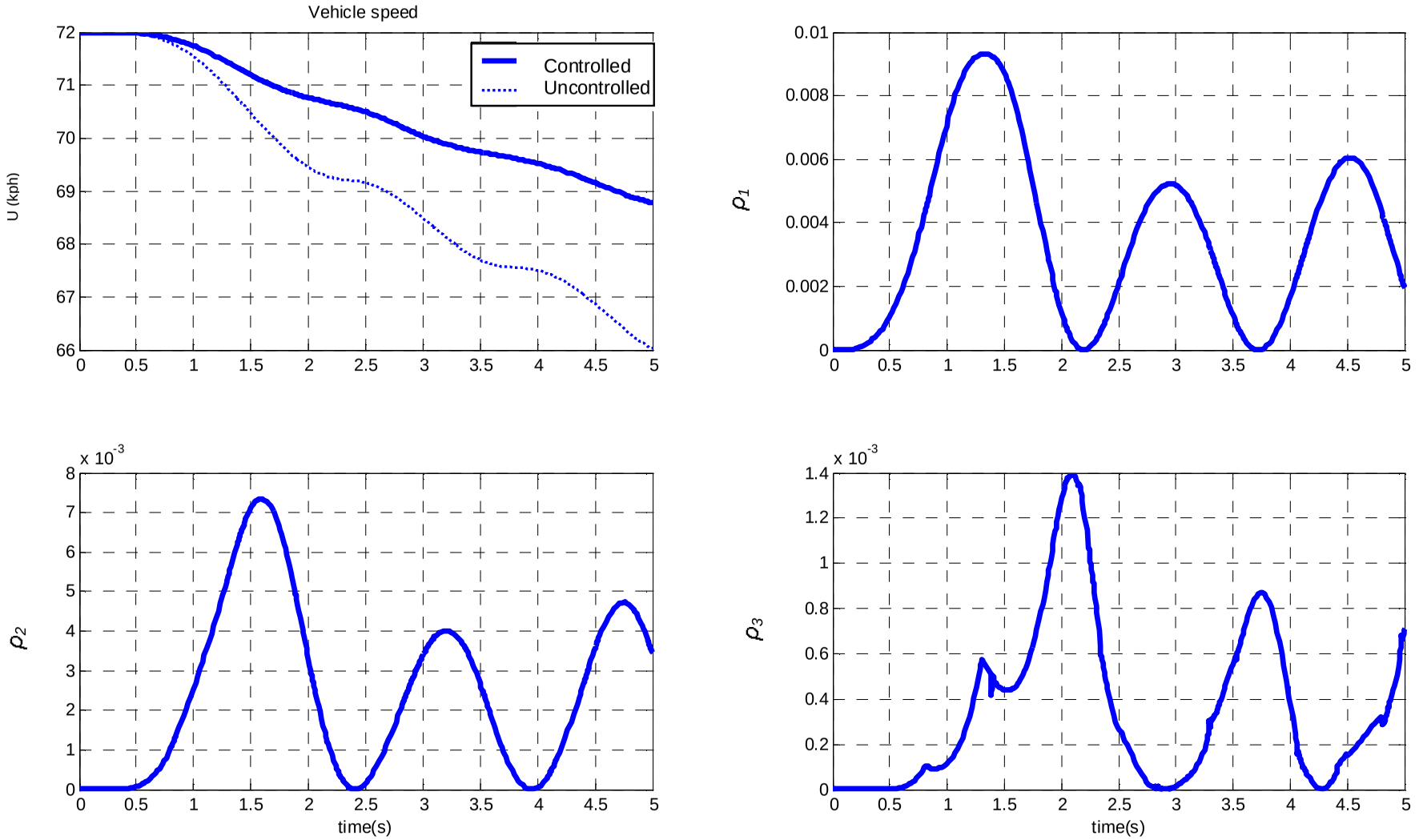


Figure 6.18. Parameter variation on dry road ($\mu = 0.8$) for sinusoidal steering maneuver

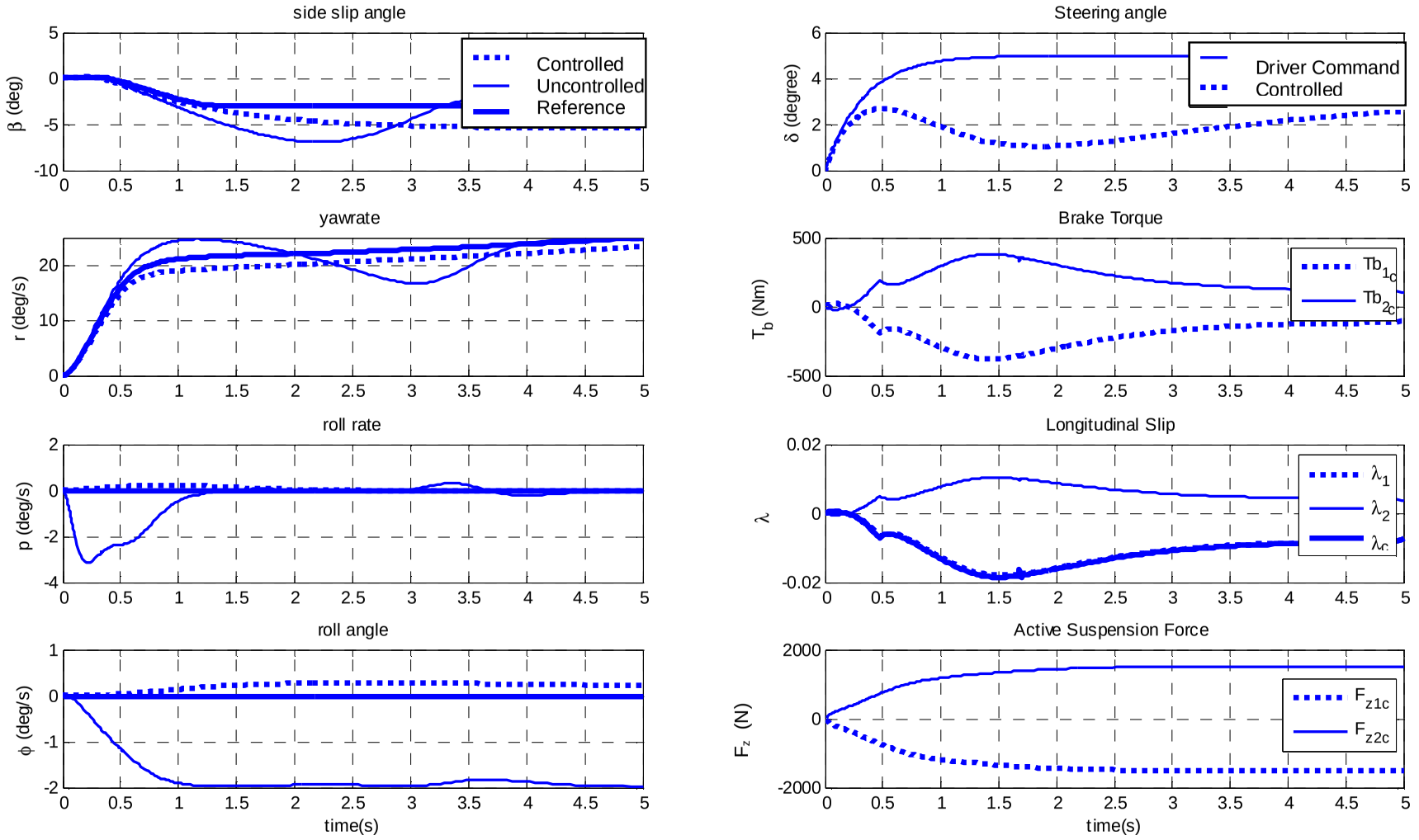


Figure 6.19. Combined steering, differential and suspension controller performance on dry road ($\mu = 0.8$) for J turn cornering maneuver

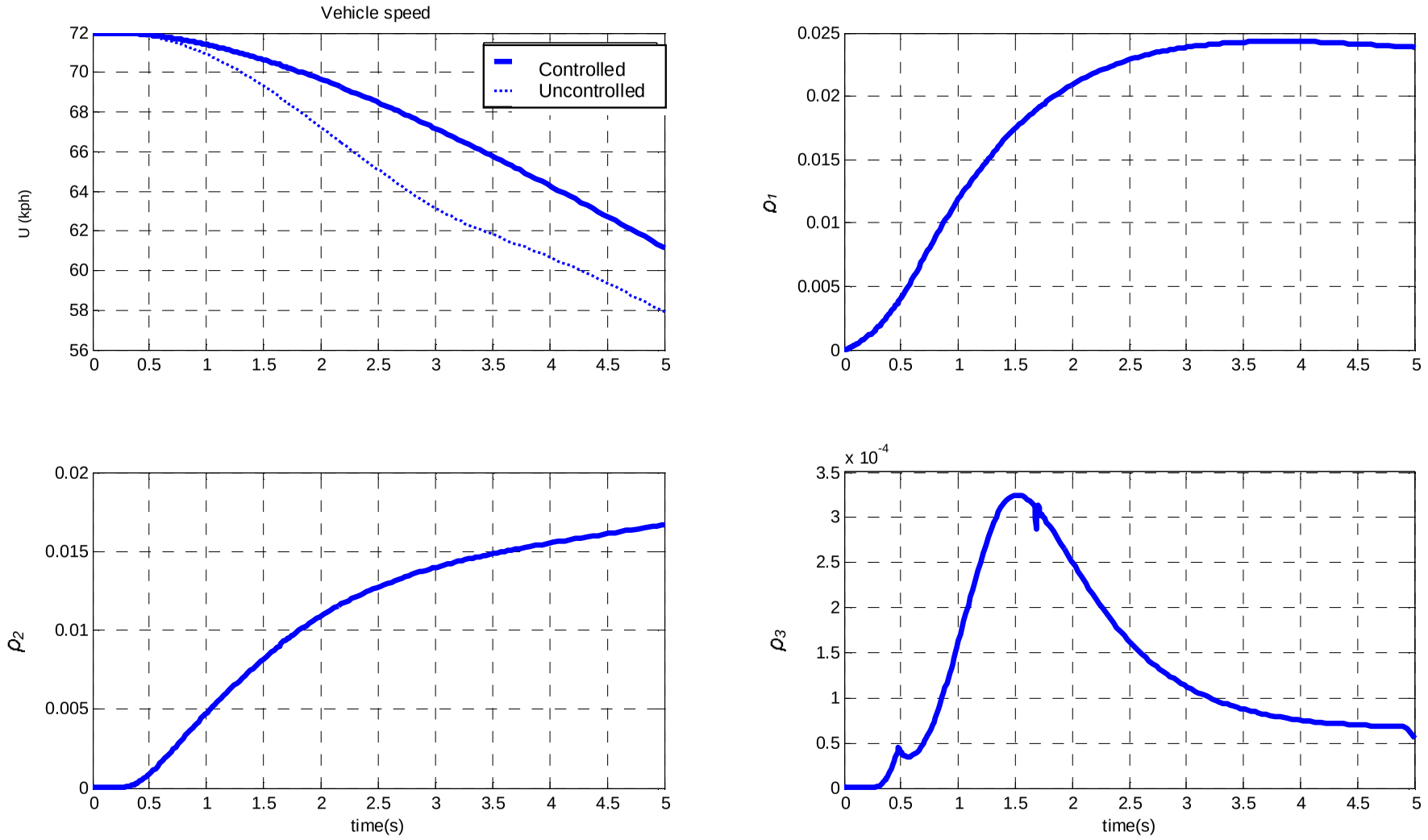


Figure 6.20. Parameter variation on dry road ($\mu = 0.8$) for J turn cornering maneuver

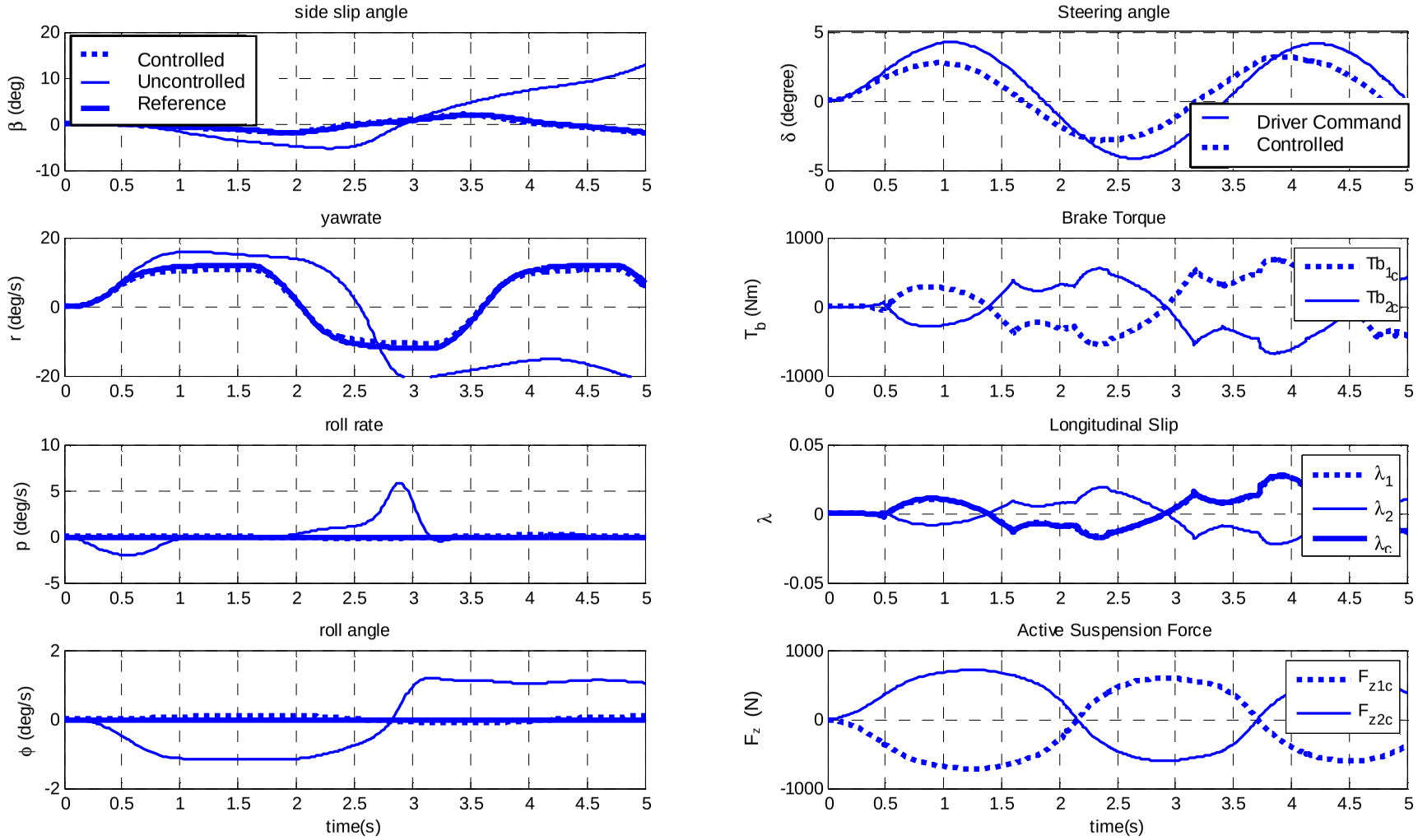


Figure 6.21. Combined steering, differential and suspension controller performance on slippery road ($\mu = 0.4$) for sinusoidal steering maneuver

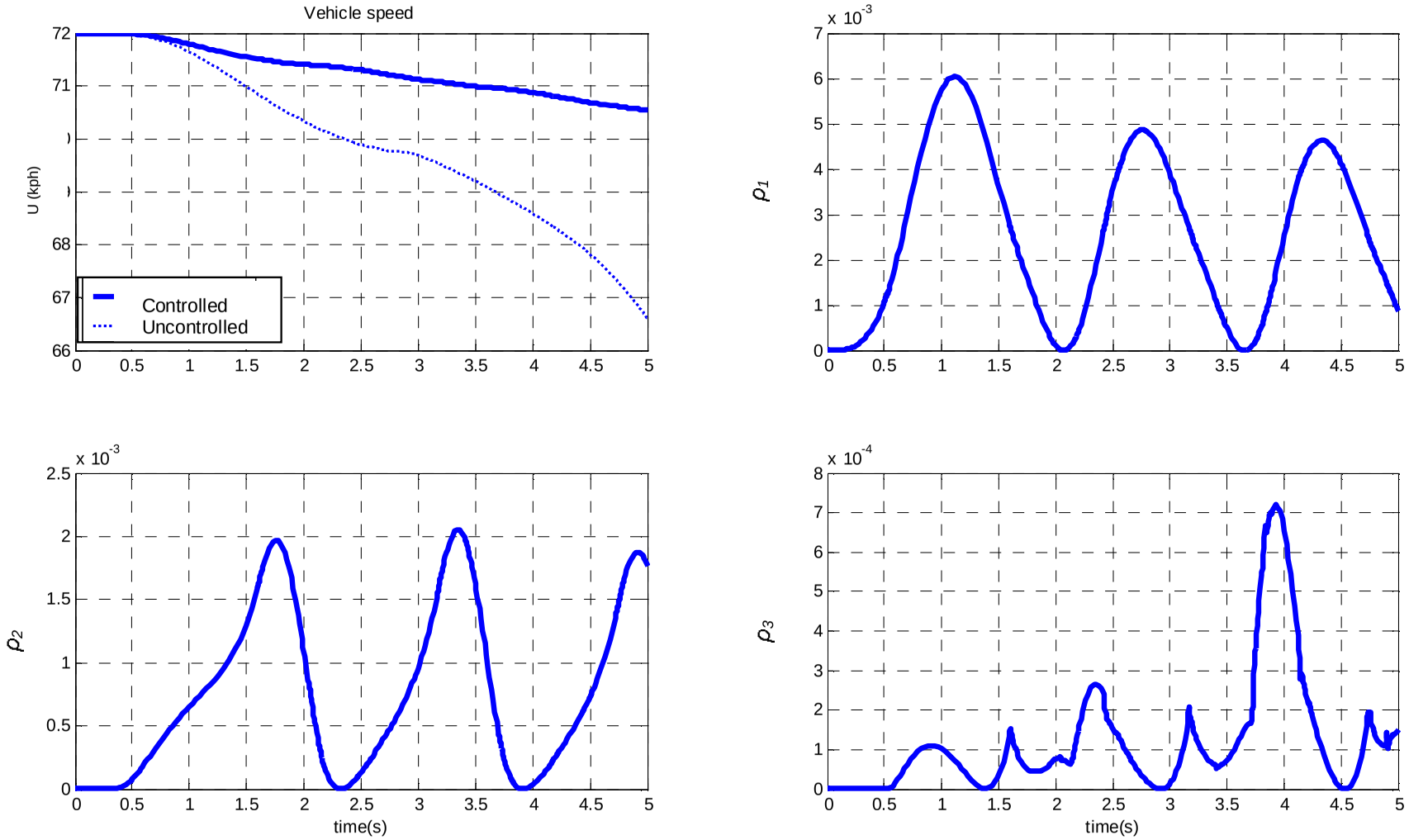


Figure 6.22. Parameter variation on slippery road ($\mu = 0.4$) for sinusoidal steering maneuver

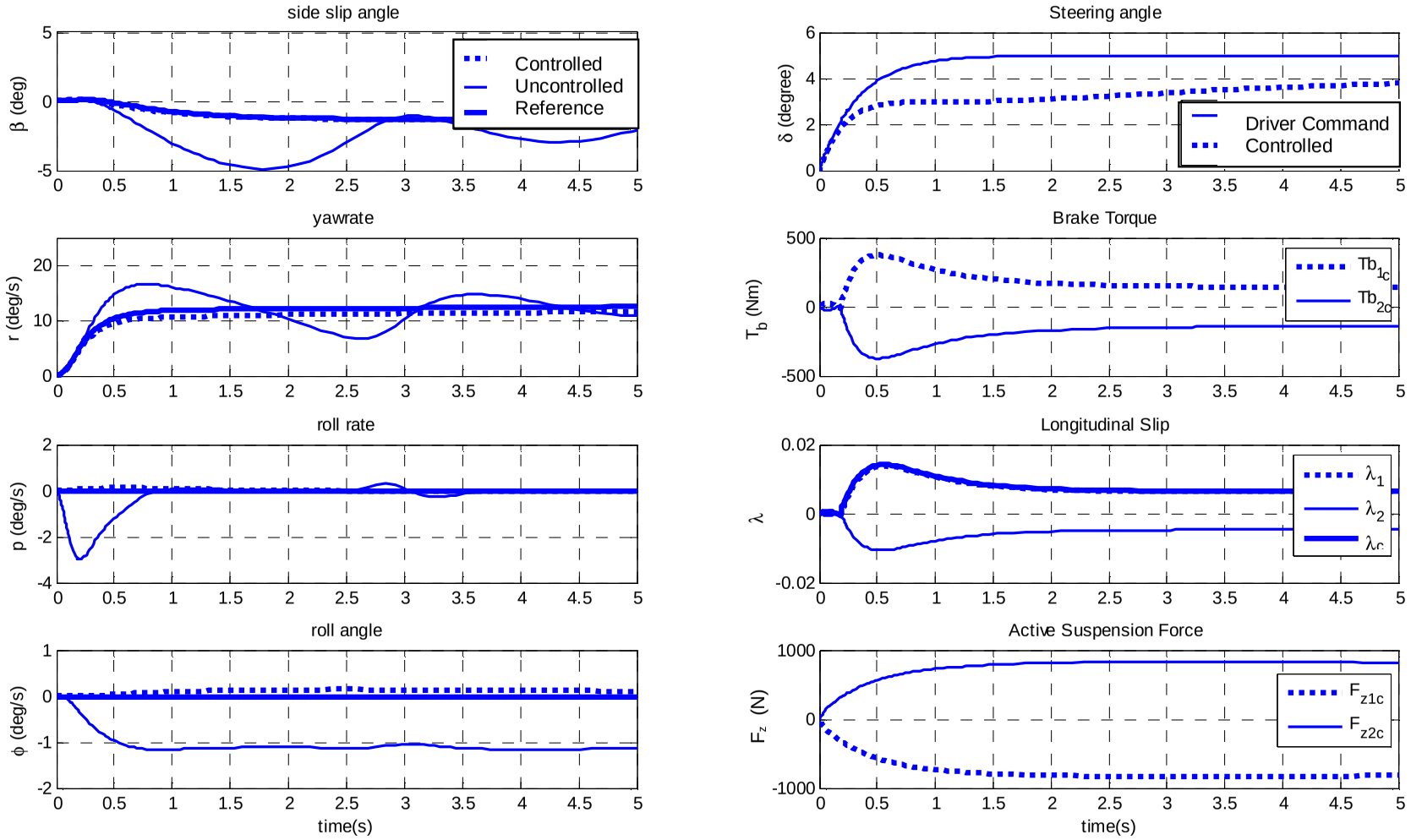


Figure 6.23. Combined steering, differential and suspension controller performance on slippery road ($\mu = 0.4$) for J turn cornering maneuver

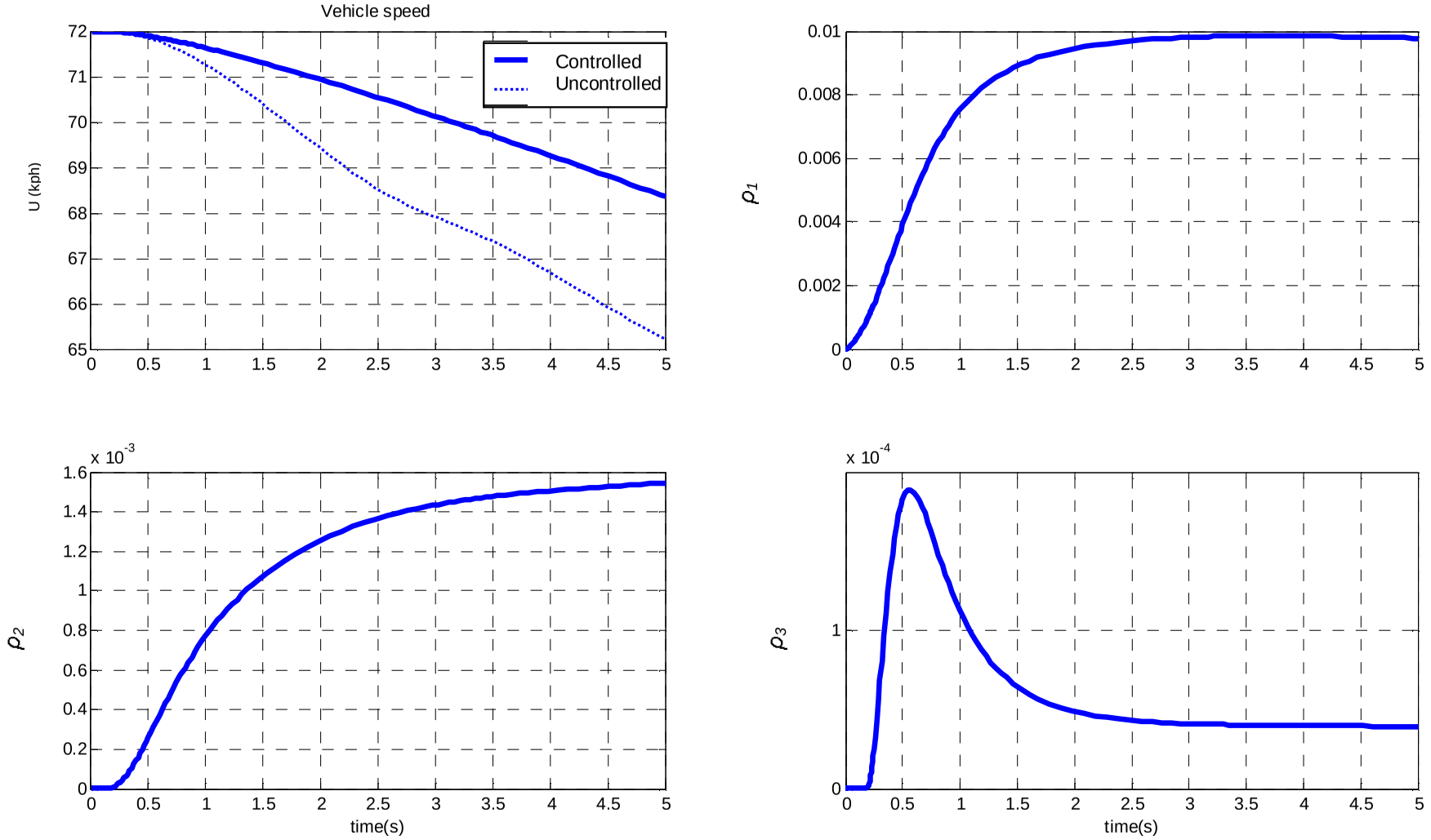


Figure 6.24. Parameter variation on slippery road ($\mu = 0.4$) for J turn cornering maneuver

6.6. Comments

Simulations have revealed the robustness of both integrated controllers under varying road conditions. The decoupling property of both integrated controllers at small driver commanded steering angle is remarkable: sideslip angle is completely eliminated and yaw rate is observed to perfectly track a given reference.

For the first controller, the action of the active steering controller has been towards increasing the driver commanded steering angle. While this has proved to improve vehicle response at small steering angles, the effect is questionable at large steering angles at the onset of tire saturation, however vehicle performance keeps to be acceptable. One would expect the active steering to reduce total steering angle in such cases. The reason of such behavior should be sought in the simplifications implemented to reduce the total number of parameters which has somewhat impaired the modeling of tire force generation characteristics during controller synthesis. Another reason is the variation of normal tire loads which hinders the performance of the active differential controller. This issue has been taken into account in the present analysis through the optimization of η and χ terms but a better approach could have consisted in including F_z terms in the parameter set.

For the second controller, the action of the active steering controller has a tendency to increase the driver commanded steering angle when it is small (relying less on active differential control) and to decrease it when it is large (relying more on active differential control). All nonlinear effects except the product of squares of scheduling terms that have again been neglected have been taken into account in this final case. Hence, the tire friction concept has been incorporated into controller synthesis in the most effective way in this last case study.

7. CONTROL AUTHORITY SHARING IN ROLLOVER PREVENTION

In this chapter, the idea of constructing a reactive steering system to warn against rollover danger is proposed as a prospective research direction. While conventional vehicle dynamics control systems interfere without the driver becoming aware of the intervention, a valuable contribution is expected to be made here by giving the driver a physical feedback concerning the rollover threat through counter-torque acting on the steering handwheel in order to make the vehicle stability limit explicit. The necessity of integrating the proposed reactive front steering as part of a global vehicle control architecture is explained.

7.1. Motivation

Reports show that about 10 % of road accidents that happen in the United States every year are results of non-collision crashes and it is a striking fact that in 90 % of this kind of accidents, rollover is involved [59]. Many different vehicle control algorithms have been implemented up to now to prevent rollover. These can be summarized as four wheel steering [60], active suspension anti-roll bars [61], [62], differential braking [3], [63] and active steering [64].

All the above-mentioned systems interfere preferably without the drivers becoming aware of the intervention. We believe that the drivers may adapt in time to the performance of the vehicle and their driving style may become more dangerous, which increases the probability of accidents. In this chapter, the control objective is to prevent the vehicle from rolling over by the aid of a control torque applied on the steering column. Hence, the idea of reactive steering is investigated in this chapter, where a valuable contribution is expected to be made by giving the driver a physical feedback concerning the rollover threat through a counter-torque acting on the steering wheel.

It is aimed to provide a preliminary study towards investigating whether a prac-

tical steering system can be built so as to prevent further turning and regulation of the steering handwheel in impending rollover situations while preserving vehicle stability by mitigating the effects of the driver's adverse reactions or whether it is necessary to consider the active systems presented previously in this thesis.

The case of a critically loaded commercial vehicle with very limited roll stability (impending rollover achieved in the linear regime of tires) is treated.

7.2. The Load Transfer Ratio (LTR)

A measure for roll stability is the load transfer ratio, which is defined as

$$LTR := \frac{F_{z,R} - F_{z,L}}{F_{z,R} + F_{z,L}}. \tag{7.1}$$

In the above formulation, $F_{z,R}$ is the total force under the right tires and $F_{z,L}$ is the total force under the left tires. It can be seen by inspection of the above formula that the critical values of LTR are 1 and -1, which is when vehicle load is supported by the tires on the same side and an impending rollover situation prevails. A linear approximation is given for the load transfer ratio in [64]: linear control theory tools can be used for controlling LTR.

7.3. Steering System Model

The design of a reactive steering controller to improve vehicle response during critical maneuvers is undertaken. Hence, accurate modeling of the steering system with all acting inputs and reactions is necessary. The steering system model presented here accepts the torque applied by the driver on the steering handwheel, the control input on the rack or the steering column and the self-aligning torque on the steering wheels as inputs and produces δ_f as output.

The steering system is analyzed in two parts: the steering column and the rack

constitute the first sub-assembly, which can be described with a simple fourth order system of differential equations. The second sub-assembly is the rack-and-pinion mechanism, a linkage that has the rack displacement as input and tire rotations as outputs. In order to accurately model rack dynamics, we must solve for the effect of the road loads on the rack. Hence, we must solve for the kinematics and dynamics of the rack-and-pinion mechanism. The study at hand is based on the following assumptions:

- The first sub-assembly is derived from the model given in Figure 7.1 and Figure 7.2. All nonlinear effects (hysteresis, coulomb friction generally taken into account in similar studies) are neglected. Viscous damping is acting on the rack to represent dissipative forces. The restoring effect of the spring acting on the rack represents the aligning effect of the suspension system. Another restoring effect is the self-aligning torque acting on the tires. It is known that suspension kinematics (toe, camber, caster, kingpin angles, caster offset, etc) play the most important role in the self-centering of the steering system. Hence, it is here assumed that this effect can be represented by a spring with a large stiffness constant.
- All the links that make up the rack-and-pinion mechanism can be taken as massless, neglecting inertia forces.

For a steering system with rack type controller, the equations of motion are given as (Figure 7.1):

$$J_c\ddot{\theta}_c + B_c\dot{\theta}_c + K_c\theta_c = \frac{K_c}{r_p}x_r + T_d + f_c(\theta_c, \dot{\theta}_c) \tag{7.2a}$$

$$M_r\ddot{x}_r + B_r\dot{x}_r + K_r x_r = \frac{K_c}{r_p}(\theta_c - \frac{x_r}{r_p}) + F_{t2} + f_r(x_r, \dot{x}_r) + u \tag{7.2b}$$

For a steering system with column type controller, the equations of motion are given

as (Figure 7.2):

$$J_c\ddot{\theta}_c + B_c\dot{\theta}_c + K_c\theta_c = \frac{K_c}{r_p}x_r + T_d + f_c(\theta_c, \dot{\theta}_c) + u \tag{7.3a}$$

$$M_r\ddot{x}_r + B_r\dot{x}_r + K_r x_r = \frac{K_c}{r_p}(\theta_c - \frac{x_r}{r_p}) + F_{t2} + f_r(x_r, \dot{x}_r) \tag{7.3b}$$

where θ_c is the steering wheel angle and x_r is the rack displacement, T_d is the driver torque on the steering handwheel, F_{t2} represents road loads on rack. One should note that these equations also contain frictional terms f_c and f_r, due to viscous damping and nonlinear coulomb friction. However, in the analysis, only linear terms are taken into account.

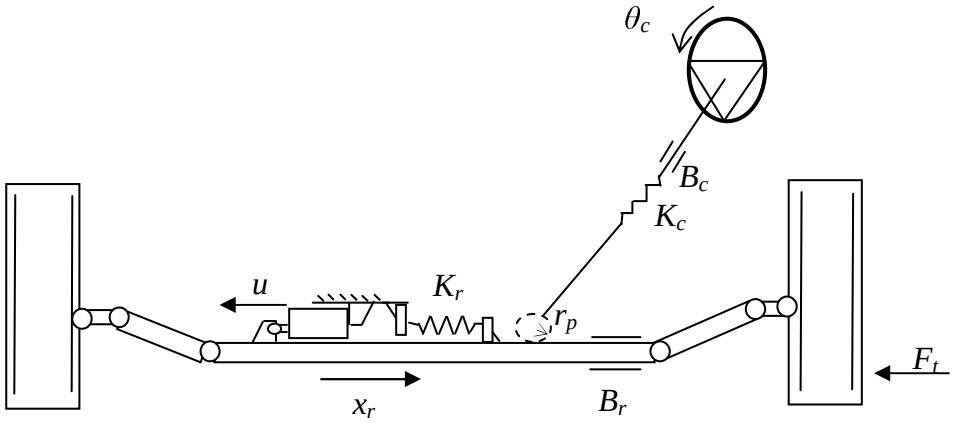


Figure 7.1. Steering system model with rack type controller

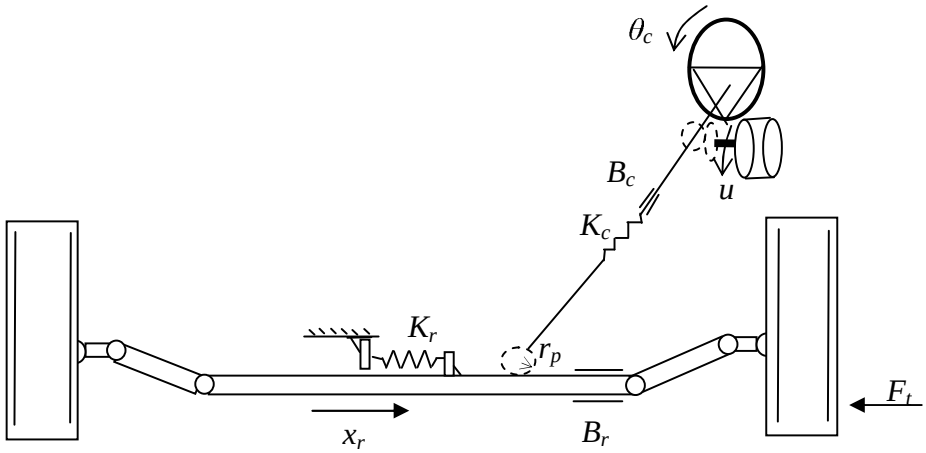


Figure 7.2. Steering system model with column type controller

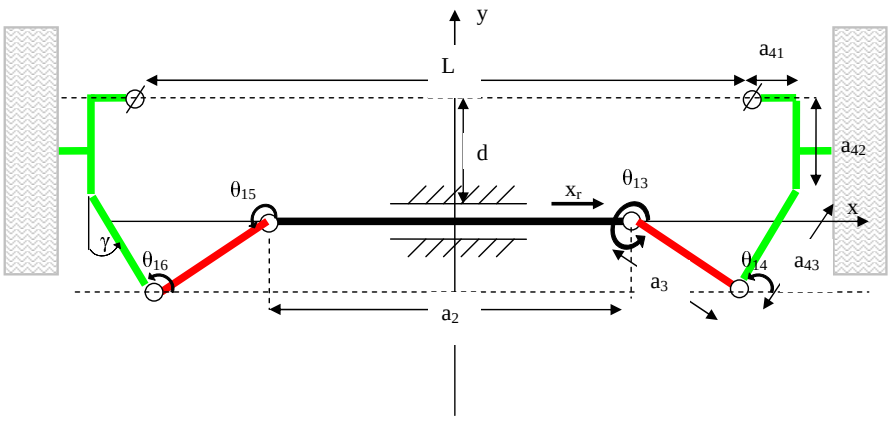


Figure 7.3. Rack-and-pinion mechanism

The part of the steering system that links the rack to the tires is now considered. The inputs to the system are the rack displacement x_r, the self aligning torques M_{zr} (acting on the right tire) and M_{zl} (acting on the left tire). It is possible after many manipulations involving solving the kinematics and the dynamics of the mechanism to express the contribution of the road load on the rack in terms of the states of the vehicle. As the self-aligning torques are functions of the tire slip angles and normal forces, which can themselves be written in terms of vehicle states, a linearized version of the road load on the rack around the undisturbed tire position can be given as

$$F_{t2} = F_{t2\beta}\beta + F_{t2r}r + F_{t2p}p + F_{t2\phi}\phi + F_{t2x_r}x_r \tag{7.4}$$

where terms like

$$F_{t2\beta} = \frac{\partial F_{t2}}{\partial \beta} \tag{7.5}$$

are appropriate partial derivatives of F_{t2}.

7.4. Automatic Vehicle Controller Model

The automatic vehicle controller (AVC) is a controller that tracks a given input steering handwheel angle θ_d. The necessity of designing an AVC arises from the re-

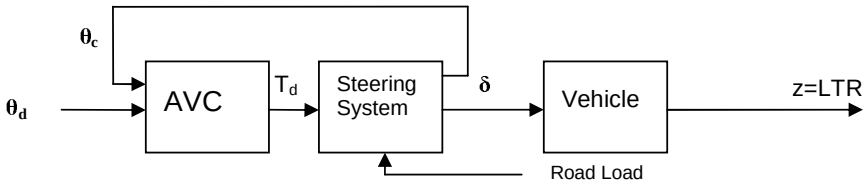


Figure 7.4. AVC activity control loop

quirement to track the critical steering maneuvers considered in a report by NHTSA [54].

The control loop in which the AVC is effective is given in Figure 7.4. The task of minimizing the error between θ_d and θ_c can be achieved by a PID controller or an H_∞ controller.

7.5. Controller Design

Let us assume that a steering controller has been added in either one of the configurations represented in Figure 7.1 or Figure 7.2. We formulate the present problem as a disturbance attenuation problem, with disturbance $w = \theta_d$, controlled output $z = LTR$, measured output $y = LTR$ and control input u as torque applied on the steering column or force applied on the rack by appropriate controllers.

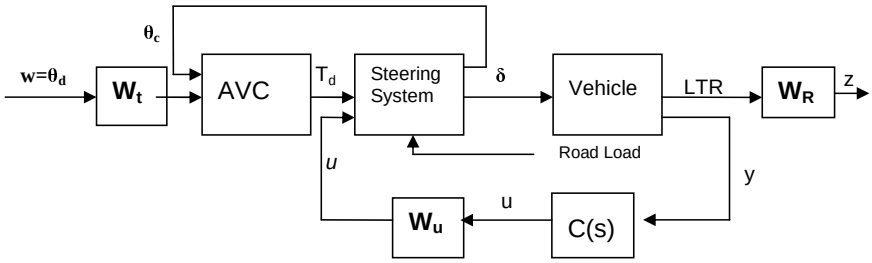


Figure 7.5. Closed loop system

The final closed loop system block diagram is given in Figure 7.5. Note that frequency weights have been added to the inputs and outputs of the system. W_t is added to filter out high frequency steering angle requirements as it is known that the steering activity has a bandwidth which is not greater than 2 Hz. W_u is added

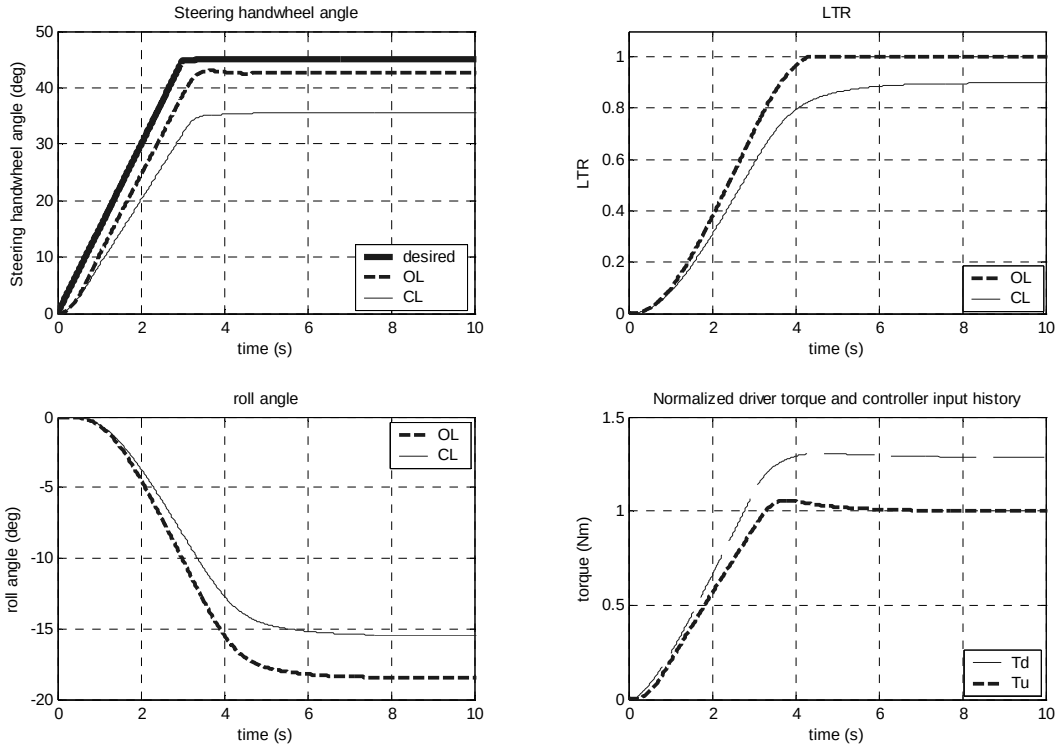


Figure 7.6. Results of preliminary simulation

to filter out high frequency controller input, somehow playing the role of a low pass steering actuator. W_R is set to penalize the controlled output. In the following section, simulation results for a ramp steering scenario is given where a controller designed using the above methodology is used.

7.6. Simulation Results

This section considers the design of a column type steering controller for rollover prevention. The vehicle driven at 60 kph is subject to a ramp steering input. The desired steering handwheel input is given in the top left part of Figure 7.6.

7.6.1. Preliminary Simulation

In a first simulation, the load transfer ratio of the uncontrolled vehicle is seen to reach the critical limit and the uncontrolled vehicle does roll over (Figure 7.6). The

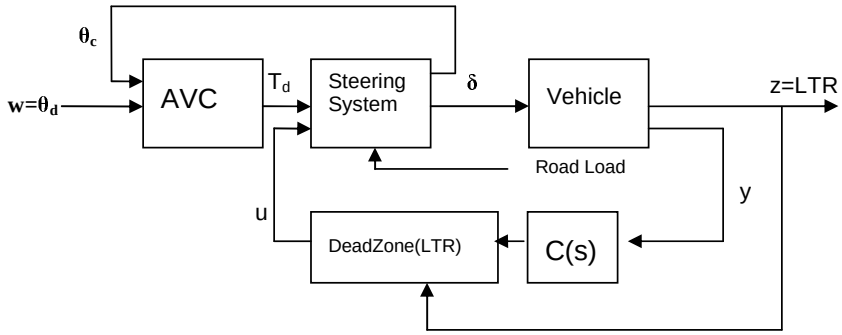


Figure 7.7. Controlled system configuration with dead-zone

controlled vehicle is stable as the steering actuator prevents the steering handwheel to be turned further than 37^o. The activity of the steering actuator can be controlled by tuning the weight W_R.

7.6.2. Supervisory Control

It is then decided to control the activity of the steering controller by a very basic supervisory controller: a dead-zone that prevents the controller to become active as long as LTR does not exceed some critical value. As it is not known how a human operator would react to such a counter-torque, we have decided to start controller activity at $LTR = 0.5$, a relatively uncritical situation. The controlled system configuration is given in Figure 7.7. The results of the second simulation are given in Figure 7.8. It was observed that by tuning W_R to make the controller act faster, the same performance could be obtained as in the configuration where supervisory control is not used. Of course, the advantage of this second control architecture is to eliminate unnecessary control activity in uncritical situations at the expense of sudden rise of control input.

Finally, we have simulated two scenarios where the driver overreacts by excessive steering inputs against the unusual controller action.

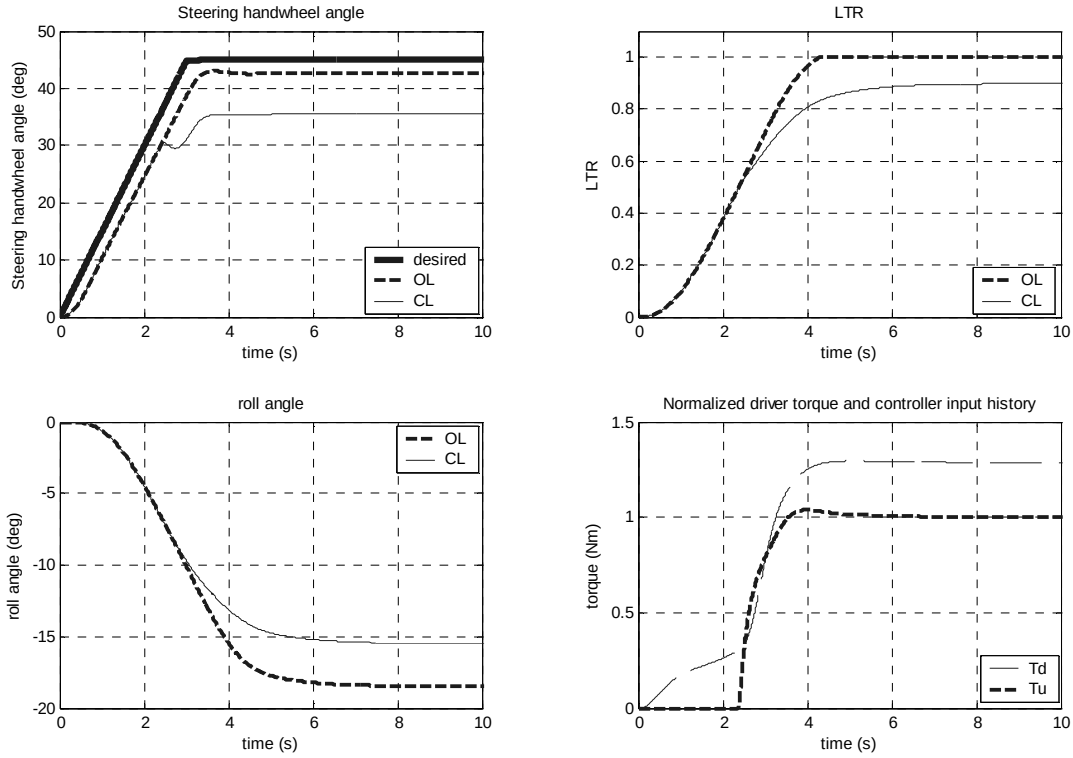


Figure 7.8. Results obtained with supervisory control

7.6.3. First Panic Scenario

In the first panic scenario, the driver tries to resist the stiffening of the steering handwheel by applying extra effort during the first two seconds of controller action. Then as the vehicle enters an impending rollover situation, the driver applies normal effort. The vehicle seems to roll very dangerously. Still, controller efficiency can be observed in Figure 7.9 as the situation seems to be much less critical than the uncontrolled case.

7.6.4. Second Panic Scenario

In the second panic scenario, the driver is surprised by the controller activity and releases the steering handwheel during the first two seconds of controller operation. Then, in order to compensate for the course deviation, the driver applies extra steering effort. Again, the vehicle seems to roll very dangerously (Figure 7.10). Still, the

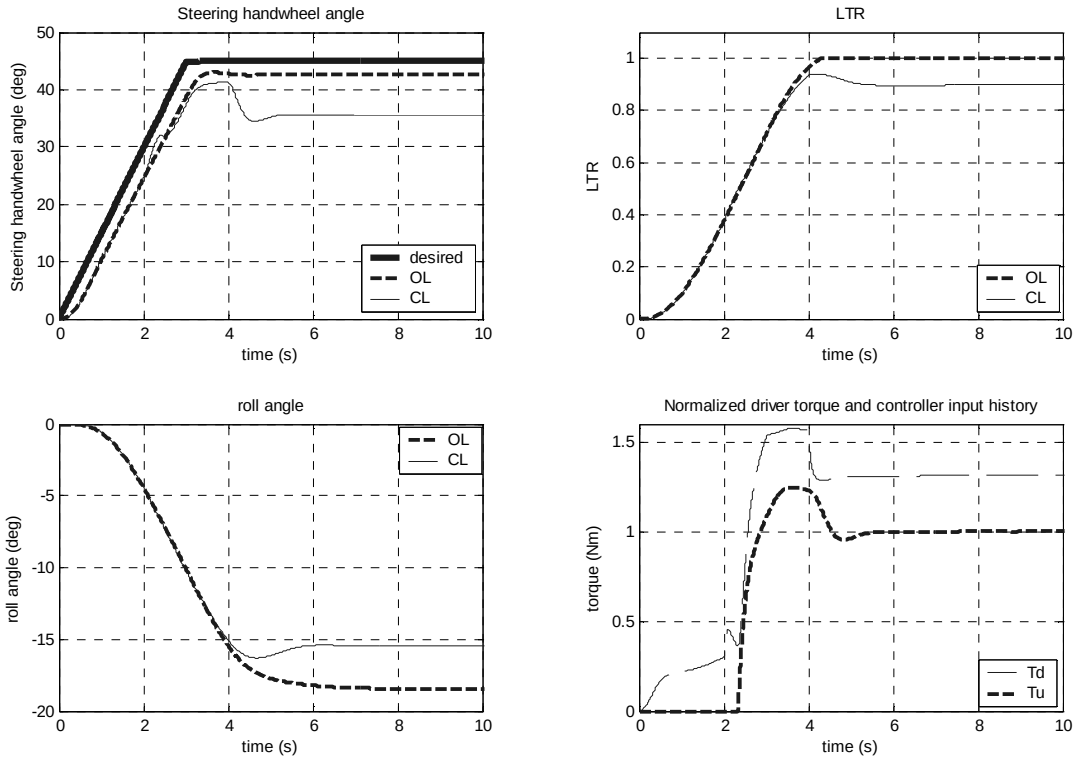


Figure 7.9. Results of first panic scenario

controller is fast in applying counter steering and again this last scenario is still safer than the uncontrolled version.

7.7. Comments

The conflict between the driver and the reactive steering controller is a serious issue to be resolved before implementation in a real application. The present design has revealed that the brute force activation of the active steering system may lead to unpredictable panic reactions of the driver. The integration of the proposed reactive system as part of the multivariable control approach presented in this thesis may achieve more ergonomic reaction of the steering system as the rollover prevention task is then handled together with other vehicle modes. Moreover, the potential application of the system aiming the coordination of driver commanded steering angle towards safer driving is dependent on an extensive preliminary research on driver modeling.

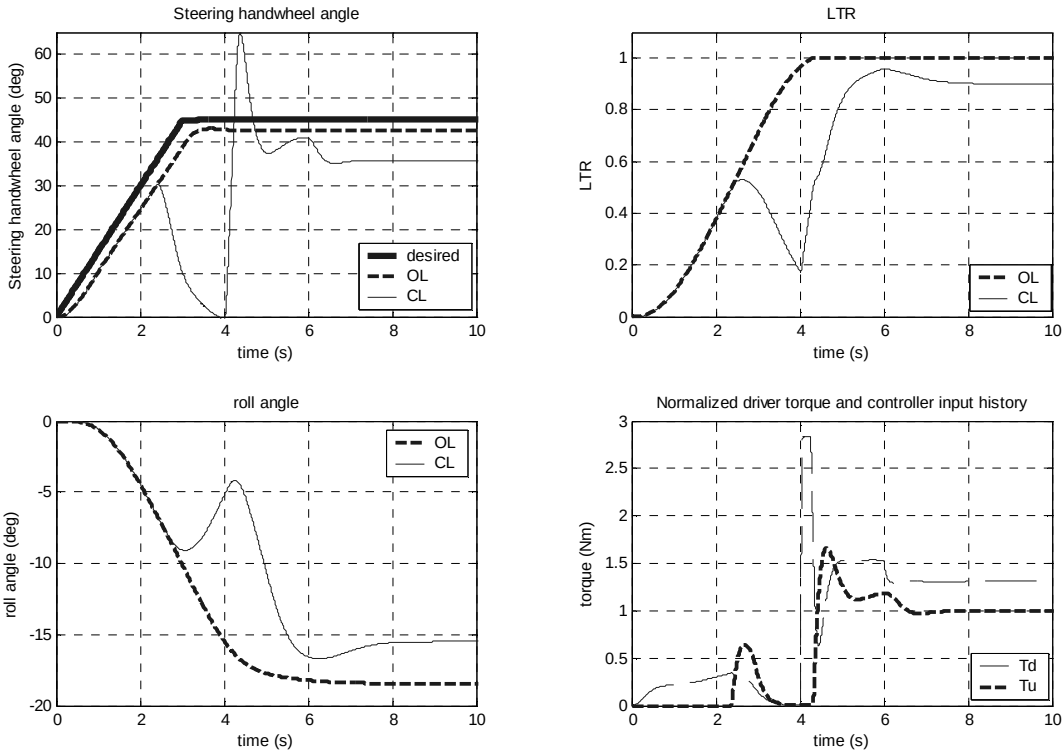


Figure 7.10. Results of second panic scenario

8. CONCLUSIONS AND RECOMMENDATIONS FOR FURTHER WORK

Modeling and control of nonlinear vehicle dynamics at large driver commanded steering angle have been investigated in this thesis. In this respect, both robust static state feedback and LPV gain scheduled controllers have been designed in the H_∞ control framework. Controller intervention in the steering channel has revealed to be a benchmark for testing the validity of the proposed LPV vehicle models and following controller synthesis. Two approaches have been undertaken to reduce the size of the parameter set to minimize solver time during the controller synthesis step.

The first approach has been based on modeling tire stiffnesses as parametric uncertainties. This has led to an LFT model of the combined vehicle body and tire subsystems. Afterwards, the design of an integrated static state feedback controller intended to be robust against large variations in parameters has been undertaken. At small driver commanded steering angle, the controller has achieved decoupling of sideslip and yaw rate modes. Nevertheless, saturating steering actuator response has been observed at the physical limit of the vehicle due to the shortcomings of the parametric uncertainty model in predicting tire behavior at large lateral slip. In the second approach, a rational fit has been proposed for the Magic Formula tire model and parametric vehicle models have been derived by integrating the fitting model into the equations of motion. This has led to the design of gain scheduled LPV integrated controllers where scheduling is based on lateral and longitudinal tire slips. These controllers have achieved decoupling of all vehicle modes for the whole range of driver commanded steering angles up to the physical limit of the vehicle.

The good performance of gain scheduled integrated controllers shows the importance of incorporating the tire friction circle concept into the controller synthesis. Indeed, the H_∞ control framework has proved to be capable of producing high performance controllers even for a system including a component as complex and uncertain

as a pneumatic tire provided that proposed LPV models adequately reflect actual nonlinear behavior in the range of operating conditions considered.

8.1. Contributions

8.1.1. LPV Modeling of Vehicle Subsystems

LPV models of economical size for vehicle body and tire subsystems have been proposed. In Chapter 5, it has been shown that the number of varying parameters can be up to 17 during VDC controller design. Current LMI solvers are unlikely to solve the optimization problem in reasonable time for such a high number of parameters. It has then been proposed to regroup some of the parameters having similar bounds together in order to reduce the total number of parameters and the efficiency of such simplification has been justified at a later step when analyzing robustness properties of designed controllers.

8.1.2. Rational Tire Modeling Formulation and Vehicle Parametric Descriptor Formulations

A rational tire model has been proposed as a simple fitting alternative for the Magic Formula with validity extending into the nonlinear tire regime. Vehicle parametric descriptor formulations derived by implementing the proposed tire model in vehicle dynamics equations have rendered the prediction of nonlinear vehicle behavior possible, based on only the knowledge of a limited set of shaping factors (η and χ). This explains the efficiency of LPV controllers whose synthesis is based on the parametric descriptor formulation.

8.1.3. Robust Anti-Lock Braking System Design

A robust control algorithm for anti-lock brake system has been proposed. The linear parameter varying modeling and ensuing controller design have proved to provide a very effective wheel slip regulation method displaying high performance on

roads with constant and varying adhesion coefficients, with nice robustness properties against large vehicle speed and road adhesion coefficient variations. But the essential contribution consists in using the proposed wheel slip regulation algorithm in realizing the braking/tractive inputs of active differential controller, which has made the gain scheduled integrated control problem more tractable.

8.1.4. Robust Integrated Vehicle Control Design

A robust control framework has been proposed for designing robust full state feedback combined active steering and differential controllers. This framework offers a systematic way for dealing with large parameter variations that occur in extreme handling situations and has been proposed in this thesis as an alternative to control allocation based designs available in the VDC literature. It has proved to be efficient for small driver commanded steering angle ensuring decoupling of sideslip and yaw rate modes but inefficient at large angles due to its shortcomings in predicting nonlinear tire behavior. Still, for the latter case, the framework provides a sound basis for designing active differential controllers.

8.1.5. Gain Scheduled Integrated Vehicle Control Design

Gain-scheduled control design results available in this thesis are based on the vehicle parametric descriptor modeling and allow a more direct incorporation of tire characteristics into controller synthesis than that provided by full state feedback control design. In fact, by considering six vehicle parameters (C_α, C_λ, η_α, η_λ, χ_α and χ_λ) instead of two (front and rear axle cornering stiffnesses) as is commonly done in the VDC literature, a prospective direction of research towards obtaining more effective VDC controllers has been revealed.

8.2. Recommendations for Further Work

8.2.1. Further Verification of Controller Robustness

Obviously, the controllers designed in this thesis have to be tested in a more intensive manner before being acceptable for application:

- Most of the simulations have been performed for an initial speed of $20\,m/s$. Further analysis can be undertaken by considering higher speeds;
- Two kinds of critical maneuvers have been considered: J turn and sinusoidal steering. Further analysis can be undertaken by considering worst case maneuvers designed specifically for the vehicle at hand;
- Steering and suspension actuator dynamics may be considered during controller synthesis;
- Estimation algorithms may be included into the control loops. This step may encompass considering a sideslip angle estimator on the one hand and an estimator for shaping factor η and χ whose values determine the efficiency of gain scheduled controllers on the other;
- Robustness of designed controllers may be tested against estimator noise.

8.2.2. Enhancement of the Performance and Robustness of the LPV Controller by Scheduling on More Parameters

In this thesis, controllers have been scheduled on three parameters at most. The reason for keeping the parameter set small has been to achieve reasonable solver time during controller synthesis. If however solver time could be somehow reduced then the size of the parameter set would be of no concern and the following interesting problems could be dealt with:

1. Scheduling on vehicle speed could be added to the controller synthesis procedure undertaken in Chapter 6. This would be particularly useful when considering vehicle handling under combined cornering and harsh braking where vehicle speed

is expected to vary substantially;

2. There would be no need to neglect the product of parameters, i.e. $\alpha_i^2\alpha_j^2$ or $\lambda_i^2\alpha_j^2$, as has been done in Chapter 6 so that one could freely assign new parameters for each of these and thereby expect to obtain even better results.

8.2.3. Consideration of Other LFT/LPV Controller Synthesis Methods

In the literature, there exist LFT/LPV controller synthesis methods which are especially suitable for LPV plants that accept an LFT dependence on the scheduling parameters [65]. They provide an attractive framework for searching a single Lyapunov function that establishes stability and performance bounds for the LPV system. They allow the design of output feedback controllers which are expressed in the LFT form. The controller uncertainty matrix is obtained as a function of the plant uncertainty matrix, which provides the basis of controller scheduling. The efficiency of these methods could be investigated and compared with the present gain-scheduled controller synthesis method. A particular point of interest again concerns the product of scheduling parameters, i.e $\alpha_i^2\alpha_j^2$ and $\lambda_i^2\alpha_j^2$. While in the present controller scheduling strategy, the only way of incorporating these parameters is through the definition of new parameters, LFT/LPV methods resolve this growth of parameter set issue by increasing the size of the uncertainty matrix and keeping the original parameters. Hence, the structure of the problem is conserved as fictitious parameters are not introduced.

8.2.4. Inclusion of a Driver Model in the Control Loops

The driver is the most critical and uncertain part of the vehicle control system and during VDC design it is tried to put the average driver and the human behavior at the center of all considerations regarding vehicle handling- *nevertheless without modeling human behavior*. While it is crucial that the driver be able to input commands to the vehicle without being interfered by active systems, benefits to be earned from tactile warning means, such as steering wheel hardening during high speed cruising have already been considered in the industry. However, this strategy still has not been developed for VDC control. Such an approach could alleviate the burden on the VDC

by guiding the driver in reacting favorably during a critical maneuver as proposed in Chapter 7 but also requires the incorporation of a realistic driver model into the control loop.

APPENDIX A: VEHICLE AND TIRE DATA

Numerical data for the vehicle considered in the study [59]:

$M_s = 1663\,kg$	$M_u = 324.935\,kg$		
$I_{xxs} = 602.8220\,kgm^2$	$I_{xzs} = 89.9914\,kgm^2$	$I_{zzs} = 2163.7\,kgm^2$	$I_{zzu} = 540\,kgm^2$
$a = 1.1473\,m$	$b = 1.4307\,m$	$c = 0.4217\,m$	$d = 1.8600\,m$
$e = 2.1566\,m$	$h_s = 0.1000\,m$	$h_\phi = 0.3060\,m$	
$\theta_R = 0.0873\,rad$	$\frac{\partial \delta_r}{\partial \phi} = 0.07$	$\frac{\partial \gamma_f}{\partial \phi} = 0.8$	
$C_{\alpha f} = 108000\,N$	$C_{\alpha r} = 98000N$	$C_{\gamma f} = 2038.8\,m$	
$k_i = 25000\,N/m$	$c_i = 1600\,Ns/m$	$k_R = 56957\,Nm$	$c_R = 3495.7\,Nms$

Numerical data for the tire considered in the study [38]:

$F_{zo} = 4000\,N$	$\varepsilon_x = 0.1$	$\varepsilon_y = 0.1$	$\mu_o = 1$
$p_{Cx1} = 1.6850$			
$p_{Dx1} = 1.2100$	$p_{Dx2} = -0.037$		
$p_{Ex1} = 0.3440$	$p_{Ex2} = 0.0935$	$p_{Ex3} = -0.02$	
$p_{Kx1} = 21.510$	$p_{Kx2} = -0.163$	$p_{Kx3} = 0.245$	
$p_{Hx1} = -0.002$	$p_{Hx2} = 0.0020$		
$p_{Vx1} = 0.0000$	$p_{Vx2} = 0.0000$		
$p_{Cy1} = 1.193$			
$p_{Dy1} = -0.9900$	$p_{Dy2} = 0.145$	$p_{Dy3} = -11.23$	
$p_{Ey1} = -1.0000$	$p_{Ey2} = -0.537$	$p_{Ey3} = -0.083$	$p_{Ey4} = -4.787$
$p_{Ky1} = -14.95$	$p_{Ky2} = 2.130$	$p_{Ky3} = -.028$	

$p_{Hy1} = 0.003$	$p_{Hy2} = -0.001$	$p_{Hy3} = 0.075$	
$p_{Vy1} = 0.045$	$p_{Vy2} = -0.024$	$p_{Vy3} = -0.532$	$p_{Vy4} = 0.039$
$r_{By1} = 6.461$	$r_{By2} = 4.196$	$r_{By3} = -0.015$	
$r_{Cy1} = 1.081$			
$r_{Hy1} = 0.009$			
$r_{Vy1} = 0.053$	$r_{Vy2} = -0.073$	$r_{Vy3} = 0.517$	
$r_{Vy4} = 35.44$	$r_{Vy5} = 1.9$	$r_{Vy6} = -10.71$	
$\kappa_{Cx} = 1.0000$	$\kappa_{Ex} = 1.0000$	$\kappa_{Vx} = 1.0000$	$\kappa_{Kx\lambda} = 1.0000$

$\kappa_{\mu x}$ is taken to be equal to μ_{max}. $\kappa'_{\mu x}$ is calculated from $\kappa'_{\mu x} = \frac{10\kappa_{\mu x}}{1+9\kappa_{\mu x}}$.

APPENDIX B: LPV MATRICES FOR ROBUST COMBINED ACTIVE STEERING AND ACTIVE DIFFERENTIAL CONTROL DESIGN

The LPV system representation may be decomposed, momentarily ignoring the control input (which will be added later on the system representation by just inverting the sign of matrices describing the disturbance coupling) as

$$\dot{x} = \left(A_0 + CA_1 + \frac{C}{v}A_3 + \frac{C}{v^2}A_5 + \frac{\rho}{v}A_{15}\right)x + \left(CB_1 + \frac{C}{v}B_2 + \frac{1}{v}B_3\right)w,$$

where

$$A_0 := \begin{pmatrix} -1 \\ 0 \\ 0 \\ 0 \\ 0 \\ 0 \end{pmatrix} \begin{pmatrix} 0 & 1 & 0 & 0 & 0 & 0 \end{pmatrix} =: A_0^L A_0^R,$$

$$A_1 := \begin{pmatrix} 0 \\ 1 \\ 0 \\ 0 \\ 0 \\ 0 \end{pmatrix} \begin{pmatrix} -2\frac{a+b}{J_z} & 0 & -\frac{d}{2J_z} & \frac{d}{2J_z} & -\frac{d}{2J_z} & \frac{d}{2J_z} \end{pmatrix} =: A_1^L A_1^R$$

$$A_3 := \begin{pmatrix} -\frac{4}{m} & 0 & 0 & 0 & 0 & 0 \\ 0 & -2\frac{a^2+b^2}{J_z} & 0 & 0 & 0 & 0 \\ 0 & 0 & -\frac{R_w^2}{J_w} & 0 & 0 & 0 \\ 0 & 0 & 0 & -\frac{R_w^2}{J_w} & 0 & 0 \\ 0 & 0 & 0 & 0 & -\frac{R_w^2}{J_w} & 0 \\ 0 & 0 & 0 & 0 & 0 & -\frac{R_w^2}{J_w} \end{pmatrix} = A_3 I_6 =: A_3^L A_3^R$$

$$A_5 := \begin{pmatrix} 2\frac{-a+b}{m} \\ 0 \\ 0 \\ 0 \\ 0 \\ 0 \end{pmatrix} \begin{pmatrix} 0 & 1 & 0 & 0 & 0 & 0 \end{pmatrix} =: A_5^L A_5^R,$$

$$A_{15} := \begin{pmatrix} 0 & 0 & 0 & 0 \\ 0 & 0 & 0 & 0 \\ 1 & 0 & 0 & 0 \\ 0 & 1 & 0 & 0 \\ 0 & 0 & 1 & 0 \\ 0 & 0 & 0 & 1 \end{pmatrix} \begin{pmatrix} 0 & 0 & 1 & 0 & 0 & 0 \\ 0 & 0 & 0 & 1 & 0 & 0 \\ 0 & 0 & 0 & 0 & 1 & 0 \\ 0 & 0 & 0 & 0 & 0 & 1 \end{pmatrix} =: A_{15}^L A_{15}^R$$

$$B_1 := \begin{pmatrix} 0 \\ 2\frac{a}{J_z} \\ 0 \\ 0 \\ 0 \\ 0 \end{pmatrix} \begin{pmatrix} 1 & 0 & 0 & 0 & 0 \end{pmatrix} =: B_1^L B_1^R,$$

$$B_2 := \begin{pmatrix} \frac{1}{m} \\ 0 \\ 0 \\ 0 \\ 0 \\ 0 \end{pmatrix} \begin{pmatrix} 1 & 0 & 0 & 0 & 0 \end{pmatrix} =: B_2^L B_2^R$$

$$B_3 := \begin{pmatrix} 0 & 0 & 0 & 0 \\ 0 & 0 & 0 & 0 \\ \frac{R_w}{J_w} & 0 & 0 & 0 \\ 0 & \frac{R_w}{J_w} & 0 & 0 \\ 0 & 0 & \frac{R_w}{J_w} & 0 \\ 0 & 0 & 0 & \frac{R_w}{J_w} \end{pmatrix} \begin{pmatrix} 0 & 1 & 0 & 0 & 0 \\ 0 & 0 & 1 & 0 & 0 \\ 0 & 0 & 0 & 1 & 0 \\ 0 & 0 & 0 & 0 & 1 \end{pmatrix} =: B_3^L B_3^R$$

Now we assume that C, v and ρ vary around selected nominal values of C_o, v_o and ρ_o as $C = C_o + \delta_C$, $v = v_o + \delta_v$ and $\rho = \rho_o + \delta_\rho$. Then, we use

- $\tilde{p}_1 := (C_o + \delta_C)(A_1 x + B_1 \delta) = C_o A_1 x + C_o B_1 \delta + A_1^L p_{10} + B_1^L p_{11}$, where

$$p_{10} := \delta C q_{10}, \quad q_{10} := A_1^R x, \quad p_{11} := \delta C q_{11}, q_{11} := B_1^R \delta,$$

- $\tilde{p}_3 := \dfrac{(C_o + \delta_C)}{v_o + \delta_v}(A_3 x + B_2 \delta) = \dfrac{C_o A_3 x}{v_0} + \dfrac{C_o B_2 \delta}{v_o} + C_o p_{30} + A_3^L p_{33} + B_2^L p_{34}$, where

$$\begin{aligned}
p_{30} &:= \delta_v q_{30} & q_{30} &:= -\tfrac{A_3}{v_o^2} x - \tfrac{B_2}{v_o^2}\delta - \tfrac{1}{v_o} p_{30} \\
p_{31} &:= \delta_v q_{31} & q_{31} &:= -\tfrac{A_3^R}{v_o^2} x - \tfrac{1}{v_o} p_{31} \\
p_{32} &:= \delta_v q_{32} & q_{32} &:= -\tfrac{B_2^R}{v_o^2}\delta - \tfrac{1}{v_o} p_{32} \\
p_{33} &:= \delta_C q_{33} & q_{33} &:= \tfrac{A_3^R}{v_o} x + p_{31} \\
p_{34} &:= \delta_C q_{34} & q_{34} &:= \tfrac{B_2^R}{v_o}\delta + p_{32}
\end{aligned}$$

- $\tilde{p}_5 = \dfrac{(C_o + \delta_C)}{(v_o + \delta_v)^2} A_5 x = \dfrac{C_o A_5 x}{v_o^2} + \dfrac{C_o}{v_0} p_{50} + \dfrac{A_5^L}{v_o} p_{52} + p_{53} + p_{54} + p_{55}$, where

$$\begin{aligned}
p_{50} &:= \delta_v q_{50} & q_{50} &:= -\tfrac{A_5}{v_o^2} x - \tfrac{1}{v_o} p_{50} \\
p_{51} &:= \delta_v q_{51} & q_{51} &:= -\tfrac{A_5^R}{v_o^2} x - \tfrac{1}{v_o} p_{51} \\
p_{52} &:= \delta_C q_{52} & q_{52} &:= \tfrac{A_5^R}{v_o} x + p_{51} \\
p_{53} &:= \delta_v q_{53} & q_{53} &:= -C_o \tfrac{A_5}{v_o^3} x - \tfrac{1}{v_o} p_{53} \\
p_{54} &:= \delta_v q_{54} & q_{54} &:= -\tfrac{C_o}{v_o^2} p_{50} - \tfrac{1}{v_o} p_{54} \\
p_{55} &:= \delta_v q_{55} & q_{55} &:= -\tfrac{A_5^L}{v_o^2} p_{52} - \tfrac{1}{v_o} p_{55}
\end{aligned}$$

- $\tilde{p}_{15} = \dfrac{\rho_o + \delta_\rho}{v_o + \delta_v} A_{15} x = \dfrac{\rho_o A_{15} x}{v_o} + \rho_o p_{150} + A_{15}^L p_{152}$, where

$$\begin{aligned}
p_{150} &:= \delta_v q_{150} & q_{150} &:= -\tfrac{A_{15}}{v_o^2} x - \tfrac{1}{v_o} p_{150} \\
p_{151} &:= \delta_v q_{151} & q_{151} &:= -\tfrac{A_{15}^R}{v_o^2} x - \tfrac{1}{v_o} p_{151} \\
p_{152} &:= \delta_\rho q_{152} & q_{152} &:= \tfrac{A_{15}^R}{v_o} x + p_{151}
\end{aligned}$$

- $\tilde{p}_{19} = \dfrac{B_3}{v_o + \delta_v} u = \dfrac{B_3^R}{v_o} u + B_3^L p_{190}$, where

$$p_{190} := \delta_v q_{190}, \quad q_{190} := -\tfrac{1}{v_o^2} B_3^R u - \tfrac{1}{v_o} p_{190}.$$

To sum up, with $\boldsymbol{p}$ and $\boldsymbol{q}$ vectors defined as

$$\begin{aligned} p := \Big(& p_{30}^T \quad p_{31}^T \quad p_{32}^T \quad p_{50}^T \quad p_{51}^T \quad p_{53}^T \quad p_{54}^T \quad p_{55}^T \\ & p_{150}^T \quad p_{151}^T \quad p_{190}^T \quad p_{10}^T \quad p_{11}^T \quad p_{33}^T \quad p_{34}^T \quad p_{52}^T \quad p_{152}^T \Big)^T \\ q := \Big(& q_{30}^T \quad q_{31}^T \quad q_{32}^T \quad q_{50}^T \quad q_{51}^T \quad q_{53}^T \quad q_{54}^T \quad q_{55}^T \\ & q_{150}^T \quad q_{151}^T \quad q_{190}^T \quad q_{10}^T \quad q_{11}^T \quad q_{33}^T \quad q_{34}^T \quad q_{52}^T \quad q_{152}^T \Big)^T, \end{aligned}$$

where

$$A := A_o + C_o A_1 + \frac{C_o}{v_o} A_3 + \frac{C_o A_5}{v_o^2} + \frac{p_o}{v_o} A_{15}, \quad B_w := C_o B_1 + \frac{C_o B_2}{v_o} + \frac{B_3}{v_o},$$

$$B_p := \begin{pmatrix} B_{p_v} & B_{p_C} & B_{p_\rho} \end{pmatrix}$$

where

$$B_{p_v} := \begin{pmatrix} C_o I_6 & 0_{6\times 6} & 0_{6\times 1} & \frac{C_o}{v_o} I_6 & 0_{6\times 1} & I_6 & I_6 & I_6 & p_o I_6 & 0_{6\times 4} & B_3^L \end{pmatrix},$$

$$B_{p_C} := \begin{pmatrix} A_1^L & B_1^L & A_3^L & B_2^L & \frac{A_5^L}{v_o} \end{pmatrix}, B_{p_\rho} := A_{15}^L$$

$$C_q := \begin{pmatrix} -\frac{A_3^T}{v_o^2} & -\frac{(A_3^R)^T}{v_o^2} & 0_{6\times 1} & -\frac{A_5^T}{v_o^2} & -\frac{(A_5^R)^T}{v_o^2} & -C_o \frac{A_5^T}{v_o^3} & 0_{6\times 6} & 0_{6\times 6} \\ -\frac{A_{15}^T}{v_o^2} & -\frac{(A_{15}^R)^T}{v_o^2} & 0_{6\times 6} & (A_1^R)^T & 0_{6\times 1} & \frac{(A_3^R)^T}{v_o} & 0_{6\times 1} & \frac{(A_5^R)^T}{v_o} & \frac{(A_{15}^R)^T}{v_o} \end{pmatrix}^T.$$

D_{qw} is a 66×5 matrix with the following entries (entries not mentioned being 0):

$$D_{qw}(1:6,:) := -\frac{B_2}{v_o^2}, \; D_{qw}(13,:) := -\frac{B_2^R}{v_o^2}, \; D_{qw}(49:52,:) := -\frac{B_3^R}{v_o^2}, \; D_{qw}(54,:) := B_1^R,$$

$$D_{qw}(61,:) := \frac{B_2^R}{v_o}.$$

D_{qp} is a 66×66 matrix with the following entries (entries not mentioned being 0):

$$\begin{array}{ll}
D_{qp}(1:6,1:6) := -\frac{1}{v_o} I_6 & D_{qp}(7:12,7:12) := -\frac{1}{v_o} I_6 \\
D_{qp}(13,13) := -\frac{1}{v_o} & D_{qp}(14:19,14:19) := -\frac{1}{v_o} I_6 \\
D_{qp}(20,20) := -\frac{1}{v_o} & D_{qp}(21:26,21:26) := -\frac{1}{v_o} I_6 \\
D_{qp}(27:32,27:32) := -\frac{1}{v_o} I_6 & D_{qp}(33:38,33:38) := -\frac{1}{v_o} I_6 \\
D_{qp}(39:44,39:44) := -\frac{1}{v_o} I_6 & D_{qp}(45:48,45:48) := -\frac{1}{v_o} I_4 \\
D_{qp}(49:50,49:50) := -\frac{1}{v_o} I_2 & D_{qp}(27:32,14:19) := -\frac{C_o}{v_o^2} I_6 \\
D_{qp}(33:38,62) := -\frac{A_5^L}{v_o^2} & D_{qp}(55:60,7:12) := I_6 \\
D_{qp}(61,13) := 1 & D_{qp}(62,20) := 1 \\
D_{qp}(63:66,45:48) := I_4 &
\end{array}$$

Finally, $\Delta := \mathbf{diag}(\delta_v I_{52}, \delta_C I_{10}, \delta_\rho I_4)$.

The augmented LPV representation with generalized plant $\breve{G}$ and augmented state $\breve{x} = \begin{pmatrix} x^T & x_r^T & x_d^T & x_e^T \end{pmatrix}^T$ with $x = \begin{pmatrix} \beta & r & \lambda_1 & \lambda_2 & \lambda_3 & \lambda_4 \end{pmatrix}^T$ is then given as

$$\breve{A} = \begin{pmatrix} A & 0 & B_w C_d & 0 \\ 0 & A_r & 0 & 0 \\ 0 & 0 & A_d & 0 \\ B_e C_y & -B_e C_r & 0 & A_e \end{pmatrix}, \qquad \breve{B}_p = \begin{pmatrix} B_p^T & 0 & 0 & 0 \end{pmatrix}^T,$$

$$\breve{B}_w = \begin{pmatrix} B_w C_d & 0 \\ 0 & B_r \\ B_d & 0 \\ 0 & -B_e D_r \end{pmatrix}, \qquad \breve{B}_u = \begin{pmatrix} B_u^T & 0 & 0 & 0 \end{pmatrix}^T,$$

$$\breve{C}_q = \begin{pmatrix} C_q & 0 & D_{qw} C_d & 0 \end{pmatrix}, \qquad \breve{D}_{qp} = D_{qp},$$

$$\breve{D}_{qw} = \begin{pmatrix} D_{qw} & 0 \end{pmatrix}, \qquad \breve{D}_{qu} = D_{qu} = -\breve{D}_{qw},$$

$$\breve{C}_z = \begin{pmatrix} D_e C_y & -D_e C_r & 0 & C_e \end{pmatrix}, \qquad \breve{D}_{zp} = 0,$$

$$\breve{D}_{zw} = \begin{pmatrix} 0 & -D_e D_r \end{pmatrix}, \qquad \breve{D}_{zu} = 0.$$

Note that $\breve{D}_{yp}$ is a zero matrix of compatible dimensions and that Δ remains unchanged. C_y is constructed according to the states to be controlled, i.e, if all states are to be regulated then $C_y = I_6$, whereas if only β and r are to be regulated then $C_y = \begin{bmatrix} I_2 & 0_{2\times 6} \end{bmatrix}$.

APPENDIX C: PARAMETRIC DESCRIPTOR REPRESENTATION OF BICYCLE AND YAW-ROLL MODELS FOR GAIN-SCHEDULED CONTROL DESIGN

When put into the parametric descriptor form, the following system matrices are obtained for the parametric models:

$$\boldsymbol{E}(\boldsymbol{\rho}) = \boldsymbol{E_0} + \rho_1 \boldsymbol{E_1} + \rho_2 \boldsymbol{E_2} + \rho_3 \boldsymbol{E_3} \tag{C.1a}$$

$$\boldsymbol{A}(\boldsymbol{\rho}) = \boldsymbol{A_0} + \rho_1 \boldsymbol{A_1} + \rho_2 \boldsymbol{A_2} + \rho_3 \boldsymbol{A_3} \tag{C.1b}$$

$$\boldsymbol{B_w}(\boldsymbol{\rho}) = \boldsymbol{B_{w0}} + \rho_1 \boldsymbol{B_{w1}} + \rho_2 \boldsymbol{B_{w2}} + \rho_3 \boldsymbol{B_{w3}} \tag{C.1c}$$

$$\boldsymbol{B_u}(\boldsymbol{\rho}) = \boldsymbol{B_{u0}} + \rho_1 \boldsymbol{B_{u1}} + \rho_2 \boldsymbol{B_{u2}} + \rho_3 \boldsymbol{B_{u3}} \tag{C.1d}$$

Here, $\rho_1 = {\alpha_f}^2$, $\rho_2 = {\alpha_r}^2$ and $\rho_3 = {\lambda_c}^2$ naturally appear as scheduling parameters.

Matrices that appear in the parametric descriptor form of the bicycle model admit the following definitions:

$$\boldsymbol{E_0} := I_2, \boldsymbol{E_1} := \mathbf{diag}(\eta_\alpha, \epsilon_\alpha), \boldsymbol{E_2} := \mathbf{diag}(\eta_\alpha, \epsilon_\alpha), \boldsymbol{E_3} := \mathbf{diag}(\eta_\lambda, \epsilon_\lambda) \tag{C.2a}$$

$$\boldsymbol{A_0} := \begin{pmatrix} -\frac{C_{\alpha f}+C_{\alpha r}}{MU} & -1+\frac{-aC_{\alpha f}+bC_{\alpha r}}{MU^2} \\ \frac{-aC_{\alpha f}+bC_{\alpha r}}{J_z} & -\frac{a^2C_{\alpha f}+b^2C_{\alpha r}}{J_zU} \end{pmatrix} \tag{C.2b}$$

$$\boldsymbol{A_1} := \begin{pmatrix} -\frac{C_{\alpha r}\eta_\alpha}{MU} & \eta_\alpha\left(-1+\frac{bC_{\alpha r}}{MU^2}\right) \\ \frac{-aC_{\alpha f}\chi_\alpha+bC_{\alpha r}\epsilon_\alpha}{J_z} & -\frac{a^2C_{\alpha f}\chi_\alpha+b^2C_{\alpha r}\epsilon_\alpha}{J_zU} \end{pmatrix} \tag{C.2c}$$

$$\boldsymbol{A_2} := \begin{pmatrix} -\frac{C_{\alpha f}\eta_\alpha}{MU} & \eta_\alpha\left(-1+\frac{aC_{\alpha f}}{MU^2}\right) \\ \frac{-aC_{\alpha f}\epsilon_\alpha+bC_{\alpha r}\chi_\alpha}{J_z} & -\frac{a^2C_{\alpha f}\epsilon_\alpha+b^2C_{\alpha r}\chi_\alpha}{J_zU} \end{pmatrix} \tag{C.2d}$$

$$\boldsymbol{A_3} := \begin{pmatrix} -\frac{C_{\alpha r}\eta_\lambda}{MU} & \eta_\lambda\left(-1+\frac{bC_{\alpha r}}{MU^2}\right) \\ \frac{-aC_{\alpha f}\chi_\lambda+bC_{\alpha r}\epsilon_\lambda}{J_z} & -\frac{a^2C_{\alpha f}\chi_\lambda+b^2C_{\alpha r}\epsilon_\lambda}{J_zU} \end{pmatrix} \tag{C.2e}$$

$$\boldsymbol{B_{w0}} := \eta_\alpha \begin{pmatrix} \frac{C_{\alpha f}}{MU} \\ \frac{aC_{\alpha f}}{J_z} \end{pmatrix}, \boldsymbol{B_{w1}} := \begin{pmatrix} 0 \\ \frac{aC_{\alpha f}\chi_\alpha}{J_z} \end{pmatrix} \tag{C.2f}$$

$$\boldsymbol{B_{w2}} := \begin{pmatrix} \frac{C_{\alpha f}\eta_\alpha}{MU} \\ \frac{aC_{\alpha f}\epsilon_\alpha}{J_z} \end{pmatrix}, \boldsymbol{B_{w3}} := \begin{pmatrix} 0 \\ \frac{aC_{\alpha f}\chi_\lambda}{J_z} \end{pmatrix} \tag{C.2g}$$

$$\boldsymbol{B_{u0}} := \begin{pmatrix} -\frac{C_{\alpha f}}{MU} & 0 \\ \frac{-aC_{\alpha f}}{J_z} & -\frac{dC_{\lambda f}}{2J_z} \end{pmatrix}, \boldsymbol{B_{u1}} := \begin{pmatrix} 0 & 0 \\ \frac{-aC_{\alpha f}\chi_\alpha}{J_z} & -\frac{dC_{\lambda f}\eta_\alpha}{2J_z} \end{pmatrix} \tag{C.2h}$$

$$\boldsymbol{B_{u2}} := \begin{pmatrix} -\frac{C_{\alpha f}\eta_\alpha}{MU} & 0 \\ \frac{-aC_{\alpha f}\epsilon_\alpha}{J_z} & -\frac{dC_{\lambda f}\epsilon_\alpha}{2J_z} \end{pmatrix}, \boldsymbol{B_{u3}} := \begin{pmatrix} 0 & 0 \\ \frac{-aC_{\alpha f}\chi_\lambda}{J_z} & -\frac{dC_{\lambda f}\eta_\lambda}{2J_z} \end{pmatrix} \tag{C.2i}$$

where $\epsilon_\alpha := \chi_\alpha + \eta_\alpha$ and $\epsilon_\lambda := \chi_\lambda + \eta_\lambda$.

Matrices that appear in the parametric descriptor form of the yaw roll model admit the following definitions:

$$\boldsymbol{E_0} := \begin{pmatrix} (M_s + M_U)U & 0 & M_s h_s & 0 \\ 0 & I_{rr} & I_{r\dot{p}} & 0 \\ M_s h_\phi U & I_{\phi r} & I_x & 0 \\ 0 & 0 & 0 & 1 \end{pmatrix} \tag{C.3a}$$

$$\boldsymbol{E_1} := \begin{pmatrix} (M_s + M_u)U\eta_\alpha & 0 & M_s h_s \eta_\alpha & 0 \\ 0 & I_{rr}\epsilon_\alpha & I_{r\dot{p}}\epsilon_\alpha & 0 \\ 0 & 0 & 0 & 0 \\ 0 & 0 & 0 & 0 \end{pmatrix} \tag{C.3b}$$

$$\boldsymbol{E_2} := \begin{pmatrix} (M_s + M_u)U\eta_\alpha & 0 & M_s h_s \eta_\alpha & 0 \\ 0 & I_{rr}\epsilon_\alpha & I_{r\dot{p}}\epsilon_\alpha & 0 \\ 0 & 0 & 0 & 0 \\ 0 & 0 & 0 & 0 \end{pmatrix} \tag{C.3c}$$

$$\boldsymbol{E_3} := \begin{pmatrix} (M_s + M_u)U\eta_\lambda & 0 & M_s h_s \eta_\lambda & 0 \\ 0 & I_{rr}\epsilon_\lambda & I_{r\dot{p}}\epsilon_\lambda & 0 \\ 0 & 0 & 0 & 0 \\ 0 & 0 & 0 & 0 \end{pmatrix} \tag{C.3d}$$

$$\boldsymbol{A_0} := \begin{pmatrix} -(C_{\alpha f}+C_{\alpha r}) & -(M_s+M_u)U+\frac{bC_{\alpha r}-aC_{\alpha f}}{U} & 0 & 0 \\ bC_{\alpha r}-aC_{\alpha f} & -\frac{a^2C_{\alpha f}+b^2C_{\alpha r}}{U} & 0 & 0 \\ 0 & -M_s h_\phi U & -c_R & M_s g h_\phi - k_R \\ 0 & 0 & 1 & 0 \end{pmatrix} \tag{C.3e}$$

$$\boldsymbol{A_1} := \begin{pmatrix} -C_{\alpha r}\eta_\alpha & (-(M_s+M_u)U+\frac{bC_{\alpha r}}{U})\eta_\alpha & 0 & 0 \\ bC_{\alpha r}\epsilon_\alpha - aC_{\alpha f}\chi_\alpha & -\frac{a^2C_{\alpha f}\chi_\alpha+b^2C_{\alpha r}\epsilon_\alpha}{U} & 0 & 0 \\ 0 & 0 & 0 & 0 \\ 0 & 0 & 0 & 0 \end{pmatrix} \tag{C.3f}$$

$$\boldsymbol{A_2} := \begin{pmatrix} -C_{\alpha f}\eta_\alpha & (-(M_s+M_u)U-\frac{aC_{\alpha f}}{U})\eta_\alpha & 0 & 0 \\ bC_{\alpha r}\chi_\alpha - aC_{\alpha f}\epsilon_\alpha & -\frac{a^2C_{\alpha f}\epsilon_\alpha+b^2C_{\alpha r}\chi_\alpha}{U} & 0 & 0 \\ 0 & 0 & 0 & 0 \\ 0 & 0 & 0 & 0 \end{pmatrix} \tag{C.3g}$$

$$\boldsymbol{A_3} := \begin{pmatrix} -C_{\alpha r}\eta_\lambda & (-(M_s+M_u)U+\frac{bC_{\alpha r}}{U})\eta_\lambda & 0 & 0 \\ bC_{\alpha r}\epsilon_\lambda - aC_{\alpha f}\chi_\lambda & -\frac{a^2C_{\alpha f}\chi_\lambda+b^2C_{\alpha r}\epsilon_\lambda}{U} & 0 & 0 \\ 0 & 0 & 0 & 0 \\ 0 & 0 & 0 & 0 \end{pmatrix} \tag{C.3h}$$

$$\boldsymbol{B_{w0}} := \begin{pmatrix} C_{\alpha f} & 0 & 0 \\ aC_{\alpha f} & 0 & 0 \\ 0 & 0 & 0 \\ 0 & 0 & 0 \end{pmatrix}, \boldsymbol{B_{w1}} := \begin{pmatrix} 0 & 0 & 0 \\ aC_{\alpha f}\chi_\alpha & 0 & 0 \\ 0 & 0 & 0 \\ 0 & 0 & 0 \end{pmatrix} \tag{C.3i}$$

$$\boldsymbol{B_{w2}} := \begin{pmatrix} C_{\alpha f}\eta_\alpha & 0 & 0 \\ aC_{\alpha f}\chi_\alpha\epsilon_\alpha & 0 & 0 \\ 0 & 0 & 0 \\ 0 & 0 & 0 \end{pmatrix}, \boldsymbol{B_{w3}} := \begin{pmatrix} 0 & 0 & 0 \\ aC_{\alpha f}\chi_\lambda & 0 & 0 \\ 0 & 0 & 0 \\ 0 & 0 & 0 \end{pmatrix} \tag{C.3j}$$

$$\boldsymbol{B_{u0}} := \begin{pmatrix} C_{\alpha f} & 0 & 0 \\ aC_{\alpha f} & \frac{d}{2}C_{\lambda f} & 0 \\ 0 & 0 & \frac{d}{2}M_s g \\ 0 & 0 & 0 \end{pmatrix}, \boldsymbol{B_{u1}} := \begin{pmatrix} 0 & 0 & 0 \\ aC_{\alpha f}\chi_\alpha & \frac{d}{2}C_{\lambda f}\eta_\alpha & 0 \\ 0 & 0 & 0 \\ 0 & 0 & 0 \end{pmatrix} \tag{C.3k}$$

$$\boldsymbol{B_{u2}} := \begin{pmatrix} C_{\alpha f}\eta_\alpha & 0 & 0 \\ aC_{\alpha f}\epsilon_\alpha & \frac{d}{2}C_{\lambda f}\epsilon_\alpha & 0 \\ 0 & 0 & \frac{d}{2}M_s g \\ 0 & 0 & 0 \end{pmatrix}, \boldsymbol{B_{u3}} := \begin{pmatrix} 0 & 0 & 0 \\ aC_{\alpha f}\chi_\lambda & \frac{d}{2}C_{\lambda f}\eta_\lambda & 0 \\ 0 & 0 & 0 \\ 0 & 0 & 0 \end{pmatrix}. \quad \text{(C.3l)}$$

REFERENCES

1. Powers, W. F. and P. R. Nicastri, "Automotive Vehicle Control Challenges in the 21st century", Control Engineering Practice, V.8, No.2, pp 605-618, 2000.

2. Pasillas-Lépine, W., "Hybrid Modeling and Limit Cycle Analysis for a Class of Five-Phase Anti-Lock Brake Algorithms ", Vehicle System Dynamics, V.44, No.2, pp 173-188, 2006.

3. van Zanten, A. T., "Bosch ESP Systems: 5 Years of Experience", V. 109, No.7, pp 428-436, SAE paper No. 2000-01-1633, 2000.

4. Chun, K. and M. Sunwoo, "Wheel Slip Tracking Using Moving Sliding Surface", Proceedings of IMechE., Part D: Automobile Engineering, V.219, No.1, pp 31-41, 2005.

5. Lu, C. and M. Shih, "Application of the Pacejka Magic Formula Model of a Hydraulic Anti-Lock Braking System for Light Motorcycle", Vehicle System Dynamics, V.41, No.6, pp 431-448, 2004.

6. Nouillant, C., F. Assadian, X. Moreau and A. Oustaloup, "Feedforward and Crone Feedback Control Strategies for Automobile ABS", Vehicle System Dynamics, V.38, No.4, pp 293-315, 2002.

7. Solyom, S. and A. Rantzer, "ABS Control-A Design Model and Control Structure", in "Nonlinear and Hybrid Systems in Automotive Control", Rolf Johansson and Anders Rantzer, ed.s, 2003.

8. Yi, J., L. Alvarez, X. Claeys and R. Horowitz, " Emergency Braking Control with an Observer-based Dynamic Tire/Road Friction Model and Wheel Angular Velocity Measurement", Vehicle System Dynamics, V.39, No.2, pp 81-97, 2003.

9. Alvarez, L., J. Yi, R. Horowitz and L. Olmos, "Dynamic Friction Model-Based Tire-Road Friction Estimation and Emegency Braking Control", Transactions of the ASME , V.127, pp 22-32, 2005.

10. Petersen, I., T. A. Johansen, J. Kalkkuhl and J. Ludemann, "Wheel Slip Control in ABS Brakes Using Gain Scheduled Constrained LQR", Norwegian University of Science and Technology, Technical Report, 2001.

11. Petersen, I., T. A. Johansen, J. Kalkkuhl and J. Ludemann, "Wheel Slip Control in ABS Brakes Using Gain Scheduled Constrained LQ-LPV/LMI Analysis and Experimental Results", Norwegian University of Science and Technology, Technical Report, 2003.

12. Ueki, N., J.T. Kubo, K. I. Toshio and M. Uchiyama, "Vehicle Dynamics Electric Control Systems for Safe Driving", Hitachi Ltd., Technical Report, 2003. `www.hitachi.com/ICSFiles/afieldfile/2004/11/26/r2004_04_104_3.pdf`.

13. Petersen, I., *Wheel Slip Control in ABS Brakes Using Gain Scheduled Optimal Control with Constraints*, Ph.D. Thesis, Department of Engineering Cybernetics, Norwegian University of Science and Technology, Trondheim, Norway, 2003.

14. van Zanten, A. T., R. Erhardt and G. Pfaff, "VDC, the Vehicle Dynamics Control System of Bosch ", SAE Paper No. 950759, 1995.

15. Yasui, Y., K. Tozu, N. Hattori and M. Sugisawa, "Improvement of Vehicle Directional Stability for Transient Steering Maneuvers Using Active Brake Control", V.105, No.6, pp 537-543, SAE paper No. 960485, 1996.

16. Koibuchi, K., M. Yamamoto, Y. Fukada and S. Inagaki, "Vehicle Stability Control in Limit Cornering by Active Brake", V.105, No.6, pp 555-565, SAE paper No. 960487, 1996.

17. Ghoneim, A. Y., C. W. Lin, D. M. Sidlosky, H. H. Chen, Y. Chin and M. J.

Tedrake, “Integrated Chassis Control to Enhance Vehicle Stability”, Int. J. Vehicle Design, V.23, No.1, pp 124-145, 2000.

18. Boada, B.L., M. J. L. Boada and V. Díaz, “Fuzzy Logic Applied to Yaw Moment Control for Vehicle Stability”, Vehicle System Dynamics, V.43, No.10, pp 753-770, 2005.

19. Güvenç, B. A., L. Güvenç, E. S. Öztürk and Yigit, T., “ Model Regulator Based Individual Wheel Braking Control”, Proceedings of 2003 IEEE Conference on Control Applications, V.1, pp 31-36, 2003.

20. Johansson, B. and M. Gäfvert, “ Untripped SUV Rollover Detection and Prevention”, CDC 43rd IEEE Conference on Decision and Control, V.5, 2004.

21. Chung, T. and Y. Kyongsu, “ Design and Evaluation of Side Slip Angle- Based Vehicle Stability Control Scheme on a Virtual Test Track”, IEEE Transactions on Control Systems Technology, V.4, No.2, pp 224-234, 2006.

22. Hancock, M. J., R. A. Williams, T. J. Gordon and M. C. Best, “A Comparison of Braking and Differential Control of Road Vehicle Yaw-Sideslip Dynamics”, Proceedings of IMechE. Part D: Automobile Engineering, V.219, No.D3, pp 309-327, 2005.

23. Birch, S., “5 Series Changes Shape”, Automotive Engineering International, SAE Publications, Oct. 2003.

24. Ackermann, J., T. Bünte and D. Odenthal, “Advantages Of Active Steering For Vehicle Dynamics Control”, Proceedings of International Symposium on Automotive Technology and Automation, V.32, pp 263-270, 1999.

25. Ono, E., S. Hosoe, K. Asano, M. Sugai and S. Doi, “Robust Stabilization of the Vehicle Dynamics by Gain-Scheduled H_∞ Control”, Proceedings of the 1999 IEEE, International Conference on Control Applications, V.2, 1999.

26. Mammar, S. and D. Koenig, "Vehicle Handling Improvement by Active Steering", Vehicle System Dynamics, V. 38, No. 3, pp. 211-242, 2002.

27. Hecker, S., "Robust Hinf-based Vehicle Steering Control Design", IEEE International Conference on Control Applications, Munich, Germany, Proceeding of IEEE CCA, 2006.

28. Bünte, T., D. Odenthal, B. Aksun Güvenç and L. Güvenç, "Robust Vehicle Steering Control Design Based on the Disturbance Observer", IFAC Advances in Automotive Control, pp 97-106, 2003.

29. Shibahata, Y., K. Shimada and T. Tomari, "Improvement of Vehicle Maneuverability by Direct Yaw Moment Control", Vehicle System Dynamics, V. 22, pp. 465-481, 1993.

30. Trächtler, A., "Integrated Vehicle Dynamics Control Using Active Brake, Steering and Suspension Systems ", Vehicle System Dynamics, V.36, No.1, pp 1-11, 2004.

31. Elbeheiry, E.M., Y. F. Zeyada, and M. E. Elaraby, "Handling Capacities of Vehicles in Emergencies Using Coordinated AFS and ARMC Systems", Vehicle System Dynamics, V.35, No.3, pp 195-215, 2001.

32. Gáspár, P., Z. Szabó and J. Bokor, "The Design of an Integrated Control System in Heavy Vehicles Based on an LPV Method", Proceedings of the 44th IEEE Conference on Decision and Control and the European Control Conference, Sevilla, Spain, pp 6722-6727, 2005.

33. Mokhiamar, O. and M. Abe, "Active Wheel Steering and Yaw Moment Control Combination to Maximize Stability as well as Vehicle Responsiveness During Quick Lane Change for Active Vehicle Handling Safety", Proceedings of the IMECHE. Part D Journal of Automobile Engineering, V.216, no. 2, pp. 115-124, 2002.

34. Ono, E., S. Hosoe, H. D. Tuan and S. Doi, "Bifurcation in Vehicle Dynamics and Robust Front Wheel Steering Control", IEEE Transactions on Control Systems Technology, V.6, No.3, pp 412-420, 1998.

35. Ünyelioglu, K. A., Ü. Özgüner, T. Hissong and J. Winkelman, "Wheel Torque Proportioning, Rear Steering and Normal Force Control: A Structural Investigation", IEEE Transactions on Automatic Control, V.42 No.6, pp 803-818, 1997.

36. Hac, A. B., H. H. Chen, E. J. Bedner and S. P. Loudon, "Integrated Control of Active Tire Steer and Brakes", US Patent No. 6453226, 2002.

37. Gordon, T., M. Howell and F. Brandao, "Integrated Control Methodologies", Vehicle System Dynamics, V.40, No.1-3, pp 157-190, 2003.

38. Pacejka, H. B., *Tyre and Vehicle Dynamics*, Butterworth Heinemann, 2002.

39. Gillespie, T., *Fundamentals of Vehicle Dynamics*, SAE Publications, 1992.

40. Yu, C. and T. Liu , "Full Control Modes of a Four-Wheeled Vehicle with Zero Body-Sideslip Angle and Zero Body Motions", International Journal of Vehicle Design, V. 38, No.1, pp 79-95, 2005.

41. Greenwood, D. T., *Principles of Dynamics*, Prentice Hall, Englewood Cliffs, N.J., 1965.

42. Segel, L. "Theoretical Prediction and Experimental Substantiation of the Response of the Automobile to Steering Control", The Institution of Mechanical Engineers, Proceedings of the Automobile Division, No. 7, pp 310-330, 1957.

43. Kiencke, U. and L. Nielsen, " Automotive Control Systems For Engine, Driveline and Vehicle", Springer, 2000.

44. Zhou, K., J. C. Doyle and K. Glover, *Robust and Optimal Control*, Prentice-Hall, Inc. Upper Saddle River, NJ, USA, 1995.

45. Doyle, J., J. Francis and K. Tannenbaum, *Feedback Control Theory*, Macmillan Englewood Cliffs, NJ, USA, 1995.

46. Löfberg, J., "YALMIP : A Toolbox for Modeling and Optimization in MATLAB", Proceedings of the CACSD Conference, Taipei, Taiwan, pp 284-289, 2004.

47. Sturm, J. F., "Using SeDuMi 1.02, a Matlab Toolbox for Optimization Over Symmetric Cones", Optimization Methods and Software, V.11, pp 625-653, 1999.

48. Masubuchi, I., A. Ohara and N. Suda, "LMI-based Output Feedback Controller Design", Proceedings of the Conference on Decision and Control, pp 3473-3477, 1997.

49. Scherer, C. W. and S. Weiland, "Lecture Notes DISC course on Linear Matrix Inequalities in Control", Mechanical Engineering Systems and Control Group, Delft University of Technology, 2004. `www.control.aau.dk/∼jakob/courses/lmi2004/lmi.pdf`.

50. Limpert, R., *Brake Design and Safety*, SAE International, 1992.

51. Switkes, J. and C. Gerdes, "Guaranteeing Lanekeeping Performance With Tire Saturation Using Computed Polynomial Lyapunov Functions", Proceedings of IMECE, ASME International Mechanical Engineering Congress and Exposition, Orlando, Florida, USA, 2005.

52. Ray, L., "Nonlinear State and Tire Force Estimation for Advanced Vehicle Control", IEEE Transactions on Control Systems Technology, V.3, No. 1, pp 117-124, 1995.

53. Dixon, J., *Tires, Suspension and Handling*, SAE Publications, Second Edition, 1996.

54. Garrott W. R., J. G. Howe and G. Forkenbrock , "Results from NHTSA's Experimental Examination of Selected Maneuvers that may Induce On-Road Untripped,

Light Vehicle Rollover ", V.110, No.6, pp 78-104, SAE paper No. 2001-01-0131, 2001.

55. Peng, H. and A. Y. Üngören, "Rollover Propensity Evaluation of an SUV Equipped with a TRW VSC System", SAE paper 2001-01-0128, 2001.

56. Ma, W. and H. Peng, "A Worst-case Evaluation Method for Dynamic Systems", ASME J. of Dynamic Systems, Measurement and Control, V.121, No.2, pp.191-199, 1999.

57. Polat, İ., E. Eşkinat and İ. E. Köse, "Dynamic Output Feedback Control of Quasi-LPV Mechanical Systems", *Submitted to IET Control Theory & Applications.*

58. Gahinet, P., P. Apkarian and M. Chilali, "Affine Parameter-Dependent Lyapunov Functions for Real Parametric Uncertainty", *IEEE Transactions on Automatic Control*, V.41, No.3, pp.436-442, 1996.

59. Chen, B., *Warning and Control for Rollover Prevention* , PhD Thesis, Mechanical Engineering Department, The University of Michigan, Ann Arbor, 2001.

60. Furleigh, C. C., M. J. Vanderploeg, and C. Y. Oh, "Multiple Steered Axles for Reducing the Rollover Risks of Heavy Articulated Trucks", SAE paper No. 881866, 1988.

61. Sampson, D. J. M and D. Cebon, "Active Roll Control of Single Unit Heavy Road Vehicles", Vehicle System Dynamics, V.40, No.4, pp 229-270, 2003.

62. Pflug, H. C., E.-Ch. von Galsner and R. Povel, "Improvement of Commercial Vehicles'Handling and Stability by Smart Chassis Systems", Smart Vehicles, pp 318-338, 1995.

63. Chen, B. and H. Peng, "Differential-Braking-Based Rollover Prevention for Sports Utility Vehicles with Human in-the-Loop Evaluations", Vehicle System Dynamics, V.36, No.4-5, pp 359-389, 2001.

64. Ackermann, J. and D. Odenthal, "Damping of Vehicle Roll Dynamics by Gain Scheduled Active Steering", DLR, German Aerospace Center, Institute of Robotics and System Dynamics, Technical Report, 1999.

65. Scherer, C. W., "LPV Control and Full Block Multipliers", Automatica, V.37, No.3, pp 361-375 , 2001.

66. Aneke, N. P. I., J. Ackermann, T. Bünte, and H. Nijmeijer, "Application of Nonlinear Disturbance Decoupling to Active Car Steering", DLR, German Aerospace Center, Institute of Robotics and System Dynamics, Technical Report, 1999.

67. Boada, M. J. L., B. L. Boada, A. Munoz and V. Díaz, "Integrated Control of Front-Wheel Steering and Front Braking Forces on the Basis of Fuzzy Logic ", Proc. IMechE Part D. : J. Automobile Engineering, V.220, No.124, pp 253-267, 2005.

68. Carlson, C. R. and J. C. Gerdes, "Optimal Rollover Prevention with Steer by Wire and Differential Braking", Proc. IMECE, ASME International Mechanical Engineering Congress and Exposition, Washington, D.C., V.72, No.1, pp 345-354, USA, 2003.

69. Genta, G., *Motor Vehicle Dynamics: Modeling and Simulation*, Series in Advances in Mathematics for Applied Sciences, V.43, 1997.

70. Reimpell, J., H. Stoll and J. W. Betzler, *The Automotive Chassis: Engineering Principles*, Second Edition, Butterworth-HeineMann, 2001

71. Ellis, J. R., *Vehicle Handling Dynamics*, Mechanical Engineering Publications, Page Bros, Norwich, 1994.

72. Scherer, C. W., *Theory of Robust Control*, Mechanical Engineering Systems and Control Group, Delft University of Technology, 2001.

73. Macadam, C. C., "Understanding and Modeling the Human Driver", Vehicle

System Dynamics, V.40, No.1,pp 101-134, 2003.

74. Dettori, M., *LMI Techniques for Control with Application to a Compact Disc Player Mechanism*, PhD thesis, Delft University of Technology, Mechanical Engineering Systems and Control Group, Netherlands, February 2001.